MESOSCALE COMPUTATIONAL PREDICTION AND QUANTIFICATION OF THERMOMECHANICAL IGNITION BEHAVIOR OF POLYMER-BONDED EXPLOSIVES (PBXs)

A Dissertation
Presented to
The Academic Faculty

by

Ananda Barua

In Partial Fulfillment
of the Requirements for the Degree
Doctor of Philosophy in the
School of Mechanical Engineering

Georgia Institute of Technology
August, 2013

MESOSCALE COMPUTATIONAL PREDICTION AND QUANTIFICATION OF THERMOMECHANICAL IGNITION BEHAVIOR OF POLYMER-BONDED EXPLOSIVES (PBXs)

Approved by:

Dr. Min Zhou, Advisor G.W.W. School of Mechanical Engineering *Georgia Institute of Technology*	Dr. David L. McDowell G.W.W. School of Mechanical Engineering *Georgia Institute of Technology*
Dr. Naresh N. Thadhani School of Materials Science and Engineering *Georgia Institute of Technology*	Dr. Yasuyuki Horie AFRL/MNME, Munitions Directorate *Eglin Air Force Base*
Dr. Richard W. Neu G.W.W. School of Mechanical Engineering *Georgia Institute of Technology*	

Date Approved: May 8, 2013

To my grandparents, parents and brother

ACKNOWLEDGEMENTS

As I reflect back on the time I spent at Georgia Tech (GT), I feel there are many people who helped make my journey here an enriching and fulfilling experience. Firstly, I would like to thank my advisor Dr. Min Zhou who has been instrumental in my development on the academic and personal front. This body of work would not have taken shape without his advice, insight and encouragement. I would like to express my gratitude to Dr. Yasuyuki Horie who has mentored my work since the very beginning. I would like to thank Dr. Suhithi Peiris and Dr. Naresh Thadhani for their valuable suggestions and several helpful discussions. I would like to thank my committee members, Dr. David McDowell and Dr. Richard Neu for reviewing my work and providing insightful comments.

I have had the opportunity to work with several talented researchers and collaborators at the Air Force Research Labs at Eglin, FL. In particular, I wish to thank Dr. Michael Denigan, Dr. Jennifer Jordan, Dr. Chip Butler, Lt. John Cox, Dr. Mike Gunger and Harold Brown for their support and the interesting discussions.

I would like to gratefully acknowledge my friends and colleagues at GT. In particular, I wish to thank Siddharth Avachat, Seokpum Kim, Barrett Hardin, Yifan Gao, Christopher Lammi, Yan Li, Jung Boo Jung, Kwangsub Jung, Hongwei Li, Hanna Wagner, Bret Ellis, Jeff Lloyd, Sathyanarayanan Raghavan, Christine Taylor, Bhaskar Pant, Ram Subramaniam, and many others for their help and encouragement.

I would especially like to thank my friends in Atlanta, Abhishek Banerjee, Anshuman Goswami, Arindam Khan, Aritra Banerjee, Arindam Basu, Arkadeep Kumar, Atri and Lipilekha Dutta, Ayan Chakrabarti, Akash Chakrabarti, Payel Chatterjee, Debashis Banerjee, Debrup Das, Pamela Patra, Dibyendu Das, Koushik and Priya Kundu, Monodeep Kar, Padmanava Sen, Prabir and Prateeti Saha, Ranadip Acharya, Sunipa Guha, Ravi Pallantla, Sabyasachi Deyati, Saikat Sarkar, Payel Paul, Samit Ghosh, Risa Ghosh, Rimi Hazra, Sandeep Samal, Shafi and Adria Motiwalla, Shreyas Sen, Sneha Sathyanarayanan, Sourav Dutta, Subho and Proma Chatterjee, Suvadeep Banerjee, Swarnava Ghosh, Tapobrata Bandopadhyay, Zakir Ahmed, Zannatul Ferdous and many others. They have made my life much more interesting and enjoyable than I could have imagined.

Finally, I am eternally indebted to my grandparents, parents, and brother for their unconditional love and support.

TABLE OF CONTENTS

Page

LIST OF TABLES

Page

LIST OF FIGURES

Page

LIST OF SYMBOLS

α	fitting parameter for the relation between τ and v in Eq. (6.10)
α_0	normalizing constant for α
A_c	cross section area of specimen
β	fitting parameter used in Eq. (3.5)
c	specific heat capacity
c_0	effective longitudinal stress wave speed
C, C', k	fitting parameters
δ	average grain size
d_i, d_o	inner and outer diameter of annular region used for detecting hotspots
d	diameter of hotspot
d_{max}	size of the largest hotspot
d_c	critical diameter of hotspot
$\boldsymbol{\Delta}$	separation vector for cohesive element
$\boldsymbol{\varepsilon}$	Eulerian strain tensor
ε	nominal strain
$\dot{\varepsilon}$	nominal strain rate
ε_d	delay strain
Σ	kinetic energy per unit mass of the specimen ($v^2/2$)
Σ_c	critical value of kinetic energy per unit mass of the specimen ($v_c^2/2$)
E	energy absorbed by the specimen
E_c	critical energy
γ	hardening exponent

$\mathcal{G}$	critical energy release rate
G	shear modulus
η	grain volume fraction
η_{ref}	normalizing constant
l_0	initial length of the specimen along loading direction
λ	instantaneous state of mixed mode separation
$\mathbf{L}$	tensor of isotropic elastic moduli
K	bulk modulus
k	thermal conductivity
k	hardening constant used in Eq. (5.8)
l_{avg}	average spacing between hotspots
m	Weibull shape parameter
μ	coefficient of friction
n, n'	fitting parameter
N_A (N_V)	number proportional to the potential sites for hotspot formation per unit area (or volume)
ϕ	cohesive fracture energy
$P(t)$	probability of ignition at time t
P_L	number of phase boundaries encountered per unit length of test line
$\bar{P}_L$	average value of P_L over entire test domain
ρ_p	effective number density of particles per unit volume
ρ_0	effective mass density
r	inter-particle distance used in radial distribution function

$\mathbf{S}$	second Piola-Kirchhoff stress tensor
S_v	surface area per unit volume
S_0	normalizing constant for S_v
ΔS_v	standard deviation of the variation of S_v
ΔS_0	normalizing constant for ΔS_v
$\boldsymbol{\sigma}$	Cauchy stress tensor
σ_x	axial stress along x direction
σ_y	axial stress along y direction
σ_{avg}	average value of equivalent stress over the cross section of the specimen
$\mathbf{T}$	traction vector
T	temperature
T_s	temperature at the surface of a hotspot
T_i	initial temperature of the specimen
T_H	average temperature inside a hotspot
ΔT_{thres}	threshold temperature
T_{max}	maximum allowable traction in bi-linear cohesive law
T^{ref}_{max}	normalizing parameter for T_{max}
t	time from onset of loading
t_r	reduced time for viscoelastic model
t_d	delay time
t_c	time to criticality
t_0	cutoff time
t_{50}	median time to criticality

τ	Weibull time scale parameter
τ_{ref}	normalizing constant for τ
v	imposed boundary velocity
v_c	critical impact velocity below which no ignition occurs
v_0, v_{ref} ,$v_{c,ref}$	normalizing constants
V	volume of specimen or effective domain
$\omega(t)$	probability of ignition per unit volume per time at time t
W	strain energy density
W_b, W_f, W_{vf}, W_k, W_e, W_c	different forms of work and energy dissipation – boundary work, frictional dissipation, viscoelastic dissipation, kinetic energy, elastic strain energy, fracture work
x	distance from the loading surface along loading direction
ξ	number of microstructures

SUMMARY

This research aims at understanding the conditions that lead to reaction initiation of polymer-bonded explosives (PBXs) as they undergo mechanical and thermal processes subsequent to impact. The issue of impact-induced ignition of PBXs has received significant attention over the past few decades. However, the mechanisms leading to energy localization in PBXs are not well quantified, primarily due to a lack of experimental observations and quantitative analyses at the mesoscale. To analyze this issue, a cohesive finite element method (CFEM) based finite deformation framework is developed and used to quantify the thermomechanical response of PBXs at the microstructure level. This framework incorporates the effects of large deformation, thermomechanical coupling, failure in the forms of micro-cracks in both bulk constituents and along grain/matrix interfaces, and frictional heating. Digitized micrographs of actual HMX/Estane PBX materials and idealized microstructures are analyzed, which have a range of volume fractions of different constituents, grain morphology and defects such as imperfect bonding.

To understand the link between hotspot formation and ignition sensitivity, a novel criterion for the ignition of heterogeneous energetic materials under impact loading is developed. The new criterion is used to quantify the critical impact velocity, critical time to ignition, and critical input work at ignition for non-shock conditions as functions of microstructure of granular HMX and PBX. A modified James [1] threshold relation between impact velocity and critical input energy at ignition for non-shock loading is developed, involving an energy cutoff and permitting the effects of microstructure and loading to be accounted for.

A novel approach for computationally predicting and quantifying the stochasticity of the ignition process in PBX and GX is developed, allowing prediction of the critical time to ignition and the critical impact velocity below which no ignition occurs based on basic material properties and microstructure attributes. Results are cast in the form of the Weibull distribution and used to establish microstructure-ignition behavior relations. The statistical approach allows specific confidence levels to be applied to the results. Finally it is shown that the probability distribution in the Weibull form can be reduced to an ignition threshold relation similar to the James relation [1].

The framework and subsequent analyses shall serve as a useful tool for the design of energetic composites. Ultimately, better understanding of the initiation mechanisms will help build predictive models that will enable the efficient development of new energetic composites with desired property attributes.

CHAPTER 1: INTRODUCTION

1.1 Background and Motivation

Polymer bonded explosives (PBXs) are a class of particulate composites consisting of explosive crystals in a soft polymeric binder (see e.g. Figure 1). They are used in a wide variety of civil and military applications such as detonators and solid rocket propellants. The content of explosives in the composites typically varies between 60-95% by mass, similar to that in pressed explosives. The explosive content is usually HMX (Octahydro-1,3,5,7-tetranitro-1,3,5,7-tetrazocine), RDX (1,3,5-Trinitroperhydro-1,3,5-triazine), PETN (pentaerythritol-tetranitrate), or TATB (triamino-trinitrobenzene) in the form of small crystals [2].

Common binder materials employed in particulate composites comprise a variety of high polymers, including thermoplastic resins (e.g., polyurethane, polypropylene, polystyrene), thermosetting plastics (e.g. epoxies, silicones), elastomers (e.g., rubber), and other plasticized polymer and copolymer systems (e.g., polypropylene glycol, acrylate, hydroxyterminatedpolybutadiene - HTPB and Viton) [3]. The binder is inert but is mixed with other additives such as oxidizers to improve explosive output. The selection process for a binder relies on its thermal, mechanical and surface properties. The mechanical properties of PBXs are strongly influenced by the binder whose elastic modulus is approximately three to four orders of magnitude lower than that of the granules under ambient conditions. This allows the binder to deform and absorb most of the mechanical work imparted to the composites during impact loading. Hence, the binder provides structural toughness to and reduces the impact sensitivity of the composites. This attribute also allows PBXs to be pressed and machined to desired shapes and sizes.

Solid high explosives such as HMX and RDX have high energy densities on the order of 1 kcal·g^{-1}. They are powerful sources of energy for propulsion as well as civil and military applications. Under ambient conditions, these materials release energy relatively slowly. However, their combustion can result in catastrophic detonations that propagate at speeds on the order of 7-9 km·sec^{-1}. During such a detonation process, the release rate of energy is known to be on the order of 100 GW·cm^{-2} at the detonation front. As a reference, the current total electric generating capacity of the United States is on the order of 400 GW (Fickett and Davis [4], Asay [5]). Thus, an accidental detonation of these explosives (or even near detonation) could result in catastrophic tragedies. Unfortunately, history is full of events that cost not only huge monetary and materials losses, but also human lives. Tragic accidents are a good motivator for research in the safety (safe handling and use) of explosives.

However, as remarked by Asay [5], “the problem is that with all of the study and the thousands of years of experience, we still cannot predict with any precision, in general, what will happen to an explosive if we hit it, heat it, drag it, drop it, or do anything else outside of its design envelop”. What is worse, the design envelop is “historically rooted in test protocols used in the qualification of the material that address its performance as well as safety and handling characteristics.” (Foster [6]). Hence, many different relative safety tests must be run to improve the probability that all detonation scenarios have been identified. The tests include a variety of stimuli to energy release, both intentional and accidental, that are mechanical, thermal, electrical, and shock-wave-induced in nature. The accidental detonation of solid high explosives is a hazard that depends on the sensitivity of the materials to these stimuli with regard to the initiation of chemical reaction. Other hazards include chemical instability and toxicity. The focus of this research relates to the sensitivity to impact-induced mechanical insult. Ultimately the goal is to move the development of energetic materials from empiricism based on protocols to design science based on modeling and simulation that capture relevant physics.

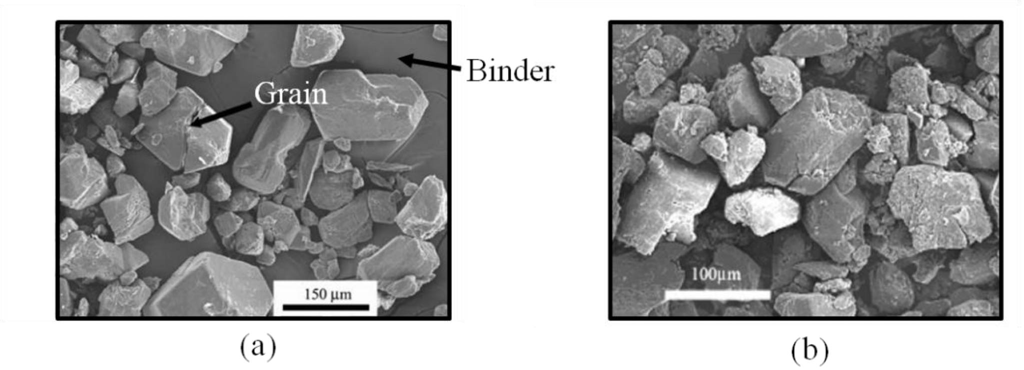

Figure 1: Morphologies of HMX grains in a pressed PBX, (a) before impact loading and (b) after impact loading [7].

1.2 Experimental Characterization of PBXs

The dynamic response of energetic materials at the grain scale has received significant attention over the past two decades [8, 10-16]. Empirical approaches have been developed [17] to model the response under different loading conditions [18]. Especially for PBXs subjected to high strain rates e.g. in a split Hopkinson pressure bar (SPHB). The SHPB allows stress-strain relationships to be measured over a limited range of strain rates and a wider range of temperatures. The strain rate can be controlled by a combination of changing the sample dimensions and the speed at which the incident bar is fired at the sample [19]. Since the impact sensitivity of a PBX is dependent on its composition, a large portion of experimental work has focused on the mechanical properties of PBXs and their individual constituents. The experimental research can be broadly divided into externally applied constraints and internal composition.

1.2.1 Effect of Externally Applied Constraints

The dynamic response of PBX is dependent on both strain rate and initial temperature primarily due to the binder. The viscoelastic binder behaves as a glassy, brittle material at temperatures below the glass transition temperature (T_g), while at temperatures above it, the response is that of a ductile material. Gray et al. [8] measured the stress strain profiles for PBX 9501 at 2000 s^{-1} over a temperature range of -50 to +50 °C. This study serves as an important benchmark for calibration or comparison of numerical models for PBX 9501. The critical strain at which fracture occurred was found to be approximately independent of temperature and strain rate. This indicated that the overall content of explosive might be the dominant influence on the failure strain. The experiments revealed that at high strain rates, PBX failed by cleavage fracture of the HMX granules.

On the other hand, Govier et al. [9] reported that the failure strain of another PBX composition (EDC37), showed dependence on temperature at high strain rates. Moreover, the maximum strength of EDC37 and PBX9501 were similar ~ 150 MPa at -55 °C but were distinct (~55 MPa compared with ~ 20 MPa) at +55 °C. Williamson extended the strain rate regime from very low 10^{-8} to high 10^{3} s^{-1} over a range of temperatures. The failure stress was shown to be a monotonic function of applied strain rate or temperature.

The aspect ratio of the sample also influenced the overall strength of the PBX with smaller sample size showing a higher strength, due to the higher degree of confinement. Photographic evidence showed that shear bands form during failure; however the contribution of shear bands to weakening of the composite is different for different aspect ratios. It is important for computational models to capture this behavior since it is well known that shear bands are associated with localized temperature rises and may contribute to the sensitivity of the material to mechanical insult. These studies signify that the empirical relations derived for one PBX may not be applicable for other PBX systems. Explicit modeling using a systematic variation of properties can be used to evaluate not only the trends, but also the relative importance of these failure mechanisms responsible for the trends in mechanical properties.

The failure mechanisms may be different depending on the loading conditions. Wiegand et al. [10] investigated the effect of confinement on behavior and reported significantly higher elastic modulus and flow stress at higher confinement levels. Siviour et al. [11] argued that the fracture of crystals is unlikely to produce significant heating due to their low fracture toughness. Menikoff et al. [12], on the other hand, reasoned that frictional dissipation along fractured surfaces might lead to high temperature rises, especially under conditions of significant confinement. Chen et al. [13] performed diametric compression tests on discs of PBX. They report that, under tensile stresses, the initial failure started around the edges of larger filler particles and occurred simultaneously at several independent sites. Crystal fracture was observed along the fracture path. This is due to the fracture strength of the crystals being low and possible pre-damage in crystals during the manufacturing process.

1.2.2 Effect of Internal Composition

Palmer and Field [14] studied the mechanical deformation of β-HMX. Siviour et al. [11] showed that the compressive stress-strain behavior of a polymer-bonded sugar composite is linked to that of its binder. In particular, using tomographic scan during quasi-static loading, the authors showed that debonding across the grain-binder interface started to occur even before strain softening is observed in the material response. Their work suggests that damage mechanisms and bulk responses are inherently related to the microstructure.

To this effect, studies have focused on the characterization of heterogeneous microstructures (e.g., Skidmore et al. [15], Liu and Yu [16]), fracture and deformation (e.g., Berghout et al. [17], Rae et al. [18], Liu [19], Williamson et al. [20]), influence of temperature and strain-rate (e.g., Gray et al. [8], Cady et al. [21]) and correlation between microstructure and fracture behavior (e.g., Chen et al. [7]). In particular, Palmer et al. [2] studied different types of PBX compositions based on grain size of HMX and the binder material. The authors found the strength of the composite to be a function of the average crystal size.

The size and distribution of particles also affects the shock sensitivity. A review of literature on the effect of particle size on shock sensitivity of heterogeneous explosives can be found in [22]. Hayes [23] explored the shock sensitivity of porous HMX and found that coarse materials are more sensitive in the low-shock pressure regime (pressure < ~5 GPa) and less sensitive in the high pressure regime. A similar effect was also observed in pressed RDX by Spear and Nanut [22]. Khasainov et al. [24] suggested that this shock sensitivity reversal in PBXs is due to a change in critical hotspot size resulting from differences in the specific interface area of the granules.

1.3 Numerical Analyses

Numerical analysis of high strain-rate experiments have been performed by a number of different researchers. Resnyansky and Gray [25] used a 1D rate dependent viscoelastic constitutive model to describe the constitutive response of the pressure bars and the sample. The authors investigated the effect of the shape of the loading pulse on the calculated stress-strain response of the sample. This study is significant since complex wave behavior in SHPB may result in errors in the computed stress-strain response. Corley et al. [3] investigated the quasistatic and dynamic mechanical properties of PBXs during inverse flyer plate experiments, using an analytical formulation. In the inverse flyer plate impact test, the sample being characterized and a backing plate comprising a well-characterized aluminum are accelerated using a compressed air or powder gun. The results from uniaxial experiments were use to obtain parameters for a non-linear viscoelastic material model. However, homogenization of the PBX does not allow the study of phenomena occurring at the grain-level. Simulations with explicit account of microstructural features and processes allow the delineation of the influences of different microstructural attributes, deformation and failure mechanisms, and heat generation mechanisms.

An early attempt at using a micro-mechanical model for PBX was by Mas et al. [26] at Los Alamos. In this study, HMX was modeled using an elastic plastic constitutive formulation accounting for brittle fracture. The remainder of the finely distributed HMX in the matrix was accounted for by using a dirty binder model. The stress strain curve agreed well with experimentally observed data. Analysis of the pressure contour showed that there was significant variation between phases, which would not have been captured in homogenized models. Much of this flavor can be seen in later numerical works on mesoscale models of PBXs. A brief summary of recent work related to the numerical analyses of PBX at the mesoscale is provided in Sections 1.3.1 and 1.3.2.

1.3.1 Studies Using Eulerian Framework

A significant amount of work has been done on the shock compression of heterogeneous materials using Eulerian-formulation-based approaches. The Eulerian finite-element method uses a mesh which is fixed in space and the material flows through the mesh. This approach is particularly attractive since it eliminates numerical issues associated with mesh distortion. Since individual elements may contain multiple phases, the phase interface needs to be reconstructed. For this purpose, a mixture theory is used, which defines how elements containing more than one element partitions the mean element strain rate among the materials.

Studies using Eulerian framework have yielded useful results with respect to large deformation shock loading of granular composites, response of voids, melting of grains and chemical reactions in explosives [27-30]. Benson et al. [28] used an Eulerian formulation to analyze the shock densification of granular HMX powder. In this study, a methodology was developed for importing experimentally acquired micrographs. The focus was on formation of hot-spot due to localized energy dissipation as the shock wave passed through the HMX granules. This framework was also used by Austin et al. [30-33]

to study the shock compression of microstructures with aluminum-iron oxide (thermite) particles in a polymer binder. Baer [27] studied the consolidation, deformation and reaction of HMX crystals using highly resolved 3D simulations. Their results suggest that the stress state in a heterogeneous material shows large fluctuations and localization of heating or formation of 'hot-spots' is due to inelastic deformation and interaction between crystals which cannot be modeled using a continuum level approach. Menikoff [34-35] studied pore collapse, another important mechanism responsible for the formation of hotspots.

Although Eulerian based codes can capture the shock propagation very well, they cannot explicitly track interfaces, and employ a mixing algorithm to account for the interface between different particles/phases. In this respect using a Lagrangian framework allows explicit tracking of interfaces (Ortiz et al. [36], Espinosa et al. [37]). Consequently phenomena like debonding at interfaces, fracture of grains and friction between contacting surfaces can be studied.

1.3.2 Studies Using Lagrangian Framework

During high strain rate impact of PBXs, damage occurs both as a result of debonding at the grain-matrix interface and fracture of grains. It has been shown experimentally (Banerjee et al. [38]) that debonding at the grain-matrix interface significantly affects the strength of the composite. The authors also performed 2D and 3D numerical simulations on mock PBX over a range of temperatures and strain rates. Their simulations used idealized PBX microstructures having spherical granules. While studying the RVE size on the predicted properties of the composites, the authors report that 2D unit cells containing 10-20 spherical particles are adequate for modeling PBXs containing up to 60% explosive by volume. The authors studied the effect of grain/binder debonding on the elastic modulus of a glass-Estane PBX simulant.

In a recent study, Wu et al. [39] used a rate-dependent viscoelastic cohesive zone model for the binder and a continuum damage model for the HMX grains to simulate the response of PBX 9501 in Brazilian compression tests. The results in the form of stress strain profiles matched those measured by Gray et al. [8]. These were one of the first studies to explicitly account for microstructural damage mechanisms in a Lagrangian framework. Results from these studies suggest that fracture of grains and grain/binder debonding play important roles in the failure of PBXs.

Gonthier et al. [40] studied the dynamic response of granular explosives subject to uniaxial deformation waves. Using a Lagrangian finite and discrete element technique, the authors incorporated contact and friction across the neighboring grains. The authors reported that the plastic work principally affects the average temperature, whereas friction work affects the high frequency, high-temperature fluctuations that are likely responsible for combustion initiation.

More recently, crystal plasticity based approaches using an Arbitrary Lagrangian (ALE) framework have been used to more accurately account for the non-local phenomena occurring during dynamic loading of HMX crystals. Barton et al. [41] crystal based continuum mechanics in the context of dynamic loading. The crystal plasticity model is calibrated to available molecular dynamics and single crystal gas gun.

Subsequently, the model is used to predict behaviors for the collapse of pores under various conditions.

As mentioned earlier, fracture and interfacial debonding between binder and gains and fracture of grains are failure mechanisms which can cause overall loss of strength and lead to frictional dissipation at fractured surfaces. At the outset of this work, a framework was not available which could resolve the various dissipation mechanisms occurring at the grain level, such as failure in the form of microcracks in bulk constituents, debonding along the grain/matrix interfaces, frictional heating and bulk inelastic dissipation. To understand these failure mechanisms and their effects on initiation sensitivity, a CFEM framework is developed in Chapter 2. The framework entails a fully coupled thermal-mechanical formulation, therefore, the interactions between the mechanical process of dynamic deformation and failure and the thermal process of heat generation and conduction can be resolved.

1.4 The Issue of Energy Localization

So far, the mechanisms leading to energy localization in PBXs are not well quantified, primarily due to a lack of experimental observations and quantitative analyses at the meso-scale. Because of the inherent heterogeneities in microstructures, several competing failure mechanisms such as deformation of the binder, debonding at the grain-matrix boundary, fracture of grains and frictional contact between crack faces contribute to the dissipation of the energy imparted to the material. Impurities, microcracks and voids can exacerbate the deformation and failure processes and, therefore, significantly affect the ignition sensitivity and hence the performance of the PBX [42].

While not all dissipation mechanisms directly contribute to heating, they may influence other thermal processes leading to energy localization. For instance, fracture of grains and debonding at grain-matrix boundary result in the creation of new surfaces. Localized frictional dissipation occurring along these fractured surfaces, however, can lead to very high temperatures which in turn can cause melting of the granules and subsequent reaction initiation.

Clearly, the mechanisms responsible for energy localization are complex and a systematic study is needed to evaluate their contributions to the ignition sensitivity of a PBX. In addition, loading conditions (such as strain rate and degree of confinement) influence the rate and manner in which mechanical work is imparted to the material, thereby affecting the localization of energy. Realistic characterization need to consider these factors. This is the subject of Chapters 3 and 4.

1.4.1 Ignition in Explosives

Initiation sensitivity is one of the most important considerations for PBXs. Shock loading is one type of events that can result in initiation and detonation [17, 43]. Initiation and subsequent detonation can also occur under impact loading in the absence of shock [44]. Both types of events require that the mechanisms leading to energy localization need to be better understood.

The initiation of chemical reaction is significantly affected by the local fluctuations of field quantities. The issue partly relates to the formation of hot spots when the materials are subject to mechanical impact. Dissipation associated with mechanisms operative at the grain-level causes localization of thermal energy or the formation of hot spots. Once formed, the hot spots can serve as ignition sites and react exothermally [29]. The hot spots can also lead to deflagration or detonation.

In order to predict impact-induced initiation of energetic materials, reactive models can be used [43, 45]. For such models to be predictive, account for grain-level phenomena is required. In particular, these models require input such as the distributions of the number, sizes, shapes, and temperatures of hot spots for the particular microstructure and loading involved. For example, in [45] a hydrodynamic code is used to obtain information regarding the energy localization, growth and micro-mechanics of hot spots and the information is then used in a reactive model to resolve the physics at the micro-scale. Tarver et al. [29] analyzed the effects of hot spot geometry and surrounding temperatures on ignition and showed that the critical temperature increases rapidly as the hot spot diameter decreases. Also, the critical times to ignition increases rapidly as hot spot temperatures decrease, indicating that mechanisms producing lower rates of heating must act longer over a sufficiently large volume to cause ignition.

Ignition can occur as a result of energy localization in the form of local temperature increases or hotspots. A number of thermomechanical processes occur simultaneously subsequent to impact loading and it is not straightforward to ascribe the ignition to one particular cause [5]. Impact-induced-initiation can be roughly divided into two regimes of interest: shock and non-shock conditions. A brief survey of the most relevant work in both shock and non-shock loading is provided here.

There has been significant progress in developing empirical threshold criteria for ignition under shock loading. In 1969, Walker and Wasley [46] introduced a critical energy relation to describe shock ignition of select solid explosives. This relation, commonly referred to as $P^2\tau$ = constant, relates the energy flux of a sustained plane shock to ignition. The relation was found, however, to be limited in terms of the range of conditions applicable and the number of materials which obey it. Proceedings of the Detonation Symposium (particularly the 7th) contain numerous attempts at establishing shock thresholds in terms of shock wave parameters.

Recently James [1] generalized the $P^2\tau$ = constant relation by including a specific energy "cutoff" analogous to an activation energy. The modification is significant since it allowed the relation to be extended to both homogeneous and heterogeneous explosives.

Several researchers have focused on computational modeling of shock ignition. Relevant works include the modeling of heterogeneous microstructures at the mesoscale (Baer [27, 47-48], Benson et al. [28, 30]), shock response of porous explosives (Hayes [23]), compaction of granular HMX (Menikoff [34, 49]), chemical reaction and hotspot formation (Dlott [50-51]), micromechanical burn of solid explosives (Hamate and Horie [45]), and chemical kinetics of reaction in pure explosives (Tarver et al. [29], Henson et al. [52]), among others.

In the case of non-shock loading, the stress wave front is more diffused. Experimental evidence from Idar [44] suggests that the processes associated with non-shock loading occur over a time span of several microseconds to even milliseconds. Such loads allow slower mechanisms to play a role, including rearrangement of grains and possibly heat loss from hotspots to a cooler region. The dominating energy dissipation mechanisms in non-shock ignition are thought to be friction, followed by plasticity and viscous flow. The failure mechanisms are also significantly affected by the temperature and strain rate (Gray et al. [8]).

In terms of modeling, Dienes et al. [53] studied the impact initiation of explosives using statistical crack mechanics. This approach accounts for crack growth and coalescence. Frictional heating caused by sliding of crack faces can also be analyzed. The authors showed that the overall load displacement response using the approach matches well with experimental results. However, since microstructure is not considered, the spatial distribution of quantities is not captured explicitly.

Wu et al. [54] focused on developing an initiation model using relations between macroscopic variables and conditions at intergranular contact areas. An early effort by Browning [55] is unique in that he developed an analytical threshold condition by combining heat conduction equation with chemical kinetics and sliding friction in both one and two space dimensions.

The challenge associated with the study of ignition in non-shock loading is that the thermal-mechanical-chemical processes may occur over time spans of a few microseconds to several milliseconds. This issue of thermal criticality of hotspots is studied in Chapter 5. Here a generalized approach is developed for analysis of ignition during non-shock loading.

1.4.2 Statistical Approaches to Ignition Sensitivity

The sensitivity of solid high explosives is a difficult, if not intractable, subject (Asay [5]). There have been efforts to move the development of these materials from empiricism based on protocols to design science based on modeling and simulation that capture relevant physics. The trend is to relate design, synthesis, test and evaluation to control and ensure functionality (Foster [6]). These efforts are stimulated by progress in experimental techniques (e.g., Sheffield and Engelke [56], Thadhani [57]), theory (e.g., Asay [5]), numerical models (Benson and Conley [28], Baer and coworkers [27, 48], Panchadhara and Gonthier [40]), and computing tools (high performance computing).

The use of statistical or probabilistic approaches to understanding chemical initiation dates back many years. Cochran was the first to introduce a statistical treatment of heterogeneities that influence shock initiation (Cochran [58]). He carried out a preliminary calculation for PBX 9404 and indicated that, with refinement, the model can duplicate the success of the ignition and growth model (Lee and Tarver [59]). Indeed, this approach was expanded to include local thermo-chemical reactions and showed that the model has the capability to capture essential features of (1) shock-induced ignition and growth leading up to detonation, (2) quenching, and (3) curved detonation (Horie and Hamate [60], Hamate and Horie [45]).

Recently, Nichols and Tarver [61] adopted a different route for extending the Cochran approach by introducing a statistical hotspot model in ALE3D which considers the effects of initial shock pressure and density of hotspots on the shock-induced initiation of PBXs. Hill et al. [62] reduced this model into an analytically solvable problem. Baras et al. [63] explored a stochastic description of exothermic reactions leading to adiabatic explosion. Chemical reactions are modeled as a Markovian birth and death process that bears some resemblance to the approach by Nichols and Tarver [61]. Browning [55] developed an analytical threshold condition by combining heat conduction with chemical kinetics and sliding friction in both one and two dimensions. Gruau et al. [64-65] expanded on the work by Browning on frictional heating. Using a concrete-like constitutive law for PBX with pressure-dependent plasticity, the authors were able to replicate the dot- or ring-shaped ignition seen in the Steven test [66].

Baer and his colleagues [67] have pursued a PDF (probability density function) approach in the manner of turbulent flow modeling. Although the mathematics is elegant, it is not yet clear how the solutions can be related to explosive sensitivity in terms of inherent material heterogeneities. The separation of cause and effect is itself an unfinished research topic.

The issue of stochasticity associated with ignition sensitivity is addressed in Chapter 6. Here, an approach for computationally predicting and quantifying the stochasticity of the ignition process in PBX and GX is developed. This approach can be used to predict the critical time to ignition and the critical impact velocity below which no ignition occurs based on basic material properties and microstructure attributes. Results are cast in the form of the Weibull distribution and used to establish microstructure-ignition behavior relations. Additionally, the statistical approach allows specific confidence levels to be applied to the results.

CHAPTER 2: MESOSCALE MODELING FRAMEWORK

2.1 Introduction

In this chapter, a CFEM-based framework is developed and used, accounting for microstructure and the thermal-mechanical processes outlined in Chapter 1. Such a framework has been extensively used to study a wide variety of issues related to delamination and fracture such as tensile decohesion (Needleman [68]), quasi-static crack growth (Tvergaard and Hutchinson[69]), ductile fracture (Tvergaard and Needleman [70-71]), dynamic fracture (Xu and Needleman [72]), dynamic fragmentation (Camacho and Ortiz [73], Espinosa et al. [74]), delamination in composites (Camanho et al. [75], Minnaar and Zhou [76]) and microstructural fracture (Zhai and Zhou [77]). Here, cohesive elements are embedded throughout the microstructure, along all elements boundaries, as in [77]. This form of CFEM obviates the need for criteria for fracture initiation and propagation but requires the model to satisfy limitations on mesh density and cohesive stiffness (Tomar et al. [78]). Contact and friction between failed crack surfaces are accounted for, allowing heating due to interfacial sliding to be analyzed along with heating due to bulk constitutive inelasticity. A range of actual and idealized microstructures with varying attributes are considered in order to establish relationships between microstructural features such as grain size, distribution and contiguity and stress-strain response, failure and heating.

This chapter is based on the work published in Refs. [79-80].

2.2 Microstructures Analyzed

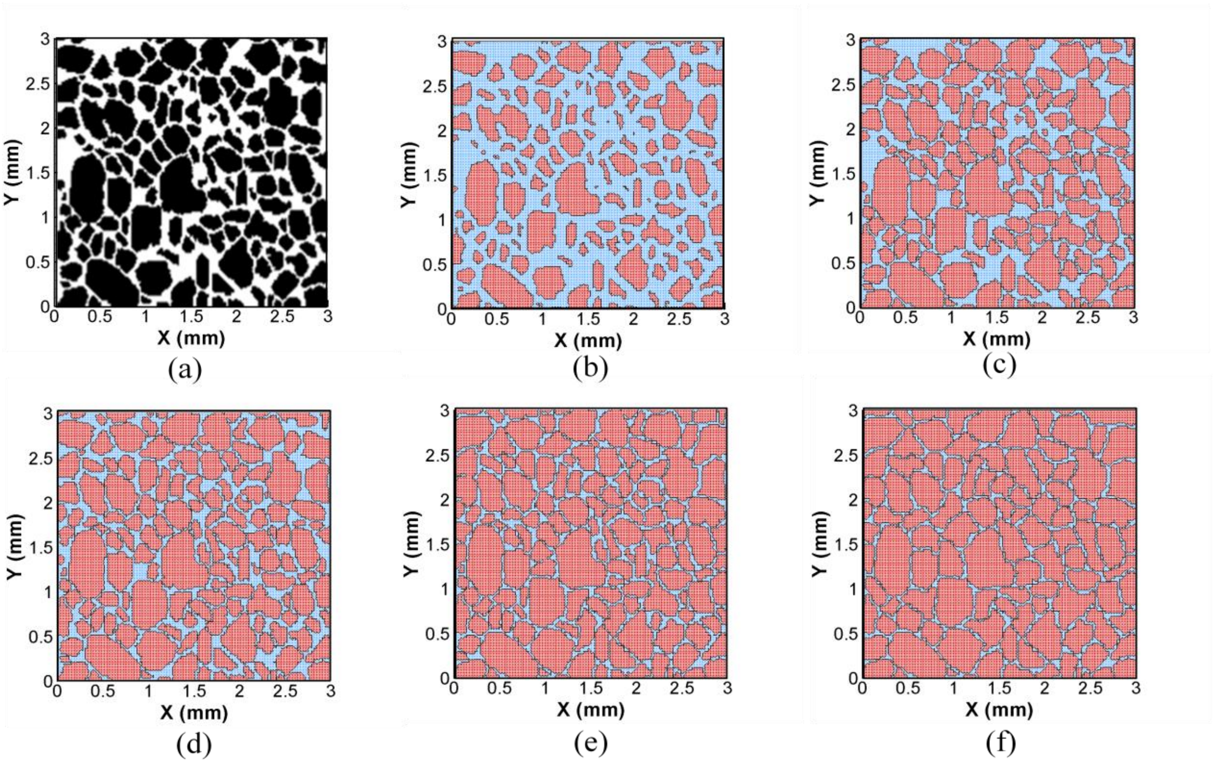

(a) (b) (c)

(d) (e) (f)

Figure 2: (a) Digitized image of a PBX microstructure from [11] and variations with grain volume fractions of (b) 0.42, (c) 0.64, (d) 0.69, (e) 0.77 and (f) 0.82.

As shown in Figure 1, a typical PBX microstructure consists of explosive particles such as HMX or RDX in a soft polymer matrix. The preparation of PBXs involves mixing, in a solvent, the explosive powder, binder and a small amount of additives such as plasticizers and oxidizers. Once the mixture has dried up, it is compressed at an elevated temperature to increase density and in turn the explosive output of the charge. A detailed description of the preparation of PBX 9501 may be found in [81]. Explosive crystals have multifaceted irregular shapes and are distributed randomly. Most PBX composites are essentially isotropic at scales above several interparticle distances.

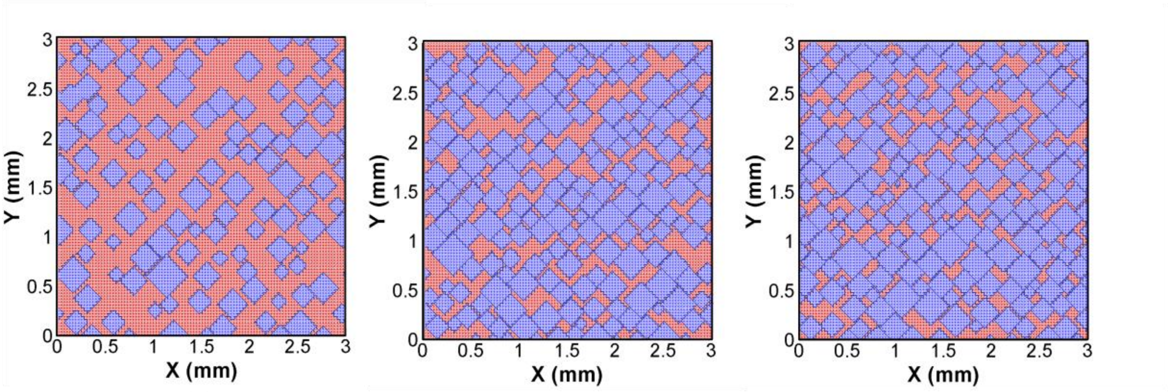

(a) (b) (c)

Figure 3: Idealized microstructures with different grain volume fractions, (a) η = 0.42, (b) η = 0.69 and (c) η = 0.74.

Grain morphology, distribution and volume fraction play an important role in determining the explosive output and the thermomechanical response of PBXs. Figure 2(a) shows the digitized image of an actual PBX microstructure. Variations of this microstructure with a range of grain volume fraction (η) between 0.42 and 0.82 are shown in Figure 2(b-f). Morphological parameters for these random microstructures are coupled and their effects cannot be easily analyzed independently. To delineate the influence of phase attributes such as phase size, phase arrangement, phase shapes and phase size distribution, a series of idealized microstructures with systematically varying arrangement, size, and shape of HMX grains are generated and used in the numerical simulations. These idealized microstructures consists of

(a) randomly distributed diamond-shaped grains (Figure 3) with normal distributions of grain size (Figure 4) and grain volume fraction η = 0.42 – 0.74;

(b) randomly distributed circular grains [Figure 5(a)] with a normal distribution of grain size [Figure 6(a)] and grain volume fraction $\eta = 0.69$; and

(c) randomly distributed circular grains [Figure 5(b)] with a bimodal distribution of size [Figure 6(b)] and grain volume fraction $\eta = 0.69$.

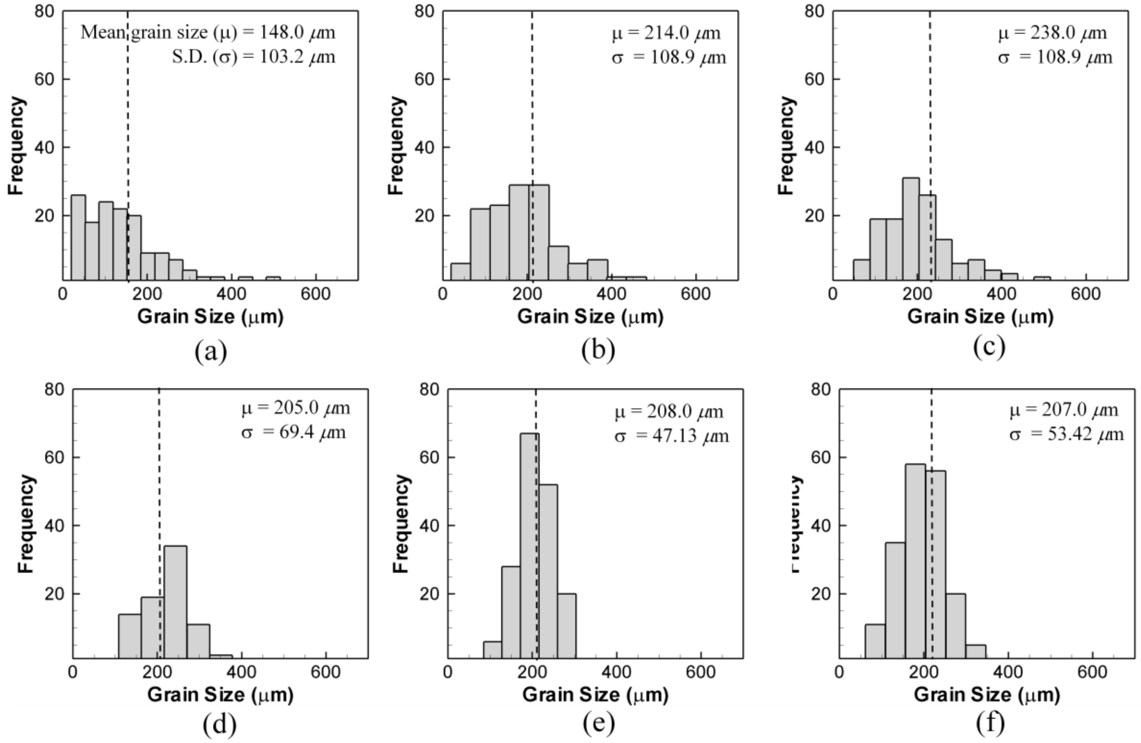

(a) (b) (c)

(d) (e) (f)

Figure 4: Grain size distributions for the digitized microstructures in Figure 2[(a) $\eta = 0.42$, (b) $\eta = 0.69$, (c) $\eta = 0.77$] and the idealized microstructures in Figure 3 [(d) $\eta = 0.42$, (e) $\eta = 0.69$ and (f) $\eta = 0.74$].

The grain size distributions for the microstructures in Figure 2, Figure 3 and Figure 5(a) are monotonous, with means between 148-255 μm and standard deviations between 47.13-121.35 μm. The grain size distribution for the microstructure in Figure 5(b) is bimodal, with two mean values, one at 294 μm and the other at 98 μm. The standard deviations for these two peaks are 50 μm and 16 μm, respectively, as shown in Figure 6(b). The bimodal distribution is an effective means to increase the proportion of explosives in a composite. Packing densities up to 99% of the theoretical maximum density (TMD) have been achieved using this approach [2]. The more intimate packing enhances the interactions between the particles and affects the thermomechanical responses of the compact. This microstructure allows the issue of packing intimacy to be analyzed.

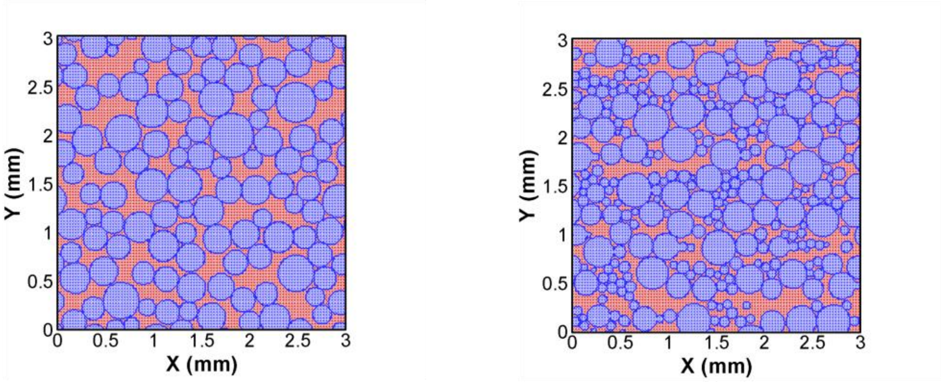

(a) (b)

Figure 5: Idealized microstructures with η = 0.69 (a) mono-modal and (b) bi-modal distributions.

Together, the microstructures discussed above allow the effects of volume fraction (Figure 3), particle shape [Figure 4(b) and Figure 5(a)] and particle arrangement [Figure 5(a-b)] to be characterized.

In subsequent chapters, additional microstructures with systematically varying attributes are also analyzed. They shall be introduced in later sections.

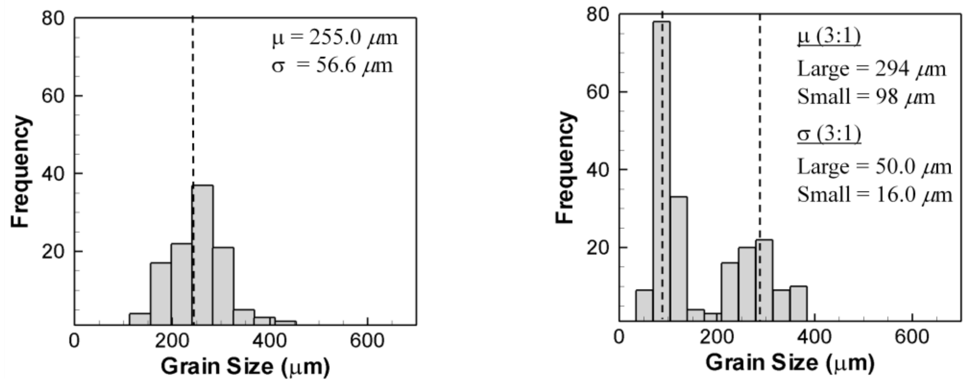

(a) (b)

Figure 6: Grain size distributions for idealized microstructures in (a) Figure 5(a) and (b) Figure 5(b).

2.2.1 Microstructure Characterization using Correlation Functions

Microstructures of heterogeneous explosives, such as the ones presented in Figure 2, Figure 3 and Figure 5 contain an ensemble of particles of different sizes and shapes. Each microstructure has associated with it several geometrical attributes. Statistical distributions of such geometric attributes collectively specify the geometric state of the microstructure [82]. Statistical *n*-point correlation functions can be used to characterize the microstructure geometry in a mathematical framework [83]. Detailed analyses of correlation functions can be found in [84-86] and only the relevant mathematics is provided here.

The lowest order correlation function is the one-point correlation function, which is the probability that any randomly chosen point in the microstructural domain belongs to a particular phase. This probability is equal to the volume fraction of that particular phase. The one-point correlation function does not provide any information regarding the spatial distribution of particles. Such information can be obtained using the two-point correlation function $P_{ij}(r,\theta,\phi)$. This represents the probability that a straight line of length *r* and angular orientation (θ,ϕ), which is randomly located in the microstructure, has one end in phase – *i* and another end in phase - *j*. The orientation averaged value of $\langle P_{ij}(r)\rangle$ can be obtained using the relation [82],

$$\langle P_{ij}(r)\rangle = \frac{1}{2\pi}\int_0^{2\pi}\int_0^{\pi/2} P_{ij}(r,\theta,\phi)\mathrm{Sin}\theta\,\mathrm{d}\theta\,\mathrm{d}\phi. \tag{2.1}$$

Note that $\langle P_{ii}(r)\rangle$ in Eq. (2.1) approaches the volume fraction of the *i*-th phase in the microstructure as *r* approaches zero. Figure 7(a) shows the orientation averaged two-point correlation function for the digitized microstructures in Figure 2[(b) η = 0.42, (c) η = 0.63, (d) η = 0.69, (e) η = 0.77, (f) η = 0.82]. The value of P_{11} (1 - denotes the HMX phase) approaches the HMX grain volume fraction as *r* approaches zero. At small values of $r < 100$ μm, P_{11} decreases rapidly with increase in *r*. Beyond $r \sim 120$ μm, P_{11} reaches a steady value and oscillates about it. This distance ($r \sim 120$ μm) quantifies the length scale of microstructural heterogeneity. For the ideal monomodal and bimodal microstructures in Figure 5(a-b), the corresponding length scale of microstructural heterogeneity is slightly larger at $r \sim 200$ μm. The domain size used in calculations needs to be sufficiently large for the macroscopic properties evaluated to be representative of a homogeneous material. The smallest microstructure domain used in the analyses is 3 mm which is at least an order of magnitude larger than the length scale of microstructural heterogeneity.

The two point correlation function alone may not be able to capture all relevant aspects of microstructural heterogeneity [85]. For microstructures which have non-uniform spatial arrangement of particles and morphological anisotropy, additional information may be required to characterize the geometry variations along different orientations. For this purpose, a lineal path probability function $L_{ij}\left(r,\theta,\phi\right)$ may be used. $L_{ii}\left(r,\theta,\phi\right)$ represents the probability that randomly located test lines of length *r* and angular orientation $\left(\theta,\phi\right)$, is completely contained within *i*-th phase [85]. Although $L_{ij}\left(r,\theta,\phi\right)$ is of the same order as $P_{ij}\left(r,\theta,\phi\right)$, it provides additional geometric information that is not reflected in the two point correlation function.

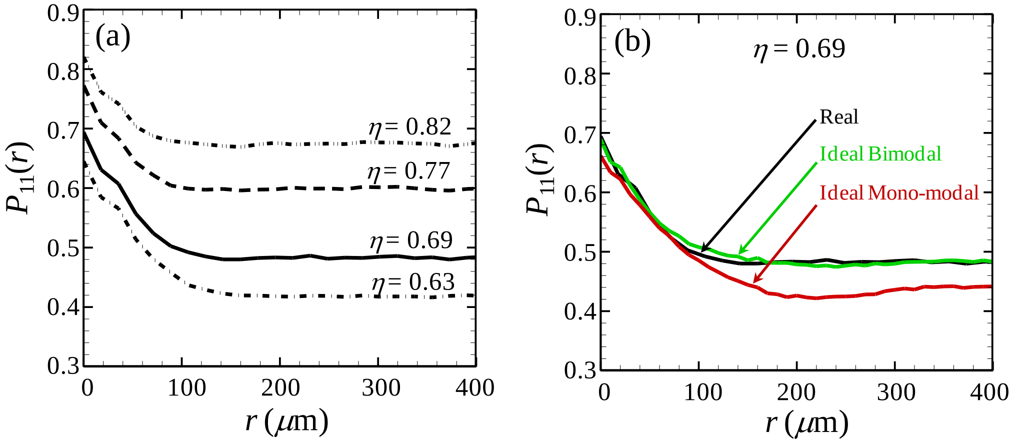

Figure 7: Two-point correlation functions for (a) the digitized microstructures in Figure 2[(b) η = 0.42, (c) η = 0.63, (d) η = 0.69, (e) η = 0.77, (f) η = 0.82] and (b) the idealized microstructures in Figure 5(a-b), η = 0.69.

Figure 8(a-c) show the lineal path correlation functions in three different directions for three microstructures having the same grain volume fraction of η = 0.69.

The directions chosen are 0°, 45° and 90° with respect to the horizontal direction in the respective microstructures shown in Figure 2(d), Figure 5(a), and Figure 5(b). In Figure 8, L_{22} represents the lineal path correlation function for test lines located in the matrix phase. Figure 8(a) shows that the value of L_{22} for the digitized microstructure [Figure 2(d)] is similar for all orientations considered. The results for other digitized microstructures shown in Figure 2(b-f) also follow similar trends and are not plotted here. This indicates that the digitized microstructures in Figure 2(b-f) are isotropic at the length scales considered in this analysis (3mm and above).

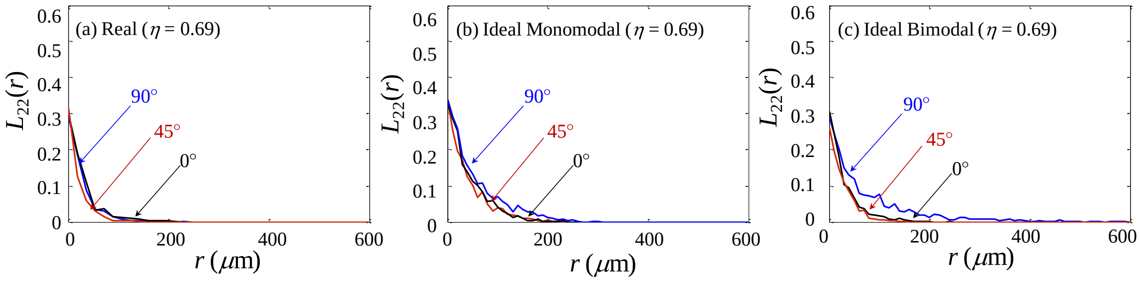

Figure 8: Comparison of the lineal path functions in three different directions for microstructures having a similar packing density of η = 0.69, (a) the digitized microstructures in Figure 2(d), (b) the idealized monomodal microstructure in Figure 5(a), and (c) the idealized bimodal microstructure Figure 5(b).

L_{22} for the idealized monomodal and bimodal microstructures in Figure 5(a) and (b) are shown in Figure 8(b) and (c) respectively. It can be seen that the value of L_{22} for the idealized monomodal microstructure [Figure 5(a)] does not show any appreciable orientation dependence. However, for the idealized bimodal microstructure [Figure 5(b)], the value of L_{22} along the 90° direction is higher than that along 0° and 45°. This indicates that the microstructure in Figure 5(b) has spatial anisotropy, which might affect the macro-level response along different directions.

It is noted that geometric isotropy is enforced while generating the monomodal and bimodal microstructures considered in Sections 3-6.

2.3 Finite Deformation Viscoelastic Model for the Binder

The binder considered is a commercially available polymer known as ESATNE 5703 and used in explosive PBX 9501. It has a glass transition temperature (T_g) of −40°C. The composition and mechanical properties of plasticized Estane can be found in [21, 87]. This material is viscoelastic, with properties sensitive to both strain rate and temperature. Table 1 lists the properties of Estane at T = 296 K, $\varepsilon = 10\ \%$ and $\dot{\varepsilon} = 2200\ \mathrm{s}^{-1}$. Below T_g, Estane is rather brittle and fractures easily; while above T_g, it is ductile. Following the Generalized Maxwell Model (GMM) in [88], a 22-element Prony series is used to characterize the variation of the shear modulus G of the binder with relaxation time. The bulk modulus K, of the polymer is assumed to be a constant, as in [39, 88]. The generalized stress-strain relation for a Maxwell model in the current configuration can be expressed in the integral form of

$$\boldsymbol{\sigma}(t) = \int_0^t 2\mathrm{G}\left(t_r - t_r'\right)\frac{\partial \boldsymbol{\varepsilon}^{\mathrm{D}}}{\partial t_r'}\,dt_r' + \int_0^t \mathrm{K}\left(t_r - t_r'\right)\frac{\partial \boldsymbol{\varepsilon}^{\mathrm{H}}}{\partial t_r'}\,dt_r', \tag{2.2}$$

where $\boldsymbol{\sigma}$ represents the Cauchy stress, $\boldsymbol{\varepsilon}^{\mathrm{D}}$ and $\boldsymbol{\varepsilon}^{\mathrm{H}}$ refer to the deviatoric and hydrostatic portions of the Eulerian strain tensor, and t and t_r refer to the physical and reduced times, respectively. The shear modulus G is assumed to vary with the reduced or relaxation time t_r according to a Prony series formulation [88] of the form

$$\mathrm{G}(t_r) = \mathrm{G}_\infty + \sum_{i=1}^{\mathrm{N}_p} \mathrm{G}_i e^{-\frac{t_r}{t^p_{r,i}}} = \mathrm{G}_0 \left(\mathrm{g}_\infty + \sum_{i=1}^{\mathrm{N}_p} \mathrm{g}_i e^{-\frac{t_r}{t^p_{r,i}}} \right), \tag{2.3}$$

where $\mathrm{G}_0 = \mathrm{G}_\infty + \sum_{i=1}^{\mathrm{N_p}} \mathrm{G}_i$ and represents the instantaneous shear modulus at reference temperature T_0, G_∞ represents the steady-state shear modulus, $\mathrm{g}_i = \mathrm{G}_i / \mathrm{G}_0$ is the relative modulus of the *i*-th term, N_p represents the number of terms in the Prony series and $t^p_{r,i}$ are the relaxation times.

The modulus of a viscoelastic material at a given strain level is a function of time and temperature. A convenient and appropriate way to describe the dual dependence is to use time-temperature superposition to generate master curves with a shift factor $\mathrm{A_T}$. The time-temperature superposition principle states that the viscoelastic behavior at one temperature can be related to that at another temperature by a change in time scale. The reduced τ time is related to the physical time t via

$$\mathrm{d}t_r = \frac{\mathrm{d}t}{\mathrm{A_T}\left(\mathrm{T}(t)\right)}. \tag{2.4}$$

Here, $\mathrm{A_T}$ is a shift function which depends on the current temperature T and a reference temperature T_0. In this analysis, a Williams-Landell-Ferry (WLF) shift function is used, i.e.,

$$-\log A_T = \frac{C_1\left(T - T_0\right)}{C_2 + \left(T - T_0\right)}. \tag{2.5}$$

Here, $C_1 = 6.5$ and $C_2 = 120$ K are constants and $T_0 = 292$ K [88]. Equation (2.5) describes the equivalent isothermal difference in strain rate between two experiments performed at the same strain rate, one at the reference temperature T_0 and the other at an elevated temperature T. The finite strain viscoelasticity formulation used here is similar to that in [89]. The Jaumann rate of Kirchhoff stress is obtained from the rate of deformation **D** through

$$\hat{\boldsymbol{\tau}} = \hat{\boldsymbol{\tau}}^{\mathrm{H}} + \hat{\boldsymbol{\tau}}^{\mathrm{D}} = \mathbf{L} : \mathbf{D}, \tag{2.6}$$

where **L** is the isotropic elastic modulus of the binder in the form of

$$\mathbf{L} = \frac{E}{1+\nu}\left(\mathbf{II} + \frac{\nu}{1-2\nu}\mathbf{I}\otimes\mathbf{I}\right) \tag{2.7}$$

and $\hat{\boldsymbol{\tau}}^{\mathrm{H}}$ and $\hat{\boldsymbol{\tau}}^{\mathrm{D}}$ refer to the hydrostatic and deviatoric parts of $\hat{\boldsymbol{\tau}}$, respectively. Also, $\mathbf{II}$ is the fourth-order identity tensor, $\mathbf{I}$ is the second-order identity tensor, and $\mathbf{I}\otimes\mathbf{I}$ denotes the tensor product of two tensors. Since the variation of shear modulus G only affects the deviatoric portion of the stress, $\hat{\boldsymbol{\tau}}$ can be rewritten as

$$\hat{\boldsymbol{\tau}} = \left(1 - \sum_{\mathrm{i}=1}^{\mathrm{N}_p} \alpha_{\mathrm{i}} g_{\mathrm{i}}\right)\hat{\boldsymbol{\tau}}^{\mathrm{D}} + \hat{\boldsymbol{\tau}}^{\mathrm{H}}, \tag{2.8}$$

where $\alpha_i = 1 - \frac{t_{r,i}}{\Delta t_r}\left(1-\gamma_i\right)$ and $\gamma_i = e^{-\frac{\Delta t_r}{t_{r,i}}}$, with Δt_r being the increment of the reduced time t_r during the current time step. Substitution of Eqn. (2.6) into Eqn. (2.8) yields the deviatoric part of the Jaumann rate of the Kirchhoff stress as

$$\hat{\boldsymbol{\tau}}_{new}^{\mathrm{D}} = \left(1 - \sum_{\mathrm{i}=1}^{\mathrm{N}_p} \alpha_{\mathrm{i}} \mathrm{g}_{\mathrm{i}}\right) \cdot \left(\mathbf{L} : \mathbf{D}\right)^{\mathrm{D}}. \tag{2.9}$$

The above equation can be further simplified by using the instantaneous shear modulus G_0 as

$$\hat{\boldsymbol{\tau}}_{new}^{\mathrm{D}} = \left(1 - \sum_{\mathrm{i}=1}^{\mathrm{N}_p} \alpha_i \mathrm{g}_i\right) \cdot 2\mathrm{G}_0 \mathbf{D}^{\mathrm{D}} = 2\mathrm{G}_0 \mathbf{D}^{\mathrm{D}} - 2\mathrm{G}_0 \sum_{i=1}^{\mathrm{N}_p} \alpha_i \mathrm{g}_i \mathbf{D}^{\mathrm{D}}. \tag{2.10}$$

The first term in the above relation represents the instantaneous elastic response and the second term represents the viscous response. This allows the deviatoric part of the Kirchhoff stress to be updated. Note that the hydrostatic part is unaffected by the viscous strain and, therefore, can be updated using

$$\hat{\boldsymbol{\tau}}^{\mathrm{H}} = \left(\mathbf{L} : \mathbf{D}\right)^{\mathrm{H}}. \tag{2.11}$$

Finally, the rate of viscous dissipation can be calculated as the scalar product of the average Kirchhoff stress and the viscous strain rate for each time step. This energy dissipation is manifested as temperature rises in the binder phase. The model parameters are calibrated using experimental data reported in [21] through direct simulations of the experiments.

2.4 Constitutive Model for the HMX Grains

In this analysis, HMX granules are the explosive content. Depending on the temperature and pressure, HMX can have four different forms, α, β, γ, and δ, with β being the most stable under ambient conditions. The α phase has a limited domain of stability from 376 – 435 K [90]. As temperature is increased beyond 438 K at atmospheric pressure, the β phase begins to transform to the γ phase. At the melting temperature of 522 K, the γ phase is the most thermodynamically stable form [91].

Table 1: Material parameters for HMX and Estane

Material Property	**HMX**	**Estane** (T = 296 K, ε = 10 %, $\dot{\varepsilon}$ = 2200 s^{-1})
Young's Modulus	25325.0 MPa	0.77 MPa (Loading modulus, [21])
Density	1.58 g/cc	0.90 g/cc
Specific Heat	1254.0 J/kg-K	1500 J/kg-K
Poisson's Ratio	0.250	0.499

While considerable information is available regarding the equation of state (EOS) for HMX (see, e.g., Sewell [92]), less information is available on constitutive relations. In Eulerian simulations, an equation of state (EOS) is often used for the volumetric part of the response while the deviatoric part is described by an elastic-plastic strength model (Benson [28] and Menikoff [34]). Mas and Clemens [93] assumed the grains are elastic-plastic and undergo brittle fracture through crack development. Wu et al. [39] used a continuum damage model which accounts for the weakening effect of microcracks through decreases in the elastic stiffness.

It is commonly acknowledged that HMX is brittle at ambient pressures [28] and therefore undergo very little plastic deformation. Hence, dissipation associated with plastic deformation is very small compared with the energy spent on fracture development and subsequent frictional dissipation along crack faces. Experiments reveal significant relative displacements of crack surfaces and relative sliding of neighboring grains [94]. Therefore, friction at the contact surfaces is a much more important dissipation and heat generation mechanism for HMX granules than any inelasticity in constitutive response.

Here, a hyperelastic constitutive formulation is used for HMX, the material properties for which are listed in Table 1. The constitutive relation is

$$\mathbf{S} = \frac{\partial \mathrm{W}}{\partial \mathbf{E}}, \tag{2.12}$$

where W is the strain energy density in the reference configuration, $\mathbf{S} = \mathbf{s} \cdot \mathbf{F}^{-T}$ is the second Piola-Kirchhoff stress and **E** is the Lagrangian strain given by

$$\mathbf{E} = \frac{1}{2}(\mathbf{F}^{T} \cdot \mathbf{F} - \mathbf{I}). \tag{2.13}$$

In the above formulas, $\left(\cdot\right)^{T}$ and $\left(\cdot\right)^{-T}$ denote inverse and inverse transpose, respectively. The strain energy density is taken to be

$$W = \frac{1}{2}\mathbf{E} : \mathbf{L} : \mathbf{E}, \tag{2.14}$$

where **L** is the tensor of isotropic elastic moduli defined in Eqn.(2.7).

Damage accumulation in the crystals is accounted for via cohesive surfaces embedded throughout the microstructure, as described in the following section.

2.5 Cohesive Finite Element Framework

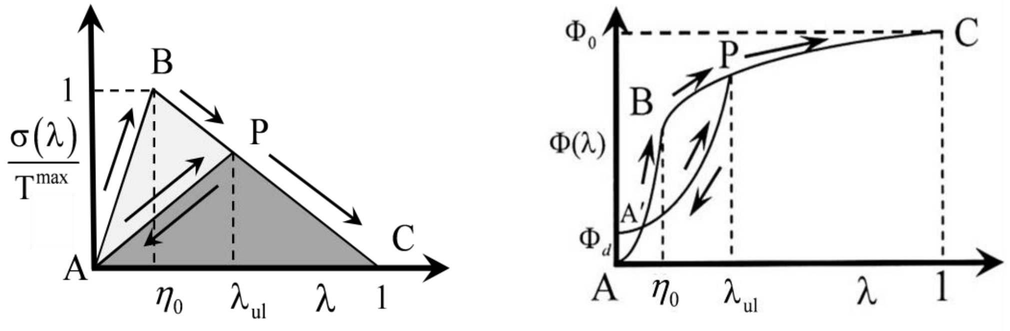

(a) (b)

Figure 9: Bilinear traction-separation cohesive law.

In the cohesive model used, the traction **T** applied on any cohesive surface is work-conjugate to interfacial separation **Δ**. Reckoned in the reference configuration, the cohesive law is

$$\mathbf{T}(\mathbf{x}) = \mathbf{T}\left[\boldsymbol{\Delta}(\mathbf{x})\right] \tag{2.15}$$

Implied here is the assumption that cohesive traction-separation relations are locally determined, i.e., the cohesive traction at one point is fully determined by the separation at the point itself. In this analysis, a bilinear traction-separation law developed by Zhai and Zhou [95] is used. This relation can be regarded as a generalized version of those given by Tvergaard and Hutchinson[69] and Ortiz and Pandolfi [36]. The law is derived from a potential Φ which is a function of the separation vector **Δ** through a state variable defined as

$$\lambda = \begin{cases} \sqrt{\left(\dfrac{\Delta_n}{\Delta_{nc}}\right)^2 + \left(\dfrac{\Delta_t}{\Delta_{tc}}\right)^2}, & \Delta_n \geq 0; \\ \left|\dfrac{\Delta_t}{\Delta_{tc}}\right|, & \Delta_n < 0. \end{cases} \tag{2.16}$$

Here, $\Delta_n = \mathbf{n} \cdot \mathbf{\Delta}$ and $\Delta_t = \mathbf{t} \cdot \mathbf{\Delta}$ denote, respectively, the normal and tangential components of **Δ**, with **n** and **t** being unit vectors normal and tangent to the cohesive surface respectively. Δ_{nc} and Δ_{tc} are the critical normal and shear separations at which the cohesive strength of an interface vanishes under conditions of pure normal ($\Delta_t = 0$) and pure shear ($\Delta_n = 0$) deformation. The specific form of λ varies with the mode of separation. If the value of Δ_n is positive, λ describes the instantaneous state of mixed-mode separations. While if Δ_n is negative (compressive case), λ assumes the value of instantaneous shear separation. This ensures that in case of compressive loading, the material only fails by shearing.

In order to account for the irreversibility of separations, a parameter $\eta = \max\{\eta_0, \lambda_{ul}\}$ is defined. As illustrated in Figure 9(a), η_0 is the initial value of η which defines the stiffness of the original undamaged cohesive surface and λ_{ul} is the hitherto maximum value of λ at which an unloading process was initiated. λ_{ul} represents the (reduced) current stiffness of the cohesive surfaces after damage and unloading have occurred. Also, one always has $\eta < 1$. λ_{ul} is the critical level of λ at which σ reaches the reduced strength of the hitherto damaged cohesive surface pair. The cohesive potential is assumed to be of the form derived in Zhai and Zhou [95].

The bilinear cohesive relation between σ and λ is illustrated in Figure 9(a) and the variation of Φ is shown in Figure 9(b). The value of Φ_0 is set to be equal to the respective critical energy release rate $\mathcal{G}$ of the particular fracture surface pair (within a HMX granule, inside the ESTANE binder, and along a HMX-ESTANE interface). Experimental values of $\mathcal{G}$, when available, are used to guide the determination of the cohesive parameters. The values of $\mathcal{G}$ for the binder and interface are taken from Tan et al. [96]. The cohesive parameters used for the three types of interfaces are listed in Table 2.

Under compression, penalty traction is used to apply sufficient normal traction on the corresponding node pairs to strongly discourage interpenetration of cohesive surfaces. Specifically, the penalty traction is of the form

$$T_{\mathrm{n}} = T_{\mathrm{n}}^{\max} \exp\left(\frac{\Delta_{\mathrm{n}}}{\Delta_{\mathrm{nc}}}\right), \text{ for } \Delta_{\mathrm{n}} < 0. \tag{2.17}$$

This penalty traction is applied as long as λ is less than 1 for the pair of surfaces. Once $\lambda \geq 1$, i.e., the cohesive element has failed, a contact algorithm (for both free and fractured surfaces) described in the next section is used to prevent interpenetration and account for interfacial friction.

Table 2: Cohesive parameters for the three types of interfaces

Interface Type	Critical Separations Δ_n, Δ_t (μm)	Maximum Traction T_{max} (MPa)
Grain	5.0	100.0
Matrix	10.0	38.4
Grain-matrix interface	4.62	35.0

As analyzed in Tomar et al. [78], there is an issue of cohesive–surface–induced stiffness reduction associated with this type CFEM approach when a finite initial stiffness is used in the cohesive law. This issued is addressed by the use of a sufficiently large initial cohesive stiffness (η_0 = 0.001) and a finite element size of 15 μm. These choices satisfy the solution convergence criterion in Tomar et al. [78] for this type of CFEM models. The issue of mesh convergence is discussed in detail in Section 2.9.1.

2.6 Contact Algorithm

A robust contact algorithm is required to properly account for the interactions between initial boundaries and surfaces that arise out of fracture and debonding inside the material. An algorithm similar to that in Camacho and Ortiz [73] is developed and used. This algorithm works in two steps, the first step involves the detection of potential contact surfaces and the second step involves the application of penalty forces to prevent interpenetration.

Potential contact surfaces include initial free surfaces/boundaries and fractured surfaces. The latter are created when failure of a cohesive surface pair occurs ($\lambda = 1$). The algorithm treats all free surface segments as potential contact surfaces. For each surface segment, a contact region is defined as the area occupied by all of the adjoining elements. At the beginning of every step, the nodal displacements, velocities and accelerations are predicted assuming no contact has occurred. The new nodal coordinates are employed to check for interpenetration within the contact region. Once interpenetration is detected, penalty forces are applied normally on the pair of surfaces to set them back into alignment. The Coulomb friction law is used to determine the frictional force between a contacting surface pair and in turn the tangential component of the nodal force vector (see Section 2.6.1). Frictional work results in the generation of heat and increases the thermal energy of the nodes on the contact surfaces. The thermal force is distributed between the two surfaces according to [73],

$$\frac{h_1}{h_2} = \sqrt{\frac{k_1 \rho_{0,1} c_1}{k_2 \rho_{0,2} c_2}}, \tag{2.18}$$

where h_i represents the thermal energy changes, k_i, $\rho_{0,i}$ and c_i represent the thermal conductivities, effective mass densities and the heat specific heats of the two materials (i = 1, 2), respectively. To keep track of thermal conduction across adjacent elements, temperature continuity is maintained across every node junction. Since a node pair on the two sides of a cohesive surface pair corresponds to the same material point in the reference configuration, a thermal energy averaging scheme is used to evaluate the temperature rise ΔT at each node junction according to

$$\Delta T = \frac{\sum_{i=1}^{n} h_i}{\sum_{j=1}^{n} m_j c_j}, \tag{2.19}$$

where n represents the number of nodes at the node junction, m_j is the lumped mass and c_j is the lumped thermal capacitance of the jth node at the junction.

2.6.1 Friction

Friction is a significant source of ignition in explosive materials [5]. Frictional interactions occurring as a result of glancing or normal impact may lead to conditions for ignition and propagation of reaction. In case of normal loading, frictional dissipation occurring at fractured surfaces may be much larger than at locations which have a simple sliding interaction.

In this analysis, a classical Coulomb's friction model is used, where friction is modeled as a force F which opposes the relative motion of two sliding surfaces as,

$$F = \mu L \tag{2.20}$$

where L is the normal force between the surfaces and μ is the coefficient of friction. In general, the value of μ depends on the materials in contact, the surface roughness and temperature. Bowden and Tabor [97] provide a more detailed treatments of homogeneous friction theory, including surface temperature calculations, but these are of limited applicability to explosives [5].

In general, the coefficient of friction depends on whether the surfaces are in relative motion (sliding friction) or stationary (static friction). The coefficient of sliding friction μ_k is usually lower than the coefficient of static friction μ_s [5]. For the purpose of this analysis, μ_s is assumed to be equal to μ_k ($\mu_\mathrm{s} = \mu_\mathrm{k} = \mu$). When sliding occurs between two surfaces, the rate of frictional work is calculated based on,

$$\dot{W}_f = \mu L v_{\mathrm{rel}} \tag{2.21}$$

where v_{rel} is the relative sliding velocity between the two surfaces. The frictional work is dissipated as heat and is distributed among the two surfaces in contact according to Eq. (2.18). The frictional coefficients selected for this analysis are discussed in Section 2.9.2.

2.7 Finite Element Method

The finite element discretization is based on linear-displacement triangular elements arranged in a ‘crossed-triangle’ quadrilateral pattern. Neighboring elements are connected through cohesive surfaces. Thus in the undeformed configuration, the cohesive elements are oriented along four directions, horizontal (0°), vertical (90°) and along the diagonals of the quadrilateral ($\pm 45^\circ$). Finite element discretization of the field equations results and the numerical integration scheme is similar to that in Zhou et al. [98] and only a brief description of the field equations is presented here.

Using momentum balance on the finite element approximation of the displacement field results in an equation of the form,

$$\mathbf{M}\frac{\partial^2 \mathbf{U}}{\partial t^2} = \mathbf{R}, \tag{2.22}$$

where **U** is the vector of nodal displacements, **M** is the lumped mass matrix and **R** is the mechanical force vector. Similarly, performing energy balance on the temperature field results in,

$$\boldsymbol{c}\frac{\partial \boldsymbol{T}}{\partial t} = -\boldsymbol{k}\boldsymbol{T} + \mathbf{H}, \tag{2.23}$$

where $\boldsymbol{T}$ is the vector of nodal temperatures, $\boldsymbol{c}$ and $\boldsymbol{k}$ are the heat capacitances and the heat conductance matrices and **H** is the thermal force vector. A lumped mass matrix is used in Eq. (2.22) for reasons of efficiency and accuracy (see [98] and references therein). Additionally, a lumped heat capacitance matrix is used in Eq. (2.23).

At time t_n, it is assumed that the state of the specimen is known. The field equations are integrated using the Newmark β-method [99] with $\beta = 0$ and $\gamma = 0.5$. Specifically, Eq. (2.22) yields the displacements and velocities at time $t_{n+1} = t_n + \Delta t_n$ as,

$$\frac{\partial^2 \mathbf{U}^{n+1}}{\partial t^2} = \mathbf{M}^{-1}\mathbf{R}, \tag{2.24}$$

$$\frac{\partial \mathbf{U}^{n+1}}{\partial t} = \frac{\partial \mathbf{U}^{n}}{\partial t} + \frac{1}{2}\Delta t_n \left(\frac{\partial^2 \mathbf{U}^{n}}{\partial t^2} + \frac{\partial^2 \mathbf{U}^{n+1}}{\partial t^2} \right), \tag{2.25}$$

$$\mathbf{U}^{n+1} = \mathbf{U}^{n} + \frac{\partial \mathbf{U}^{n}}{\partial t} + \frac{1}{2}\left(\Delta t_n\right)^2 \frac{\partial^2 \mathbf{U}^{n}}{\partial t^2}, \tag{2.26}$$

where $\left(\cdot\right)^{-1}$ denoted the matrix inverse. The temperatures at t_{n+1} are obtained via

$$\frac{\partial \boldsymbol{T}^{n+1}}{\partial t} = \boldsymbol{c}^{-1}\left(-\boldsymbol{k}^{n}\boldsymbol{T}^{n} + \mathbf{H}^{n}\right), \tag{2.27}$$

$$\boldsymbol{T}^{n+1} = \boldsymbol{T}^{n} + \Delta t_n \frac{\partial \boldsymbol{T}^{n+1}}{\partial t}. \tag{2.28}$$

2.8 Loading Configurations Analyzed

In this analysis, calculations are performed using two different types of loading configurations – small samples which account for wave reflections (see Section 2.8.1) and larger samples without wave reflections (see Section 2.8.2). This is a 2D model and the conditions of plane-strain prevail.

2.8.1 Small Sample with Wave Reflections

Three different variations of this loading configuration are used as shown in Figure 10(a-c). All of the loading configurations of this type use a 3-mm square microstructural region. The size of the sample is chosen to

(1) obtain a sufficiently large representative sample of the microstructures – note that this sample size is at least one order of magnitude larger than the length scale of

the mean grain size for this type of PBX, giving reasonable representation of the microstructures as discussed in Section 2.2.1; and

(2) allow nominally homogeneous states of stress to be reached through stress wave reverberation over the duration of the calculations. This configuration simulates the conditions of split Hopkinson pressure bar experiments.

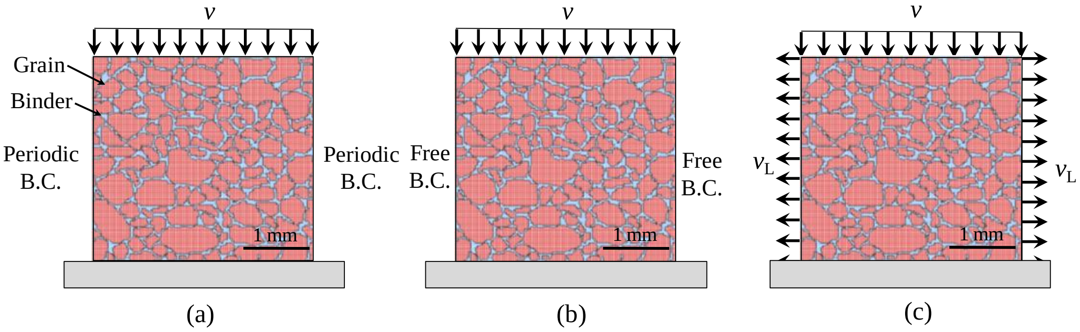

Figure 10: Loading configurations, (a) confined specimen with periodic boundary conditions on lateral sides, (b) unconfined specimen with traction-free boundary conditions on lateral sides and (c) with the lateral sides having fixed or traction-free boundary conditions which correspond to confined or unconfined specimens respectively.

For the loading configurations shown in Figure 10(a-c), the specimen is initially stress-free and at rest. The loading configurations in Figure 10(a-c) are designed to account for a range of loading rates and different load triaxialities. The velocity boundary condition at the top surface and the fixed displacement boundary condition at the bottom surface allow prescribed overall deformation rates to be imposed. Loading is effected by applying a constant normal velocity on the top of the sample. The strain-rate $\dot{\varepsilon}$ is calculated by dividing the velocity of the top surface v by the initial height of the specimen. Since the bottom surface is fixed, this configuration considers the effect of stress wave reflection. For a typical calculation for the PBX, the wave reaches the bottom surface at ~1.15 μs. This can be considered as a delay time before the stress distribution becomes nominally uniform in the sample.

The periodic boundary condition in Figure 10(a) and the traction-free boundary condition in Figure 10(b) for the lateral sides allow conditions of nominally uniaxial strain (confined, high stress triaxiality) and nominally uniaxial stress (unconfined, low stress triaxiality) to be simulated, respectively. The loading configuration shown in Figure 10(c) is designed to account for a range of loading rates and different load triaxiality levels. The lateral sides have imposed velocity v_L, where $0 < v_L < v$, allowing the degree of confinement to be varied from nominally uniaxial strain to nominally uniaxial stress.

2.8.2 Larger Sample without Wave Reflections

The second type of loading configuration involves a $15\,\mathrm{mm} \times 3\,\mathrm{mm}$ rectangular microstructural region. Similar to the sample described in Section 2.8.1, this sample size is at least one order of magnitude larger than the length scale of the mean grain size for the PBX considered, giving sufficient volume representation of the microstructures.

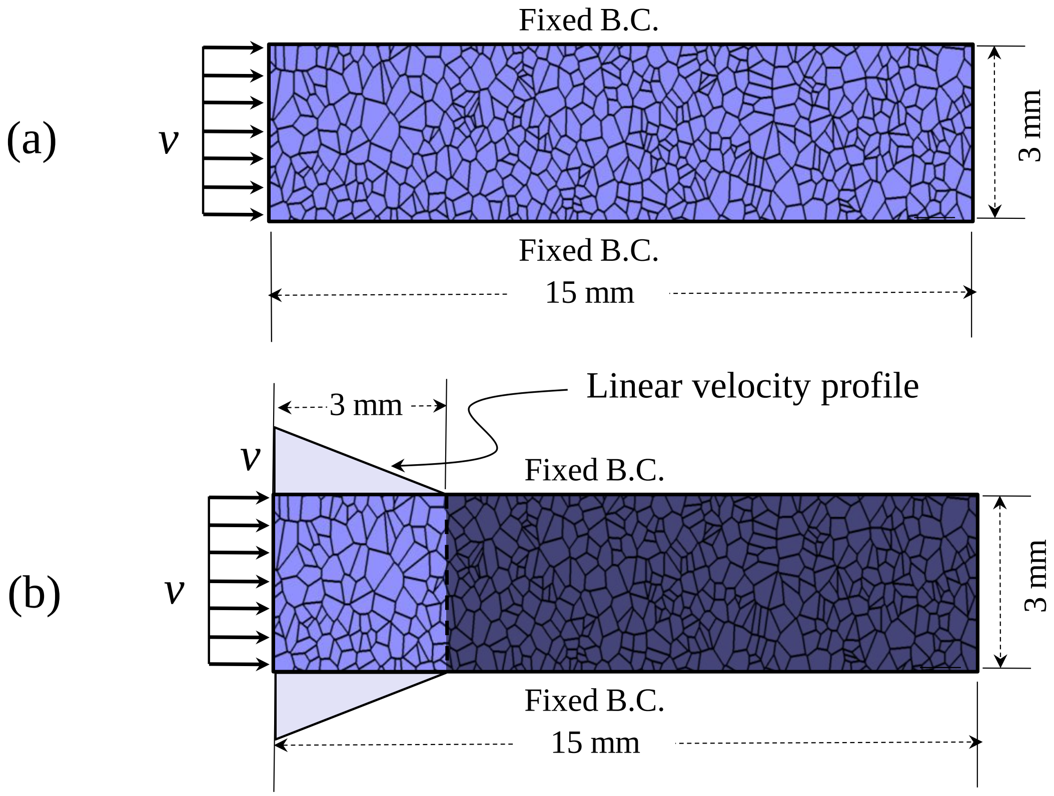

Figure 11: Configurations for (a) transient impact loading and (b) macroscopically uniform loading without stress wave propagation.

The primary loading configuration is shown in Figure 11(a). The specimen is initially stress-free and at rest. Impact loading is effected by applying a constant normal velocity on the left end of the sample. The upper and lower boundaries are constrained such that lateral expansion (up for the upper edge and down for the lower edge) does not occur. This configuration approximates the normal impact loading of an infinitely wide material block under conditions of macroscopic uniaxial strain. The specimen length is chosen to allow approximately the first 5.5-8.5 microseconds of the propagation of the stress wave from the left surface toward the right to be analyzed, before the wave arrives at the right end.

The second loading configuration using the $15\text{ mm}\times 3\text{ mm}$ microstructural region is shown in Figure 11(b). This configuration is similar to the configuration in Figure 11(a) and is used to simulate loading under a uniform state of stress without the effects of stress wave propagation. This configuration involves a linear initial particle velocity distribution over the 3 mm × 3 mm region on the left. Other aspects of this configuration are the same as those for the loading configuration in Figure 11(a). The prescribed initial particle velocity decreases linearly from the imposed boundary velocity v to 0 over the 3 mm length of the region. This treatment generates a macroscopically "uniform" deformation state in an average sense in the 3 mm × 3 mm region. This configuration allows the ignition behavior to be studied for conditions of macroscopically uniform deformations, without the effects of transient stress wave propagation.

An important quantity for analyzing the effect of specimen length is the ratio between the domain size in the loading direction and the effective thickness of the steady stress wave. For very small specimens (the ratio being less than unity), the loading configuration allows the effects of high strain rates and full stress wave reflection being analyzed. The loading configurations in Figure 10 are designed with this type of conditions in mind. On the other hand, for the loading configurations in Figure 11, the ratio is much larger than unity. That configuration allows the response under conditions of transient stress waves to be analyzed. Naturally, this effect is also dependent on the speed of sound through the specimen and the boundary velocity.

2.9 Model Calibration

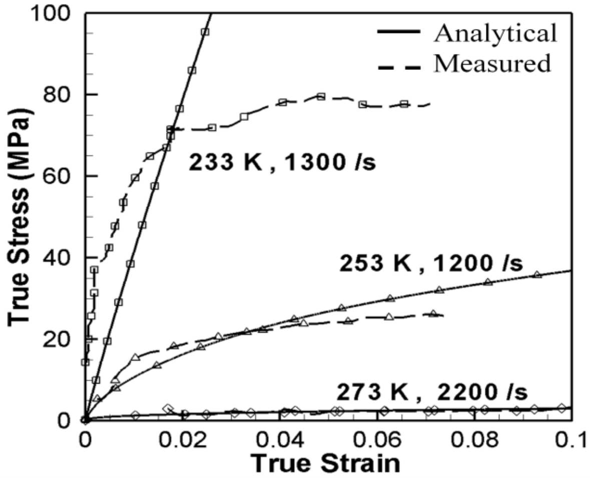

Figure 12: Calculated and measured stress-strain curves for Estane 5703 (experiments by Cady et al. [21]).

Depending on temperature and strain rate, the dynamic response of PBXs can vary significantly. For the pure polymeric binder, the viscoelastic response obtained from analytical relations is compared with measured compressive stress–strain ($\sigma - \varepsilon$) response from [21] for a range of strain rates and initial temperatures (see Figure 12). Note that the glass transition temperature for the binder T_g = 233 K. For temperatures above the glass transition region, viscoelastic response predicted by the analytical relations is in good agreement with the measured response. However, at temperatures lower than T_g the measured response deviates significantly from the analytical prediction. This is due to damage in the form of brittle fractures decreases the load carrying capacity of the material. The cohesive traction-separation law for the binder has been calibrated to account for this brittle behavior observed at low temperatures.

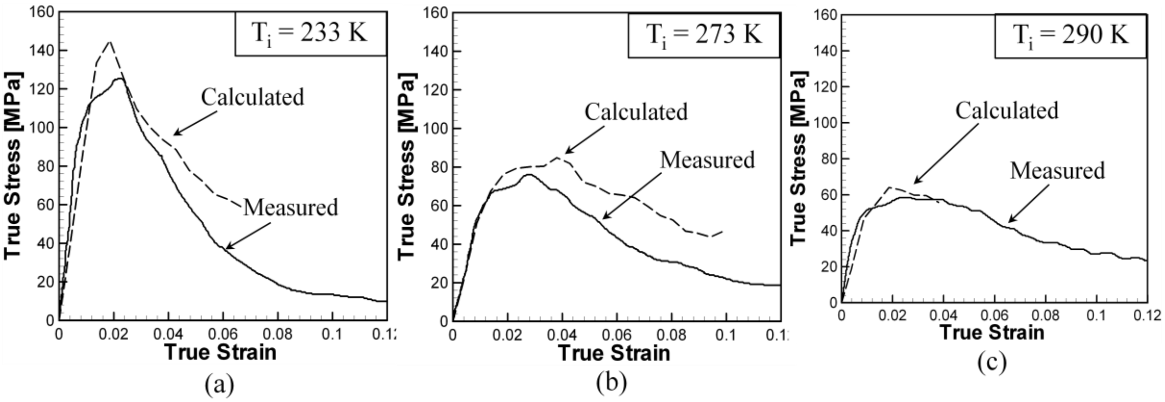

Figure 13: Calculated and measured stress-strain curves for PBX 9501 (experiments by Gray et al. [8]), $\dot{\varepsilon}$ = 2500 s^{-1}, η = 0.69).

The overall response of PBX includes contributions from both the deformation of bulk constituents and the debonding at grain-matrix interfaces. Figure 13 shows a comparison between measured and calculated $\sigma - \varepsilon$ responses of PBX 9501 for three initial temperatures from 233 K and 290 K, at a strain rate of $\dot{\varepsilon}$ = 2500 s^{-1}. The calculations are based on the microstructure shown in Figure 2(d). Note that for the calculations at lower temperatures (233 and 273 K), the calculations over-predict the stress in the softening portion of the $\sigma - \varepsilon$ response. One possible reason is that at low temperatures, the brittle behavior of the binder causes the $\sigma - \varepsilon$ response to be more sensitive to the microstructural heterogeneity. At higher temperatures (293 K) the binder behaves in a more ductile manner and the calculated and measured responses are in good agreement with each other. The above comparisons between calculated and experimental results serve as a justification for the bulk constitutive and fracture parameters used in the present analyses.

2.9.1 Mesh Convergence

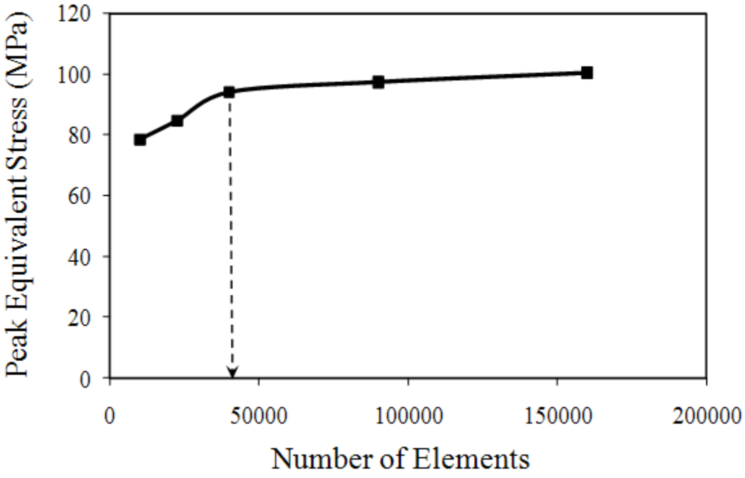

Figure 14: Variation of peak stress with number of elements in the discretized the microstructure.

A convergence study is carried out using meshes with a range of element sizes. The meshes used consist of uniform distributions of "crossed triangle" squares, each square having 4 bulk elements. The effect of mesh density or element size is analyzed by varying the number of elements from 10×10^3 to 160×10^3 in the 3 mm square microstructural region. The corresponding element sizes range between 15 – 60 μm. A set of calculations is performed using the PBX microstructure shown in Figure 2(c). The loading configuration shown in Figure 10(c) is used, with $v_L = 0$. The equivalent stress at the location of maximum stress concentration in the microstructure is plotted in Figure 14. The relative error in the peak stress is approximately 2.6% of the value for the smallest element sizes.

A second convergence study is carried out using meshes with element sizes varying between 10 and 20 μm. For this set of calculations, the loading configuration shown in Figure 11(a) is used. The microstructure used has a grain volume fraction of η = 0.82. The impact velocity is 100 ms^{-1}. The evolution of various forms of mechanical work and energy dissipation are shown in Figure 15. Specifically, the variation of mesh size leads to a variation of boundary work at t = 3 μs of less than 8.5% for a 50% reduction in the mesh size from 20 to 10 μm, suggesting that the mesh resolution chosen (15 μm) is adequate for the purpose of the current study. The corresponding variations in elastic strain energy and fracture work are 9.1% and 2.5% respectively.

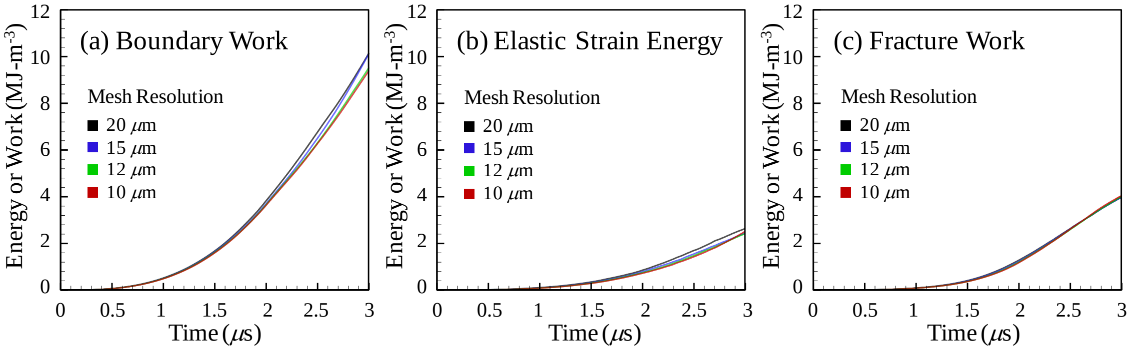

Figure 15: Evolution of (a) boundary work, (b) elastic strain energy and (c) fracture work as functions of time for calculations using different mesh resolutions, (T_i = 300 K, η = 0.81 and v = 100 ms^{-1}).

Based on the convergence studies, an element size of 15 μm is chosen for the calculations presented in this analysis. In later chapters, justifications shall be provided for the mesh resolution chosen, based on other convergence criteria such as hotspot density and resolution of hotspots.

2.9.2 Coefficient of Friction

In the field of explosive testing, powder friction tests have been used to examine the threshold for reaction initiation. However, these tests do not examine the microscale processes that lead to frictional heating and hotspot formation in explosives. Green et al. [100] studied the frictional response of a number of PBXs subject to drop weight impact tests. From their studies, the authors found the coefficient of friction to vary only slightly with the drop height for a 45-degree impact. The coefficient of friction was determined to be approximately 0.3 - 0.7 for PBX9404 [94% HMX, 3% Nitrocellulose, 3% Tris (2-chloroethyl) phosphate]. Based on the study by Green et al. [100], Chidester et al. [101] used a frictional coefficient of 0.5 to calculate the frictional dissipation during projectile impact on a similar explosive LX-10-1 (94.5% HMX, 5.5 % Viton A). Later, Dickson et al. [102] reported frictional heating and ignition of a HMX/Estane explosive, PBX9501. The authors computed the coefficient of friction by measuring the normal and lateral forces occurring between a glass disk coated with sand particles and a sample of PBX9501. The coefficient of friction was found to vary between 0.4 and 0.5.

For the calculations presented in this analysis, the coefficient of friction between HMX surfaces in contact is assumed to be μ_{gg} = 0.5. Note that this value of μ_{gg} is also used for frictional interaction between surfaces generated as a result of transgranular fracture of HMX. The coefficient of friction between the grain and binder is lower and is assumed to be μ_{gb} 0.25. It is noted that the higher temperature increases which characterize hotspots is primarily due to localized fracture and frictional dissipation inside the HMX granules or at locations of grain-grain interactions. The binder being softer develops relatively lower levels of stress. Hence it does not contribute significantly to frictional dissipation. Rather, the common modes of failure in the binder are shear banding and debonding across the grain-binder interface.

The value of coefficient of friction chosen does not significantly change the trends obtained in this analyses. However, it is important to identify the sensitivity of the frictional energy dissipation to changes in the frictional coefficient. To analyze this issue, calculations are carried out for a range of grain-grain frictional coefficients μ_{gg} = 0.1 – 0.7 using a PBX microstructure with η = 0.82. The grain-binder frictional coefficient is taken as μ_{gb} = 0.25. The calculations are carried out using the loading configuration shown in Figure 11(a) at an impact velocity of 100 ms^{-1}. Results show that at low values of frictional coefficient, small changes in μ_{gg} result in large changes in the energy dissipation. Specifically, for an increase of μ_{gg} from 0.1 to 0.3, the frictional dissipation at 5 μs increases from 0.38 to 0.53 MJ/m^3, which is a change of 39.4%. On the other hand, when μ_{gg} is varied between 0.5 and 0.7, the corresponding variation of frictional dissipation is from 0.70 to 0.72 MJ/m^3 which is a change of 2.8%. This shows that the value of the coefficient of friction chosen does not cause large changes in results in the neighborhood of μ_{gg} = 0.5. This allows relative comparisons to be made when used consistently for difference cases.

2.10 Parametric Variation of Microstructural Attributes

A systematic analysis is carried out using the actual and idealized PBX micrographs detailed in Section 2.2. The effects of varying microstructural attributes such as volume fraction, grain size distribution and grain phase morphology are analyzed. This analysis allows for quantification of the relationship between the dynamic response of PBXs and their initial compositions and microstructural makeup. The framework is inert, so the effects of possible phase transitions and chemical reactions are not considered. Unless otherwise noted, the imposed boundary velocity at the top surface of the configurations in Figure 10(b) is $v = 50$ ms^{-1} (which gives rise to a nominal strain rate of $\dot{\varepsilon}$ = 16,667 s^{-1}) with a linear ramp from zero to v in the first 1 μs of loading. The initial temperature is T_{i} = 300 K. First use one calculation is used to illustrate the processes and failure mechanisms captured by the model under the conditions analyzed.

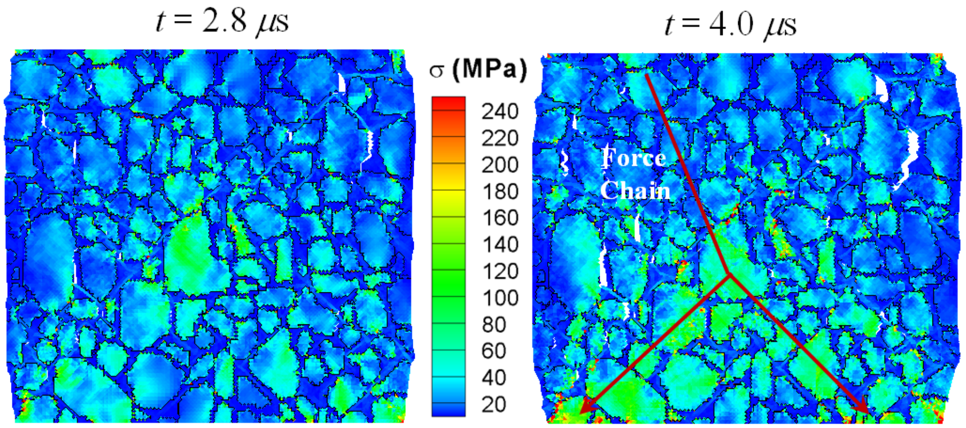

(a) Distribution of equivalent stress

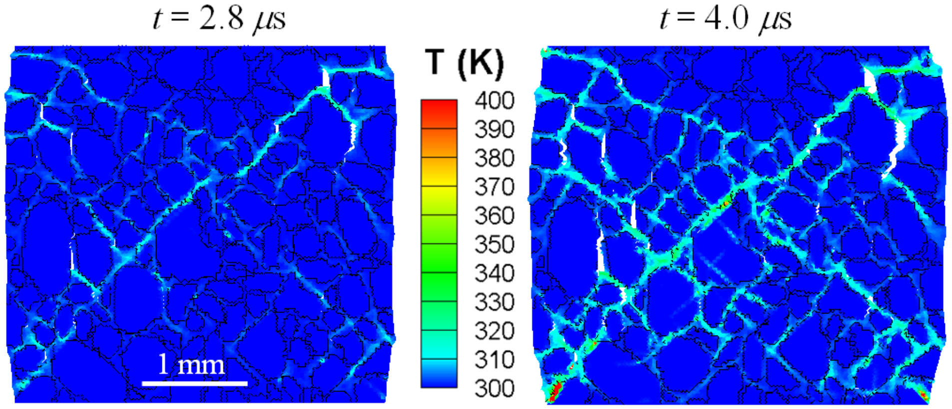

(b) Distribution of temperature

Figure 16: Evolution of (a) equivalent stress and (b) temperature in the microstructure with time for the microstructure in Figure 2(d).

The microstructure used for this calculation is that in Figure 2(d) and the loading configuration is that in Figure 10(b). Figure 16 shows the distributions of the equivalent stress at times *t* = 2.8 and 4.0 μs after the onset of loading. The HMX grains, which are stiffer than the binder, sustain higher stresses. The grains are not uniformly stressed – higher stresses are seen for grains which are part of one of the ‘force chains’, as outlined in Figure 16(a). These force chains can be regarded as assemblies of grains positioned such that they support higher levels of compressive and shear stresses [103]. The overall level of stress in the microstructure increases with the progression of deformation until interfacial debonding and transgranular fracture initiate. Figure 16(b) shows the evolution of temperature. Initially, viscous dissipation in the soft binder is primarily responsible for the temperature increase. The hard grains cause more intense deformation in the binder, leading to localized regions of high temperatures. As time progresses, these regions coalesce to form shear bands which tend to extend diagonally through the microstructure, approximately following the direction of maximum shear stress. It is noted that shear bands in the binder alone typically do not generate sufficient heat to cause melting of the HMX grains.

The relative motion of grains also activates other energy dissipation mechanisms. Figure 17(a) shows the deformed configuration at *t* = 4.2 μs. A region of this microstructure is shown in Figure 17(b) at a higher magnification to highlight the failure mechanisms. Debonding along the relatively weak grain-matrix interface is the primary mode of damage. Such interfacial debonding has also been experimentally observed in experiments at both low and high strain rates (see, e.g., Rae et al. [18] and Siviour et al [11]). This form of damage reduces the effective modulus of the over microstructure

(Banerjee et al. [38]). At higher levels of nominal strain (>3%), grain-grain interactions occur. The locations where grains come into contact with each other are sites of severe stress concentration, crack development and grain-matrix sliding. Crack formation, sliding and the ensuing frictional dissipation cause more intense heating and higher temperatures. Further deformation lead to transgranular fracture of the grains. Crack development, grain-matrix debonding and transgranular fracture create more surfaces which may come into contact and slide against one another, giving rise to additional frictional dissipation and heating. These processes ultimately can lead to severe heating in the microstructure, resulting in what is known as the hot-spots which can cause ignition of energetic materials. Obviously, the interplay between the constituents and interfaces in the microstructure determines the thermomechanical outcome of a dynamic loading event. The outcome defines the ignition sensitivity of the energetic materials.

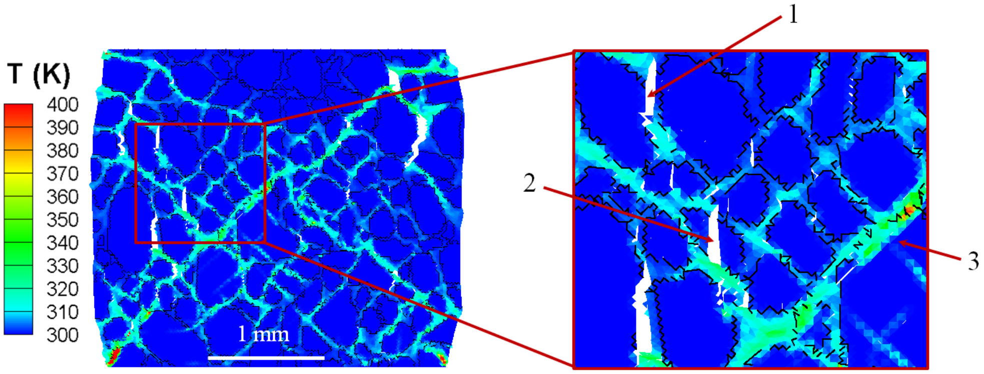

(a)

(b)

Figure 17: (a) Failure mechanisms in the digitized microstructure with η = 0.69 shown in Figure 2(d) at t = 4.2 μs, T_i = 300 K and $\dot{\varepsilon}$ = 16,667 s^{-1}; (b) Close-up view of a region of the microstructure showing (1) debonding at grain-matrix interface, (2) transgranular fracture and (3) localized heating due to grain-grain interactions.

Figure 18(a) shows the overall stress-strain response corresponding to the results in Figure 16 and Figure 17. The stress increases rapidly for strains up to 3%. In this regime, the deformation is primarily accommodated by the softer matrix. Beyond this regime, two competing processes are at work. First, debonding of the grain-matrix interface and transgranular fracture of the grains occur, weakening the load-carrying capacity and contributing to strain softening. This has been observed experimentally by Gray et al. [8]. Second, as grains are pushed closer, the overall stiffness tends to increase due to enhanced intergranular interactions. These two counteracting mechanisms balance out, leading the stress-strain relation to flatten out in this case.

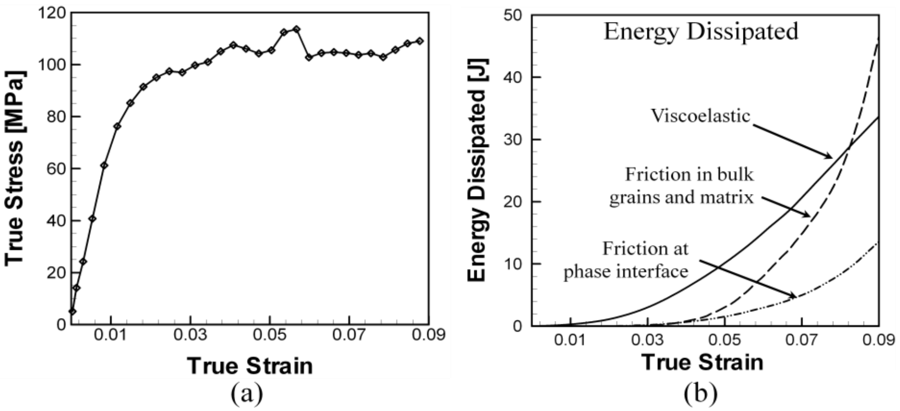

(a) (b)

Figure 18: (a) Stress-strain response and (b) time history of energy dissipation in the microstructure shown in Figure 2(d) (η = 0.69, T_i = 300 K and $\dot{\varepsilon}$ = 16,667 s^{-1}).

The time history of energy dissipation in the microstructure is shown in Figure 18(b). The profiles for all dissipation mechanism are shown. Viscoelastic dissipation in the binder is the primary dissipation mechanism in early stages of the deformation, as the softer binder absorbs most of the input energy and accommodates most of the imposed deformation. Accordingly, temperature increase occurs primarily in the binder. A portion of the thermal energy is conducted into the grains through the grain-matrix interface. As the overall strain increases, the viscoelastic dissipation continues to increase steadily. Since no fracture occurs in the early stages, frictional dissipation remains zero for strains up to approximately 3% beyond which frictional dissipation initiates in both bulk phases and along the grain-matrix interfaces. The strain at which frictional dissipation initiates also approximately corresponds to the flattening of the stress strain curve, suggesting a transition in heating mechanism from viscoelastic dissipation to frictional dissipation, with the latter occurring between crack surfaces.

2.10.1 Effect of Grain Volume Fraction

Higher grain volume fractions lead to a larger energy output since the binder is inert. On the other hand, higher grain volume fractions decrease the average thickness of binder between adjacent grains, thereby increasing the reaction initiation sensitivity of the PBX due to more severe binder deformation and grain failure under the same loading condition. To quantify the effect of grain volume fraction on response, a comparative study is carried out using the digitized and idealized microstructures shown in Figure 2 and Figure 3. The loading configuration in Figure 10(a) is used.

Figure 19(a-b) show the distributions of temperature at an overall strain of ε = 5.5% for two microstructures, one with a grain volume fraction of η = 0.64 [Figure 2(c)] and the other with a grain volume fraction of η = 0.82. For the microstructure with η = 0.64, temperature rises are primarily limited to the binder since essentially no fracture occurs in the grains. In contrast, for the microstructure with η = 0.82, extensive grain fracture occurs, giving rise to more significant temperature increases in the grains. This is in addition to the higher temperatures in the binder due to more severe deformation. Thus, higher grain contents cause more intense deformation in the binder, hasten the onset of grain-binder interfacial failure and grain-grain interactions, promote grain fracture, and increase frictional dissipation, resulting in more pronounced heating under the same loading condition.

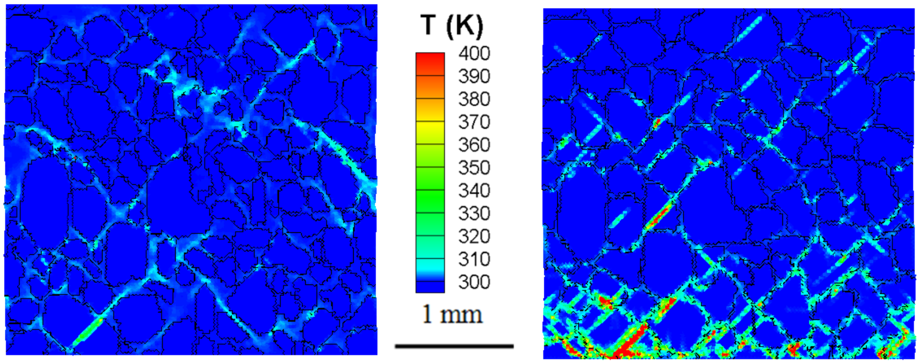

(a) $\eta = 0.64$ (b) $\eta = 0.82$

Figure 19: Distributions of temperature at $t = 3.8\ \mu s$ for $T_i = 300$ K and $\dot{\varepsilon} = 16{,}667\ s^{-1}$ for two microstructures with different grain volume fractions, (a) $\eta = 0.64$ [microstructure in Fig. 2(c)] and (b) $\eta = 0.82$ [microstructure in Figure 2(f)].

The temperature field in Figure 19(b) shows more intense deformation and severe heating near the bottom surface. This is due to the fact that the lower boundary is taken as a rigid boundary without transmission of the loading wave into the surrounding medium. Upon impinging on the lower boundary, the incident stress wave is reflected back into the material, subjecting the lower portion of the material to slightly more intense loading.

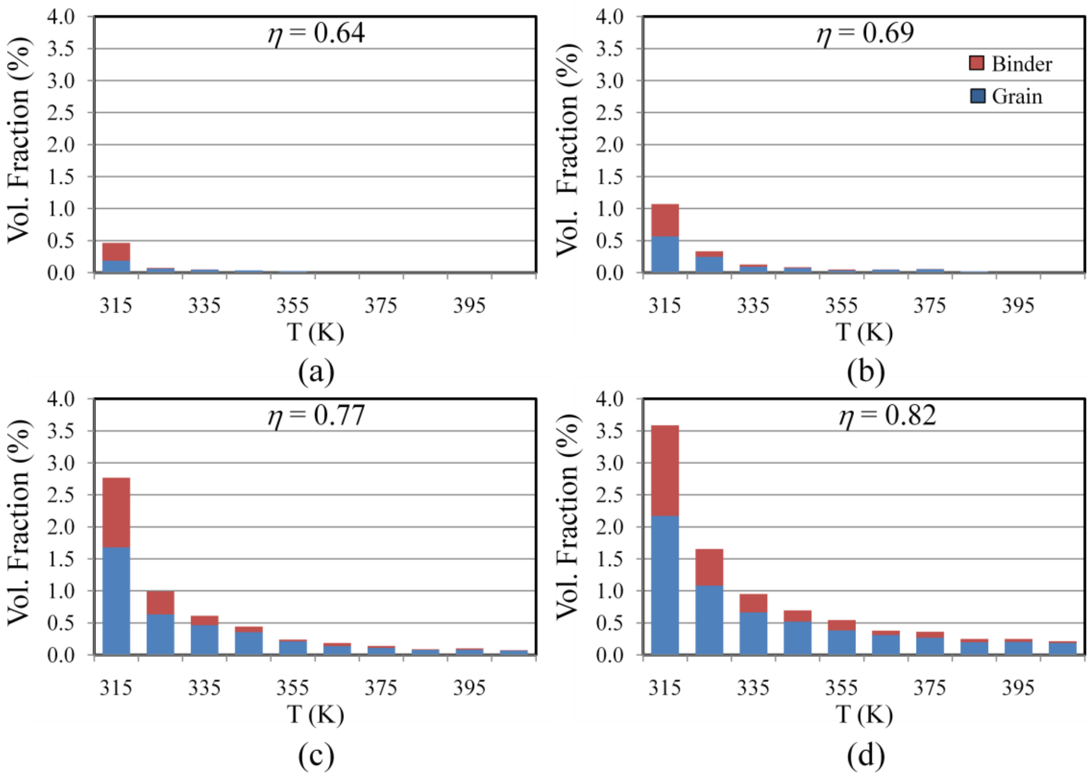

Figure 20: Histograms showing fractions of binder and grains in terms of volume at different temperature ranges for T_i = 300 K, $\dot{\varepsilon}$ = 16,667 s^{-1} and ε = 5.5%, results for four microstructure compositions [Figure 2] are shown.

The temperature rises in the binder and grains are quantified separately in Figure 20. The histograms show the volume percentage of each phase having a certain value of temperature after 3.6 μs of deformation at a strain rate of $\dot{\varepsilon}$ = 16,667 s^{-1} (total nominal strain of ε = 5.5%). Clearly, as the grain content (measured by grain volume fraction η) increases heating of both phases in the microstructures intensifies. At the low temperature end (~315-355 K), the volume percentages for the binder and the grains are similar or of the same order of magnitude. This can be attributed to the lower intensity of heating due to viscoelastic dissipation in the binder and heat conduction into the grains. However, at high temperature rises (>355 K) the amount of heating in grains is much more significant due to transgranular fracture and subsequent frictional dissipation. This effect is more pronounced for higher grain volume fractions (η = 0.77 – 0.82). Calculations using idealized microstructures follow the same trend.

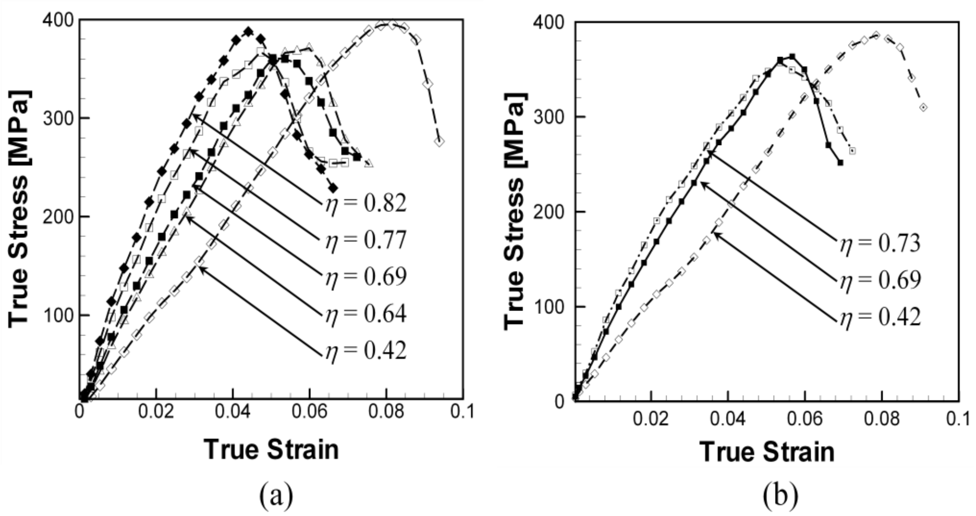

Figure 21: Comparison of calculated stress-strain curves for (a) digitized microstructures with variation of grain volume fractions [shown in Figure 2] and (b) idealized microstructures [shown in Figure 3] (η = 0.42 – 0.82, T_i = 300 K and $\dot{\varepsilon}$ = 16,667 s^{-1}).

The stress-strain responses for digitized microstructures with variation of grain volume fractions and idealized microstructures are quantified in Figure 21(a-b), respectively. The stress rises rapidly with strain until it reaches peak values of nearly 400 MPa before strain softening occurs. In the pre-peak regime, the response is quite sensitive to the amount of binder in the microstructures, as indicated by the slopes of the stress-strain curves. Specifically, as the binder volume fraction decreases from 0.58 to 0.18, the slope increases from 5.15 GPa to 9.52 GPa. The relationship between the binder volume fraction (η') and the slope of the stress-strain curves (s), can be approximated by a linear fit of the form,

$$s = \left(-10.93 \cdot \eta' + 11.36\right) \text{GPa}, \tag{2.29}$$

This trend applies to both digitized and idealized microstructures. Note that $\eta + \eta' = 1$.

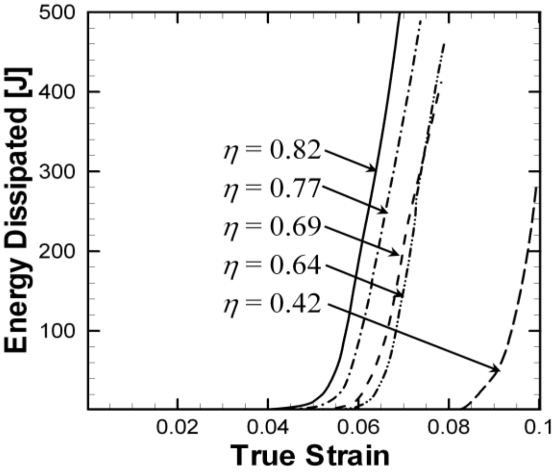

Figure 22: Frictional dissipation in the digitized microstructures with variation with grain volume fractions [shown in Figure 2] (T_i = 300 K and $\dot{\varepsilon}$ = 16,667 s^{-1}).

In contrast to what is seen for the stiffness, the peak stress is quite insensitive to the binder content and is similar for all the microstructures analyzed. Obviously, failure through crack development, rather than bulk deformation, plays the deciding role in determining the strength of the materials. However, the strain at which the peak stress occurs shows a clear dependence on binder content. Specifically, as the binder content changes from 0.58 to 0.18, this strain changes from 8.16% to 4.40%. This correlation can also be described by a linear fit. A detailed analysis shows that this strain has a clear significance in quantifying the transition between heating mechanisms in the microstructures. This issue will be the topic of a future publication. Here, the focus is on the onset of frictional dissipation. Figure 18 shows the total amount of frictional dissipation in the actual microstructures as a function of time. A comparison of Figure 22 and Figure 21(a) shows that the initiation of frictional dissipation corresponds to the peaking of stress. This observation is supported by experimental results of Siviour et al. [104] who reported that localization of deformation leads to cracking near the peak stress. This correlation clearly demonstrates the effects of binder volume fraction on ductility, failure and energy dissipation in PBX microstructures. The relations obtained provide guidance for the design and formulation of specific materials.

2.10.2 Influence of Grain Morphology and Particle Size Distributions

The effect of particle shape and size has been experimentally studied in the literature. Specifically, van der Heijden [105] showed that grain content, size distribution and smoothness of grains affect the initiation pressure of RDX- and HMX-based PBXs. In this section, the CFEM framework is used to study the relative importance of the different failure mechanisms for various microstructures. A comparative study is carried out using four microstructures with different grain shapes and size distributions. The microstructures have various grain morphologies and size distributions – (A) digitized microstructure [Figure 2(d)], (B) idealized microstructure with circular grains with a bi-modal size distribution [Figure 2(b)], (C) circular grains with a normal (or Gaussian) size distribution [Figure 5(a)] and (D) diamond shaped grains with a normal size distribution [Figure 3(b)]. The volume fractions of grains for all the microstructures considered are essentially the same ($\eta \approx 0.69$). Henceforth, these microstructures will be referred to as A, B, C and D.

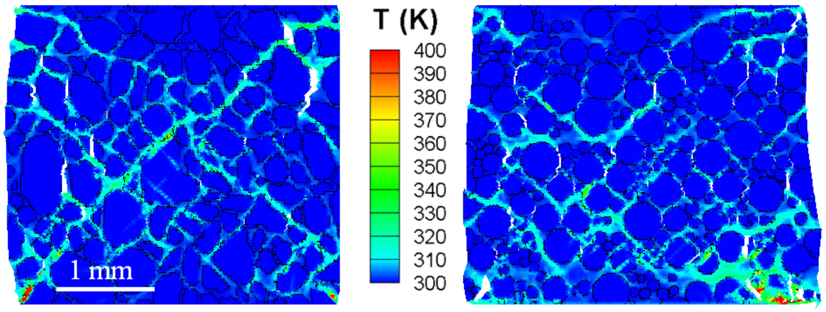

Real microstructure (A)

Spherical grains:
bi-modal distribution (B)

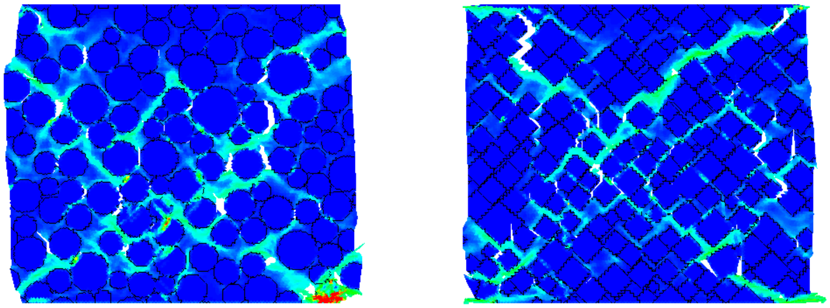

Spherical grains:
monomodal distribution (C)

Diamond shaped grains (D)

Figure 23: Distributions of temperature and damage in microstructures A-D (T_i = 300 K, $\dot{\varepsilon}$ = 16,667 s^{-1} and ε = 5.83%).

The four microstructures (A-D) are subject to loading under conditions of nominally uniaxial stress or no lateral confinement [configuration in Figure 10(b)]. Figure 23 shows the distributions of temperature and microcracks in these microstructures at an overall strain of ε = 5.83%. All the microstructures show extensive deformation and shear banding in the binder matrix. Interfacial debonding occurs throughout the microstructures, constituting the primary mode of failure in all cases irrespective of the differences in grain morphologies and grain size distributions. Although the failure mechanism is similar among the microstructures, their stress-carrying capability as measured by the $\sigma - \varepsilon$ curves differ, as shown in Figure 24. At strains below approximately 2%, the curves are similar, reflecting the fact that, before the initiation of damage, the stress-strain response is determined by the composition or phase fractions. At strains beyond approximately 2%, the response varies significantly among the microstructures. While microstructures A and B exhibit higher peak stresses and higher subsequent flow stresses, microstructures C and D show lower peak stresses and gradual decreases of stress. This indicates strain softening resulting from sliding of grains and progressive damage through the development of microcracks.

Figure 25(a-b) show the total energy dissipated in creating crack surfaces (fracture energy) and the total energy dissipated due to the viscoelastic deformation of the binder phase (hereafter referred to as viscoelastic dissipation), for the four microstructures A–D. Beyond a strain of 2%, fracture energy dissipations for A and B are higher than for C and D. This indicates that a higher amount of fractured surfaces is generated in case of A and B. However, viscoelastic dissipation for microstructures A and B is lower than in case of C and D. This can be attributed to the larger shear deformation of the binder in C and D due to enhanced sliding between grains, echoing what is seen in Figure 24. This indicates that in this loading regime, strain softening in microstructures C and D is more due to sliding of grains than development of microcracks.

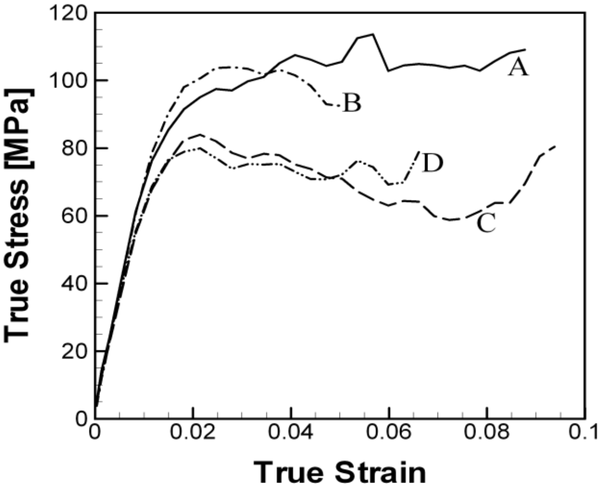

Figure 24: Comparison of stress-strain curves for microstructures with different grain morphologies (T_i = 300 K, $\dot{\varepsilon}$ = 16,667 s^{-1}).

The difference in the post-yield response between microstructure B and microstructures C and D has to do with the distribution of grain size. In microstructures C and D (which have monomodal Gaussian grain size distributions), the packing of grains is less compact than in B, leading to larger areas of binder between adjacent grains. Consequently, more pronounced sliding can occur between granules, leading to lower overall stress levels in these microstructures and the strain softening behavior seen in Figure 24. Also, the similarity in the $\sigma - \varepsilon$ responses of C and D indicates that the change in grain morphology from circular to diamond does not have a significantly effect on the overall mechanical response.

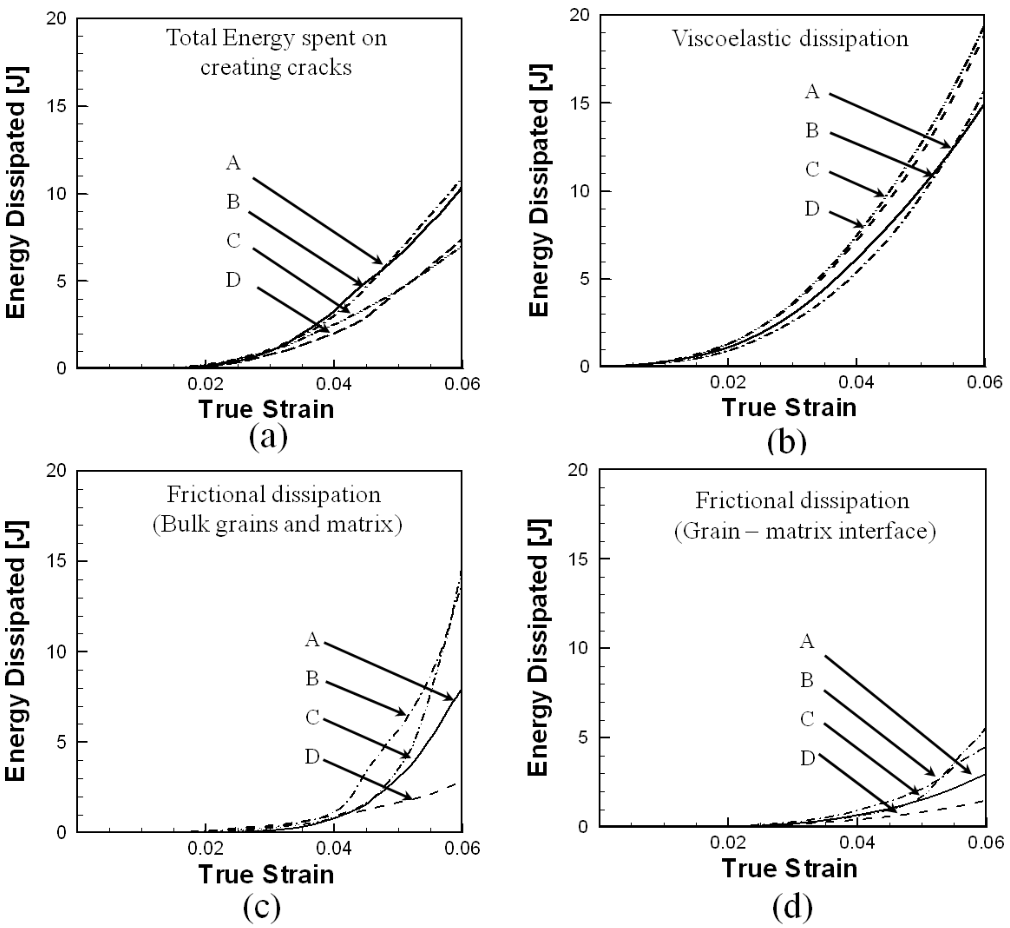

(a) (b) (c) (d)

Figure 25: Histories of Energy dissipation in microstructures A–D (T_i = 300 K, $\dot{\varepsilon}$ = 16,667 s^{-1}).

On the other hand in microstructure B which has a bimodal size distribution of grains, smaller granules packed in between larger grains create interlocking arrangements of small and large grains. Such arrangements hinder sliding of grains. As a result, higher stresses develop in the microstructure. The bi-modal packing also poses an obstacle to the formation of large, continuous crack surfaces, partly because the tearing of the matrix requires more mechanical work than the debonding of grain matrix-interfaces as quantified by fracture energies implied by the cohesive parameters in Table 2. Thus, bimodal size distributions of grains are beneficial to the load-carrying-capacity of PBXs under dynamic loading due primarily to enhanced grain-grain interactions and efficient packing of smaller grains between larger grains. Consequently, bi-modal distributions are especially desirable for PBXs with higher grain volume fractions.

At the grain scale, the geometry of the particles influences the nature and severity of stress distribution and concentration. This effect in turn affects the debonding at the grain-matrix interfaces and the subsequent energy dissipation due to friction. The time histories of the total energy dissipated due to friction along crack surfaces (both along the interfaces between the two phases and inside each of the phases) for the four microstructures are shown in Figure 25(c-d). For strains up to approximately 4%, the profiles are similar for the cases. At strains beyond 4%, higher frictional dissipation is observed for the microstructures with circular grains (B and C), followed by the microstructure with multifaceted grains (A), and the microstructure with diamond-shaped grains (D). The planar grain facets in A and D appear to facilitate interfacial debonding. At higher nominal strains, interfacial cracks coalesce, causing the constituents to separate from each other and resulting in the lateral splitting seen in Figure 23. This process leads to a decrease in intergranular interactions. On the other hand, the curved interfaces associated with the circular grains in B and C make it less likely for the cracks to coalesce and the phases less likely to separate, thereby maintaining a higher level of constituent interactions and leading to higher frictional dissipation. From the point of view of designing PBXs, especially PBXs with high packing densities, multifaceted grain morphologies with planar facets may help keep frictional dissipation low under conditions with low lateral confinement or low hydrostatic pressures.

2.11 Effect of Initial Temperature

In this section, the effects of changes in the initial temperature on the impact response of a HMX/Estane PBX are evaluated. Fracture mechanisms considered include crack initiation, growth and coalescence inside bulk constituents and along interfaces between the HMX and Estane binder. Initial temperatures between 210 and 300 K are considered, covering the glass transition temperature T_g (243 K) of the binder. The objective is to obtain a correlation between the grain-level failure mechanisms and macroscopic behavior of the PBX over the temperature regime.

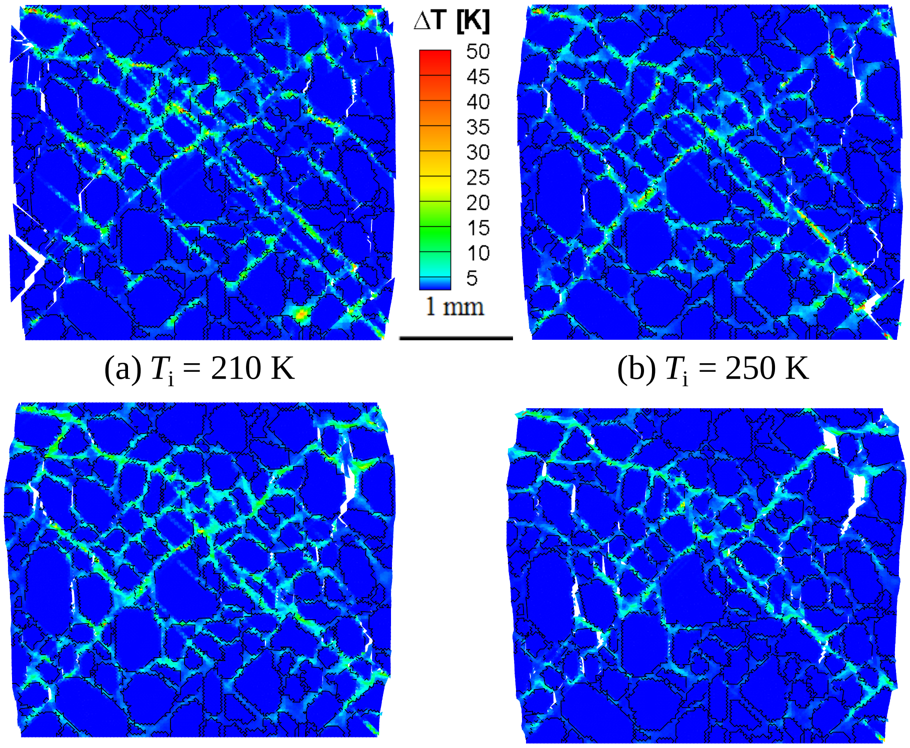

(a) T_i = 210 K (b) T_i = 250 K

(c) T_i = 270 K (d) T_i = 300 K

Figure 26: Distribution of temperature increase in the microstructure at t = 4.0 μs (ε = 5.83%) for four different cases: (a) T_i = 210 K, (b) 250 K, (c) 270 K, and (d) 300 K (the nominal strain rate is $\dot{\varepsilon}$ = 16,667 s^{-1})

A systematic analysis is carried out, focusing on the effect of initial temperature. The imposed boundary velocity at the top surface of the configurations in Figure 10(b) is v = 50 ms^{-1} (which gives rise to a nominal strain rate of $\dot{\varepsilon}$ = 16,667 s^{-1}) with a linear ramp from zero to v in the first 1 μs of loading. Here, results at four different initial temperatures (210, 250, 270 and 300 K) are discussed.

Figure 26 shows the distribution of temperature rise over the initial temperature $\left(\Delta T = T - T_{\mathrm{i}}\right)$ at time t = 4.0 μs (ε = 5.83%) after the onset of loading for different values of initial temperature. For all calculations, the distribution of temperature is influenced by the microstructural heterogeneity. High temperature rises are localized mainly in bands in the matrix. These high temperature bands extend diagonally across the microstructure, approximately following the direction of maximum shear stresses. The temperature sensitivity of the binder causes different failure mechanisms to be active at different temperature regimes.

At 210 K ($T_{\mathrm{i}} < T_{\mathrm{g}}$), the dominant failure mechanism is the fracture of bulk constituents. Cracks develop in the binder and coalesce with transgranular cracks in the grains to form continuous failure paths. The fracture paths run through the grains and binder, resulting in fragmentation of the composite [see Figure 27(a)]. This can be observed at the lateral surfaces of the microstructure in Figure 26(a). At this temperature, the binder is hard and brittle, causing high stresses to be developed. Consequently, the stress-strain profiles show higher peak stresses (Figure 13). Subsequent loading causes the binder to fail by brittle fracture characterized by a sharp drop in stress. Relative sliding of fractured surfaces results in high frictional dissipation and temperature rises in the microstructure [Figure 13(a)].

As the initial temperature is increased beyond T_g, the binder increasingly behaves as a soft, viscous material. In early stages of loading, deformation is primarily accommodated by the softer binder, causing heating in the binder and heat conduction into the grains across the grain-binder interface. Initially, higher temperature rises occurs in regions of the binder between neighboring grains carrying high normal and shear stresses. Subsequently, these areas coalesce to form shear bands. It is noted that shear bands in the binder alone typically do not generate sufficient heat to cause melting of the HMX grains.

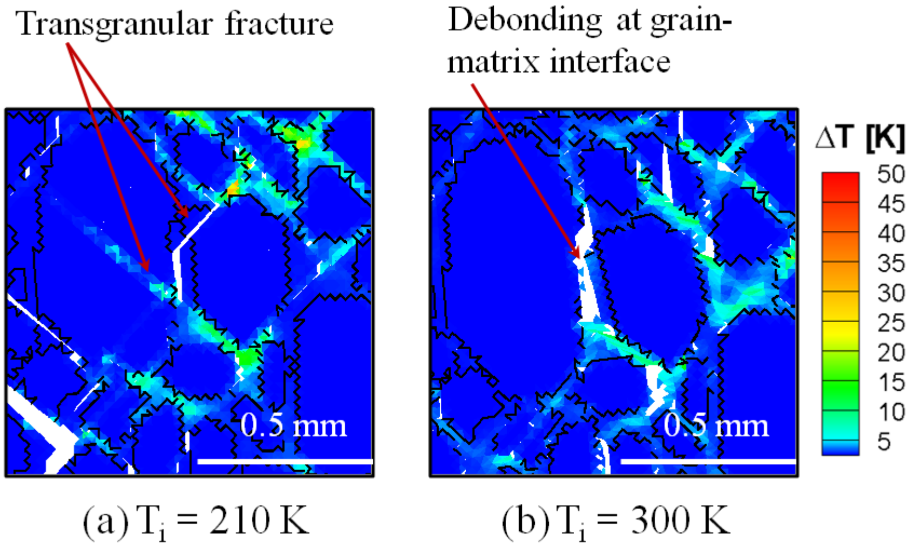

Figure 27: Close-up view of a region of the microstructure at t = 4.0 μs (ε = 5.83%) showing the different failure mechanisms at (a) T_i = 210 K and (b) 300 K (the nominal strain rate is $\dot{\varepsilon}$ = 16,667 s^{-1}).

The soft binder allows relative motion of grains to take place, activating other energy dissipation mechanisms. Debonding along the relatively weak grain-matrix interface is the primary mode of damage [Figure 27(b)]. Such interfacial debonding has also been experimentally observed in experiments at both low and high strain rates (see, e.g., Rae et al. [18] and Siviour et al. [11]). This form of damage reduces the effective modulus of the overall microstructure (Banerjee et al. [38]). At higher levels of nominal strain (> 3%), grain-grain interactions occur.

The locations where grains come into contact with each other are sites of severe stress concentration, crack development and grain-matrix sliding. Crack formation, sliding and the ensuing frictional dissipation cause more intense heating and higher temperatures. Further deformation leads to transgranular fracture of grains. Crack development, grain-matrix debonding and transgranular fracture create more surfaces which may come into contact and slide against one another, giving rise to additional frictional dissipation and heating. These processes ultimately lead to more severe heating in the microstructure, resulting in what is known as the hot-spots which can cause ignition of energetic materials [91].

At first, the case with T_{i} = 300 K is considered and it is used as the basis for comparison. Figure 28 shows the evolution of total mechanical work imparted to the microstructure by the applied load or boundary work (W_b), elastic strain energy (W_e), and kinetic energy (W_k). The three forms of energy dissipation –energy spent on causing fracture or fracture energy (W_c), viscoelastic dissipation (W_{ve}) and frictional dissipation (W_f) – are also shown. Only W_{ve} and W_f contribute to temperature rises in the microstructure. Boundary work (W_b) increases nearly linearly to 60 J as the nominal strain reaches 0.07. Initially, the increase in kinetic energy (W_k) is higher than the increase in elastic strain energy (W_{ve}), indicating that more energy is stored in the specimen as kinetic energy than as elastic strain energy. Beyond a nominal strain of 0.04, the rate of change of W_k decreases and becomes approximately equal to the rate of change of W_f, indicating a gradual decrease in specimen acceleration and the intensification of fracture and heating due to viscoelastic and frictional dissipation. Energy dissipated through fracture increases linearly up to 30 J as the overall strain increases to 0.07. At this value of overall strain, W_c constitutes the largest portion of W_b (68.3%), followed by W_{ve} (23.1%) and W_c (8.6%). The viscoelastic dissipation (W_{ve}) is primarily associated with the shear deformation of the binder and accounts for approximately 15.9% of the overall boundary input (W_b). In contrast, elastic strain energy (W_e) accounts for approximately 10.2%.

The evolution of elastic strain energy, viscoelastic dissipation and frictional dissipation with overall strain for four initial temperatures between 210 and 300 K are shown in Figure 29(a–c). The elastic strain energy is higher at lower initial temperatures, indicating the effect of higher elastic modulus of the binder at lower temperatures. In contrast, viscoelastic dissipation in the binder does not show a clear trend with the variation of initial temperature. Specifically, W_{ve} is low at both T_i = 210 K and 300 K and is highest at an intermediate temperature of 270 K. At 210 K (< T_g), the binder is relatively brittle, consequently, viscous dissipation is insignificant. At $T_i > T_g$, the softer binder absorbs most of the input energy and accommodates most of the imposed deformation. Increasing the initial temperature beyond T_g causes higher viscoelastic dissipation. Between 250 and 270 K, the binder is hard enough for high stresses to be developed, causing higher viscous dissipation. At 250 K, the rate of viscous dissipation decreases beyond a nominal strain of 4%, owing to increased fracture in the microstructure. At a higher temperature of 300 K, the binder is soft enough to prevent high stresses from being developed, causing viscous dissipation in the binder to decrease.

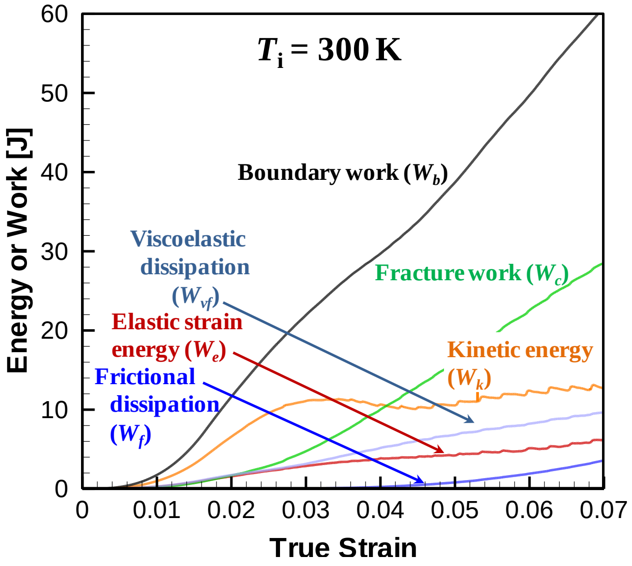

Figure 28: Evolution of mechanical work and dissipation, T_i = 300 K and $\dot{\varepsilon}$ = 16,667 s^{-1}.

Viscoelastic dissipation in the binder is the primary dissipation mechanism in early stages of the deformation. Accordingly, temperature increase occurs primarily in the binder. Although the binder is typically inert, a portion of the thermal energy is conducted into the grains through the grain-matrix interface. Thus, part of the temperature increase in the grains is due to viscous dissipation in the binder.

Figure 29(c) shows the energy dissipated due to frictional heating in bulk grains and matrix. Clearly, higher overall stresses and more extensive fracture at lower initial temperatures lead to higher levels of frictional dissipation. Since no fracture occurs in early stages of loading, frictional dissipation remains zero for strains up to 3%. Beyond this strain, frictional dissipation initiates in both bulk phases and along the grain-matrix interfaces.

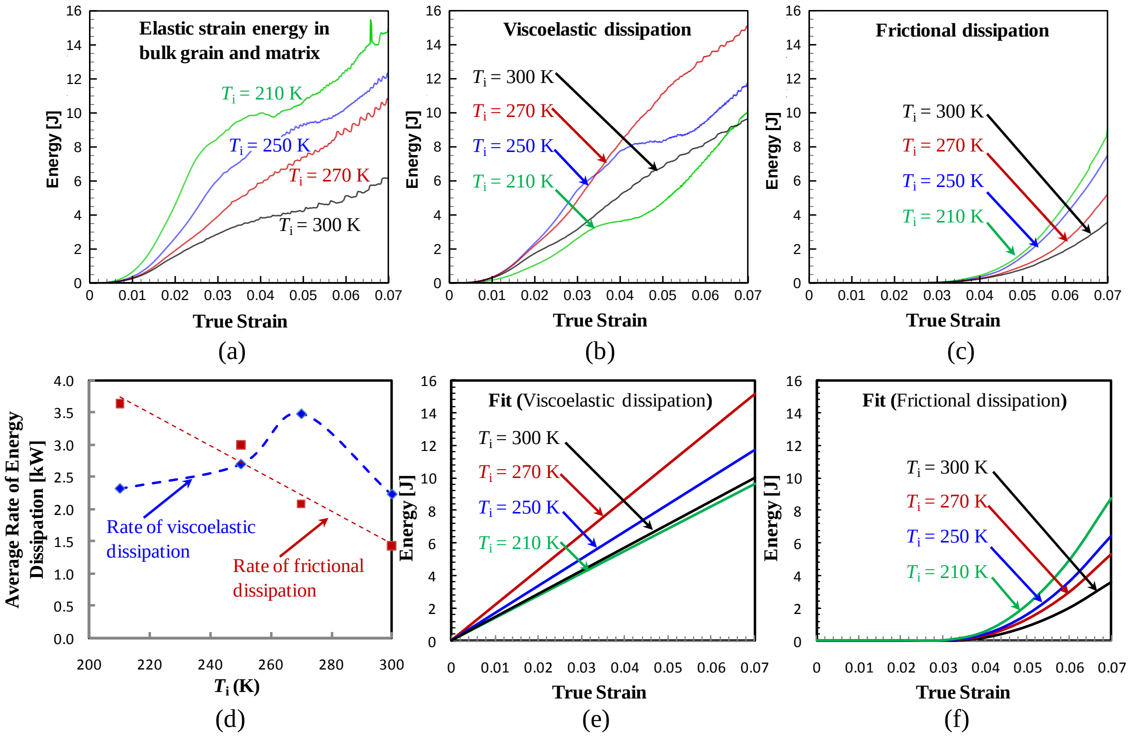

(a) (b) (c)

(d) (e) (f)

Figure 29: Evolution of elastic strain energy and dissipation with over strain (T_i = 210 - 300 K and $\dot{\varepsilon}$ = 16,667 s^{-1}), (a) elastic strain energy, (b) viscoelastic dissipation, (c) frictional dissipation, (d) average dissipation rates, (e) fit for viscoelastic dissipation, and (f) fit for frictional dissipation.

The contributions of viscoelastic and frictional dissipations to temperature rises in the microstructure vary with initial temperature. Quantifying the dissipations provides insight into the heating mechanisms and their temperature- and time-dependence. Figure 29(d) plots the rates of viscoelastic and frictional dissipations at different values of initial temperature. The rates are averaged over the duration of deformation up to 0.07. It can be seen that the rate of viscoelastic dissipation is low (~ 2.3 kW) at both ends of the temperature range (210 K and 300 K) and reaches a maximum value of around 3.48 kW at the intermediate temperature of T_i = 270 K. Deformation and viscoelastic dissipation in the binder are lower at low temperatures (e.g., 210 K) because the brittle nature of the binder enhance failure and frictional dissipation in both phases. While at high temperatures (e.g., 300 K), lower overall stresses translate into lower viscoelastic dissipation. For each initial temperature, viscoelastic dissipation (W_{ve}) increases essentially linearly with time [Figure 10(b)]. In such cases, the rate of viscous dissipation $W'_{ve}(t)$ can be assumed to be a constant which dependents only on T_i, i.e.,

$$W'_{ve}(t) = C(T_\mathrm{i}); \quad t \geq 0. \tag{2.30}$$

where $C(T_\mathrm{i})$ is the average rate of viscous dissipation as shown in Figure 29(d). Thus, the viscous dissipation can be obtained as a function of time by simply integrating Eq. (2.30) as,

$$W_{ve}(t) = C(T_\mathrm{i}) \cdot t; \quad t \geq 0. \tag{2.31}$$

In contrast to viscoelastic dissipation, frictional dissipation does not initiate until a delay strain (ε_d) or delay time (t_d) has elapsed. Once frictional dissipation (W_f) initiates, its rate (W_f') varies linearly with time. Thus, the variation of frictional dissipation rate W_f' can be expressed as,

$$W_f'(t) = \begin{cases} 0; & 0 \le t \le t_\mathrm{d} \\ D(T_\mathrm{i}) \cdot t; & t \ge t_\mathrm{d}, \end{cases} \tag{2.32}$$

where $D(T_\mathrm{i}) = -71.9816 \cdot T_\mathrm{i}$ (kW). The variation of frictional dissipation with time is, therefore,

$$W_f(t) = \begin{cases} 0; & 0 \le t \le t_\mathrm{d} \\ D(T_\mathrm{i}) \cdot (t - t_\mathrm{d})^2; & t \ge t_\mathrm{d}. \end{cases} \tag{2.33}$$

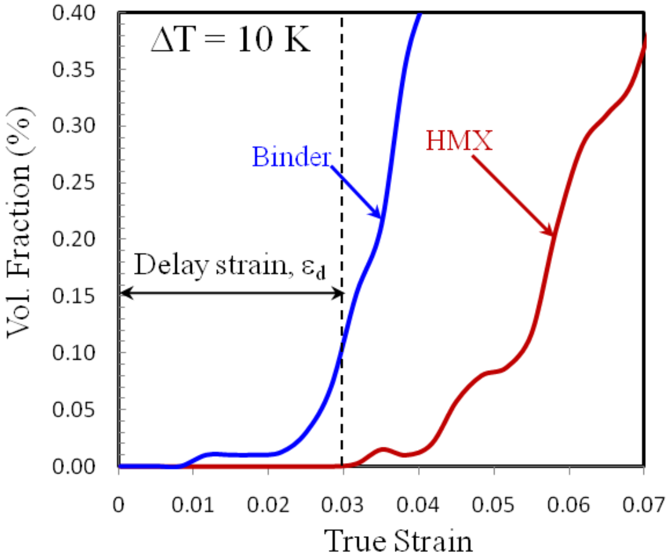

Figure 30: Volume fractions of HMX grains and binder having a temperature rise of at least 10 K (T_i = 300 K and $\dot{\varepsilon}$ = 16,667 s^{-1}).

Equations (2.32) and (2.33) are plotted in Figure 29(d-e). The fit for frictional dissipation agrees well with the calculated curves in Figure 29(c). A comparison of and

W_{ve} and W_f shows that the onset of frictional dissipation has no appreciable impact on viscoelastic dissipation. Since W_{ve} has a linear dependence on time and W_f is a quadratic function of time, the onset of frictional dissipation signifies a transition in heating mechanism from one dominated by viscoelasticity to one dominated by internal friction. Figure 30 shows the volume fractions of binder and HMX granules having temperature rises of at least 10 K for the case with T_i = 300 K. Heating in the HMX phase initiates at a nominal strain of 0.03 which is identical to the delay strain obtained earlier. Clearly, heating in the grains is primarily due to frictional dissipation which dominates the overall heating process once it sets in.

It can be inferred from Figure 29(c) that the delay strain is not dependent on initial temperature and frictional dissipation initiates at the same level of overall strain. Previous experimental study by Govier et al. [9] showed that the failure strain or strain corresponding to peak stress of the PBX is invariant with respect to initial temperatures between 218-328 K. The experimental result and the results obtained here show that the initiation of fracture and friction in this PBX is not sensitive to initial temperature. On the other hand, packing density and loading rate are expected to play a more important role in affecting damage initiation consequently the delay strain.

The temperature rises in the binder and grains are quantified separately in Figure 31. The histograms show the percentage by volume of each phase having a certain value of temperature increase after 5.0 μs of deformation at a strain rate of $\dot{\boldsymbol{\varepsilon}}$ = 16,667 s^{-1}. The strain (ε = 7.5%) is identical for all four cases while the temperature rise is relative to the initial temperature. For all cases, most of the microstructure experiences lower temperature rises (~5 K) and only smaller fractions of the volume experience higher values of Δ*T*. At both 210 K and 300 K, significant heating takes place in the binder and grains, with the binder being heated more than the grains. More severe heating occurs in the binder at T_i = 300 K, particularly at the low temperature end (~5–10 K). Temperature increases at the lower end are primarily due to viscous dissipation in the binder which is partly conducted to the grains.

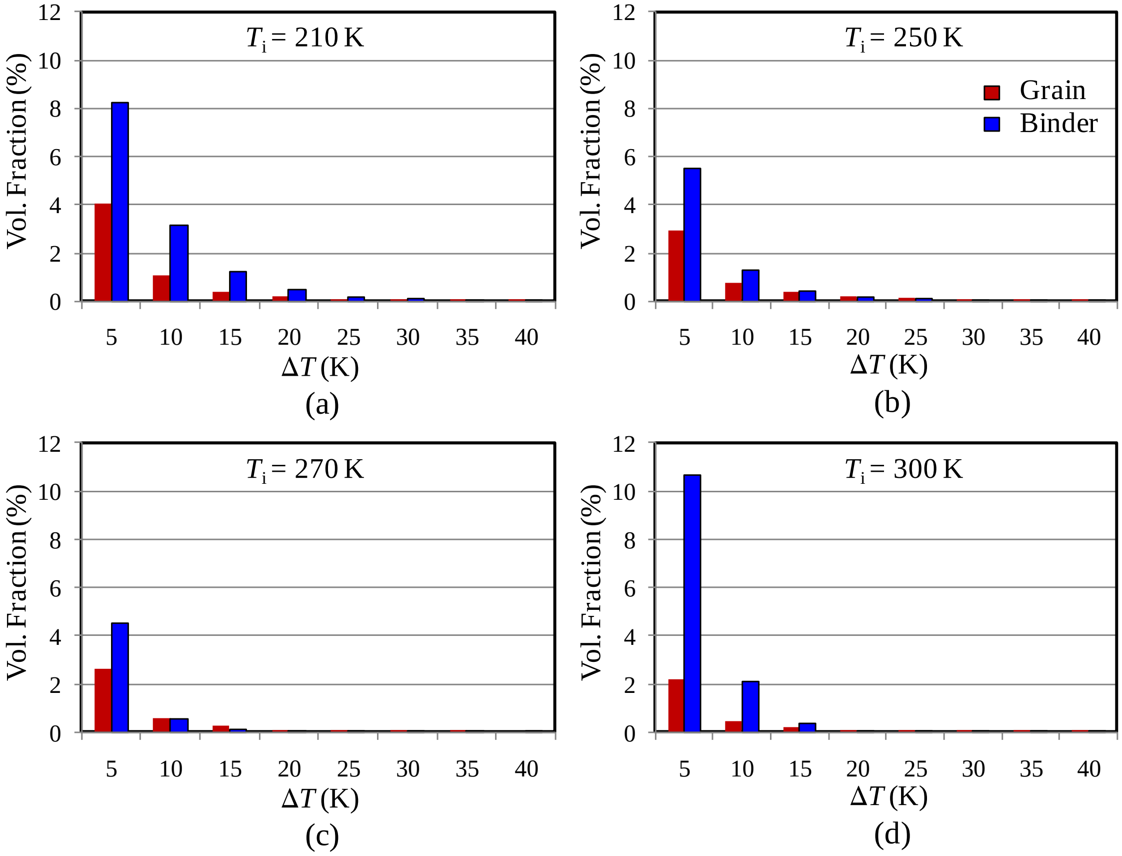

Figure 31: Histograms showing fractions of binder and grains in terms of volume at different temperature ranges for T_i = 210 – 300 K, $\dot{\varepsilon}$ = 16,667 s^{-1}, at *t* = 5.0 *μ*s, (ε = 7.5%).

At T_i = 210 K, temperature rises in the grains are almost twice that at T_i = 300 K. This can be attributed to earlier fracture and higher frictional dissipation at lower initial temperatures. Thus, as the initial temperature is increased, viscous deformation of the binder delays the onset of grain-binder interfacial failure and more importantly, grain-grain interactions.

2.12 Conclusions

A fully coupled thermomechanical finite-deformation framework is developed to analyze the response of polymer-bonded explosives (PBXs). The framework is based on the cohesive finite element method and provides explicit tracking of failure through crack development and frictional heating as well as explicit account of microstructure. The analyses carried out focus on composites consisting of HMX granules bonded by an Estane matrix under conditions of deformation at strain rates on the order of 16-17×10^3 s^{-1}. Digitized micrographs of an actual material and idealized microstructures are used to investigate the effects of composition, phase arrangement, phase size distribution and phase morphology on the evolution of temperature field, damage and failure. Calculations show that higher volume fractions of HXM granules correspond to more severe heating and a lower threshold for fracture initiation. Under the conditions analyzed, bimodal distributions of granule sizes are more beneficial to the mechanical integrity of the composites than monomodal distributions. Grains with planar facets increase the likelihood of failure through grain-matrix debonding relative to grains with rounded shapes.

CHAPTER 3: ENERGY LOCALIZATION

3.1 Introduction

Dissipation mechanisms occurring at the grain-level result in localized high temperature regions or hot-spots which eventually lead to chemical reactions. Once formed, the hot-spots can react exothermally creating an ignition site [3]. As the hot-spot grows, higher temperature and pressure might lead to a deflagration or detonation. Shock initiation of explosives has been studied extensively in literature [4-5]. However, initiation and subsequent detonation can occur in the absence of shock [5], indicating that the mechanisms leading to energy localization need to be well understood. During low velocity impact, the effect of fracture and frictional dissipation in grains and in the grain-matrix interface and the viscoelastic nature of the binder play an important role in energy dissipation. Thus mechanisms leading to hot-spot formation are dependent on microstructure and loading conditions.

Quantification of the contributions of different dissipation mechanisms and how the contributions evolve as deformation progresses is essential in order to develop predictive models that can be used to characterize the formation of hot spots. In this chapter, the CFEM framework, developed in Chapter 2 is used to quantify the effects of microstructure and thermal-mechanical processes such as matrix deformation, interfacial debonding and fracture of grains on hot spot formation. Simulations are carried out for a range of strain rates, grain volume fraction and confinement condition. The focus is characterizing energy localization as a function of loading and microstructural attributes.

This chapter is based on the work published in Barua et al. [106].

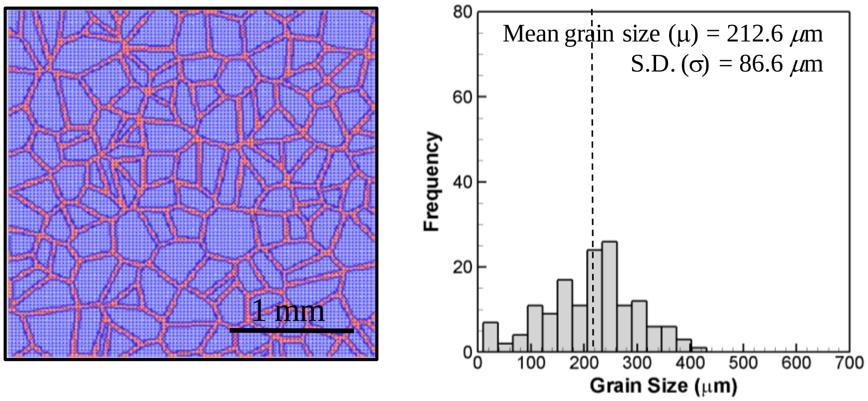

(a) Microstructure – 1 (b) Grain Size Distribution

Figure 32: (a) A representative idealized microstructure with a grain volume fraction of η = 0.69 and (b) the grain size distribution of the microstructure.

3.2 Microstructure Modeling

In this analysis, both idealized and actual microstructures are used. The actual microstructure is obtained from [11] and its grain volume fraction is digitally varied between 0.69 and 0.82. The micrographs are given and quantified in Figure 2 and Figure 4. Additionally, a set of six idealized microstructures are used. These are generated using 2D Voronoi tessellation functions in MATLAB. This approach allows multifaceted grains with morphologies similar to those of actual HMX grains to be obtained. Previously, Wu et al. [39] used a similar approach to generate idealized PBX microstructures. Figure 32(a) shows a representative idealized microstructure having a grain volume fraction of η = 0.69. The grain size distributions for this set of six microstructures are similar and have means between 203.6 and 224.2 μm and standard deviations between 86.6 and 111.4 μm [e.g. the grain size distribution for the microstructure in Figure 32(a) is shown in Figure 32(b)]. The microstructures analyzed in this chapter, along with their attributes are listed in Table 3. Together, these allow the evaluation of statistical variation in response for microstructures having similar attributes.

Table 3: Microstructures analyzed in Chapter 3.

Microstructure	Grain Volume Fraction (η)	Average Grain Size (μm)	Standard Deviation (μm)	N_A (mm^{-2})
Digitized	0.69	214.0	108.9	12.08
Digitized	0.77	238.0	121.4	14.17
Digitized	0.82	287.4	120.6	11.10
Idealized (6 instantiations)	0.69	203.6 - 222.4	86.6 - 111.4	-

3.3 Results and Discussion

A parametric study is carried out, focusing on the effects of (i) strain rate, (ii) confinement and (iii) grain volume fraction (η = 0.69 to 0.82). For all calculations presented, the initial temperature is $T_i = 300$ K. The loading configuration used is shown in Figure 10(c). In the calculations carried out in this chapter, three confinement levels are considered, (1) uniaxial strain ($v_L = 0$), (2) $v_L/v = 0.5$, and (3) uniaxial stress (v_L not specified, lateral sides are traction-free). The velocity v of the top surface is varied between 50 to 300 ms^{-1}, yielding overall strain rates of $\dot{\boldsymbol{\varepsilon}} = (16.6 – 100) \times 10^3$ s^{-1}. The velocity is imposed at the top surface of the configurations in Figure 10(c), with a linear ramp from zero to v in the first 2 μs of loading. Unless otherwise noted, the nominal strain rate used is $\dot{\varepsilon} = 16.6 \times 10^3$ s^{-1}.

The overage velocity of the stress waves in the microstructure varies with the binder volume fraction of the PBX. For $\eta = 0.82$, the wave velocity is 2.65×10^3 ms^{-1}. The wave reaches the bottom surface at 1.1 μs. Since the top boundary is displaced at a constant velocity, the stress state in the sample can be considered as nominally homogeneous after the stress wave reaches the bottom surface. Analysis yields similar results for the other volume fractions considered.

3.3.1 Methodology for Detection of Hotspots

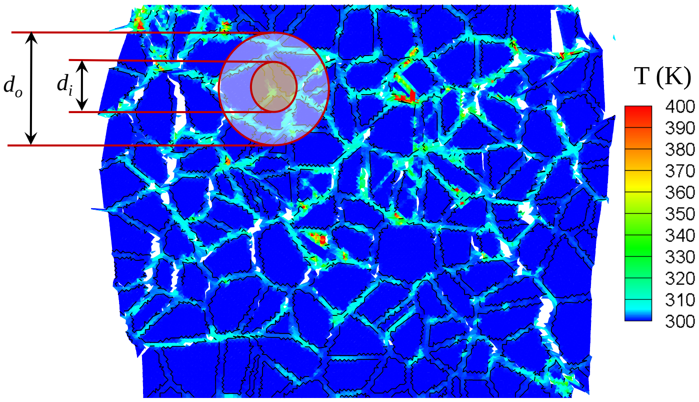

Figure 33: Scheme for hot spot detection.

To determine the size and temperature distributions of hot spots, a systematic scheme is used. A “microscope” with an inner diameter d_i and outer diameter d_o sweeps through the microstructure to identify potential hot spots (see Figure 33). The process involves the use of a threshold temperature (ΔT_{thres}). At each time step, the microstructure is scanned by calculating the average temperature over successive circular regions of diameter d_i. If the average temperature in the region exceeds the average temperature in the annulus region defined by d_i and d_o surrounding it by $\Delta T_{\mathrm{thres}}$, the region is identified as a hot spot.

The choice of the threshold temperature $\Delta T_{\mathrm{thres}}$ and sieve diameters d_i, and d_o are somewhat arbitrary. To identify the trend, different values for d_i, d_o and $\Delta T_{\mathrm{thres}}$ are used. First, d_i and d_o are held constant while $\Delta T_{\mathrm{thres}}$ is varied. Figure 34(a) shows the variation of the number density of hot spots with $\Delta T_{\mathrm{thres}}$ at the nominal strains of ε = 6.0 and 8.6 %. As $\Delta T_{\mathrm{thres}}$ increases, the number of hot spots initially decreases but gradually attains a steady value beyond $\Delta T_{\mathrm{thres}}$ = 20 K. This value of $\Delta T_{\mathrm{thres}}$ is used for all subsequent hot spot analyses.

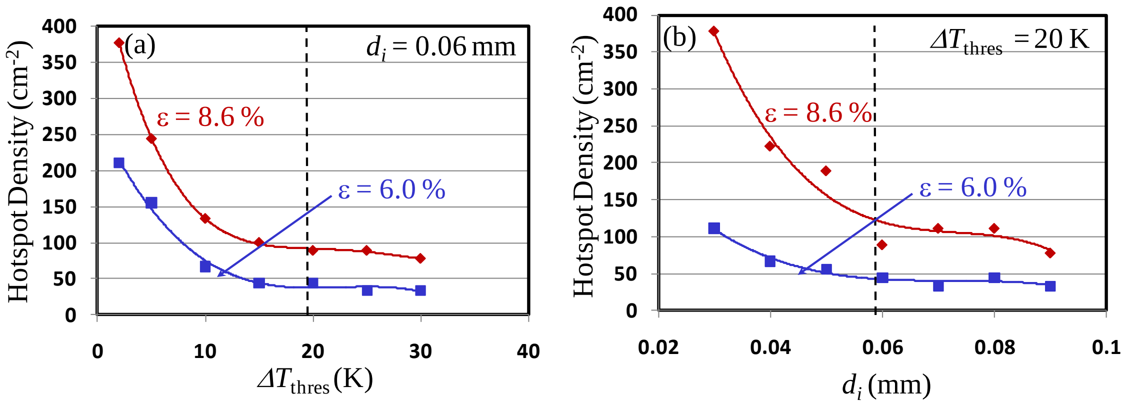

Figure 34: (a) Hot spots detected using different threshold temperatures; (b) number of hot spots detected using different critical sizes (η = 0.69, $\dot{\varepsilon}$ = 16.6×10^3 s^{-1}).

Similarly, in order to select the appropriate critical size value, d_i (d_o = 2d_i) is varied with $\Delta T_{\mathrm{thres}}$ = 20 K. The results in Figure 34(b) show that higher critical diameter values yield lower numbers of hot spots, however, beyond a critical diameter of d_i = 0.06

mm, the number of hot spots remain essentially the same. This trend is consistent at all strain values.

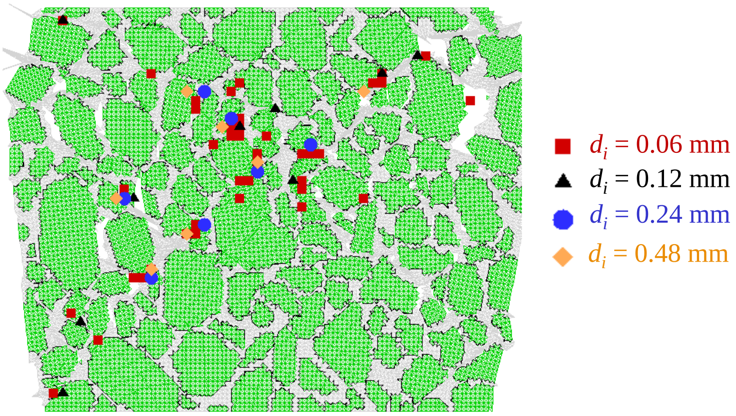

Figure 35: Hot spot detected using different values of d_i

The distribution of hot spots in the microstructure with $\eta = 0.69$ at a strain rate of 16.6×10^{3} s^{-1} and strain of $\varepsilon = 0.06$ is shown in Figure 35. The locations of the hot spots detected using different values of d_i overlap, suggesting that the approach used to define and identify hot spots produces results consistently. Although the specific threshold for defining hot spots is somewhat arbitrary, the approach has a benefit in that it allows the size distributions of hot spots in different cases to be compared on a relative basis. Note that most hot spots occur at locations of grain-grain interactions and are captured when the sieve size is in the range of d_i = 0.06 - 0.12 mm. This size range corresponds to the average thickness of the binder for microstructures with $\eta = 0.69$. At higher values of d_i, fewer hot spots are detected and are more sparsely distributed spatially. In all subsequent calculations, a critical size of d_i = 0.06 mm is used. The evolution of hot spots is dependent on several time-dependent thermo-mechanical processes. At first, one set of calculations is presented to illustrate the mechanisms responsible for hot spot formation.

3.3.2 Variation in Response among Microstructures with the Same Statistical Attributes

A set of six idealized microstructures is used in the analysis. These microstructures are different instantiations with the same statistical attributes [η = 0.69, grain size distribution in Figure 32(b)]. The overall strain rate is 16.6×10^{3} s^{-1}. Figure 36(a) shows the distribution of temperature at $\varepsilon = 0.05$ for microstructure 1 [Figure 32(a)]. Initially, temperature rises due to viscoelastic dissipation in the soft binder. As the binder deforms, damage occurs through grain-matrix debonding and tearing of the binder. These mechanisms allow neighboring grains to come into contact with each other, causing subsequent fracture and frictional dissipation. At higher levels of overall deformation, transgranular fracture occurs. Figure 36(b) shows the distribution of hot spots at $\varepsilon = 0.05$. A majority of the hot spots occur at locations of grain-grain interactions. These locations are characterized by severe stress concentration, crack development and grain-matrix sliding [79].

The failure processes are highly non-linear and the response of the material is consequently stochastic. Here, the statistical variations in the stress-strain relation and the hot spot count due to microstructural sample differences are characterized. Figure 37 shows the stress-strain relations at a strain rate of $\dot{\varepsilon}$ = 16,667 s^{-1} for the six idealized microstructures with η = 0.69. In the early stages of loading, deformation is primarily accommodated by the softer binder. Consequently, the variation in the stress-strain responses between the samples is small. Specifically, the variation is ~ 6 % up to a nominal strain of 0.04. As the nominal strain increases to 0.11, the variation in the stress-strain curves increases to 16%. The stress level at larger strains is influenced by two competing failure mechanisms: softening resulting from debonding at the grain-matrix interfaces and stiffening due to grain-grain interactions.

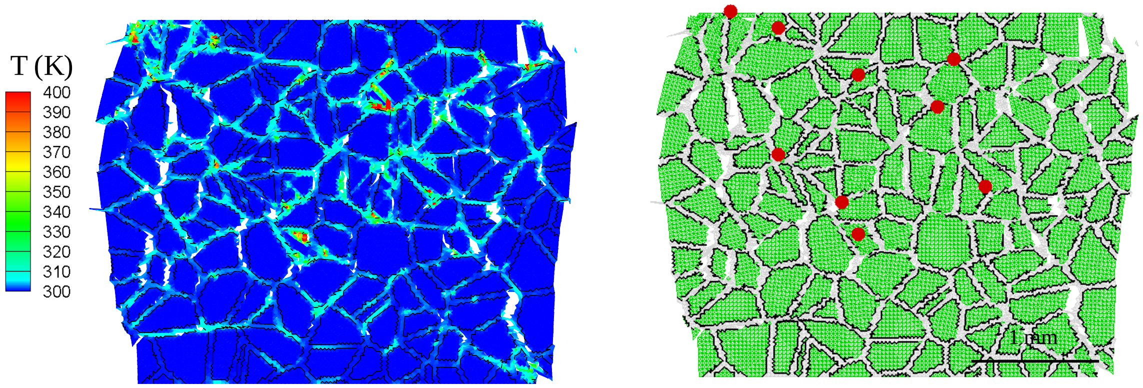

(a) (b)

Figure 36: (a) Distribution of temperature in the idealized microstructure in Figure 32(a) and (b) distribution of hot spots. (t = 4.2 μs, ε = 0.05 and $\dot{\varepsilon}$ = 16.6×10^3 s^{-1})

Figure 38 shows the evolution of the number of hot spots with the nominal strain for the six idealized microstructures. Unlike the variation in the stress-strain curves, the evolution of the number of hot spots is more consistent among the specimens.

3.3.3 Distribution of Hotspots

The formation of hot spots is analyzed over a range of strain rates and confinement conditions for PBXs with different volume fractions. A number of studies have focused on the effect of strain rate and the effect of constituent binders [8-9, 21, 107]. It is generally acknowledged that the rate dependency of the polymeric binder significantly influences the response of the composite. Corley et al. [3] used a non-linear viscoelastic material model to predict the high strain rate behavior of a particulate composite with HTPB as the binder. Rate dependency also influences microstructure-specific damage evolution which is difficult to quantify using analytical models.

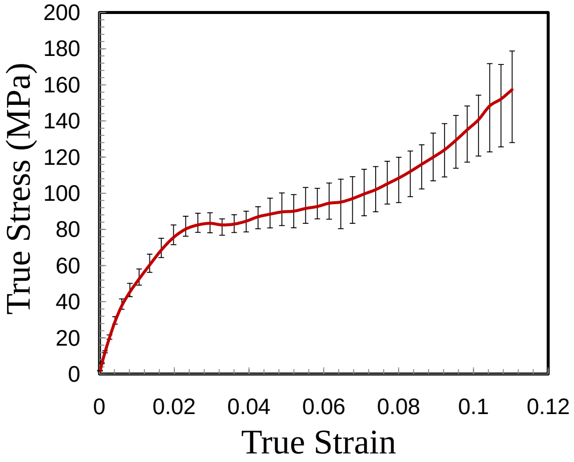

Figure 37: Stress-strain relations for six idealized microstructures with the same statistical attributes (η = 0.69, $\dot{\varepsilon}$ = 16,667 s^{-1}).

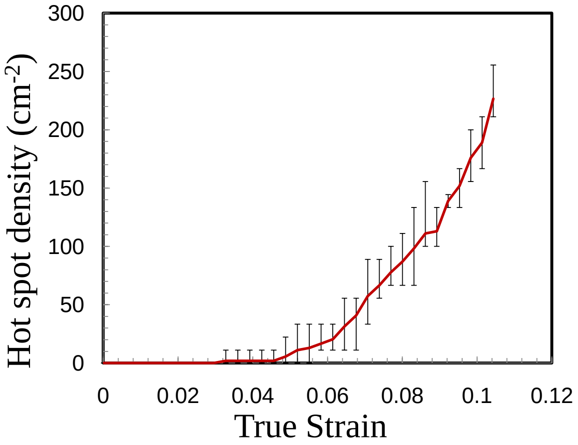

Figure 38: Evolution of hot spots with nominal strain for six idealized microstructures with the same statistical attributes (η = 0.69, $\dot{\varepsilon}$ = 16,667 s^{-1}).

The effect of strain rate is analyzed by deforming the microstructure in Figure 2(a), henceforth referred to as microstructure A in this chapter, at four strain rates in the range of $\dot{\varepsilon} = (16.6 – 100) \times 10^3$ s^{-1}. Figure 39 shows the distributions of temperature at a nominal strain of 0.05. At lower strain rates, the binder is softer and more prone to shear banding. This allows viscoelastic deformation to be spread out over the entire microstructure. Significant debonding of the grain-matrix interface occurs at the lower rates. Viscoelastic dissipation in the binder causes temperature to increase along the shear bands. These bands tend to follow the directions of the principle shear stresses in the specimen. In contrast, at higher strain rates the binder is much harder and resists deformation to a greater extent, resulting in less shear banding and concentration of deformation near the impact surface. Higher overall stresses are also generated in the grains and cause fracture in grains to occur earlier. At higher strain rates, there is intense heating near the impact surface. The heating in the binder is also accompanied by frictional dissipation at fractured surfaces.

Figure 40(a-b) show the distribution of hot spots for the strain rates of 16.6×10^3 and 10^5 s^{-1} at a nominal strain of 0.1. Two different mechanisms take prominence at the two rates. At the lower strain rate, shear banding in the binder (along with debonding) is the primary mode of failure. This allows grains to come into contact with each other along the shear band. These locations are sites of severe stress concentration, crack development and grain-matrix sliding. As a result, the hot spots are distributed preferentially along the shear bands [see Figure 40(a)]. At the higher strain rate [see Figure 40(b)], the distribution of hot spots is concentrated near the impact face where the most severe temperature rises occur. The hot spots are not uniformly distributed and seem to occur in clusters. The hot spots occur both inside grains and between grains, in contrast to what is seen in Figure 40(a) where all hot spots are located in between grains. The formation of hot spots inside the grains is a result of grain fracture and subsequent frictional dissipation along the fractured surfaces.

The evolution of the number of hot spots as a function of strain for the four strain rates between $\dot{\varepsilon} = 16.6 \times 10^3$ and 10^5 s^{-1} is summarized in Figure 41(a). The overall numbers of hot spots are similar at the different strain rates. This trend is seen for other microstructures with different volume fractions as well (results not shown).

In applications, it is desirable to have higher grain volume fractions for larger energy output. However, this decreases the amount of binder available for absorption of the impact energy. Figure 40(c) shows the distribution of hot spots for $\eta = 0.82$ at a strain rate of 16.6×10^3 s^{-1}. Clearly, the number of hot spots is higher compared with the case for $\eta = 0.69$ [Figure 40(a)]. Additionally, for $\eta = 0.82$, a larger number of hot spots occur inside the granules as a result of more extensive transgranular fracture, in contrast to what is seen in Figure 40(a) for $\eta = 0.69$. It is interesting to note that for both levels of η, the hot spots are distributed preferentially along the shear bands, signifying that the effect of shear banding is not significantly affected by the volume fraction.

Volume fraction also significantly affects the evolution of hot spots. In Section 2.10.1, it was shown that increasing the volume fraction resulted in earlier frictional heating and higher temperatures. Figure 41(b) shows evolution of the hot spot density (per unit area) with nominal strain for $\eta = 0.69 - 0.82$ at $\dot{\varepsilon} = 16.6 \times 10^3$ s^{-1}. Clearly, the hot spot density increases with η, for the same value of overall strain.

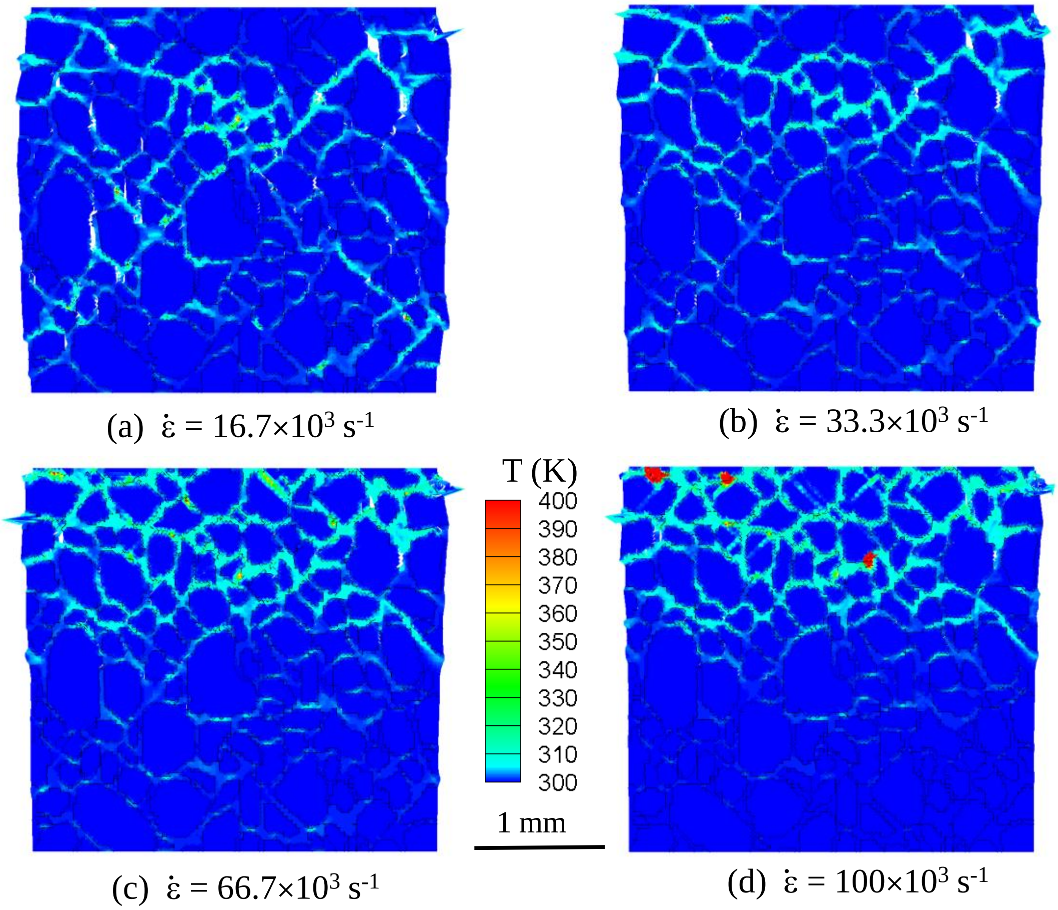

(a) $\dot{\varepsilon} = 16.7\times10^{3}\ \mathrm{s}^{-1}$
(b) $\dot{\varepsilon} = 33.3\times10^{3}\ \mathrm{s}^{-1}$
(c) $\dot{\varepsilon} = 66.7\times10^{3}\ \mathrm{s}^{-1}$
(d) $\dot{\varepsilon} = 100\times10^{3}\ \mathrm{s}^{-1}$

Figure 39: Distribution of temperature for the strain rates of (a) $16.6\times10^{3}\ \mathrm{s}^{-1}$, (b) $30\times10^{3}\ \mathrm{s}^{-1}$, (c) $66.7\times10^{3}\ \mathrm{s}^{-1}$ and (d) $10^{5}\ \mathrm{s}^{-1}$ at $\varepsilon = 5.0\ \%$ ($\eta = 0.69$).

Higher packing densities decrease the inter-particle distance, thereby enhancing grain-grain interactions and intensifying heating. Additionally, denser packing results in higher stress levels in the grains and the microstructures in general. Both mechanisms tend to increase the rate of hot spot formation. This effect is qualitatively similar to that of increasing confinement.

The response of a PBX is also strongly influenced by the confinement conditions. Wiegand et al. [10] studied the mechanical properties of explosives as a function of mechanical confinement at low strain rates. The authors reported that there is a significant increase in modulus and flow stress as the confinement stress increases. In the case of unconfined samples, the dominant failure mechanism is crack propagation; while for samples under confinement, the dominant failure mode is plastic deformation. Here, calculations using microstructure A are discussed, at a strain rate of $\dot{\boldsymbol{\varepsilon}} = 16.6\times10^{3}\ \mathrm{s}^{-1}$.

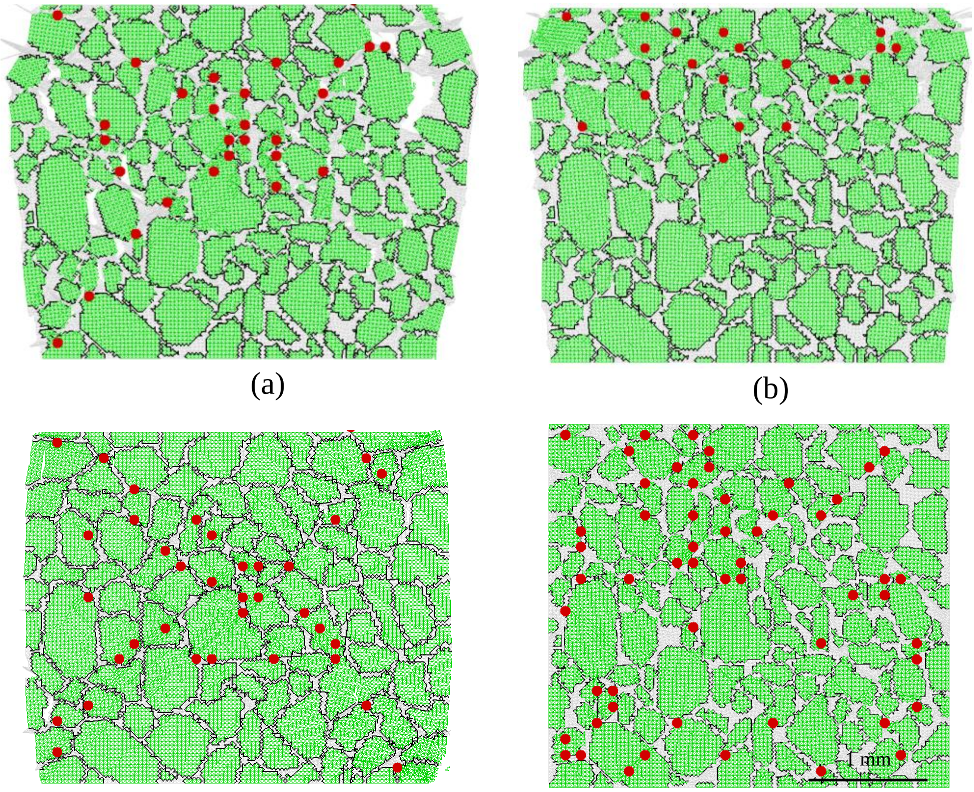
(a) (b)

(c) (d)

Figure 40: Distribution of hot spots at $\varepsilon = 9.0$ %, for an unconfined specimen with (a) $\eta = 0.69$ at $\dot{\varepsilon} = 16.6\times10^{3}\ \mathrm{s}^{-1}$, (b) $\eta = 0.69$ at $\dot{\varepsilon} = 10^{5}\ \mathrm{s}^{-1}$ (c) $\eta = 0.82$ at $\dot{\varepsilon} = 16.6\times10^{3}\ \mathrm{s}^{-1}$, and (d) confined specimen with $\eta = 0.69$ at $\dot{\varepsilon} = 16.6\times10^{3}\ \mathrm{s}^{-1}$.

Figure 40(d) shows the distribution of hot spots at an overall strain of 9.0% for the confined case. The high level of stress triaxiality enhances frictional heating and causes the hot spots to be more evenly distributed spatially compared with the unconfined case in Figure 40(c). As seen previously, a high proportion of the hot spots are generated at locations of grain-grain interactions. Figure 41(c) shows the evolution of the density (number per unit volume) of hot spots with nominal strain for the different cases of confinement. For $\varepsilon < 5.0\%$, the unconfined case has more hot spots due to more extensive debonding at the grain-matrix interfaces and the intense shear deformation of the binder matrix. At $\varepsilon > 5.0\%$, the higher stress triaxiality in the confined cause causes a larger number of hot spots to form, owing to the fact that fracture occurs primarily through shear failure and higher compressive stresses on crack faces give rise to more intense frictional heating in later stages of deformation.

3.3.4 Quantification of the evolution of hot spots

It is desirable to quantify the formation of hot spots as a function of loading conditions and microstructural attributes. The results can be used to obtain useful insight into the relative importance of energy localization mechanisms under different loading scenarios and microstructural settings.

At first, the microstructural attributes which may influence the distribution of hot spots are determined. The most obvious one is the volume fraction η. Under the same conditions, a higher volume fraction leads to a higher number of hot spots. However, η is a measure of the overall grain fraction and does not give any information regarding the size or distribution of grains. The failure mechanisms leading to energy localization occur at the grain level. Consequently, the distribution of hot spots is also influenced by the grain size and morphology. It is difficult to obtain a direct correlation between the size distribution and the number of hot spots since a single grain can interact with multiple neighboring grains.

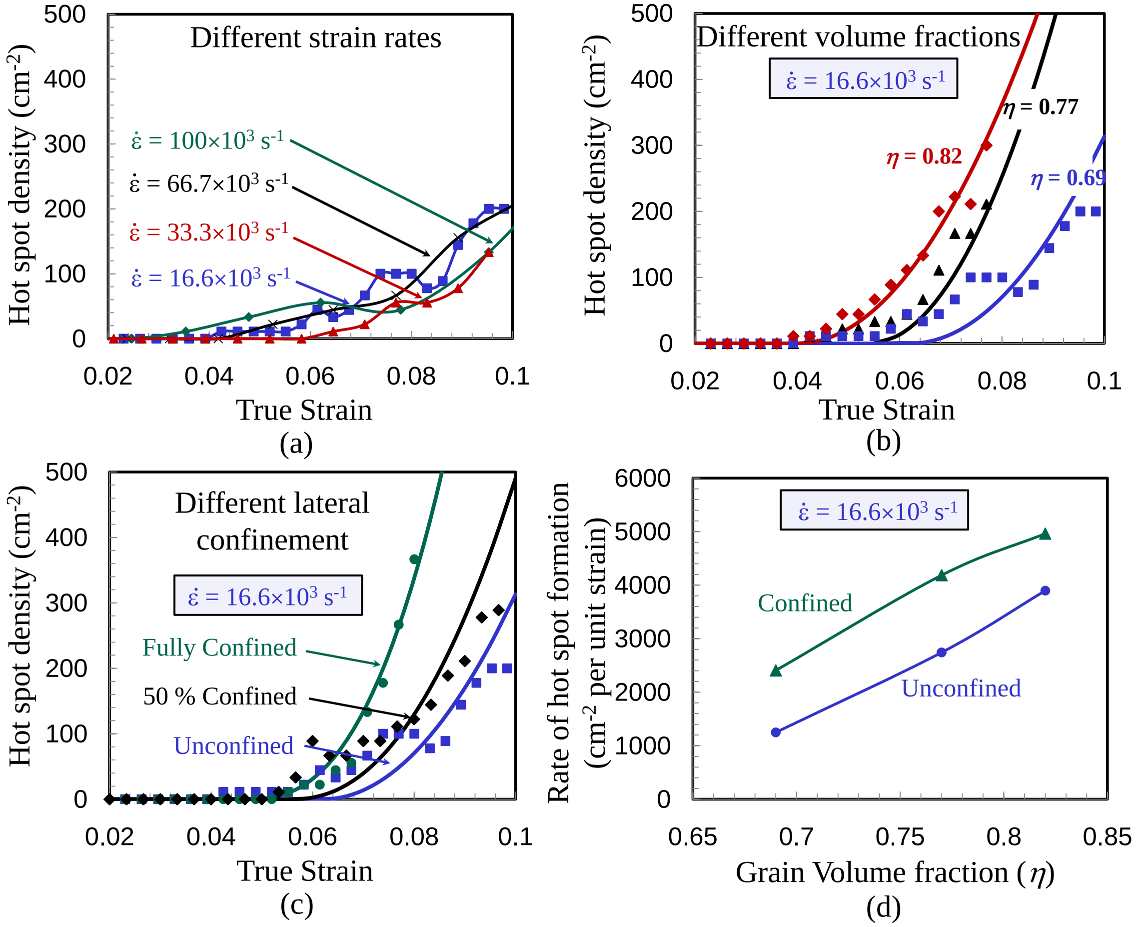

Figure 41: Evolution of hot spots for (a) different strain rates (η = 0.69), (b) different volume fractions ($\dot{\varepsilon} = 16.6\times10^3$ s^{-1}, unconfined), (c) different lateral confinement ($\dot{\varepsilon} = 16.6\times10^3$ s^{-1}, η = 0.69) and (d) average rate of hot spot formation (averaged up to ε = 0.73, $\dot{\varepsilon} = 16.6\times10^3$ s^{-1}).

One way to assess the combined effect of size and shape of grains is to estimate the number of potential locations of grain-grain interactions. This can be estimated by analyzing the 2D micrographs using a set of parallel test lines and counting the number of phase boundaries encountered by the test lines. Let P_L represent the number of phase boundaries encountered per unit length and $\overline{P}_L$ be the average value of P_L measured over the entire specimen. It is assumed that the grains are convex in shape (i.e. a test line intersects any grain at only two locations). In such a situation, $\frac{1}{2}\overline{P}_L$ represents the average number of grain-grain interactions per unit length. It can be further shown that for any given two phase microstructure [108],

$$\overline{P}_L = \frac{S_V}{2} \tag{3.1}$$

where, S_v is the total area of grain-matrix interfaces per unit volume. For an isotropic microstructure, P_L can be assumed to be identical for test lines in any orientation. Thus, N_A, which is proportional to the number of potential sites for hot spot formation, per unit area (2D) is

$$N_A = \left(\frac{\overline{P}_L}{2}\right)^2 = \left(\frac{S_V}{4}\right)^2 \tag{3.2}$$

and the number per unit volume is

$$N_V = \left(\frac{\overline{P}_L}{2}\right)^3 = \left(\frac{S_V}{4}\right)^3. \tag{3.3}$$

The parameter N_v (or N_A), incorporates the effects of both grain size and distribution and is applicable for all two phase microstructures having convex shaped grains. It is noted that the effect of grain morphology is not explicitly considered by N_v

(or N_A). The effect of morphology may be the subject of a future study. The values of N_A for the microstructures analyzed, are listed in Table 3.

The rate at which hot spots are formed is a function of nominal strain. For all calculations, hot spots do not develop until a delay time (t_d) or delay strain (ε_d) has elapsed. The delay strain is the nominal strain at which the dominant heating mechanism changes from viscoelastic dissipation in the binder to frictional heating at fractured surfaces where frictional dissipation occurs [109]. This strain primarily dependents on the packing density of the composite. Once hot spots start to form, the evolution of the number count can be described by a power-law function of the nominal strain.

In general, the evolution of hot spots with strain can thus be expressed as a function in the form of

$$\mathrm{H} = \mathrm{H}\left\{\eta, \mathrm{N}, \alpha, \varepsilon, \dot{\varepsilon}\right\}, \tag{3.4}$$

where H represents the number of hot spots per unit volume at any given level of nominal strain ε, N (= N_V in 3D or N_A in 2D) measures the number of potential hot spot sites per volume and α is a parameter which measures the rate of growth of the hot spot density.

Calculated results show that, for the conditions analyzed confinement significantly influences the hot spot count. In contrast, H is quite insensitive to strain rate, although the spatial distribution of hot spots are different at different strain rates [see Figure 40(a-b)].

The form that provides a good description of the hot spot data is

$$H(\varepsilon)=\begin{cases}0, & 0\le\varepsilon\le\varepsilon_d; \\ H_0\eta N\left(\dfrac{\varepsilon}{\varepsilon_d(\eta)}-1\right)^{\psi}, & \varepsilon\ge\varepsilon_d;\end{cases} \tag{3.5}$$

where H_0 is a proportionality constant. While N is proportional to the number of potential sites for hot spot formation, the rest of the terms can be regarded as the fraction of potential sites that actually become hot spots which depends on η and the level of deformation. In addition to the calculated results, Figure 41(b-c) also show fits using Eq. (3.5) for volume fractions between η = 0.69 - 0.82 and different levels of confinement. Clearly, ψ depends on the degree of confinement, and hence, the stress triaxiality in the specimen. In other words, ψ is a function of the ratio between the stresses in the lateral and the longitudinal directions. Here, ψ is assumed to be a linear function of the stress ratio as

$$\psi=\psi_0+\beta\frac{\sigma_x}{\sigma_y}, \tag{3.6}$$

where ψ_0 and β are constants, *y* represents the loading direction and *x* is the direction perpendicular to y. σ_x and σ_y are the stresses in the *x* and *y* directions averaged over the entire specimen. The values of the constants providing the best fit to the calculated data are shown in Table 4.

The value of ψ increases monotonically with the level of lateral confinement. Also, the higher the value of ψ, the higher the hot spot density at the same level of overall strain. This trend can be further analyzed by comparing the rates of hot spot formation. The rates are not constant as the deformation progresses. Here, the average rate for strains up to 0.073 is used for comparison. Figure 41(d) shows the average rate for different values of η and levels confinement. The rate for the unconfined case increases proportionally from 10^4 to 4×10^3 per unit cm^2 per unit strain as the volume fraction of the granules increases from 0.69 to 0.82. For the confined case, the corresponding variation is similar, increasing from 2.4×10^3 to 5×10^3 per unit cm^2 per unit strain. For all packing densities, there is a similar increase of ~ 1-1.4 × 10^3 per unit cm^2 per unit strain in the rate as the stress state is changes from uniaxial stress to uniaxial strain.

Table 4: Values of the parameters used in Eq. (3.5)

Parameter	**Value**		
H_0	1		
ψ_0	1.8		
β	1		
	Level of Lateral Confinement		
	Traction-free boundary	v_L/v = 0.5	*Fully Confined* (v_L/v = 0)
Stress Ratio (σ_x/σ_y)	0.2	0.3	0.76
ψ	2.0	2.1	2.56

In the case with η = 0.69, $\dot{\boldsymbol{\varepsilon}}$ = 16.6×10^3 s^{-1} [see Figure 41(a)], beyond ε = 0.08 the number of hot spots is lower than what is predicted by Eq. (3.5) and is not monotonous. This observation can be explained by considering the unconfined lateral boundary conditions under which fractured surfaces move away from each other, thus decreasing the probability for grain-grain interactions.

It is noted that although the locations of hot spots are random, the total number of hot spots obtained at the macro level are consistent among microstructures with similar attributes under the same loading conditions, as seen in Section 3.3.2. Also, for most of the calculations, hot spot data and the corresponding fits are obtained up to a nominal strain of 0.1. Additional failure mechanisms may become active at higher strains, affecting hot spot formation beyond the range analyzed here.

3.3.5 Hotspot Temperatures

The histories of energy dissipations provide insight into the relative importance of the failure mechanisms. The effect of strain rate is analyzed first. Figure 42(a) shows the viscoelastic dissipation (W_{ve}) and frictional dissipation (W_f) for a microstructure with η = 0.69 at the strain rates of 16.6×10^3 s^{-1} and 10^5 s^{-1}. It can be seen that W_{ve} is higher than W_f for all the calculations presented here. However, W_{ve} is a result of deformation of the binder and is dissipated throughout the microstructure, while W_f is distributed mainly along the fractured surfaces in contact. Consequently, hot spot formation is primarily due to frictional dissipation. At the higher rate, higher stresses carried by the binder results in higher W_{ve}. Also, fracture in the grains is more extensive and frictional dissipation (W_f) is higher at the higher rate. The differences in dissipation significantly affect the average temperatures in the hot spots. Figure 43(a) shows the number of hot spots per unit area having different average temperatures at an overall strain of 0.1 for different strain rates between $\dot{\varepsilon}$ = 16.6×10^3 and 10^5 s^{-1}.

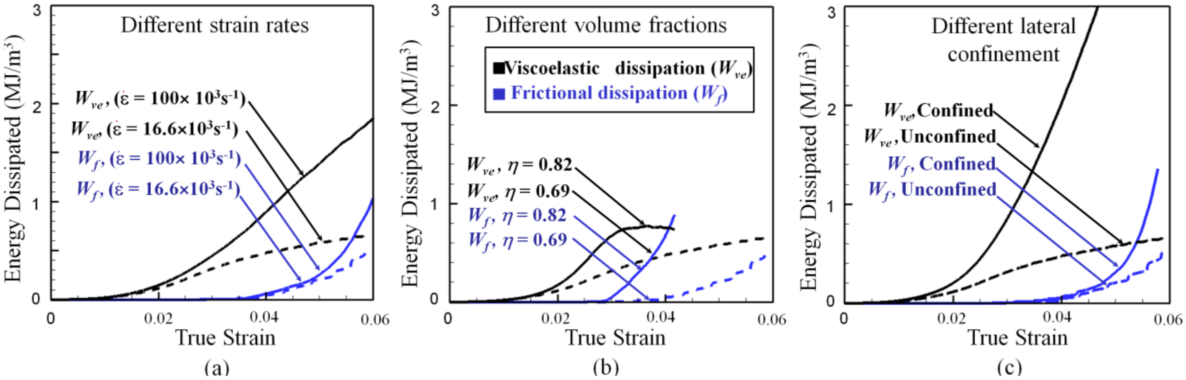

Figure 42: Evolution of dissipation with strain for different (a) strain rates (η = 0.69, unconfined), (b) volume fractions ($\dot{\varepsilon}$ = 16.6×10^3 s^{-1}, unconfined), and (c) levels of lateral confinements ($\dot{\varepsilon}$ = 16.6×10^3 s^{-1}, η = 0.69).

For all cases, the number of hot spots is highest around a certain temperature (T_H). The number of hot spots having temperatures at the high end of the spectrum oscillates and is stochastic. At higher strain rates, the number of hot spots at T_H is higher owing to an increase in the amount of frictional dissipation. T_H increases approximately linearly with strain rate, with the rate of increase being approximately 1.2 K per 10^4 s^{-1} of strain rate increase $\left(\mathrm{d}T_H / \mathrm{d}\dot{\varepsilon}\right)$. The results show that higher loading rates lead to higher temperatures in the hot spots, but it does not significantly affect the total number of hot spots. It appears that while loading rates affect the temperatures inside hot spots, microstructure (volume fraction, grain size, grain shape, and constituent properties) affects the number of hot spots, with the packing density having, perhaps, the largest influence [Figure 41(b)].

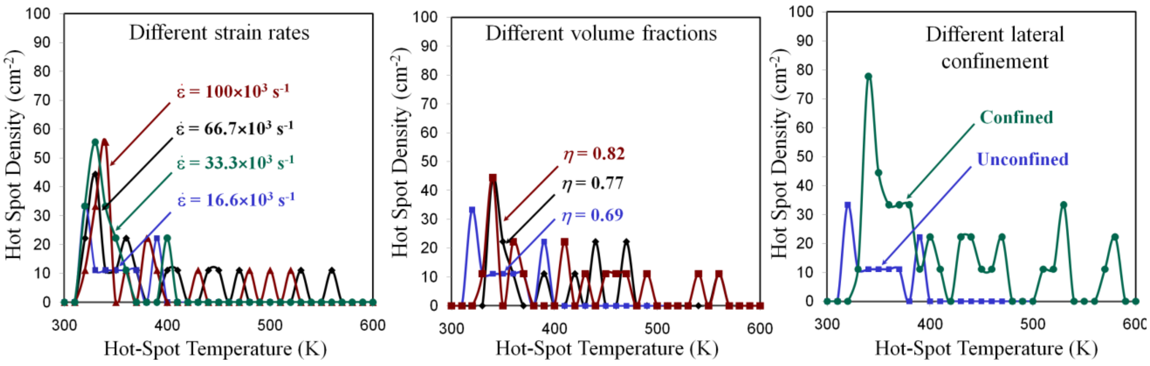

(a) (b) (c)

Figure 43: Hot spot temperatures at ε = 10% for different (a) strain rates (η = 0.69, unconfined), (b) volume fractions ($\dot{\varepsilon}$ = 16.6×10^{3} s^{-1}, unconfined), and (c) levels of lateral confinement ($\dot{\varepsilon}$ = 16.6×10^{3} s^{-1}, η = 0.69).

As the volume fraction of the grains increase, the average thickness of binder between the adjacent grains decreases. As a result, higher stresses develop, leading to earlier fracture and higher frictional dissipation. Figure 42(b) shows the histories of energy dissipation for two cases with η = 0.69 and 0.82 at $\dot{\varepsilon}$ = 16.6×10^{3} s^{-1}. Both W_{ve} and W_f increase with the volume fraction. However, the increase of W_f is larger than the corresponding increase in W_{ve}. Specifically, at ε = 3.5% the increase in W_f is 500% and the increase in compared W_{ve} is 60%. This is primarily due to the earlier and more extensive fracture and frictional dissipation in case of higher volume fraction. Consequently, at the same amount of overall strain, a higher number of hot spots develops as a result of the enhanced frictional dissipation. This is reflected in Figure 43(b), which shows the distribution of hot spots shifting in the higher temperature direction as η increases from 0.69 to 0.82.

The relative influences of different dissipation mechanisms are also affected by the degree of confinement. Figure 42(c) shows the viscoelastic dissipation in the binder and frictional dissipation at fractured surfaces for two cases, one with confined and other unconfined lateral surfaces, at an overall strain of 0.1 ($\eta = 0.69$, $\dot{\varepsilon} = 16.6 \times 10^3$ s^{-1}). For the confined case, the stress in the binder is much higher and results in higher viscoelastic dissipation. Specifically, the viscoelastic dissipation in the binder at $\varepsilon = 4.0\%$ is 2.4 MJ/m^3 for the confined case and 0.5 MJ/m^3 for the unconfined case. Up to $\varepsilon = 4.0\%$, frictional dissipation between the two cases of confinement are similar. Beyond this strain, the higher stress levels in the confined specimen lead to a higher amount of fracture and a higher level of subsequent frictional dissipation. Specifically, at $\varepsilon = 5.74$ %, frictional dissipation for the confined case is 1.4 MJ/m^3 while it is 0.5 MJ/m^3 for the unconfined case. The number of hot spots having different average temperatures at an overall strain of 10% is shown in Figure 43(c) for the two cases. The higher level of frictional dissipation under higher confinement causes the value of T_H (350 K) to be higher than that for the unconfined case (320 K). For the confined specimen, a significant number of hot spots also occur in the temperature range of 400-600 K. On the other hand, for the unconfined specimen, all hot spots have temperatures less than 400 K.

It is worth pointing out that most hot spots occur in the binder or at the binder-granule interfaces. Temperature rises inside the grains are relatively low. The calculated temperatures in a small number of hot spots may reach or exceed the melting temperature of Estane (~378 K) and approach the melting temperature of β-HMX (~522 K). Numerically, the situation is handled by formulating the constitutive equations such that as the temperature approaches the melting temperature of the material, the material gradually loses the ability to carry shear stress, but remains able to sustain hydrostatic pressure.

3.4 Conclusions

This analysis focuses on energy localization at different strain rates for microstructures with different volume fractions of grains under different confinement conditions.

A method for identifying hot spots is developed, allowing the size and temperature distributions of hot spots to be analyzed. Heating due to the viscoelastic deformation of the polymer binder and friction along crack surfaces are the primary mechanisms responsible for the formation of the hot spots. In early stages of the deformation, viscoelastic dissipation is the primary heating mechanisms. In later stages of deformation, the formation of cracks and crack surface contact under compressive stresses lead to more significant heating.

The distribution of hot spots is significantly affected by the strain-rate sensitivity of the binder. At higher loading rates, harder binder response causes hot spots to be localized near the impact face. At lower loading rates, hot spots tend to be more spread out and associated with regions of intense shear deformation of the binder. The average temperature of the hot spots increases with strain rate. The temperature at which the maximum number of hot spots occurs (T_H) increases with loading rate at a rate of approximately 1.2 K per 10^4 s^{-1} of strain rate increase under the conditions analyzed. On the other hand, the total number of hot spots appears insensitive to strain rate (density ~

100 cm^{-2}, for $\eta = 0.69$ at $\varepsilon = 0.08$ with unconfined lateral sides) over the range of conditions analyzed.

The strain at which the transition of the dominant heating mechanism from viscoelasticity to friction occurs is primarily dependent on the packing density of the composite as grain-grain interactions play an important role. As a result, the number of hot spots formed increases with packing density η, with the rate of formation being proportional to η.

The analysis shows that stress triaxiality has a significant influence on the density and spatial distribution of hot spots. The hot spots are more densely populated (density ~ 366 cm^{-2}, for $\eta = 0.69$ at $\varepsilon = 0.08$, confined), are more uniformly distributed spatially and have higher temperatures when the specimen is confined.

Finally, an empirical relation is proposed to quantify the effects of microstructural attributes (volume fraction, grain size and shape) and loading conditions (degree of confinement) on the evolution of hot spots. This relation provides useful statistical information regarding hot spots and can be used as input, for instance, in continuum level reactive burn models.

CHAPTER 4: TRANSIENT RESPONSE

4.1 Introduction

Under transient loading conditions, the stress state in the material is not homogeneous. The response of these materials to loading associated with compressive stress waves is important since such events can cause severe damage and the formation of hot spots [27, 29, 110] which affect safety and chemical stability of the materials.

Due to material heterogeneity, the structure of the compressive stress wave resulting from impact loading is complex as it traverses the material. The wave propagates faster in the grains and relatively slowly in the binder. This difference in wave speeds causes the stress wave front to be diffused over a region which is called the compaction region. The gradients of temperature and energies in this region are sharp and need to be resolved at the grain level, since significant energy dissipation occurs in this region. Behind the compaction region, the average stress is approximately constant. At the grain level, the distribution of stress is quite non-uniform. Grains in general experience high stresses and fracture, leading to subsequent frictional interactions across crack surfaces. Frictional dissipation can be the most important source of heating that leads to local temperature rises and the formation of hot spots [53, 79, 106]. The spatial distribution, size and temperature of the hot spots are critical measures for assessing the ignition sensitivity of a PBX [29, 111].

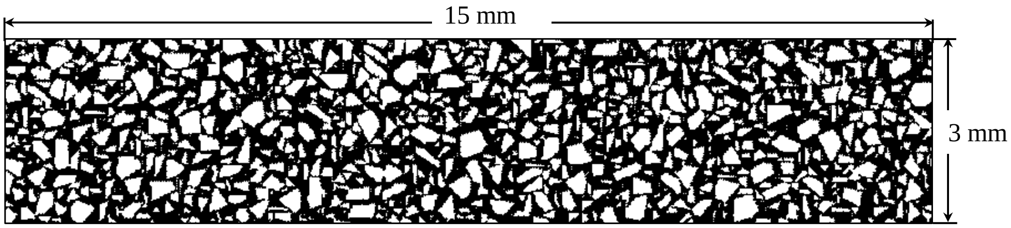

(a) $\eta = 0.50$

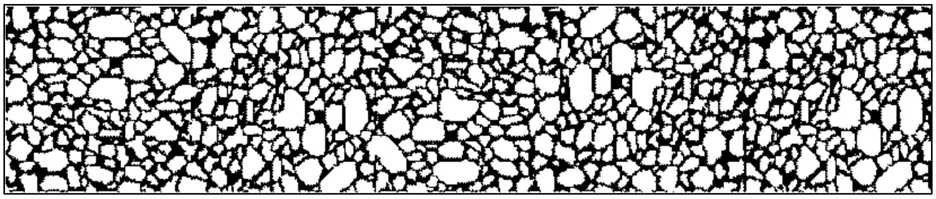

(b) $\eta = 0.69$

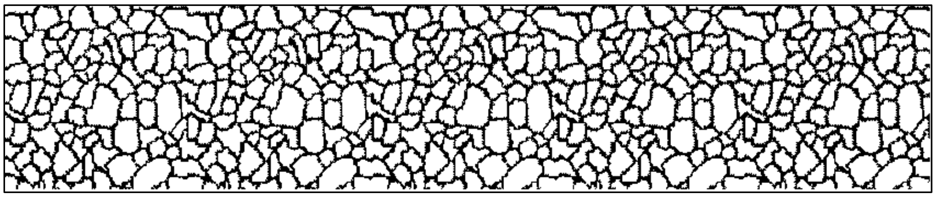

(c) $\eta = 0.82$

Figure 44: Microstructures having a range of grain volume fractions ($\eta = 0.50 – 0.82$).

In this chapter, calculations are carried out using microstructures with HMX grain sizes on the order of 200 μm and grain volume fractions in the range of 0.50 – 0.82. The microstructural samples [see Figure 44] have an aspect ratio of 5:1 (15 mm × 3 mm), allowing the transient wave propagation process resulting from normal impact to be resolved. Simulations are carried out for a range of load intensity as measured by imposed load face velocity, grain volume fraction and grain/binder interface strength. The simulations are used to quantify the stress states, temperature distributions and energy dissipation as the loading wave traverses the length of the microstructure. The focus is on characterizing the spatial and temporal distributions of temperature rises as functions of microstructural and loading attributes. Through the analysis, scaling laws regarding maximum dissipation per unit volume, maximum temperature increase and damage are developed, involving key parameters that quantify loading and microstructure.

This chapter is based on the work published in Barua et al. [112].

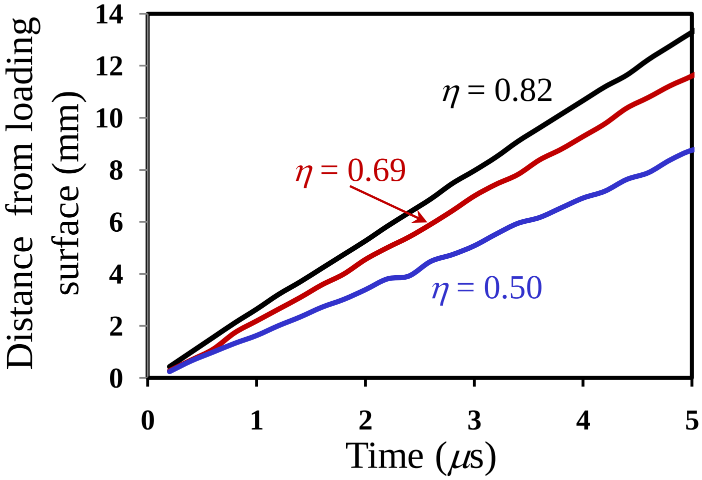

Figure 45: The position of stress wave front as a function of time (η = 0.50 – 0.82).

4.2 Microstructures Analyzed

Three different microstructures with grain volume fractions η = 0.50, 0.69 and 0.82, respectively, are used. The micrographs corresponding to η = 0.69 and 0.82 are obtained from digitized microstructures of actual PBX specimens and are similar to the ones used in [79]. The micrograph with η = 0.50 is created using 2D Voronoi tessellation. This approach allows multifaceted grains with morphologies similar to those of actual HMX grains to be obtained. The desired volume fraction is attained by increasing or decreasing the size of the grains. The grain sizes for the above microstructures have a mean value of ~ 200 μm and are used together to analyze the effect of grain volume fraction on the transient response of PBXs.

4.3 Results and Discussions

A parametric study is carried out, focusing on the effects of (i) strain rate, (ii) grain volume fraction (η = 0.50 to 0.82) and (ii) interface strength. For all calculations presented, the initial temperature is T_i = 300 K. The calculations are performed on a 15 mm × 3 mm rectangular microstructural region using the loading configuration shown in Figure 11(a). The velocity v of the left surface is varied between 50 and 200 ms^{-1}, yielding overall strain rates of $\dot{\boldsymbol{\varepsilon}}$ = (3.33 – 13.3) × 10^{3} s^{-1}. The velocity is imposed at the

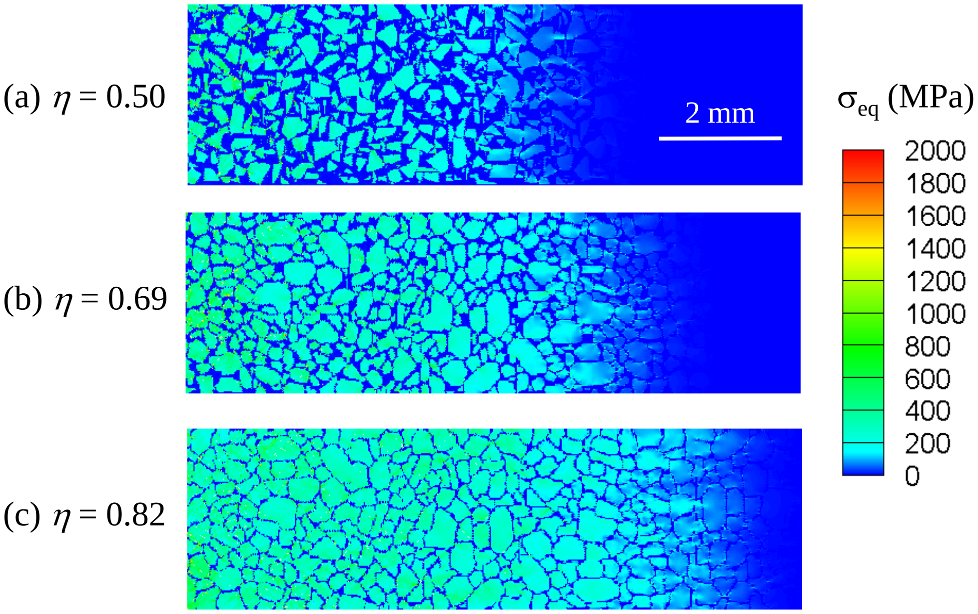

Figure 46: Distribution of equivalent stress at t = 3.6 μs for varying packing densities (a) 0.50, (b) 0.69 and (c) 0.82 (v = 200 ms^{-1}).

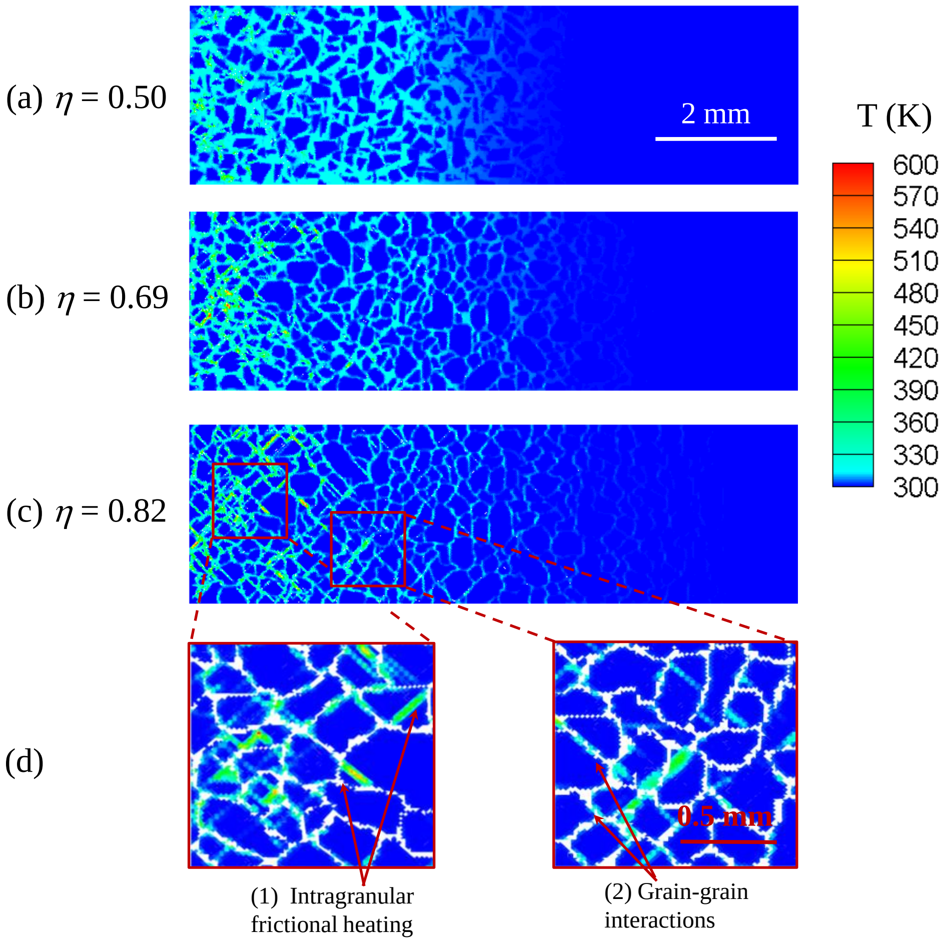

Figure 47: Distribution of temperature at *t* = 3.6 μs for varying packing densities: (a) 0.50, (b) 0.69 and (c) 0.82 and (d) close-up view of the grains in two regions showing (1) transgranular fracture and frictional heating along crack faces and (2) localized heating due to grain–grain interactions (*v* = 200 ms^{-1}).

left surface of the configurations in Figure 11(a), with a linear ramp from zero to *v* in the first 2 μs of loading. The strength of the grain/matrix interface is varied by altering the maximum allowed surface traction T_{max} at the interface from 8.75 to 35.0 MPa (refer to Table 2). This range of values represents weakly to strongly bonded interfaces. Unless otherwise stated, the value of T_{max} is taken as 35.0 MPa.

Since this analysis focuses on the transient response of PBX microstructures, the discussions are limited to times before the stress wave reaches the boundary on the right [Figure 11(a)]. The overall velocity of the stress waves in the microstructure varies with the grain volume fraction and the interface bonding strength between the phases. Figure 45 shows the location of the stress wave as a function of time, for $\eta = 0.50 – 0.82$, and T_{max} = 35.0 MPa. The slopes of the curves correspond to the wave speeds in the respective microstructures. Clearly, the wave speed increases with grain volume fraction. For instance if the grain volume fraction is $\eta = 0.82$, the wave velocity is 2.65×10^3 ms^{-1}. In comparison, the elastic longitudinal wave speed in HMX is ~ 3.5×10^3 ms^{-1}. The time taken by the wave to reach the right surface is 5.6 μs. The results presented here correspond to times up to 3.6 μs, ensuring that the focus is on the transient response of the specimen.

A set of calculations using different grain volume fractions is presented to delineate the processes at hand. Figure 46 and Figure 47 illustrate the distributions of stress and temperatures in the microstructure for packing densities of η = 0.50, 0.69 and 0.82 at t = 3.6 μs for an impact velocity v = 200 ms^{-1}. Clearly, for the higher grain volume fractions, the stress waves have propagated over a longer distance in the amount of same time. At the stress wave front, the intensity is low initially and gradually increases to a peak value. Force chains are formed in the compaction region. Behind the compaction region, the stress in each phase is higher and has no long term structure, with the harder grains carrying higher levels of stress. As the grain volume fraction increases, the overall stress level in the grains also increases. The higher stresses result in a higher tendency for transgranular fracture and frictional dissipation.

In contrast to the stress profiles, the temperature rises are highest near the impact surface and gradually decrease away from it. When the grain volume fraction is low, e.g., η = 0.50, the stresses in the grains are not high enough to cause fracture and most of the temperature rise is due to viscoelastic dissipation in the binder. Since the amount of viscoelastic dissipation is time-dependent, highest temperature rises occur near the impact surface. This observation is only for the time durations for which the stress wave is still propagating toward unstressed materials and no wave reflection occurs. This is to say that the sample size is relatively large for the time duration of interest. Such scenarios are quite relevant since when the impact velocity is high, ignition can occur within a short time upon contact and the stress wave front may not have reached any boundary of the sample yet. Note that in the loading configurations analyzed in Chapters 2 and 3, ([79] and [106]), the conditions are such that stress waves reflect from opposite boundaries of the samples for the time duration analyzed. Under those conditions, the highest temperature may not be at the impact face. Additionally, higher packing densities (η = 0.69, 0.82) lead to higher overall stresses and transgranular fracture and frictional dissipation at the fractured surfaces, even at the same impact velocity. This causes severe temperature rises of the order of 300 – 400 K to occur in the grains. Two regions of the microstructure with η = 0.82 are shown in Figure 47(d) at a higher magnification to highlight the failure mechanisms (transgranular fracture and sliding frictional heating along crack faces, intergranular interaction and heating due to binder deformation and crack face friction) captured.

The distributions of stress and temperature in the specimen vary significantly with time and distance from the impact surface. One way to represent the variation of stress in the specimen is to analyze the average stress across the width of the specimen along the loading (horizontal) direction. For this purpose, the average value across the width (perpendicular to the direction of loading) of the specimen for each field variable (e.g. equivalent stress) is computed. Figure 48(a) shows the stress profiles at different times between t = 1.2 – 6.0 μs, for η = 0.82 and v = 100 ms^{-1}. The stress profiles are qualitatively similar as the wave propagates. In the compaction region, the stress increases gradually from zero to a peak value over a distance of ~ 5 mm. Behind this region, the average stress is approximately constant, at around 200 MPa. The length of the compaction region is important since it determines the gradient across which the stress and temperature rises occur. A sharper gradient usually corresponds to higher amounts of fracture and damage. The length of the compaction region does not vary significantly with time, because (a) the microstructure is approximately homogeneous at the length scale of several grains and (b) the time scales considered here are not sufficient for any significant attenuation of the stress wave. Finally, as the wave reaches the fixed surface on the right, it is reflected back and the stress state in the specimen tends to a nominally homogeneous one.

Figure 48(b) shows the average stress profiles at t = 3.6 μs for three calculations with boundary velocities between v = 50 – 200 ms^{-1} and η = 0.82. At a higher the boundary velocity, the viscoelastic binder is harder, leading to higher stresses. The average stress behind the compaction region increases from 120 to 280 MPa as the impact velocity is increased from 50 to 200 ms^{-1}. The length of the compaction region is similar for all boundary velocities. Thus, higher impact velocities correspond to a much sharper increase of stress across the compaction region, leading to more damage and frictional dissipation.

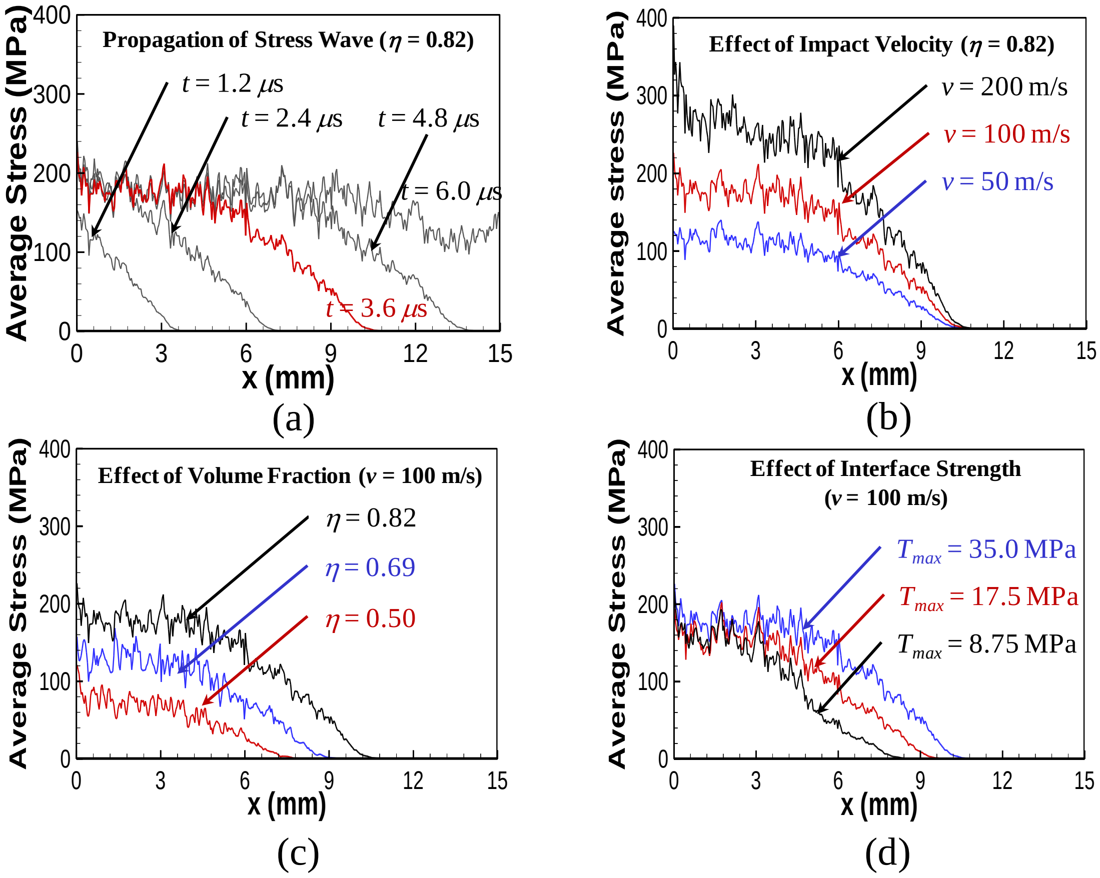

Figure 48: Variation of equivalent stress with distance from the impact surface for (a) different times between $t = 1.2 – 6.0\ \mu s$ ($\eta = 0.82$, $v = 100\ ms^{-1}$), (b) different impact velocities between $v = 50 – 200\ ms^{-1}$ ($\eta = 0.82$, $t = 3.6\ \mu s$), (c) different packing densities between 0.50 – 0.82 ($v = 100\ ms^{-1}$, $t = 3.6\ \mu s$), and (d) different interface strengths between $T_{max} = 8.75 – 35.0$ MPa ($\eta = 0.82$, $v = 100\ ms^{-1}$, $t = 3.6\ \mu s$).

Figure 48(c) plots the average stress profiles at t = 3.6 μs for different volume fractions between η = 0.5 to 0.82 and v = 100 ms^{-1}. The average stress increases with grain volume fraction. The length of the compaction zone does not change significantly with grain volume fraction. The average stress increases from 100 to 200 MPa as the grain volume fraction increases from 0.5 to 0.82. For higher grain volume fractions, the higher wave speeds result in dissipation and temperature rises occurring over a larger area in the same amount of time.

The stress profiles at t = 3.6 μs for interface strengths from T_{max} = 8.75 to 35.0 MPa, η = 0.82 and v = 200 ms^{-1} are shown in Figure 48(d). At higher interface strength values, the material is able to sustain higher stresses without fracture. Consequently, the wave speed increases by a factor of 1.3 (from 50 to 200 ms^{-1}) over the interface strength range analyzed. The compaction region is more spread out in cases with higher interface strengths. Behind the compaction region, the stress levels are essentially the same for the values of interface strength considered. This is due to the crack closure effect of the compressive loading. For instance, for a low interface bonding strength, a greater amount of debonding occurs. However, crack surfaces are in compression, resulting in the stress carried by the material being similar to that carried by an undamaged material. Consequently, the average stress in the material is primarily dependent on the volume fraction and the impact velocity, and is not significantly affected by the strength of the bonding between the different constituents.

Figure 49 shows the effect of the boundary velocity (v = 50 – 200 ms^{-1}) on the average stress in the grains for η = 0.5, 0.69 and 0.82. A scaling law [Eq.(4.1)] is developed to quantify the average stress as a function of the grain volume fraction, η and boundary velocity, v.

$$\sigma_{\text{avg}} = \sigma^{0}{}_{\text{avg}} \left(\frac{\eta}{\eta_{\text{ref}}} + 1 \right)^{2.5} \left(\frac{v}{v_{\text{ref}}} \right)^{0.8} \tag{4.1}$$

This relationship consists of dimensionless terms obtained by normalizing η and v by reference values η_{ref} and v_{ref}, respectively. The parameters in Eq. (4.1) are listed in Table 5. Over the range of conditions analyzed, the interface bonding strength does not affect the average stress, therefore, it is not included in Eq. (4.1). Overall, the average stress increases with volume fraction η and boundary velocity v. The average stress has a slight non-linear dependence on v as shown by the exponent of 0.8 in Eq. (4.1) [see Figure 49]. This non-linearity is primarily due to the rate-dependence of the viscoelastic binder.

On the other hand, the average stress is quite sensitive to the volume fraction of the grains, as indicated by the exponent of 2.5. The high sensitivity can be explained based on the difference in the mechanisms responsible for transmission of stress at low and high grain volume fractions. When η is low (≤ 0.5), the softer matrix is primarily responsible for carrying and transmitting stress. While at high values of η (0.69, 0.82), stress is preferentially transmitted across neighboring grains by means of forming force chains. Consequently, there is a large variation in the average stress with a small increase in grain volume fraction. For instance, the average stress increases approximately by a factor of 2 as the grain volume fraction is increased from 0.5 to 0.69.

The heterogeneity in the microstructure at the grain level gives rise to highly localized temperature distributions. Chemical reactions initiate in localized hot spots, characterized by high temperature rises. The temperature rises need to be analyzed at the grain level and the macro level using different metrics. Possible measures include (a) temperature rise (ΔT) as a function of distance from the loading surface and (b) the overall temperature rise in the microstructure measured by mass fraction having certain temperature rise. The peak temperature rise can be used to identify locations which are most susceptible to ignition. The overall temperature rise can be used to identify the contribution of the different heating mechanisms. The heating mechanisms considered here are – viscoelastic dissipation in the binder and frictional dissipation along contact surfaces. The viscoelastic dissipation results in bulk temperature rise in the binder which can be conducted into the grains through the grain-matrix interfaces. On the other hand, frictional dissipation occurs locally along crack faces and is responsible for much of the heating in the composite, especially at higher strains.

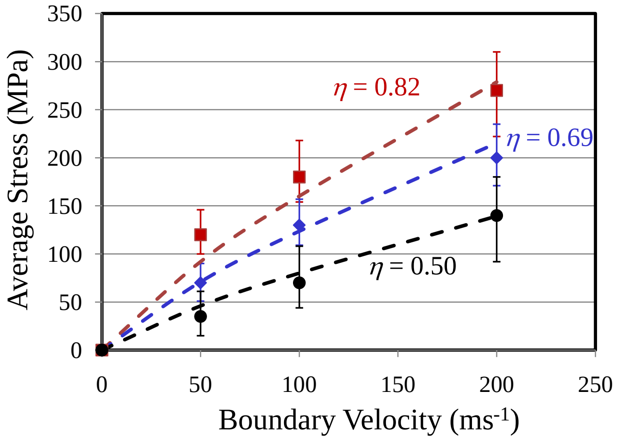

Figure 49: Variation of average stress with boundary velocity grain and volume fraction.

Figure 50(a) shows the average and maximum temperature rises at t = 3.6 μs in the constituents for a microstructure with η = 0.82 at a boundary velocity of v = 200 ms^{-1}. The average temperature is typically low, at ~350 K. However, the maximum temperature in the grains can be very high, up to 600 K. This is higher than the maximum temperature in the matrix of ~550 K. The viscoelastic dissipation associated with the matrix is typically less intense compared with frictional dissipation which occurs as a result of transgranular fracture of the grains. In general, the average temperature in the grains and matrix is highest near the impact surface and decreases gradually with distance away from it. However, the highest temperature rises are at ~2−3 mm from the impact surface. The peak temperatures are highly stochastic, but overall, are highest near the impact surface and gradually decrease away from it. The position of the wave front at 3.6 μs is at a distance of 10.5 mm from the impact surface [see Figure 48(b)]. However, at this time, the temperature rise is not significant for distances greater 5 mm from the impact surface. Since processes associated with friction and heat conduction occur at much slower time scales compared with stress wave propagation, frictional heating and heat conduction determine the time scale of delayed combustion of PBXs during non-shock loading [44].

Figure 50(b) shows the effect of the boundary velocity (v = 50 − 200 ms^{-1}) on the maximum temperature rises in the grains at t = 3.6 μs for η = 0.82. At the low impact velocity of 50 ms^{-1}, the maximum temperature recorded is ~ 310 K, while at 100 ms^{-1} and 200 ms^{-1}the corresponding temperatures are ~ 400 K and 600 K respectively. The large differences in peak temperature at low and high impact velocities suggest that the transition of heating mechanism from viscoelastic to frictional dissipation occurs much earlier at high impact velocities. This will be quantified later in the section.

Table 5: Parameters in Eqs. (4.1), (4.2) and (4.3).

Parameter	Value	Units
η_{ref}	0.5	–
v_{ref}	90	ms^{-1}
$T^{\mathrm{ref}}_{\mathrm{max}}$	35	MPa
t_{d}	1.6	μs
$\sigma^{0}_{\mathrm{avg}}$	13	MPa
T_0	1.55	K
W_{f}^{0}	0.025	MJ-m^{-3}

Figure 50(c) shows the peak temperatures in HMX for varying volume fractions, η = 0.50 to 0.82, at a boundary velocity of 100 ms^{-1}. Clearly, higher volume fractions correspond to higher temperature rises. For η = 0.82, peak temperatures near the impact surface can reach 400 K, whereas for η = 0.50, the corresponding peak temperatures are < 310 K. Once fracture and frictional dissipation initiates, severe temperature rises occur in the grains. The temperature rise occurring in the microstructure increases with grain volume fraction, however, the variation itself is highly non-linear, with a lower rate of temperature rise during viscoelastic dissipation, followed by higher rate of heating during frictional dissipation.

Figure 50(d) shows the maximum temperatures at t = 3.6 μs for samples with different interface strengths in the range of T_{max} = 8.75 – 35.0 MPa and η = 0.82. The impact velocity is v = 100 ms^{-1}. The material with lower interface strength suffers more damage, leading to higher amount of frictional dissipation and higher temperature rises. The maximum temperature generally increases as the interface strength decreases. For this set of calculations, the maximum temperature increases from 400 to 500 K as the interface strength is decreased by a factor of 4, from 35.0 to 8.75 MPa.

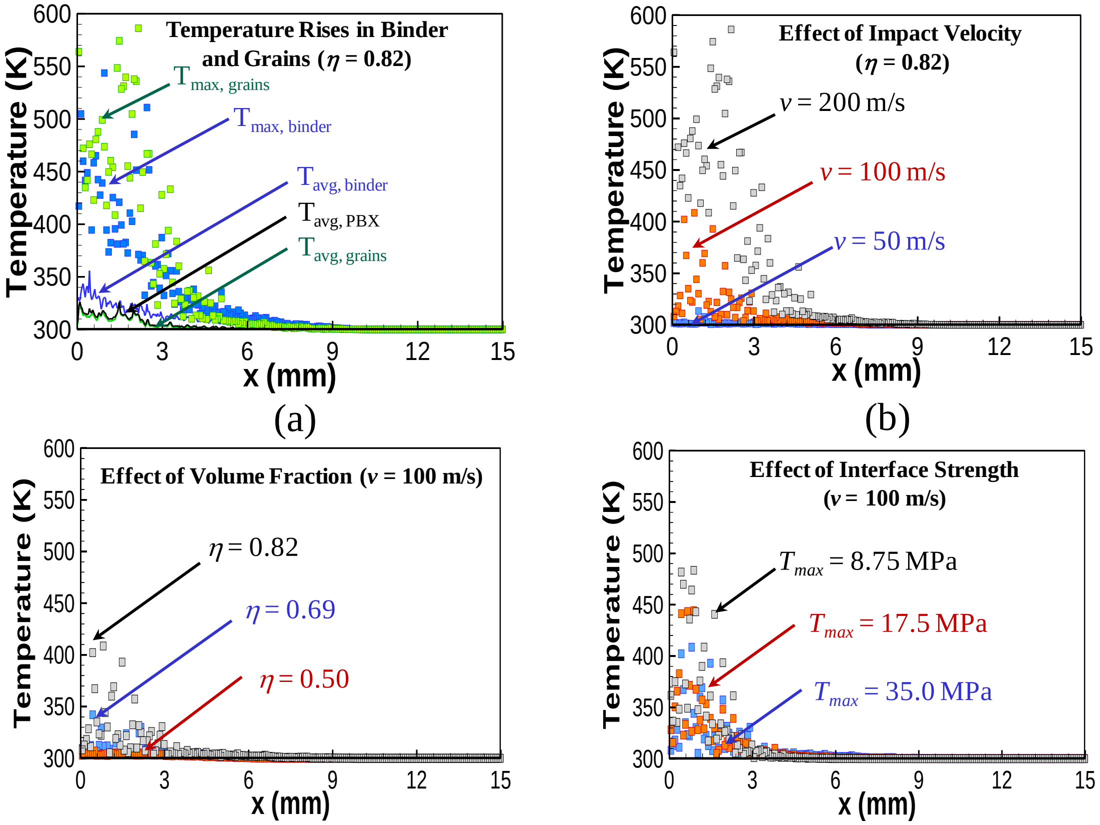

(a)

(b)

Figure 50: Peak temperature in the microstructure at different distances from the impact surface

(a) in grains and binder at t = 3.6 μs (η = 0.82, v = 200 ms^{-1}),

(b) for different impact velocities between v = 50 – 200 ms^{-1} (η = 0.82, t = 3.6 μs),

(c) for different packing densities between 0.50 – 0.82 (v = 100 ms^{-1}, t = 3.6 μs), and (d) for different interface strengths between T_{max} = 8.75 – 35.0 MPa (η = 0.82, v = 100 ms^{-1}, t = 3.6 μs).

The critical (ignition) temperature for HMX under a constant heat flux is estimated to be ~775 K [53]. The heat generation rate due to frictional dissipation in the current setting varies with time. Nevertheless, the results strongly suggest that frictional heating can lead to temperature rises in the grains which are sufficient for melting and reaction initiation. The preceding results can be used to obtain a quantification of the maximum hot-spot temperature as a function of loading and microstructure. Specifically, the evolution of peak temperature rise can be expressed as a function of grain volume fraction, boundary velocity, interface bonding strength as,

$$T_{\text{peak,grains}} = \begin{cases} 0, \quad t < t_{\text{d}} \\ T_{\text{i}} + T_0 \left(\dfrac{\eta}{\eta_{\text{ref}}} + 1 \right)^{5.0} \left(\dfrac{v}{v_{\text{ref}}} \right)^{1.3} \left(\dfrac{T_{\text{max}}}{T^{\text{ref}}_{\text{max}}} + 1 \right)^{-1} \left(\dfrac{t}{t_{\text{d}}} - 1 \right)^{2}, t \geq t_{\text{d}}. \end{cases} \tag{4.2}$$

Here, dimensionless terms are obtained by normalizing η, v, T_{max} and t, using reference values η_{ref}, v_{ref}, $T^{\text{ref}}_{\text{max}}$ and delay time t_{d}. T_{i} is the initial temperature 300 K. The parameters in Eq. (4.2) are also listed in Table 5. Equation (4.2) highlights the effect of the delay time. Temperature rise is negligible until a delay time of t_{d} has elapsed. Beyond t_{d}, the temperature rise is proportional to the second power of time. The peak temperature rise is highly sensitive to the grain volume fraction η. This can be attributed to the high sensitivity of the average stress to η [as seen in Eq. (4.1)], which results in a higher amount of frictional dissipation at the fractured surfaces. The variation of peak temperature with impact velocity is almost linear. The maximum temperature bears an inverse relationship with the interface bonding strength. A decrease in interface bonding strength leads to a higher amount of fracture at the grain-matrix interface. The resulting frictional dissipation causes higher temperature rises at the fractured surfaces.

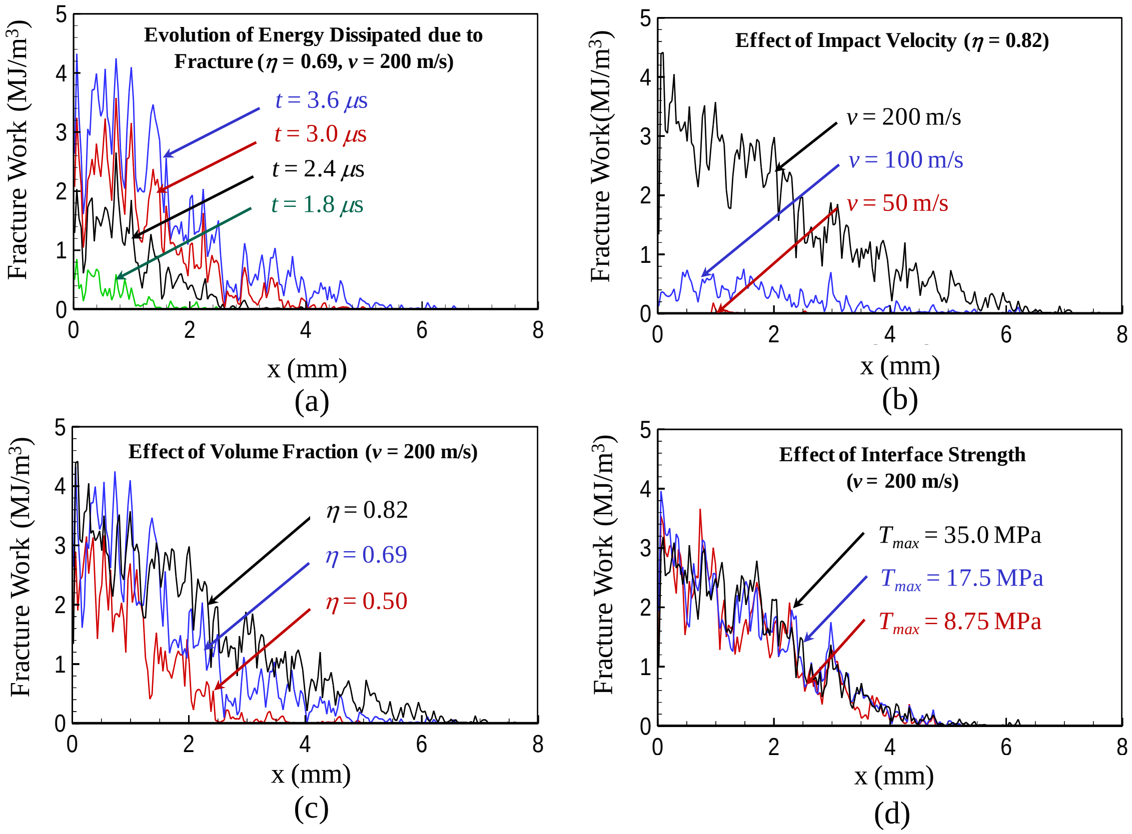

(a) (b) (c) (d)

Figure 51: Variation of fracture energy along the loading direction for (a) different times between t = 1.8 – 3.6 μs (η = 0.69, v = 200 ms^{-1}), (b) different impact velocities between v = 50 – 200 ms^{-1} (η = 0.82), (c) different packing densities between 0.50 – 0.82 (v = 200 ms^{-1}, t = 3.6 μs), and (d) different interface strengths between T_{max} = 8.75 – 35.0 MPa (η = 0.82, v = 200 ms^{-1}, t = 3.6 μs).

The preceding discussions make it clear that a significant amount of energy is dissipated as a result of fracture and friction at interfaces. To quantify the evolution of damage, the distribution of fracture energy is plotted along the length of the specimen. Figure 51(a) shows the result for a microstructure with η = 0.69 at v = 200 ms^{-1}. The fracture energy is highest near the impact surface and gradually decreases to zero at the front of the stress wave. At t = 3.6 μs, the fracture energy is ~ 4 MJ-m^{-3} near the impact surface and ~ 0.5 MJ-m^{-3} at 4 mm from the impact surface. The fracture energy at each location increases with time. As the impact velocity increases from 50 to 200 ms^{-1}, the amount of energy dissipated through fracture increases [see Figure 51(b)]. For example, at a distance of 2 mm from the loading surface, the fracture energy is ~ 3.0 and 0.5 MJ/m^3 for impact velocities of 100 and 200 ms^{-1}, respectively.

Figure 51(c) shows the fracture energy at t = 3.6 μs for microstructures with grain volume fractions between η = 0.50 – 0.82 for v = 200 ms^{-1}. For both η = 0.69 and 0.82, the fracture energy is ~ 4 MJ-m^{-3} near the impact surface. However, along the length of the specimen, fracture energy is lower for lower grain volume fractions.

Figure 51(d) shows the fracture energy dissipated at t = 3.6 μs for samples with different interface bonding strengths (T_{max} = 8.75 – 35.0 MPa) and η = 0.82 at v = 200 ms^{-1}. When T_{max} = 8.75 MPa, a higher amount of fractured surfaces are generated as compared to the case with the case with T_{max} = 35.0 MPa. However, the amount of energy dissipated per unit area of crack extension is lower when the interface strength is lower. This causes the distribution of fracture energy to remain approximately invariant over the range of interface strengths considered, as seen in the Figure 51.

The fracture energy varies non-uniformly with time and distance along the loading direction. As mentioned earlier, it is highest at the impact surface and gradually decreases to zero at the front of the stress wave. The variation of fracture energy dissipated at the impact surface can be quantified using the dimensionless terms used in Eqs. (4.1) and (4.2) as,

$$W_{\mathrm{f}} = \begin{cases} 0, \quad t < t_{\mathrm{d}} \\ W_{\mathrm{f}}{}^{0} \left(\dfrac{\eta}{\eta_{\mathrm{ref}}} + 1 \right)^{1.9} \left(\dfrac{v}{v_{\mathrm{ref}}} \right)^{4} \left(\dfrac{t}{t_{\mathrm{d}}} - 1 \right)^{1.2}, t \geq t_{\mathrm{d}}. \end{cases} \tag{4.3}$$

The effect of delay time is similar in both Eqs. (4.2) and (4.3); the fracture energy does not initiate before a delay time t_{d} has elapsed. In contrast to the evolution of average stress and peak temperature, the fracture energy has a high sensitivity to the impact velocity as shown by the exponent of 4. At the same time, a higher impact velocities results in a higher nominal strain; this in turn causes an increased fracture of grains and debonding along the interfaces. The fracture energy also increases non-linearly with volume fraction as shown by the exponent of 1.9. The increase of fracture energy is almost linear with time. The interface bonding strength does not significantly affect the fracture energy and is not included in Eq. (4.3). It is noted that, for most of the calculations, the corresponding fits are obtained up to a time of 5 - 6 μs. Additional failure mechanisms may become active at higher strains, affecting hot spot formation beyond the range analyzed here.

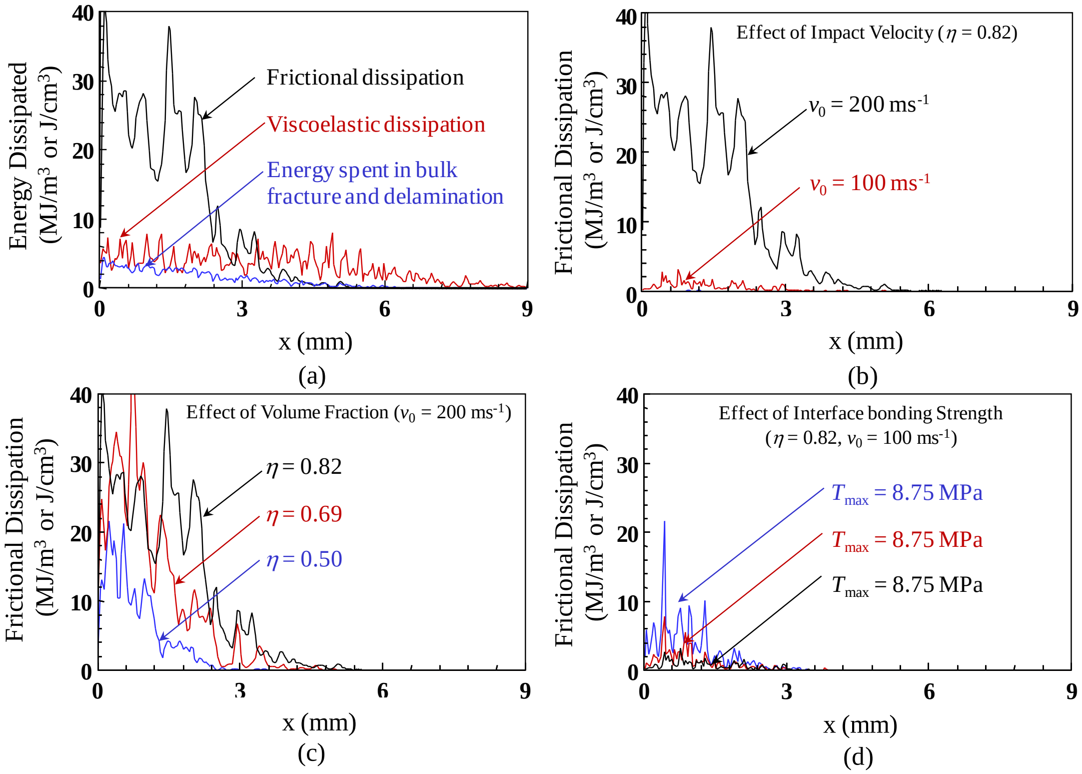

Figure 52: Variation of energy dissipated at different distances from the impact surface for

(a) all forms of dissipation at t = 3.6 μs (η = 0.82, v = 200 ms^{-1}),

(b) different impact velocities between v = 50 – 200 ms^{-1} (η = 0.82),

(c) different packing densities between 0.50 – 0.82 (v = 200 ms^{-1}, t = 3.6 μs), and

(d) different interface strengths between T_{max} = 8.75 – 35.0 MPa (η = 0.82, v = 100 ms^{-1}, t = 3.6 μs).

The evolution of temperature is directly related to the dissipation of energy. Figure 52(a) shows the different forms of energy dissipated at t = 3.6 μs, including cohesive energy spent on causing fracture, frictional and viscoelastic dissipations – for a microstructure with η = 0.82 subject to a boundary velocity of v = 200 ms^{-1}. Frictional dissipation is the dominant mechanism of heat generation, followed by viscoelastic dissipation. The amount of fracture energy dissipated is also highest near the impact surface and decreases approximately linearly with distance away from the surface. The viscoelastic dissipation per unit volume of ~ 6 MJ-m^{-3} is highest near the impact surface and gradually decreases with distance away from the impact surface. Since viscoelastic dissipation is a form of bulk dissipation, it results in a more uniform distribution of temperature in the binder, in contrast to the distribution of frictional dissipation which occurs along interfaces.

Since frictional dissipation is responsible for high temperature rises, the focus is on its variation with the impact velocity and loading conditions. Figure 52(b) shows the variation of frictional dissipation along the length of the specimen at t = 3.6 μs for different impact velocities in the range of v = 50 – 200 ms^{-1} and η = 0.82. At v = 100 ms^{-1}, the delay time for the onset of frictional heating is long [see Figure 53] and no significant frictional dissipation occurs. At higher impact velocities, frictional dissipation is significant. For instance, as the impact velocity is increased from 100 to 200 ms^{-1}, frictional dissipation near the impact surface increases by almost an order of magnitude, from less than 3 MJ-m^{-3} to around 30 MJ-m^{-3}. This increase in frictional dissipation with impact velocity is highly non-linear and is responsible for the significant variation of peak temperatures observed in Figure 50(b).

Frictional dissipation also increases as the grain volume fraction η increases from 0.50 to 0.82 [see Figure 52(c)]. However, this increase (from 10 to 40 MJ-m^{-3} near the impact surface) is more gradual, in comparison to the increase associated with the impact velocity. Finally, the effect on frictional dissipation at t = 3.6 μs of interface bonding strength in the range of T_{max} = 8.75 – 35.0 MPa for η = 0.82 and v = 100 ms^{-1} is shown in Figure 52(d). At T_{max} = 8.75 MPa, frictional dissipation is higher and more stochastic, with local peak values up to 20 MJ/m^3, indicating the formation of hot spots having significantly high temperatures.

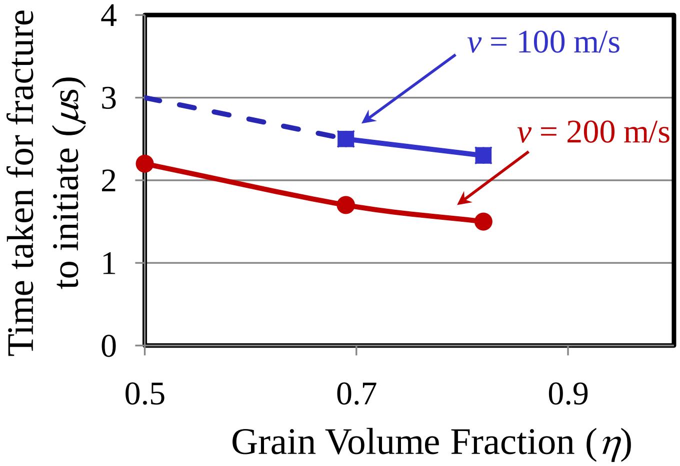

Figure 53: Variation of delay time (t_d) with grain volume fraction and boundary velocity.

Frictional dissipation typically occurs at later stages of loading and does not initiate until a delay time t_{d} has elapsed [106]. The delay time denotes the point at which the dominant heating mechanism changes from viscoelastic dissipation in the binder to frictional heating at fractured surfaces. The variation of delay time is investigated previously for square samples subject to uniaxial loading [106, 109]. Figure 53 shows the variation of delay time with grain volume fraction η in the range of 0.50 – 0.82 and impact velocity between v = 100 – 200 ms^{-1}. For the same impact velocity, the delay strain decreases with grain volume fraction. At higher impact velocities, the delay time decreases by a similar amount for all grain volume fractions considered. During the delay time, the wave front traverses a considerable length of the specimen. It is found that the distance travelled by the wave in time t_d is quite insensitive to the grain volume fraction and is only dependent upon the boundary velocity. At v = 200 ms^{-1} and 100 ms^{-1}, the corresponding distances are approximately d_0 = 3.70 mm and 5.44 mm, respectively, for all volume fractions considered. This indicates that fracture and friction will not occur until the width of the stress wave exceeds d_0. It is noted that the initial ramp of loading can influence the overall delay time. Such loads with gradually increasing intensity initially can occur during impact because of surface roughness or impactor property gradation. However, regardless of if a ramp is specified in loading, the trends outlined are applicable for the comparison of responses of materials with different microstructures under the same loading conditions.

4.3.1 Temperature Rises

The ignition sensitivity of the PBX is affected by several parameters, one of them being the mass fraction of the material having temperature rises above a certain value. The higher the mass fraction at elevated temperatures, greater the probability for a sustained reaction. Histograms showing mass fraction as a function of temperature increase with temperature increments of ΔT = 5 K are used to provide an overall quantification of the heating in the material.

Figure 54 shows the temperature rises in the grains and matrix at t = 3.6 μs for a microstructure with η = 0.82 and a boundary velocity of v = 200 ms^{-1}. The temperature rise profile shows a non-linear trend with two distinct heating regimes. This can be explained on the basis of the bulk heating mechanisms. The lower end of the heating curve up to a temperature rise of ~ 50 K is dominated by viscoelastic heating in the binder. The viscous binder deforms easily and does not develop high stress until it is sufficiently deformed to allow higher stresses to result. The lower stresses in the binder lead to relatively low amount of viscoelastic dissipation. The higher temperature regime is dominated by frictional dissipation. At the high end of the temperature spectrum, temperature rises of ~ 300 – 400 K are seen. As mentioned earlier, high temperature rises are primarily due to frictional dissipation in the grains. In the regime dominated by viscoelastic heating, the profile is relatively smooth. In contrast, the data in the high temperature regime (> 550 K) show large oscillations, indicating a stochastic trend in the occurrence of spots associated with high temperatures. This is a result of the highly heterogeneous nature of the microstructure and the fact that frictional dissipation is a surface phenomenon that occurs only at debonded or crack surfaces [see Figure 47(d)].

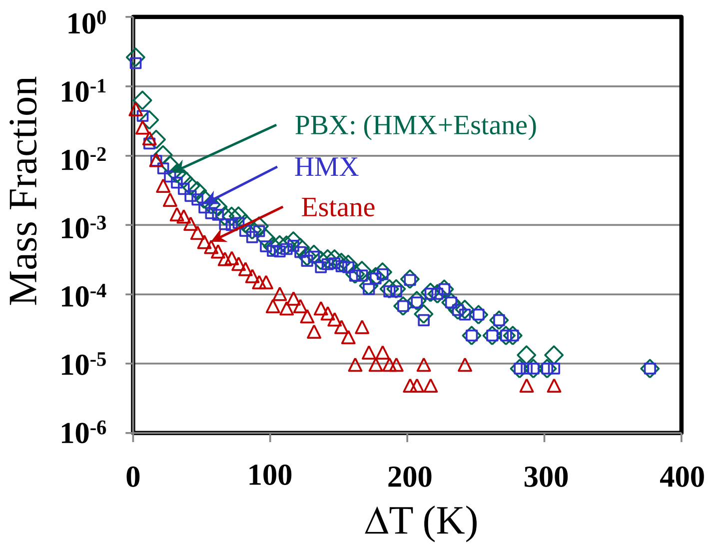

Figure 54: Temperature rises in the in grains and binder at t = 3.6 μs (η = 0.82, v = 200 ms^{-1}).

The evolution of temperature for a calculation with $\eta = 0.82$ and $v = 200$ ms^{-1} is shown in Figure 55(a). Initially at $t < t_d$ (e.g., 1.4 μs), frictional dissipation has not initiated and the temperature rise is primarily due to viscoelastic dissipation in the binder. Consequently, the variation in temperature rise is small and the maximum temperature rise is ~ 50 K. Higher temperature rises occur once frictional dissipation initiates. With time, the heating profile becomes increasingly non-linear, with the initial viscoelastic regime followed by the friction-dominated heating regime.

As seen in the previous section, the dominant heating mechanisms can vary significantly with impact velocity. The temperature rise profiles at $t = 3.6$ μs for $v = 50$, 100 and 200 ms^{-1} and $\eta = 0.82$ are shown in Figure 55(b). At 50 ms^{-1}, most of the heating is due to viscous dissipation in the binder and the maximum temperature rise is less than 60 K. As the impact velocity increases, the higher stresses increase viscoelastic and frictional dissipation. The increase in the frictional dissipation is quite significant and causes the mass fraction experiencing similar amounts of temperature rise to increase by an order of magnitude as the impact velocity increases from 100 to 200 ms^{-1}. At an impact velocity of 100 ms^{-1}, mass fractions having temperature rises greater than 100 K show more fluctuation and are more stochastic than in the case with $v = 200$ ms^{-1}. This indicates that hot spot temperatures are more uniform at higher impact velocities.

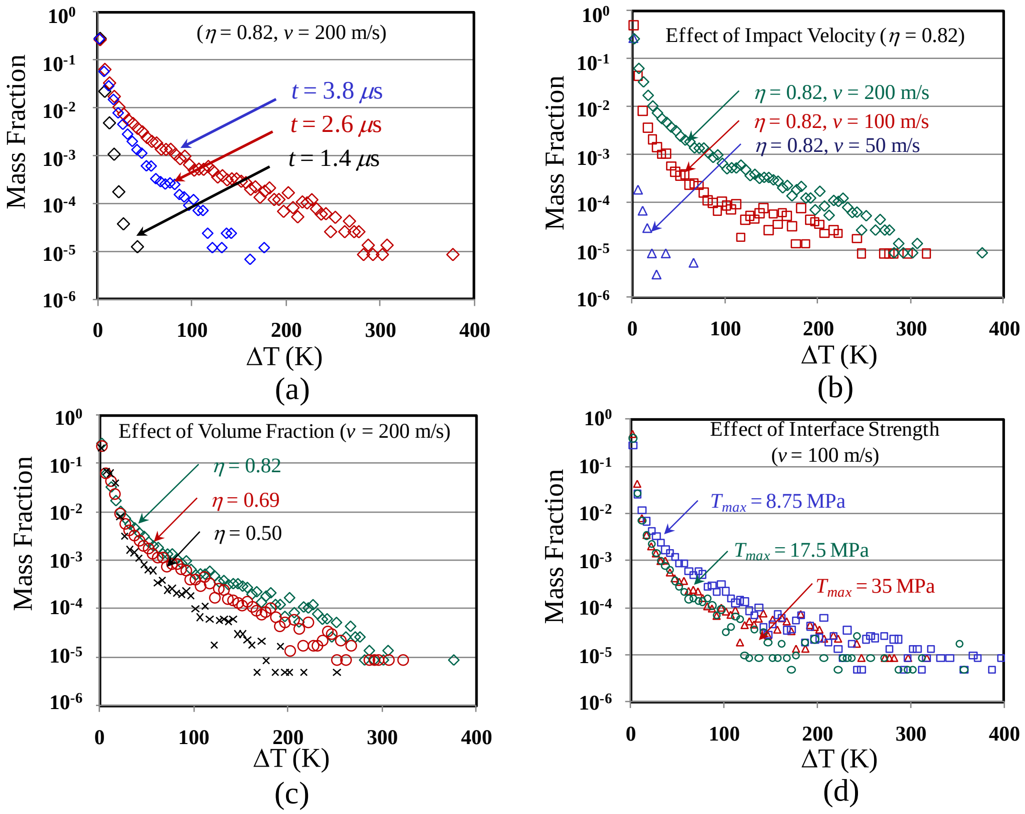

Figure 55: Temperature rises in the microstructure,

(a) at different times between *t* = 1.4 – 3.6 *μ*s (*η* = 0.82, *v* = 200 ms^{-1}),

(b) for different impact velocities between *v* = 50 – 200 ms^{-1} (*η* = 0.82),

(c) for different packing densities between 0.50 – 0.82 (*v* = 200 ms^{-1}, *t* = 3.6 *μ*s), and

(d) for different interface strengths between T_{max} = 8.75 – 35.0 MPa

(*η* = 0.82, *v* = 100 ms^{-1}, *t* = 3.6 *μ*s).

Figure 55(c) shows the temperature rises at $t = 3.6$ μs for $\eta = 0.50$, 0.69 and 0.82 and $v = 200$ ms^{-1}. The difference between the cases in the low temperature regime ($\Delta T <$ 60 K) is not significant. Here, two counteracting mechanisms are at work. As the fraction of binder decreases, the average stresses in the material increases, resulting in higher viscoelastic dissipation. On the other hand, the mass of binder available for viscoelastic dissipation also decreases. These two trends balance out to cause the low temperature portion of the heating curve to remain approximately unchanged. However, the higher stresses at higher packing densities cause the heat dissipated due to frictional dissipation to rise. As the grain volume fraction increases, the curve becomes more stochastic in the high temperature regime, for reasons discussed previously.

Figure 55(d) shows the heating profiles at t = 3.6 μs for interface strength values of T_{max} = 8.75, 17.5, and 35 MPa and η = 0.82 at v = 100 ms^{-1}. It has been shown earlier that the average stress in the compaction region is lower at lower interface strength, while behind the compaction region the average stress is similar for these cases. Overall, a decrease in interface bonding strength is associated with earlier debonding at the grain/matrix interface, more fractured surfaces for frictional dissipation, and higher temperature rises in the PBX.

4.4 Conclusions

This study focuses on the transient behavior of HMX/Estane PBX under uniaxial strain conditions of boundary loading. Results show that the overall wave speed through the microstructures depends on both the grain volume fraction and interface bonding strength between the constituents and that the distance traversed by the stress wave before frictional dissipation initiates is independent of the grain volume fraction but increases with impact velocity. The analysis of stress profile showed that the average stress behind the compaction wave-front is highly sensitive to the volume fraction of the grains indicating that at higher grain volume fractions, the load is preferentially transmitted across neighboring grains, resulting in much higher stresses. The average stress increases approximately linearly with the boundary velocity as a result of the rate dependence of the binder. On the other hand, it is insensitive to changes in interface bonding strength indicating closure effect of the compressive loading. For the time durations considered (5 – 6 μs) for which no wave reflection occurs, the fracture energy dissipated is highest near the impact face and decreases to zero at the stress wave front. On the other hand, the highest temperature rises are ~ 2 – 3 mm from the loading surface. Scaling laws are developed for the maximum fracture energy dissipation rate and the highest temperature rise as functions of the impact velocity, grain volume fraction and grain-binder interfacial bonding strength. Analysis of the temperature rise shows that in the lower temperature regime dominated by viscoelastic heating, the profile is relatively smooth. In contrast, the data in the high temperature regime show large oscillations, indicating a stochastic trend in the occurrence of spots associated with temperatures. The temperatures at the higher end of the spectrum are highly stochastic and may reach up to ~ 700 – 800 K for boundary velocities greater than 100 ms^{-1}. Such temperature rises suggest that impact at moderate velocities of the order of a few hundred ms^{-1} may be sufficient for melting and reaction initiation.

CHAPTER 5: IGNITION CRITERION

5.1 Introduction

This chapter focuses on developing an ignition criterion based on the conditions of mechanical loading and microstructural attributes. The initiation of chemical reaction is significantly affected by the local fluctuations of field quantities, which depend on both microstructural heterogeneity and loading. Most importantly, the response cannot simply be quantified by one (such as pressure in the case of shock loading) or a small number of parameters. Specifically, the issue partly relates to the formation of hotspots whose temperatures, sizes, morphologies and proximities depend on

(1) not only the hydrostatic part of the stress tensor but also the deviatoric part of the stress tensor (i.e., stress triaxiality);

(2) not only the volumetric responses but more importantly the shear response of the materials;

(3) thermal conduction; and

(4) microstructure.

However, there is also a common thread for both shock and non-shock loading. In both cases, it is the hotspots that, once formed, serve as ignition sites and react exothermally. Therefore, hotspots determine the stability of the GXs or the PBXs.

Here, the two phenomena, hotspot generation and local temperature evolution under influence of chemical reactions, are considered as separate but related processes.

The former is concerned with the quantification of the contributions of different dissipation/heating mechanisms and how the contributions evolve as deformation progresses. This task is achieved through use of the Lagrangian cohesive finite element framework to quantify the effects of microstructure and thermal-mechanical processes developed in Chapter 2. Simulations are carried out for a range of strain rates, microstructure and loading conditions for both GX and PBX.

The latter (thermo-chemical runaway) is solved independent of hotspot dynamics they are in essence “borrowed” from the existing work. The seminal work in this area was done in the 1920’s by Semenov [113] and later by Frank-Kamenetskii (FK) [114]. Semenov [113] developed a criticality model which was a solution of the heat diffusion equation with heat generation due to reaction. FK worked on the same heat conduction equation but with varying temperature distribution. Thomas [115] developed a unifying model which incorporated the elements of both Semenov and FK’s work. Together, this and other works (e.g., Gray [116-117], Boddington [118-119]) provided an analytical approach for obtaining the critical size of hotspots required for ignition as a function of temperature. The critical hotspot-size combinations form the threshold that taken as a material attribute. Such threshold relations can also be obtained using chemical kinetics calculations [29, 52]. It must be cautioned, however, that in this analysis the issue of subsequent burn after ignition is not tackled, which may result in detonation of explosives.

In summary, the objective of this chapter is to connect locally heated high temperature spots due to thermal-mechanical processes to the ignition process defined as the thermal run-away phenomenon in the localized high temperature regions. The ultimate goal is to understand and quantify the mechanisms leading to initiation in energetic materials. There is a need to validate the model calculations. However there is still a lack of data from well-defined comparable experiments with well-characterized microstructures. Hopefully this research will serve as a stimulus for such experiments to be conducted in the near future.

This chapter is based on the work published in Ref. [120] in collaboration with Seokpum Kim and Dr. Yasuyuki Horie.

5.2 Ignition Criterion

Mathematically, the criterion at the junction of the first (thermal-mechanical) phenomenon which provides hotspots and the second (thermal-chemical) phenomenon which leads to thermal runaway can be stated as

$$d(T) \geq d_c(T), \tag{5.1}$$

where, d is the diameter of the dominant hotspot resulting from a loading event whose interior temperatures are at or above temperature T and d_c is the minimal diameter of a hotspot required for thermal runaway at temperature T. Note that the right-hand side of Eq. (1) represents the boundary between "ignition" and "non-ignition" in the $d-T$ space and reflects material attributes. Information about this material properties part of the criterion has to be obtained independently, from experiments or thermal-chemical calculations. In the current analysis, this information comes from hotspot size-temperature threshold relations for solid explosives derived from thermal-chemical reaction calculations. The rest of this chapter focuses on the two sides of the criterion in

Eq. (5.1), first the right-hand side, then the left-hand-side. It is important to point out at the outset that, because the hotspot state represented on the left hand side of Eq. (5.1) can be the result of either shock or non-shock loading and the thermal-chemical threshold condition embodied on the right hand side of Eq. (5.1) is independent of loading, the criterion proposed here should in general apply to both non-shock and shock loading. However in this research, the analyses solely concern non-shock conditions. The application to shock loading can be discussed separately with appropriate computational and experimental data in the future.

5.3 Thermal Criticality Threshold

At present, hotspot sizes and temperatures cannot be measured experimentally. Hence, theoretical estimates are required to predict thermal criticality of hotspots. Criticality occurs when the temperature in a hotspot of a given size and shape is high enough so that the rate of temperature increase due to chemical reaction is higher than the rate of temperature decrease due to heat loss through conduction (and other dissipative processes if any) across the surface of the hotspot. The thermal criticality threshold is used to relate the size and temperature of hotspots at the critical condition in Eq. (5.1). Solutions of the heat diffusion equation with heat generation due to reaction have been used to predict the temperature rise in hotspots for a range of canonical shapes (spherical, planar circular, elliptical, etc.). The analytical formulation can be expressed as [5],

$$d_c = f(T_s, \text{material properties, shape}), \tag{5.2}$$

where, T_s is the temperature at the surface of the hotspot. The specific form of Eq. (5.2) obtained from the solution of the heat diffusion equation is presented in *Non-shock*

Initiation of Explosives, pg. 202 [5]. The relation considers pure explosive materials following single-step Arrhenius reaction kinetics and is independent of the loading conditions (shock or non-shock). In summary, the analytical formulation can be used to estimate the critical size of a hotspot with a specific shape, at a given surface temperature.

Tarver et al. [29] performed chemical kinetics calculations to analyze the criticality issue for HMX and TATB explosives. The calculations consider multistep reaction mechanisms and the pressure and temperature dependence of reactants and products. The black line in Figure 56 shows the calculated critical temperature as a function of size for spherical hotspots in HMX [29]. For comparison, the analytical formulation as fitted to Tarver et al.'s data, [Eq. (5.2)] from [5] for a spherical hotspot is also plotted in Figure 56 (red line). The fit provides a good description of Tarver et al.'s data [29]. This is of interest since Tarver et al. [29] considered a three-step reaction pathway for the decomposition of HMX. The close agreement with the analytical response suggests that over this range of ignition times, there could be a single rate-limiting step in the ignition mechanism.

It must be noted that Henson [52] suggested a similar possibility since the data for ignition time as a function of temperature appears to be close to linear on the log-log scale. Specifically, he also performed chemical kinetics calculations and came up with a critical size vs. temperature relationship for hotspots in HMX which is shown in Figure 56 in blue. The disparity between the results from Tarver et al. [29] and Henson [52] may stem from the way in which the hotspot temperatures are calculated. In this analysis, the relation provided by Tarver et al. [29] are used to identify critical hotspots. It is noted that, although there is a numerical difference in the relations provided in [29] and [52], the qualitative nature and the trend of the response are be similar regardless of which set of data is used.

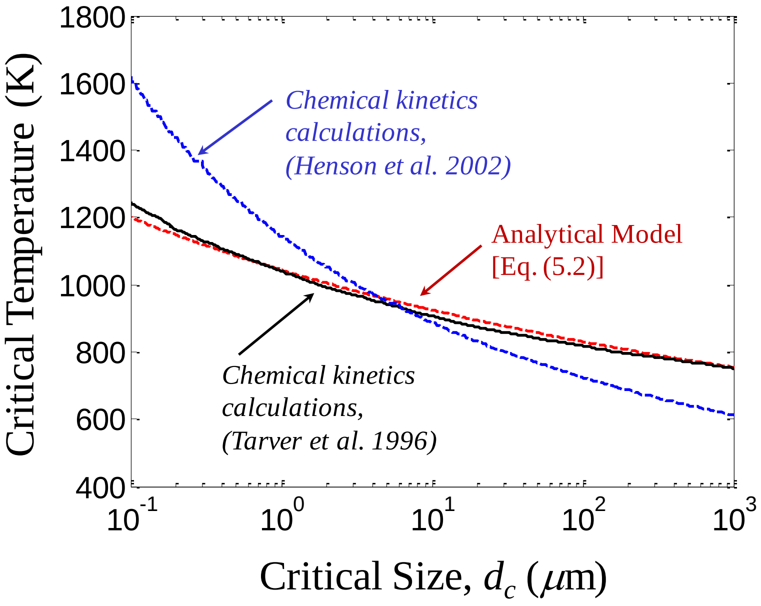

Figure 56: Temperature-hotspot size threshold curves for ignition or thermal runaway of HMX, data from chemical kinetics calculations performed by Tarver et al. [29] (used in the analyses presented here) is shown, along with the analytical relation in Eq. (5.2) which is fitted to Tarver et al.'s data. For comparison, Henson's [52] data is also shown, but not used here.

5.4 Statistical Characterization of Hotspot Field using Radial Distribution Function (RDF)

The size and temperature of hotspots need to be quantified prior to the application of any threshold criteria for ignition. In a previous work [106], the authors employed a method to identify hotspots which involves a circular “microscope” sweeping through the microstructure to identify potential hotspots. That scheme requires a rigid criterion for identifying hotspots and does not lend itself to systematic quantification of the distribution of hotspot size.

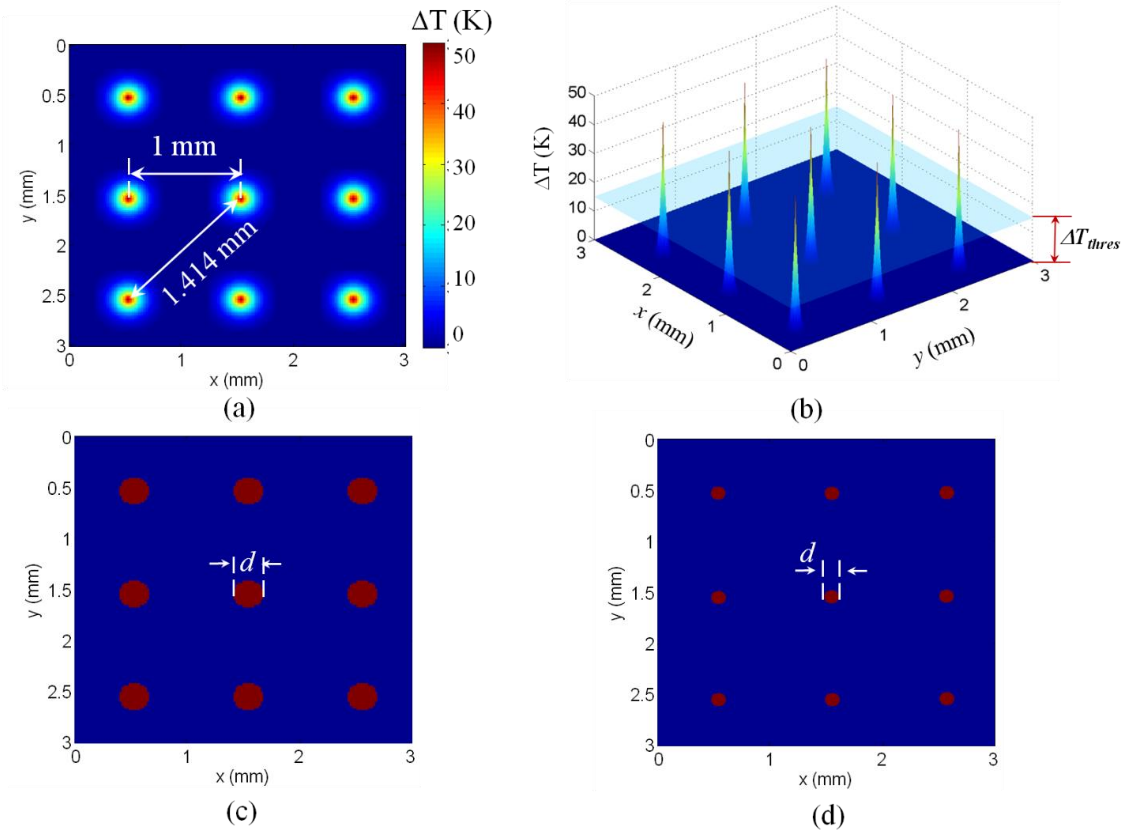

(a) (b)

(c) (d)

Figure 57: Illustration and quantification of an idealized hotspot field, (a) hotspots arranged in a regular square array, (b) 3D temperature profile of the idealized hotspots field, and a schematic sectioning of the hotspot field by a plane at a given cutoff temperature ΔT_{thres}, (c) hotspots on section with ΔT_{thres} = 15 K, and (d) hotspots on section with ΔT_{thres} = 30 K.

To avoid the use of arbitrary size-temperature criteria in identifying hotspots, a novel scheme is developed here. This new approach involves the use of a temperature threshold (ΔT_{thres}) which is of vital importance. At each time step, the microstructure is scanned for temperature rises above ΔT_{thres}. Areas of a temperature field with temperatures above the threshold are analyzed for hotspots. Successively varying ΔT_{thres} values allows the characteristics of a temperature field to be fully analyzed. In particular, strategically chosen threshold temperature values allow hotspots of interest to be identified.

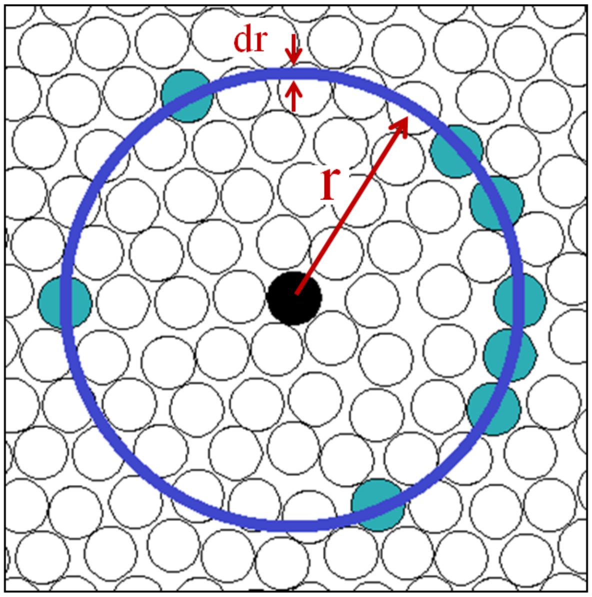

Figure 58: Schematic illustration o the radial distribution function (RDF).

To illustrate how this scheme works, Figure 57(a) shows an idealized regular array of circular hotspots, each having a temperature rise of 50 K at the center and 0 K at the periphery. The variation of temperature inside the hotspots follows a smooth polynomial function. Figure 57(b) shows a 3D visualization of the temperature field with temperature as the vertical axis. A plane representing a threshold temperature of $\Delta T_{thres} = 15\,\mathrm{K}$ is shown intersecting the hotspot fields. Obviously, varying this ΔT_{thres} would reveal the hotspots and allow them to be quantified in different ways. Figure 57(c-d) show the hotspot fields obtained by using $\Delta T_{thres} = 15\,\text{and}\,30\,\text{K}$ respectively. These quantifications can be further analyzed to obtain more detailed statistical information.

The radial distribution function (RDF) is used as a measure to statistically characterize the spatial distribution of hotspots. Historically, the RDF has been used extensively to analyze the arrangement of atoms and molecules [121-122], packing of spheres [123] and solidification and structure of metals [124]. As illustrated in Figure 58, the RDF describes how the density of a system of particles varies as a function of interparticle distance. Specifically, the RDF *f*(*r*) represents the probability of finding a particle in a shell with thickness *dr* at a distance *r* from a particle. The number of particles *dn*(*r*) at a distance between *r* and *r* + *dr* from a given particle is

$$dn(r) = \rho_p \cdot f(r) \cdot 4\pi r^2 dr, \tag{5.3}$$

where $\rho_p = N / V$ is the average density of particles in the system, with *N* the total number of particles in the system with total volume *V*. The above relation yields the RDF as

$$f(r) = \frac{1}{\rho_p \cdot 4\pi r^2} \frac{dn(r)}{dr}. \tag{5.4}$$

Numerically, Eq. (5.4) can be evaluated by converting the differential relation to a difference relation so that *dn* and *dr* can be approximated as *Δn* and *Δr* respectively.

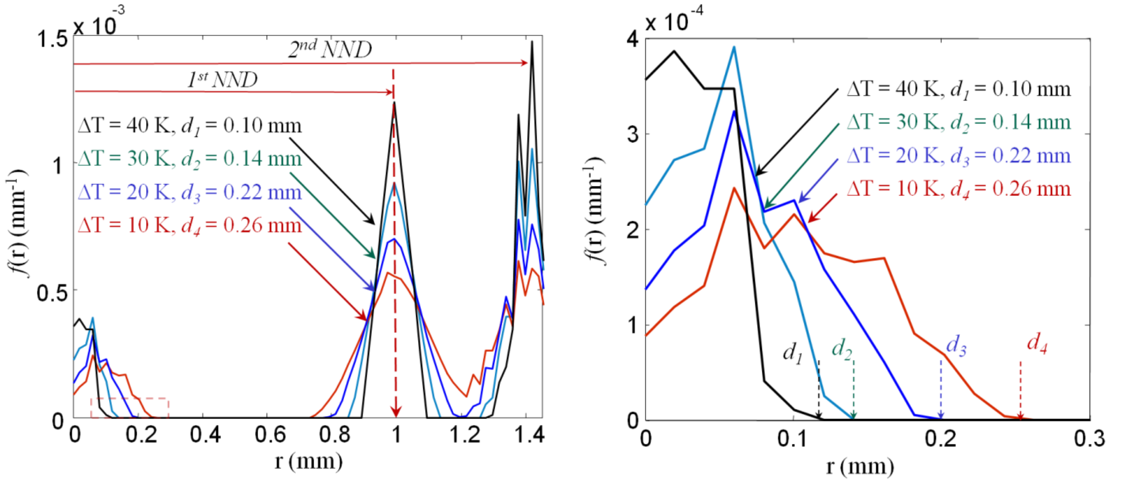

(a)

(b)

Figure 59: (a) Radial distribution function (RDF) of the idealized hotspot distribution in Figure 57 at different cutoff temperatures, and (b) a close-up view of the region where the RDFs go to zero which shows the diameter of the hotspots at the corresponding cutoff temperatures.

In the analyses presented here, $\Delta n(r)$ represents the number of digital pixels at a distance between r and $r + \Delta r$ from a given pixel having temperature rises above ΔT_{thres} (see Figure 58). Since the RDF is a probability distribution function, the area under the curve is unity, i.e.,

$$\int_{r=0}^{r=\infty} f(r)dr = 1. \tag{5.5}$$

The radial distribution function profiles computed for the idealized hotspot distribution in Figure 57 for $\Delta T_{thres} = 10, 20, 30 \text{ and } 40\,\text{K}$ are shown in Figure 59. At r = 0, $f(r)$ has a finite value. As r increases, $f(r)$ increases and decreases. The value of r at which $f(r)$ first becomes zero corresponds to the maximum size of hotspots for a given

ΔT_{thres} [see Figure 59(b)]. As r further increases, two more peaks are observed, the first at $r = 1$ mm and second at 1.41 mm. These peaks correspond to the average nearest neighbor distance (NND) between the hotspots and the average second nearest neighbor distance, respectively. Note that the peaks become higher as the hotspot size decreases due to the normalization of the curves.

When different values for the temperature threshold are used, the distributions of the shapes and sizes of hotspots with temperature increases above the threshold can be characterized. Hotspot sizes are characterized using two different methods. In the first method, the hotspot size is calculated as the diameter of a circle with the same area as the hotspot in 2D. This method is called the equivalent diameter (ED) scheme. To capture the effect of the shape of the hotspots, a second method is also used. In this method, the hotspot size is calculated as the length of the largest line that can be fitted inside the hotspot. This method is called the maximum size (MS) scheme. Together, the ED and MS schemes allow quantification of both the size and the shape of hotspots. Systematic characterizations of hotspots are presented in Sections 5.8.2 – 5.8.5.

5.5 Thermal Criticality of Hotspots

In this analysis, critical hotspots are identified using the threshold condition in Eq. (5.1). The right-hand side of the equation uses Tarver et al.'s numerical data (shown in Figure 56).

The left-hand side of Eq. (5.1) is obtained by analyzing the hotspot distributions from the CFEM calculations. To account for the variation of temperature within a hotspot (note that temperatures at different spatial locations within a hotspot are different and

ΔT_{thres} is the lowest temperature at the periphery), Tarver et al.'s criterion is stated as a band of $\pm 10\%$ about the mean value. Any hotspot is considered to be critical when it crosses the lower threshold limit (90% of the average threshold). Taking into consideration the stochastic nature of arbitrary microstructures, an approach is employed to identify the time to criticality t_c measured from the onset of dynamic loading. Specifically, instead of one single hotspot, criticality is regarded as being reached if the critical hotspot density in a specimen reaches a level equal to or greater than 0.22 mm^{-2}. This level corresponds to 2 critical hotspots in a 3 mm square domain. It is important to point out that variations in the choice of this parameter do not significantly change the results. Specifically, for a change of critical hotspot density from 0.11 to 0.44 mm^{-2}, the maximum variation in t_c is within 6% for a PBX microstructure having a packing density of 0.82 in several calculations with impact velocities between $v = 50 \text{ and } 250 \text{ ms}^{-1}$. This shows that the value of the critical hotspot density chosen is quite reasonable and does not cause large changes in results. Although this treatment contains a degree of arbitrariness, it allows relative comparisons to be made when used consistently for difference cases.

It should be pointed out that calculations are carried out using mesh sizes from 10 – 20 μm. The results converge as the mesh size is decreased beyond 15 μm. Specifically, the variation of hotspot size leads to a variation of time to criticality t_c of less than 5.0% for a 33% reduction in the mesh size from 15 to 10 μm, suggesting that the mesh resolution chosen (15 μm) is adequate for the purpose of the current study.

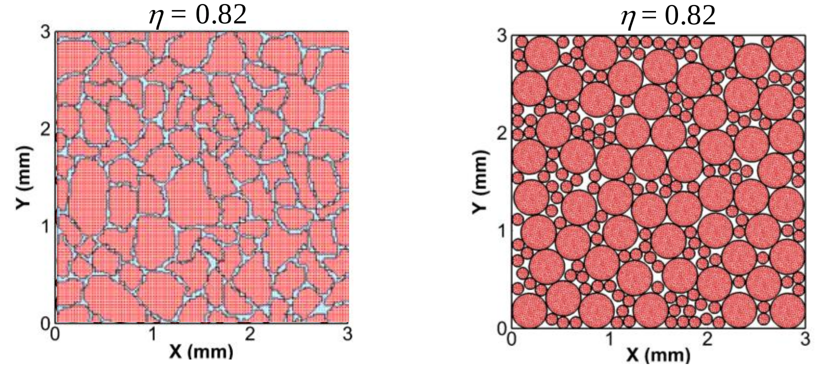

(a) PBX, Digitized Micrograph, $\eta = 0.82$

(b) Bimodal, $\delta = 120 - 360\mu m$ (1:3), $\eta = 0.82$

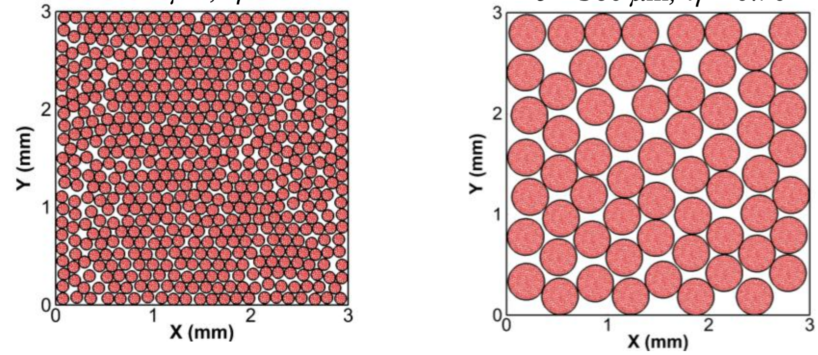

(c) Monomodal, $\delta = 120\ \mu m$, $\eta = 0.70$

(d) Monomodal, $\delta = 360\ \mu m$, $\eta = 0.70$

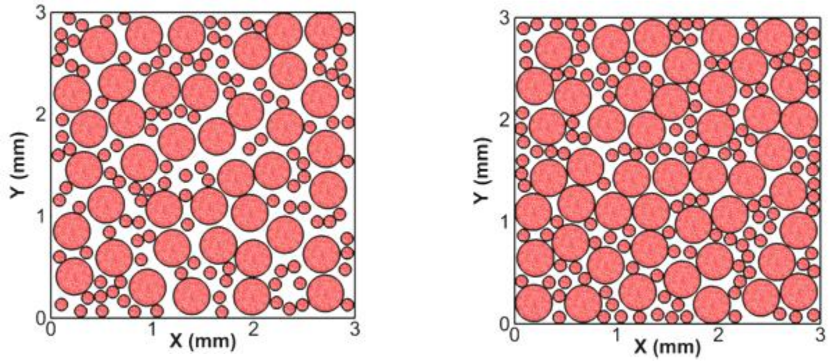

(e) Bimodal, $\delta = 120 - 360\mu m$ (1:3), $\eta = 0.60$

(f) Bimodal, $\delta = 120 - 360\mu m$ (1:3), $\eta = 0.70$

Figure 60: Microstructures analyzed -- digitized image of a PBX and idealized microstructures for granular HMX with different grain size distributions, (a) Digitized image of a PBX, (b) bimodal GX, $\delta = 120 - 360\ \mu m$, $\eta = 0.82$, (c) monomodal GX, $\delta = 120\ \mu m$, $\eta = 0.70$, (d) monomodal GX, $\delta = 120\ \mu m$, (e) bimodal GX, $\delta = 120 - 360\ \mu m$, $\eta = 0.60$ and (f) bimodal GX, $\delta = 120 - 360\ \mu m$, $\eta = 0.70$.

In experiments, there is a degree of stochasticity associated with the thermal runaway of hotspots in that quantities such as load intensity required to cause ignition, time to ignition from onset of loading, and total energy input at ignition may vary from sample to sample. One source of the stochasticity is variations in material microstructure and loading conditions. The issue of impact-induced ignition needs to be approached from a probabilistic viewpoint (see, e.g., [67]). Such studies may involve a statistical study using various levels of critical hotspot density and correlation of the results with experimental data. This issue is explored in Chapter 6.

The time since the onset of dynamic loading at which criticality is reached is taken as the critical time (t_c) and the energy imparted to the specimen per unit load contact area up to this time is taken as the critical input energy density (E).

5.6 Materials Considered

This analysis focuses on both granular HMX (GXs) and PBXs which have two-phase microstructures consisting of HMX grains and an Estane binder. Both idealized and actual microstructures are used to obtain samples with systematically varying attributes. The actual microstructure is obtained from [11] and has a grain volume fraction of 0.82. It is used to model the PBX, as shown in Figure 60(a). Additionally, a set of five idealized microstructures are used to model granular HMX. These samples are generated using monomodal and bimodal size distributions of circular grains [representative micrographs are shown in Figure 60(b-f)]. For this set of five microstructures, two grain sizes are used, with the smaller being 120 μm and the larger being 360 μm. The microstructures analyzed, along with their attributes are listed in

Table 6. For each attribute listed in Table 6, three statistically identical microstructure samples (random instantiations) are generated and used to obtain an estimate of the statistical variation in behavior. The results from the three samples are used in determine the error bounds presented hereafter.

Table 6: Microstructures analyzed in Chapter 5.

Microstructure	Grain volume fraction (η)	Average grain Size (μm)	Attributes
GX (15 instantiations)	0.60	120 – 360 (1:3)	Bimodal
	0.70	120 – 360 (1:3)	Bimodal, Mono-modal
	0.82	120 – 360 (1:3)	Bimodal
PBX (Digitized)	0.82	287.4	Real

5.7 Results and Discussions

The calculations focus on the effects of (i) strain rate, (ii) grain volume fraction ($\eta = 0.60 - 0.82$) and (iii) grain size distribution (monomodal and bimodal). For all calculations presented, the initial temperature is $T_i = 300\,\mathrm{K}$. Calculations are performed using two different loading configurations – small samples which account for wave reflections [see Section 2.8.1, Figure 10(c), v_L = 0] and larger samples without wave reflections [see Section 2.8.2, Figure 11(a)]. The imposed boundary velocity v is varied between 50 and 350 ms^{-1}, yielding overall strain rates of $\dot{\varepsilon} = (16.7 - 116.7) \times 10^3$ s^{-1} [for the loading configuration in Figure 10(c), v_L =0]. Since the configuration in Figure 11(a) focuses on the transient response of microstructures, the relevant discussions are limited to times before the stress wave reaches the boundary on the right [Figure 11(a)].

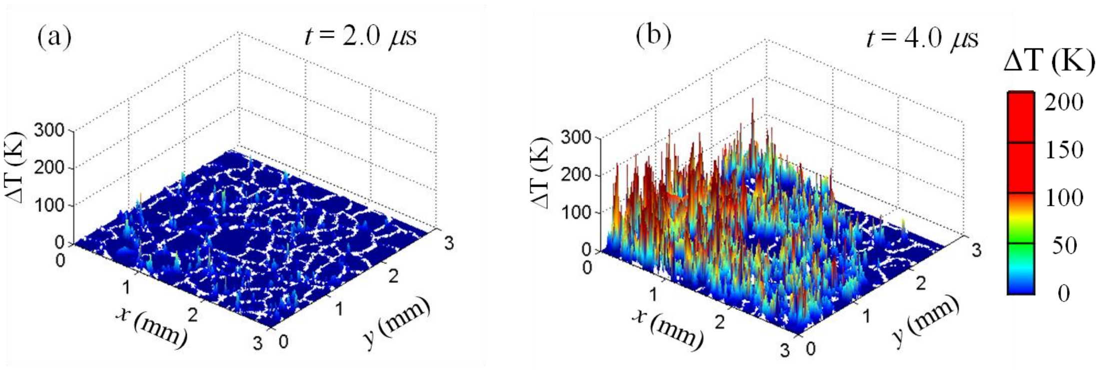

Figure 61: Evolution of temperature field in the HMX granules of the PBX in Figure 60(a), (η = 0.82, v = 100 ms^{-1}, $\dot{\varepsilon}$ = 33.3$\times$10^3 s^{-1}).

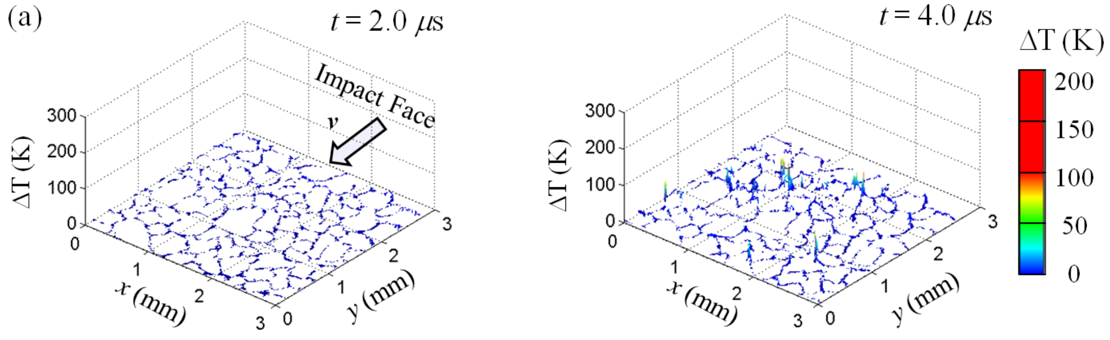

Figure 62: Evolution of the temperature field in the binder of the PBX in Figure 60(a), (η = 0.82, v = 100 ms^{-1}, $\dot{\varepsilon}$ = 33.3$\times$10^3 s^{-1}).

5.7.1 Hotspot Fields

Dissipation associated with mechanisms operative at the grain-level causes localization of thermal energy or the formation of hotspots [106]. The evolution of the size, shape and distribution of hotspots vary significantly with the microstructure and loading. Significant variations in boundary conditions and sample configurations can be encountered during loading. In Sections 5.8.2 - 5.8.5, a set of calculations on the PBX and GX is discussed to quantify the effects on hotspot fields of binder and stress wave reflection.

5.7.2 Small Samples with Wave Reflections

Figure 61 and Figure 62 show, respectively, the evolution of hotspots in the grains and binder for a PBX with η = 0.82 at $t = 2 - 4\ \mu\text{s}$. The impact velocity is v = 100 ms^{-1}. The calculation is performed using the loading configuration in Figure 10(c) with v_L = 0. Initially at $t = 2\ \mu\text{s}$, hotspots are few and form in locations of stress concentration due to grain-grain interactions. At higher levels of overall deformation [Figure 61(c)], high temperatures occur at locations of grain-grain interaction and along cracks within the grains, with the latter being a more significant heating mechanism. At $t = 4\ \mu\text{s}$, transgranular fracture of grains result in high temperature rises on the order of 200 – 300 K in the grains [see Figure 61(b)]. Although there is frictional dissipation due to sliding at grain/binder interfaces, the temperature rises in the binder is consistently lower than that in the grains [see Figure 62(b)]. In Figure 61(a-b), the temperature increases near the lower boundary are higher, due to the fact that the lower boundary is rigid and causes full reflection of the incident stress wave back into the material. This reflection subjects the lower portion of the material to slightly more intense loading.

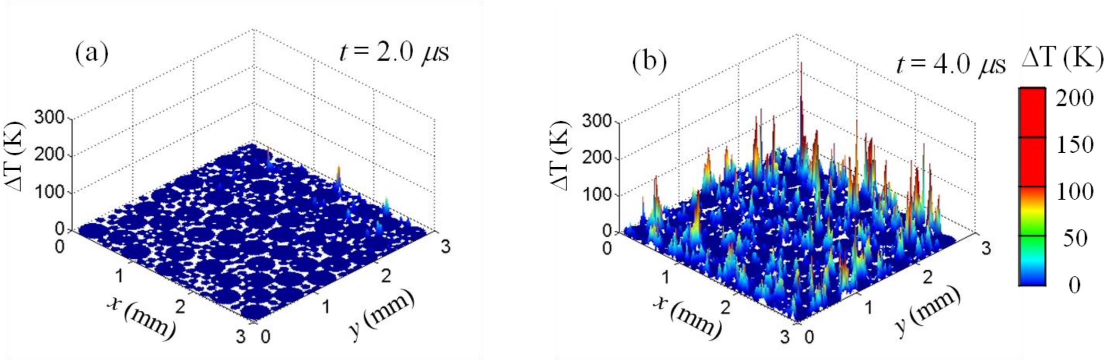

Figure 63: Evolution of the temperature field in the GX in Figure 60(b),

(η = 0.82, v = 100 ms^{-1}, $\dot{\varepsilon}$ = 33.3 $\times$10^3 s^{-1}).

The temperature rise in the GX having η = 0.82 at $t = 2 - 4\ \mu\text{s}$ is shown in Figure 63. The impact velocity is again $v = 100\ \text{ms}^{-1}$. Compared with that in the PBX, the temperature rise during the first 1-2 μs is lower in the GX, since most of the deformation is accommodated by the rearrangement of the grains and elastic intergranular interactions. However, at higher levels of overall deformation $(t = 4\ \mu\text{s})$, fracture of grains and frictional dissipation lead to significantly higher temperature increases throughout the microstructure. The temperature rises is approximately homogeneous in the domain, since the stress wave equilibrates over time (due to multiple reflections from the top and bottom boundaries).

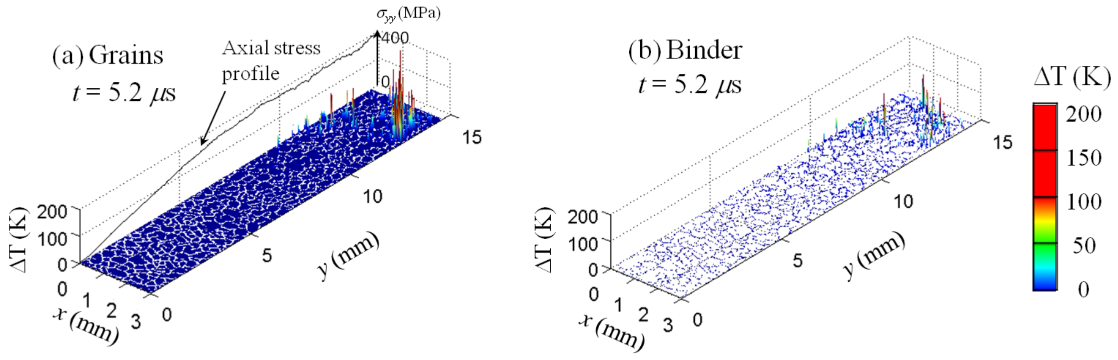

Figure 64: Temperature field in the grains and binder for loading configuration in Figure 11(a) (PBX in Figure 60(a), η = 0.82, v = 100 ms^{-1}).

Crushing of the smaller grains typically result in multiple fragments, increasing the surface area available for frictional dissipation. Thus, higher temperature rises are primarily seen at locations where smaller grains are fragmented. Whereas, the fracture of larger grains generally result in fewer fragments. Consequently, the locations of the higher temperature increases are interspaced by the larger grains [Figure 63(b)]. A more systematic study of the effect of grain size on the spatial distribution of hotspots is presented in Section 5.8.5. At higher levels of overall deformation, transgranular fracture occurs in both smaller and larger grains.

5.7.3 Large Samples without Wave Reflections

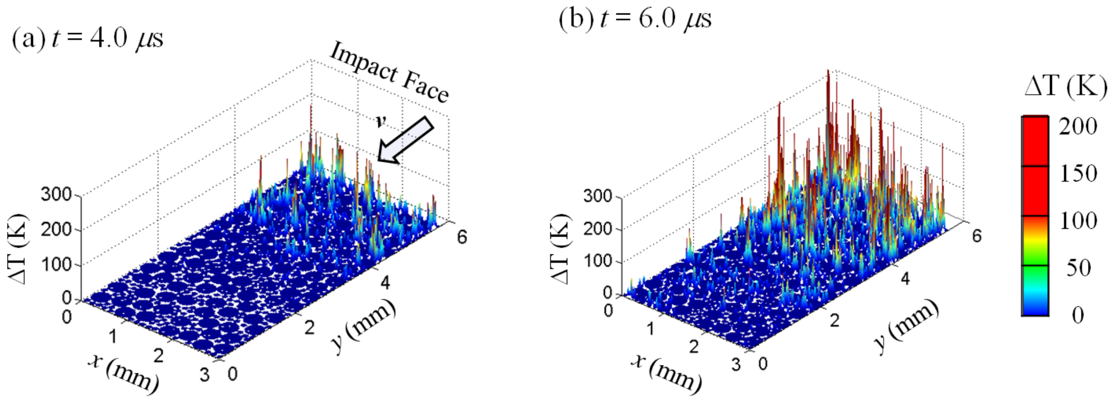

Figure 65: Evolution of the temperature field in HMX for loading configuration in Figure 11(a) (GX in Figure 60(b), η = 0.82, v = 100 ms^{-1}).

The next set of calculations illustrates the effect of stress wave propagation in long microstructures [loading configuration in Figure 11(a)]. Figure 64 shows the distributions of temperature in a PBX microstructure with a packing density of η = 0.82 at $t = 5.2\ \mu s$. The impact velocity is v = 100 ms^{-1}. The profile of the average axial stress over the cross section of the specimen is also shown in Figure 64(a). Note that the sample is long so wave reflection does not occur for the duration analyzed. The time shown here is later than those in the previous figures for the small samples for which wave reflection occurs. The average value of the axial stress behind the wave front is ~361.3 MPa. For higher volume fractions, the average stress can be obtained by extrapolating the value obtained from the CFEM calculations here, using Eq. (4.1) from Chapter 4. For a grain volume fraction of 0.95, such as that used in PBX9501, the average stress is predicted to be ~457 MPa, which is within 3.3% of the value obtained from experiments [125].

The temperature increases are highest near the impact surface and gradually decrease away from it. This is a consequence of the stress wave continuing to propagate towards the unstressed material. For this impact velocity, the failure mechanisms (transgranular fracture and sliding frictional heating along crack faces, intergranular interaction and heating due to binder deformation and crack face friction) occur much behind the initial stress wave front. This results in severe temperature rises of the order of 300 – 400 K in the grains. High temperature rises also occur in the binder phase, but are lower than those in the grains.

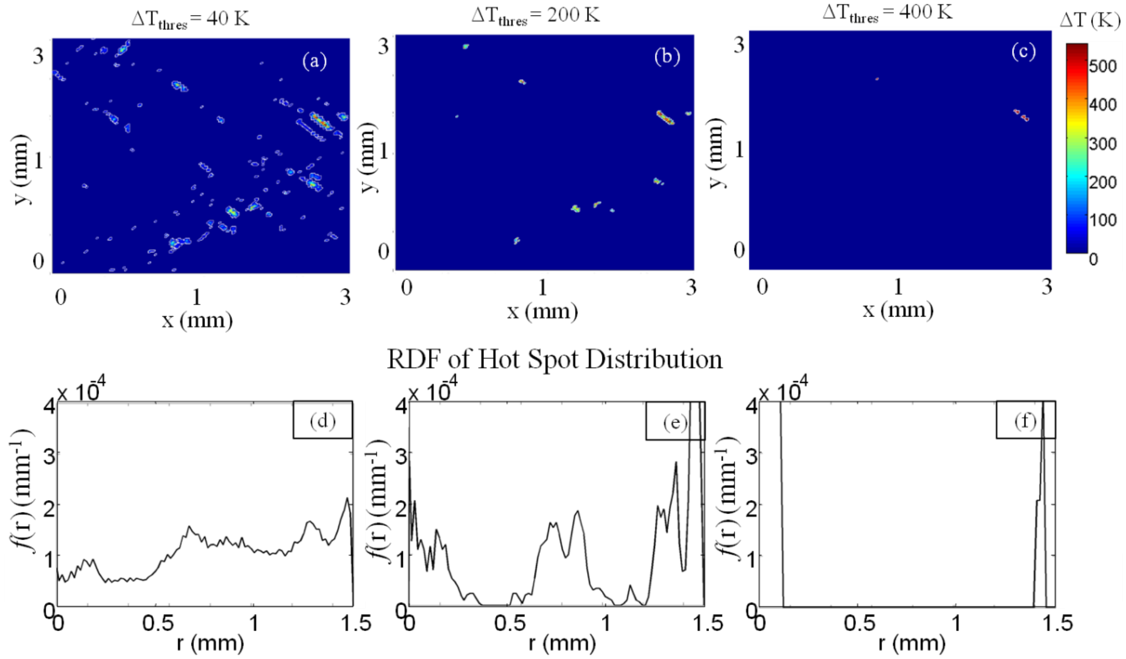

Figure 66: Distribution of hotspots obtained using different temperature thresholds (a) 40 K, (b) 200 K and (c) 400 K and the corresponding RDFs at (d) 40 K, (e) 200 K and (f) 400 K (PBX, $\eta = 0.82$, $v = 100$ ms^{-1}, $\dot{\varepsilon} = 33.3 \times 10^{3}$ s^{-1}).

The dominant mechanism responsible for hotpot formation under the conditions analyzed is frictional dissipation as a result of grain fracture. In [112], the authors quantified the evolution of fracture energy. An analysis of the spatial distribution of fracture energy showed that the maximum fracture dissipation occurs near the impact face and gradually decreases to zero at the front of the stress wave. This causes the highest temperature increases to occur near the impact face as seen in Figure 64.

Figure 65(a-b) show the distribution of temperature in a long GX sample with a packing density of η = 0.82 at $t = 4.0 - 6.0\ \mu$s. The impact velocity is v = 100 ms^{-1}. Similar to those in the PBX, the temperature rises are highest near the impact surface. However, due to the absence of any binder, more intergranular interactions occur, resulting in significantly higher hotspot density (number of hotspots per unit area). Quantifications of the hotspot distributions are presented in Sections 5.8.4 and 5.8.5.

The responses of the short [loading configuration in Figure 10(c)] and long samples [loading configuration in Figure 11(a)] are significantly different. For both GX and PBX, the shorter samples experience more uniform temperature rises as a result of multiple stress wave reflections. On the other hand, in the longer samples the temperature decreases with distance from the loading surface. The overall more uniform hotspot distributions in the smaller samples can be more directly correlated to the initial microstructure and loading conditions. In subsequent discussions on characterizations of the temperature fields and size distributions of the hotspots, the focus is primarily on calculations using loading configuration in Figure 10(c).

5.7.4 RDF and Hotspot Size Distributions

The temperature field at any given time has local peaks or hotspots. The individual hotspots can be extracted from the continuous temperature fields using the threshold scheme discussed in Section 5.4. To illustrate this scheme, Figure 66(a-c) show the hotspot distribution in a PBX microstructure with a packing density of η = 0.82 at $t = 3.6\ \mu$s. The impact velocity is v = 100 ms^{-1}. The hotspot fields in Figure 66(a-c) are obtained using three temperature thresholds of $\Delta T_{thres} = 40, 200 \text{ and } 400\,\mathrm{K}$, respectively. At a low threshold of $\Delta T_{thres} = 40\,\mathrm{K}$, the hotspots are in the form of bands [Figure 66(a)]. At the higher ΔT_{thres} values, the hotspots become more distinct and sparse. At a high threshold of $\Delta T_{thres} = 400\,\mathrm{K}$, only two hotspots remain [Figure 66(c)]. The images clearly show that while hotspot development is extensive throughout the microstructure, only a relatively small number of hotspots have the highest temperatures. It is these highest temperature hotspots that control the ignition process. Since the occurrence of these dominant hotspots is stochastic, it is important to account for the statistical nature of the ignition process resulting from it. The treatment using a critical hotspot density in Section 5.5 reflects this consideration. Although simple, it represents a step in the right direction. Further development should certainly be considered in the future.

The RDFs corresponding to the hotspot distributions in Figure 66(a-c) are shown in Figure 66(d-f). At $\Delta T_{thres} = 40\,\mathrm{K}$, the RDF is continuous and does not indicate any distinct hotspots. This indicates that most of the hotspots are still connected [see Figure 66(a)]. At a threshold of $\Delta T_{thres} = 200\,\mathrm{K}$, the RDF profile first reaches zero at r ~ 0.3 mm, which is the diameter of the largest hotspot. The next peak of the RDF occurs around r = 0.6 mm. This is the average spacing between the first near neighboring hotspots. Finally, at $\Delta T_{thres} = 400\,\mathrm{K}$, there are only two hotspots remaining [see Figure 66(c)] and the RDF [Figure 66(f)] clearly shows the size of the largest hotspot and the distance between the two.

Equivalent Diameter Scheme

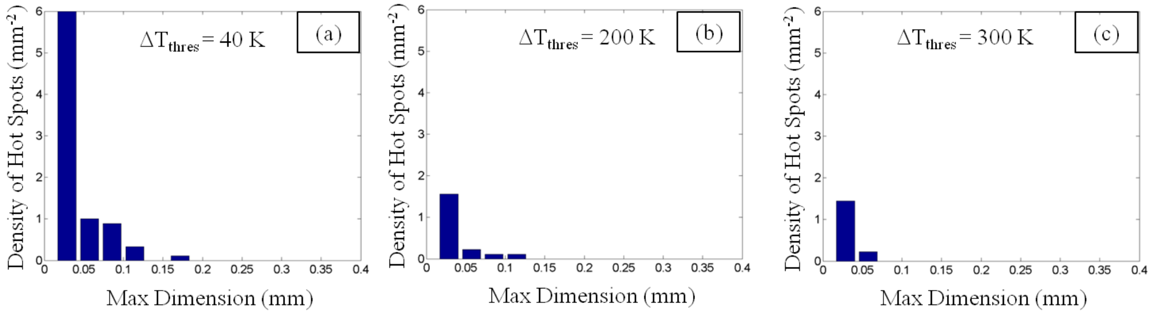

Maximum Size Scheme

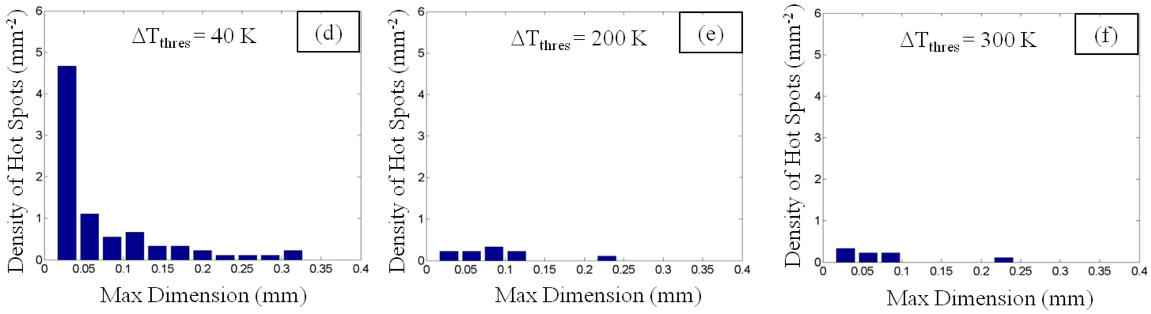

Figure 67: Size distributions of hotspot in HMX granules obtained using the diameter of a circle of equal area for different temperature thresholds (a) 40 K, (b) 200 K and (c) 400 K, and using the maximum dimension for different temperature thresholds (d) 50 K, (e) 200 K and (f) 400 K

(PBX, η = 0.82, v = 100 ms^{-1}, $\dot{\varepsilon}$ = 33.3$\times$10^{3} s^{-1}).

The morphologies of hotspots are distinct and varied. This can influence the ignition threshold and subsequent burn. Previous studies [5, 29], have analyzed the effect of hotspot shapes on the ignition threshold and the time to ignition. Specifically, Tarver et al. [29] analyzed hotspots of three different geometries and found that the critical temperature was not significantly affected by the hotspot shape. However, in a microstructural setting, the shape of the hotspots may significantly influence the connectivity of neighboring hotspots. For example, elongated hotspots may result in the formation of high temperature bands [Figure 66(a)]. This can significantly affect the propagation of reaction subsequent to ignition.

To quantify the variation of hotspot shapes, the ED and MS schemes are used to determine the hotspot distributions for the calculations shown in Figure 66. Figure 67(a-c), show the size distributions obtained using the ED scheme and Figure 67(d-f) show the corresponding size distributions using the MS scheme. Clearly, a higher density of larger-size hotspots is detected using the MS scheme. As an example of the difference in results, at a threshold of $\Delta T_{thres} = 200\,\mathrm{K}$ the maximum hotspot size using the ED scheme is ~0.1 mm while that obtained using the MS scheme is ~0.2 mm. The size of the largest hotspot predicted by the RDF [Figure 66(d-f)] is almost identical to hotspot sizes obtained using the MS scheme [Figure 67(d-f)]. However, it is noted that the overall density of the hotspots are similar in both cases. In the subsequent analysis, the MS scheme is used to quantify the size of hotspots, since it provides the largest dimensions of the hotspots and can be correlated more readily with information from the RDFs.

5.7.5 Effect of Initial Porosity

Porosity is present in all GXs and has a significant influence on their impact sensitivities [126-127]. In applications, it is desirable to have lower porosity for higher energy output. The effect of porosity is analyzed by deforming three GX microstructures having initial volume fractions of η = 0.60, 0.70 and 0.82 [Figure 60(b, e-f)], respectively. Figure 68(a-c) show the distribution of temperature at t = 5.4 μs. The impact velocity is v = 100 ms^{-1}. The calculations are performed using loading configuration in Figure 10(c), with v_L = 0. Clearly, the temperature increases with η for the same value of overall strain. For η = 0.60, the temperature increases are low and only occurs at locations of grain-grain interactions. Higher volume fractions decrease the initial porosity, thereby enhancing grains-grain interactions and transgranular fracture. The overall effective wave speed also increases with the volume fraction. Consequently, under the same impact velocity microstructures having higher grain volume fractions experience high temperature increases over a larger domain.

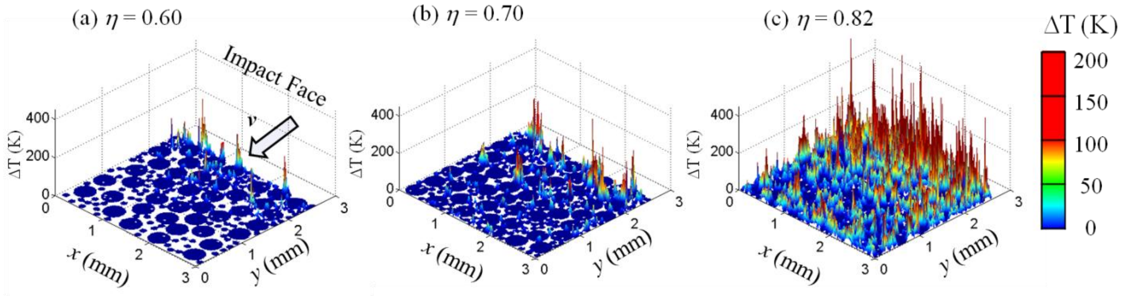

Figure 68: Distribution of hotspots in GX with different initial volume fractions: (a) η = 0.60, (b) η = 0.70, and (c) η = 0.82, (Bimodal GX, d = 120 – 360 μm, v = 100 ms^{-1}, $\dot{\varepsilon}$ = 33.3$\times$10^3 s^{-1}, t = 5.4 μs).

The distributions of hotspots are distinct for each value of porosity. To analyze the effect of initial porosity, Figure 69(a-c) show the RDFs and Figure 69(d-f) show the size distributions for the three calculations with initial volume fractions of $\eta = 0.60$, 0.70 and 0.82 at $t = 10.8$, 7.6 and $5.2\mu s$, respectively. The time at which the RDFs and size distributions are obtained correspond to the critical time for ignition (to be discussed in more detail later) t_c for each of the microstructures at an impact velocity of $v = 100\,\mathrm{ms}^{-1}$. The RDFs show the formation of distinct hotspots with an average hotspot spacing of ~0.6 mm. The maximum hotspot size and average distance between hotspots show no appreciable variation with the initial volume fraction. This indicates that the initial porosity does affect the spatial distribution of hotspots at t_c. Rather, it is the size and size distribution of the granules that set the scale for the spacing between hotspots for GXs. The hotspot size distributions are also similar for the different porosities analyzed, indicating that the heating is primarily due to fracture and frictional dissipation occurring when the GX is pressed to higher densities. It should be noted that this result is for impact velocities in the range between $v = 50$ and $250\,\mathrm{ms}^{-1}$, and may not be applicable to scenarios with much higher impact velocities (e.g., during shock loading) where additional dissipation mechanisms (such as void collapse, jetting, etc) may influence the formation of hotspots.

5.7.6 Effect of Impact Velocity

The effect of loading rate is analyzed by deforming the PBX microstructure in Figure 60(a) and the GX microstructure in Figure 60(b) at the two impact velocities of $v = 50$ and $250\,\mathrm{ms}^{-1}$. The corresponding strain rates are the range of $\dot{\varepsilon} = (16.7 - 116.7) \times 10^3$ s^{-1}. The calculations are performed on the PBX and GX microstructures using loading configuration in Figure 10(c), with $v_L = 0$. Figure 16 shows the distributions of temperature at a nominal strain of 10.0%.

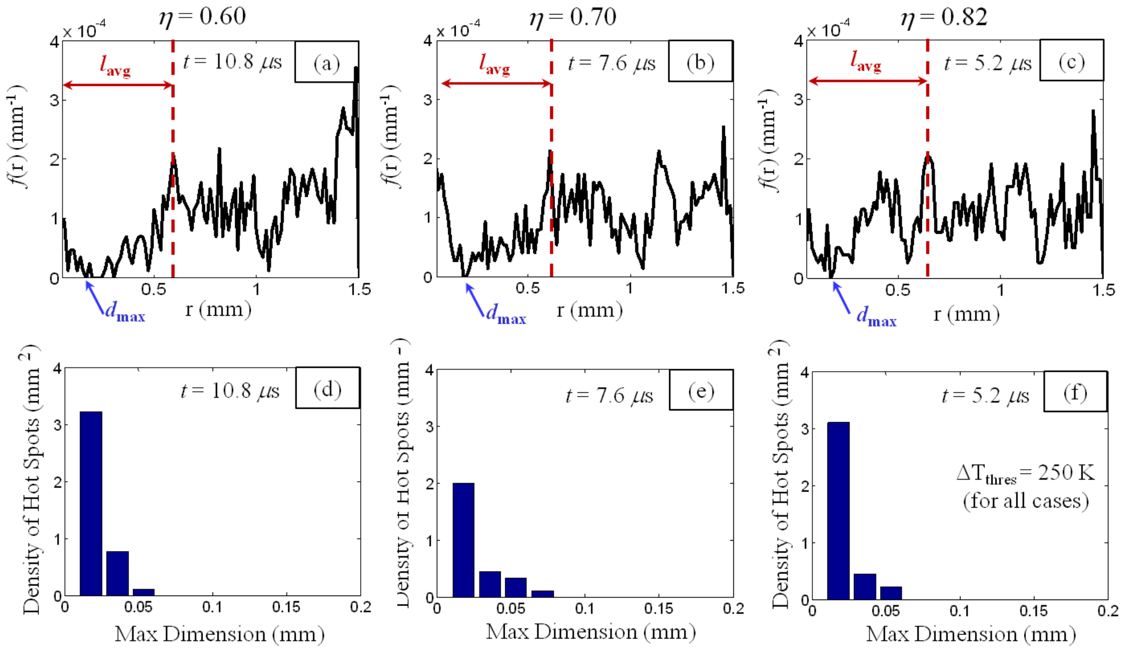

Figure 69: RDFs of the temperature field in microstructures of GX having different initial porosity levels (a) $\eta = 0.60$, (b) $\eta = 0.70$, and (c) $\eta = 0.82$, and (d – f) the corresponding hotspot size distributions obtained using the maximum dimension method (bimodal distribution GX, $v = 100$ ms^{-1}, $\dot{\varepsilon} = 33.3\times10^3$ s^{-1}).

At a low impact velocity of 50 ms^{-1}, the temperature increase in the PBX is higher than that in the GX. In the PBX, the binder is softer, allowing the temperature rise to be spread out over the entire microstructure. Additionally, the absence of any porosity in the PBX leads to higher stresses, subsequent fracture and frictional dissipation. In contrast, in the GX, rearrangement of the grains reduces the stress in the early part of loading. At later stages of loading, fragments generated from grain fracture occupy the vacant areas (pores), resulting in lower overall stresses compared to the PBX. This leads to a lower temperature increase for the GX.

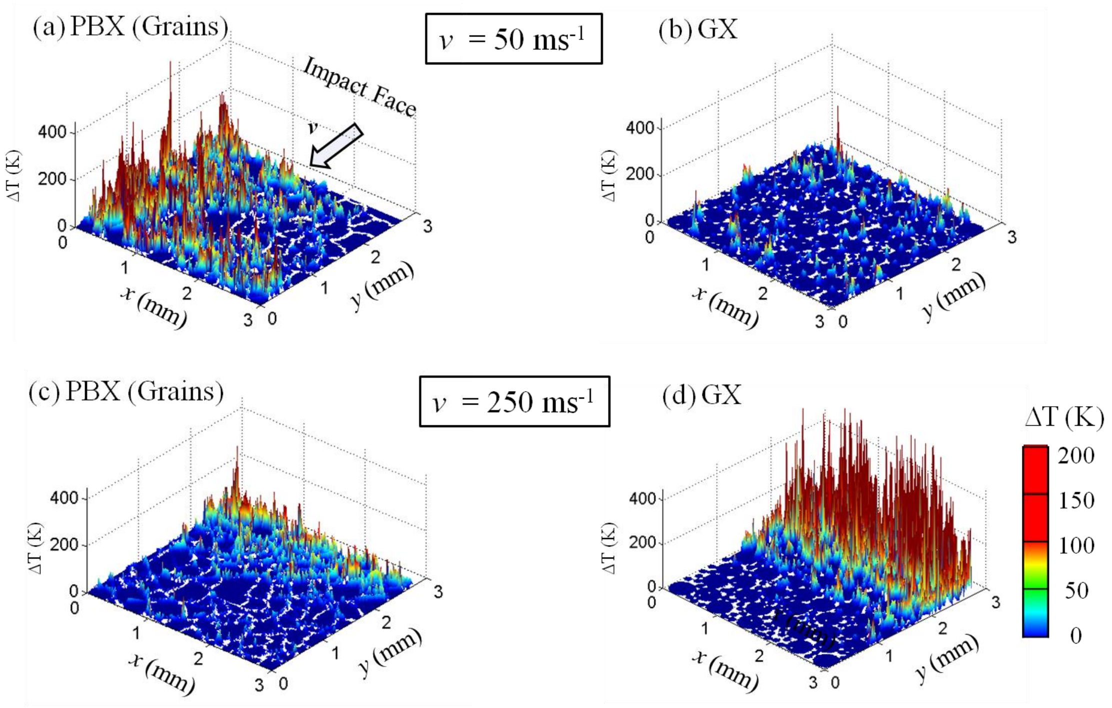

Figure 70: Distribution of hotspots in HMX at the same nominal strain of ε = 10.0 %, (a) PBX , v = 50 ms^{-1}, (b) GX, v = 50 ms^{-1}, c) PBX, v = 250 ms^{-1}, and (d) GX, v = 250 ms^{-1}, [η = 0.82, $\dot{\varepsilon}$ = (16.7 – 83.3)$\times$10^3 s^{-1}].

However, at higher impact velocities (v = 250 ms^{-1}), grain-grain interaction and transgranular fracture become the primary dissipation mechanisms even at early stages of loading. For both PBX and GX [Figure 70(c-d)], the distribution of hotspots is concentrated near the impact face where the most severe temperature increases occur. The temperature increase in the GX is higher than that in the PBX (in contrast to the behavior seen at the lower impact velocity). For the PBX, deformation of the binder reduces the stress level and prevents grain-grain interactions in the early part of loading.

On the other hand, the GX experiences grain-grain interactions and transgranular fracture immediately upon impact, which results in high temperature increases. Thus, for the conditions analyzed, the GX appears to be less sensitive at low impact velocities whereas the PBX is less sensitive at higher impact velocities.

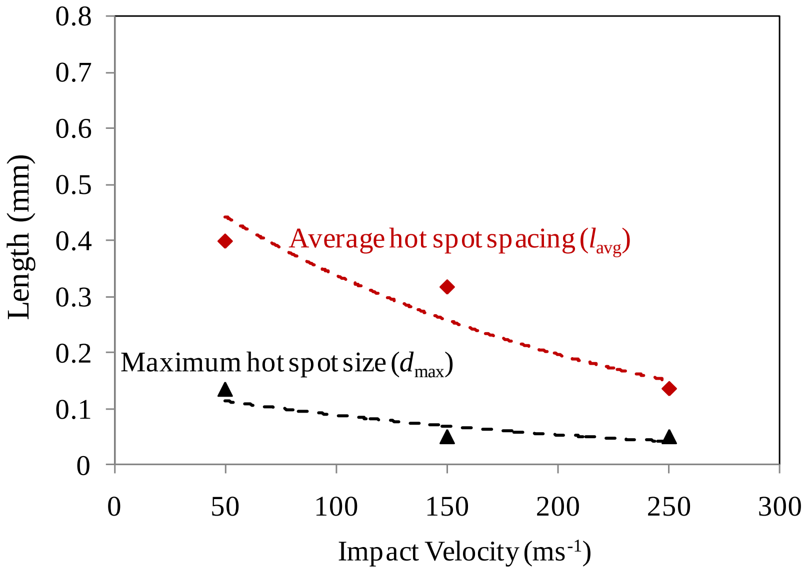

Figure 71: Effect of impact velocity on the maximum hotspot size and average hotspot spacing (η = 0.82, bimodal GX, v = 50 - 250 ms^{-1}, $\dot{\varepsilon}$ = 16.7 – 83.3$\times$10^{3} s^{-1}, ΔT_{thres} = 100 – 570 K).

The effect of loading rate on the maximum hotspot size (d_{max}) and average hotspot spacing (l_{avg}) is shown in Figure 71 for a GX with $\eta = 0.82$ at a nominal strain of 10.0%. The impact velocity is varied between $v = 50$ and $250\ \mathrm{ms}^{-1}$. The results show that d_{max} does not change significantly over $v = 50 - 150\ \mathrm{ms}^{-1}$. However, as the impact velocity increases beyond $v = 150\ \mathrm{ms}^{-1}$, d_{max} starts to decrease. This suggests that the hotspots tend to become more localized at higher loading rates. As v increases, the average hotspot spacing l_{avg} decreases approximately linearly. In the regime of $v = 50 - 250\,\mathrm{ms}^{-1}$, l_{avg} decreases by a factor of 2.5. This is due to earlier fracture and greater fragmentation of the grains at the higher impact velocities, resulting in a higher density of hotspots.

5.7.7 Effect of Grain Size Distribution

Several studies have tried to correlate the size [128], morphology [129] and surface area [130] of crystalline granules with impact sensitivity. Czerski [129] reported that there was no clear correlation between size and the sensitivities of small (~10 μm) and medium (~100 μm) sized RDX particles. Lecume [131] suggested that the surface roughness may affect impact sensitivity. The sensitivity of GX is also dependent on the strength of loading. Chakravarty [132] found that at low pressure and long duration loading waves, larger grain sizes correspond to higher impact sensitivity.

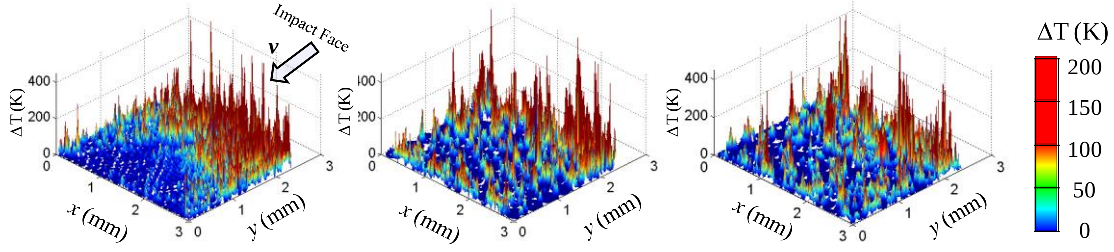
(a) Monomodal, δ = 120 μm (b) Monomodal, δ = 360 μm (c) Bimodal δ = 120, 360 μm (1:3)

Figure 72: Distribution of hotspots in GX with different grain size distributions: (a) monomodal, δ = 120 μm, (b) monomodal, δ = 360 μm, and (c) bimodal, δ = 120 – 360 μm (η = 0.70, v = 100 ms^{-1}, $\dot{\varepsilon}$ = 33.3$\times$10^{3} s^{-1}, t = 8.0 μs).

To illustrate the effect of grain size on hotspot field, three different GX microstructures having the same volume fraction (η = 0.70) are analyzed: (A) monomodal, δ = 120 μm, (B) monomodal, δ = 360 μm, and (C) bimodal, δ = 120-360 μm (henceforth referred to as microstructure A, B and C, respectively). Figure 72(a-c) show the distributions of temperature in the 3 mm square specimens, at t = 8.0 μs for an impact velocity of $v = 100\ \text{ms}^{-1}$. The temperature increases at the same amount of nominal strain are quantitatively similar for all cases, indicating that grain size may not have a significant influence on impact sensitivity.

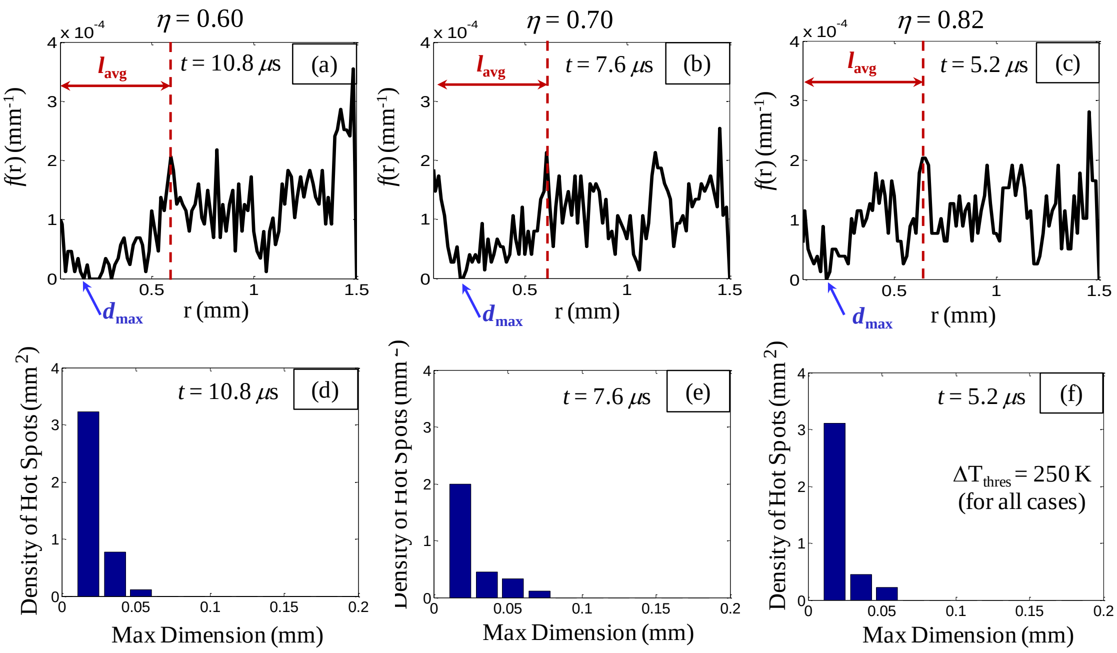

Figure 73: RDFs of the temperature fields in microstructures of GX having different grain size distributions (a) monomodal, δ = 120 μm, (b) monomodal, δ = 360 μm, and (c) bimodal, δ = 120 – 360 μm and (d – f) the corresponding hotspot size distributions obtained using the maximum dimension method (η = 0.70, v = 100 ms^{-1}, $\dot{\varepsilon} = 33.3\times10^{3}\ \text{s}^{-1}$, t = 8.0 μs).

However the spatial distributions of hotspots are affected by the grain size. Figure 73(a-c) show the RDFs and Figure 73(d-f) show the size distributions of hotspots in these microstructures at t = 8.0 μs. The RDFs show that the maximum size (0.07-0.17 μm) of hotspots increases only slightly with grain size. On the other hand, the average distance between hotspots is largest for microstructure C (0.53 μm), followed by B (0.18 μm) and A (0.13 μm). The issue relates to the temperature distributions shown in Figure 72(a-c). In the case of (A), the fragmentation of the small grains (δ = 120 μm) and subsequent frictional dissipation at the fracture surfaces result in hotspots forming very close to each other. The average distance between hotspots is low and of the order of the maximum size of hotspots (~0.15-0.2 mm). In the case of (B), which is composed of larger grains (δ = 360 μm), hotspots primarily form at locations of grain-grain interactions, rather than due to complete crushing of the grains. however, fragmentation of grains results in multiple hotspots forming close to each other, which leads to an average hotspot spacing of ~0.25 mm (in comparison, the grain size is 0.36 mm). For (C), which has a bimodal distribution of grains, hotspots arise due to the crushing of the smaller grains. The average spacing between these hotspots (~0.6 mm) is consequently influenced by the distribution of the larger grains.

Figure 74 shows the maximum hotspot size (d_{max}) and average hotspot spacing (l_{avg}) for microstructures A, B and C at t = 5.4 μs. The impact velocity is $v = 100\,\mathrm{ms}^{-1}$. Note that for each microstructure, multiple random instantiations are used, yielding the ranges of data shown. Clearly, d_{max} is varies only slight among the cases, suggesting that ignition sensitivity is not significantly affected by grain size. On the other hand, l_{avg}

increases significantly with grain size, with the bimodal distribution shows highest l_{avg} than both monomodal size distributions. Obviously, the issue is a complex one.

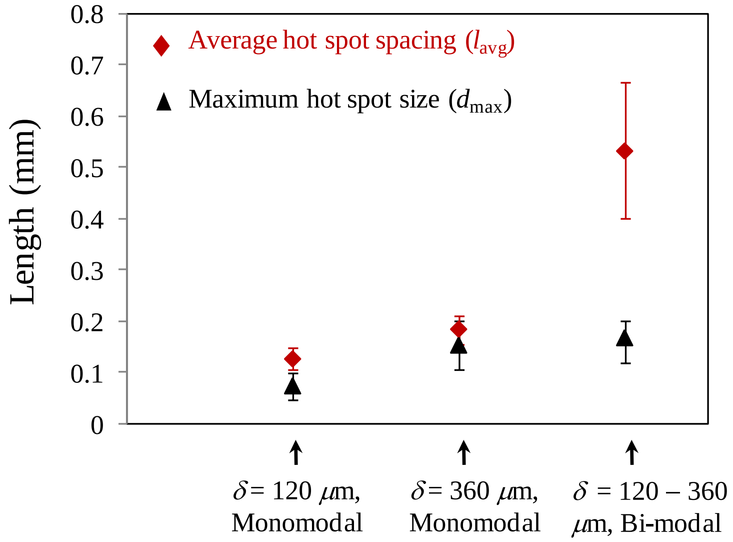

Figure 74: Effect of grain size on the maximum hotspot size and average hotspot spacing [GX in Figure 60(c-d, f)], η = 0.70, v = 100 ms^{-1}, $\dot{\varepsilon}$ = 33.3 $\times 10^{3}$ s^{-1}).

In currently available ignition theories, while the size of hotspots is considered very important, inter-hotspot distance is explicitly not considered. Indeed, it must be noted that the thermal ignition criteria presented in Section 5.2 does not account for spacing in between hotspots. However, it is generally accepted that the spatial arrangement of hotspots influences the post ignition burn, specifically the deflagration to detonation transition (DDT) phenomena. The systematic quantification that comes out of the RDF analyses here may lead to an examination of this issue in the future. Here, only the size and temperature of hotspots are considered.

5.7.8 Connecting Hotspot Statistics to Thermal Criticality Data of Tarver et al.

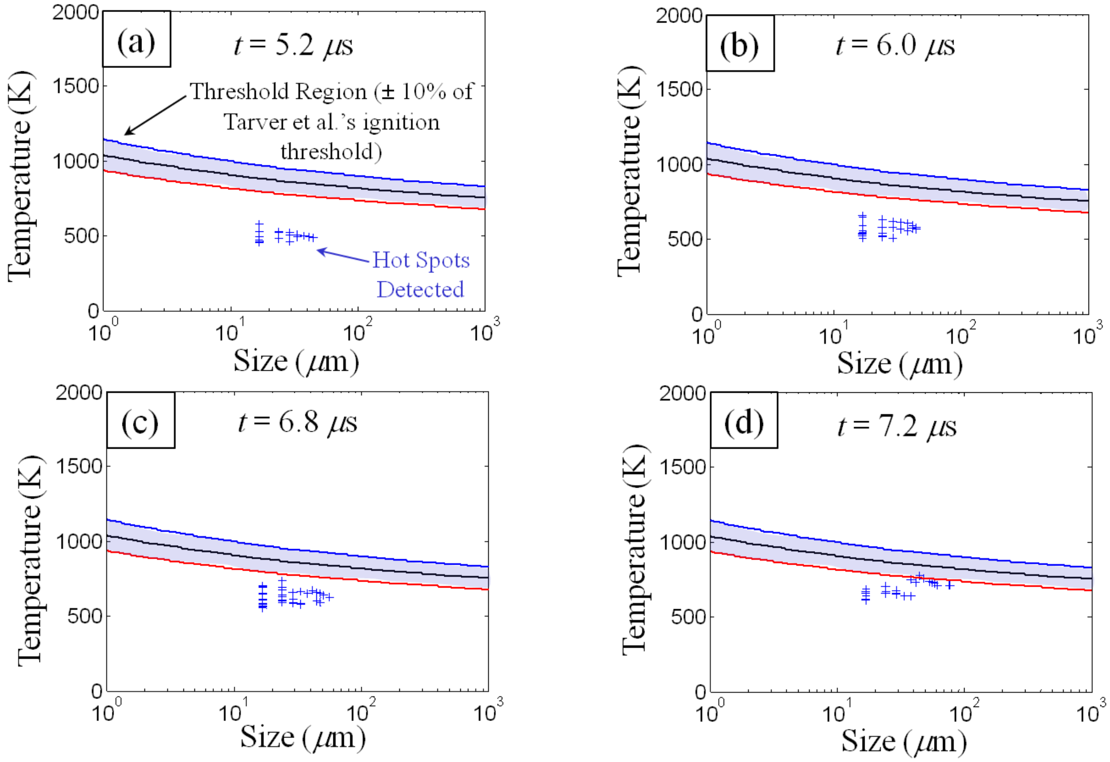

Figure 75: Size and temperature of hotspots relative to Tarver et al.'s ignition threshold at different times between *t* = 5.2 – 7.2 μs [PBX Figure 60(a)], (η = 0.82, *v* = 100 ms^{-1}).

Hotspot distributions are analyzed using the scheme presented in Section 5.3 to identify critical hotspots that may lead to ignition. To illustrate the process of how critical hotspots are identified, Figure 75(a-d) show the hotspots detected in the grains for a calculation on a PBX specimen with a HMX volume fraction of η = 0.82. The imposed boundary velocity is 100 ms^{-1}. In general, the sizes and temperatures of hotspots increase with time, as shown by the group of hotspots which move towards the threshold region for times between $t = 5.2 - 7.2\ \mu$s. The three curves denote Tarver et al.'s criticality data stated as a band of $\pm 10\%$ about the mean value, as discussed in section 5.3. A hotspot is considered to be critical when it crosses the lower threshold limit (90% of the average threshold). The figure shows that the hotspots, up to a time of $t = 6.8\ \mu$s, are below the threshold and not considered critical. At $t = 7.2\ \mu$s, the hotspots having the highest temperatures cross the lower threshold. Once the criterion outlined in Section 5.3 is satisfied, the material is assumed to have reached the critical state for thermal runaway. The time (measured from the beginning of loading) at which this is taken as the time to criticality (t_c) and is obtained for different cases of impact velocity, grain volume fraction and size distribution.

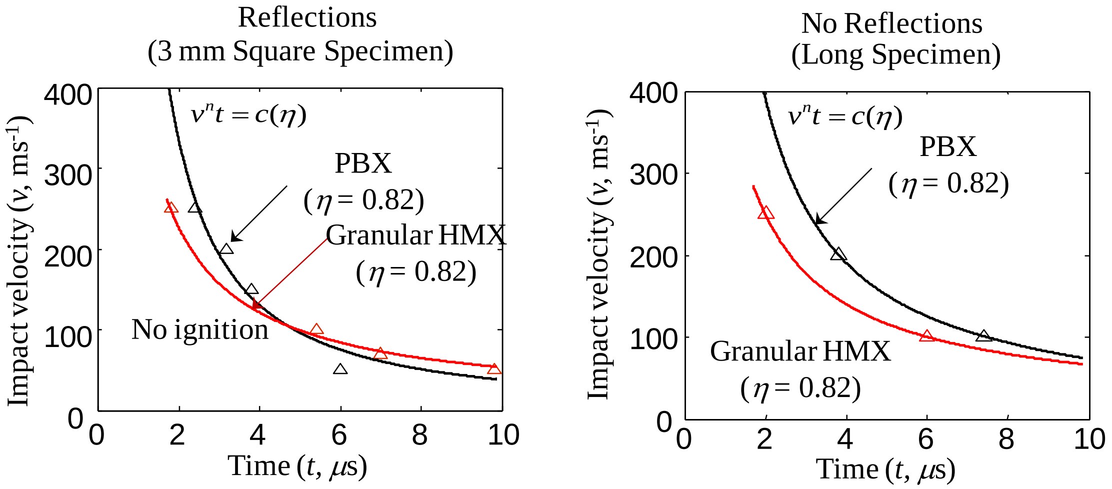

(a) (b)

Figure 76: Time to criticality for PBX and GX using (a) 3 mm square specimen and (b) long specimen (η = 0.82, v = 50 – 250 ms^{-1}).

Figure 76(a) shows the variation of critical time t_c with boundary velocity v for PBX and GX microstructures having an initial volume fraction of η = 0.82 [Figure 60(a-b)]. The calculations are performed for a range of impact velocities between

$v = 50$ and $250\ \mathrm{ms}^{-1}$, using loading configuration in Figure 10(c). The results are fitted to a curve of the form $v^n t = c(\eta)$ to illustrate the overall trends. Here, $c(\eta)$ is a function of initial porosity. In general, for both PBX and GX, as the boundary velocity increases, the time to criticality decreases. This is similar to the shock response of explosives [1, 133-134].

At high impact velocities $(v > 100\ \mathrm{ms}^{-1})$, the time to criticality for the PBX is 2-4 times that for the GX. This is supported by the results presented in Section 5.8.6. In the case of the PBX, the binder deforms to absorb the loading due to the impact, thereby preventing direct grain-grain interactions and minimize fracture during the initial stages of loading. On the other hand, at lower impact velocities $(v < 100\ \mathrm{ms}^{-1})$, the PBX is more sensitive than the GX and has a lower time to criticality. This is due to the higher confinement stresses which arise from the lack of room for compaction, leading to greater fracture and higher temperature rises in the grains. Another aspect of the loading which may contribute to the difference in the sensitivities of PBX and GX is the thickness of the stress wave front. This rise time is smaller for the PBX than for the GX. This difference is more pronounced at lower impact velocities.

For the loading configuration used and over the range of conditions analyzed, t_c continues to decrease as v increases Figure 76(a)] and there appears to be a minimum time required for ignition regardless of impact velocity. On the other hand, the range of data does not appear to suggest the existence of a low velocity cutoff below which no ignition occurs. One possible explanation is that the successive wave reflections from the top and bottom surfaces [Figure 10(c)], leads to continuing accumulation of elastic strain energy in the specimen. This accumulation can lead to sudden fracture and frictional dissipation with sustained loading, causing high temperature rises even at low impact velocities.

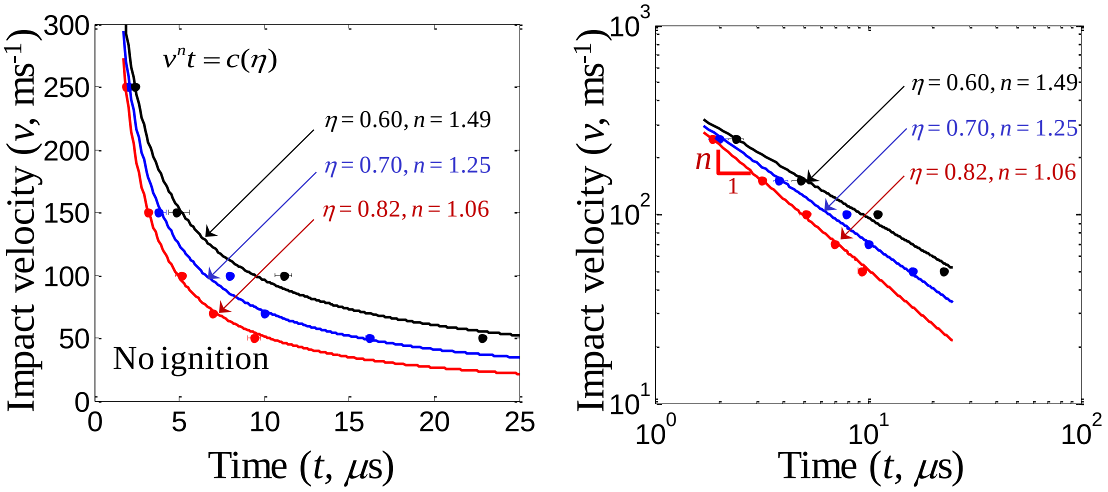

(a) (b)

Figure 77: Time to criticality for GX having a range of initial grain volume fractions η = 0.60 – 0.82, plotted using (a) linear scale (b) log-log scale (η = 0.70 – 0.82, v = 50 – 250 ms^{-1}).

Figure 76(b) shows the results of calculations having the same initial conditions as those in Figure 76(a), but for loading configuration in Figure 11(a). Two important differences are clear in the responses of the short and long samples. First, in the calculations using the long specimen [Figure 11(a)] the PBX is always less sensitive than the GX. However, the difference in sensitivities of the PBX and GX increases with the impact velocity, suggesting that the protective effect of the binder in the PBX is more pronounced under severe loading. Second, for a long specimen no critical hotspots are obtained at impact velocities lower than 100 ms^{-1}. This indicates the existence of a minimum velocity below which no critical hotspot (and, therefore, no ignition) occurs.

The existence of the lower velocity threshold can be explained on the basis of the constant strength of the stress wave behind the initial wave front. Since there is no wave reflection, no significant temperature increase occurs in the grains once the stress wave has passed.

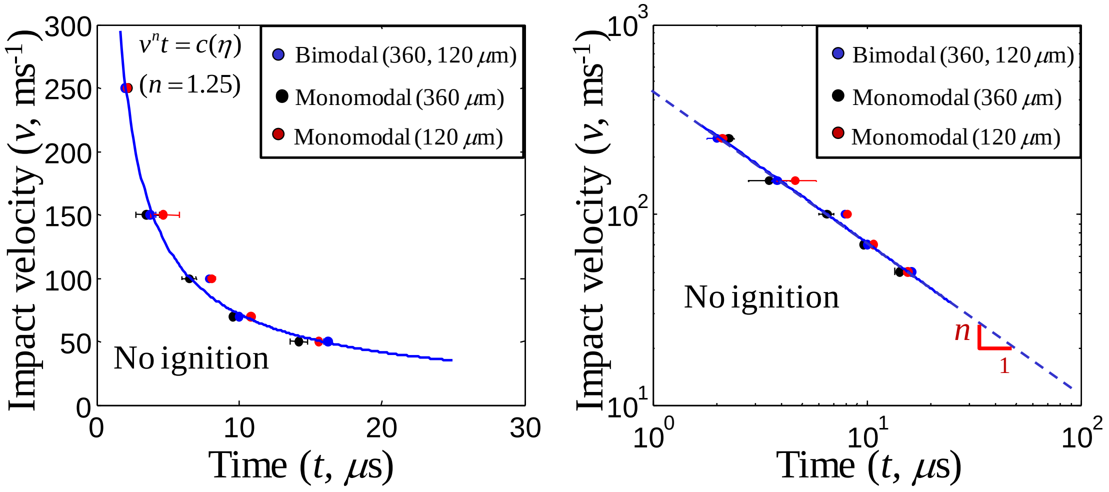

(a)

(b)

Figure 78: Time to criticality for GXs having different grain size distributions: monomodal, δ = 120 μm, δ = 360 μm, and bimodal, δ = 120 – 360 μm, plotted using (a) linear scale (b) log-log scale (η = 0.70, v = 50 – 250 ms^{-1}).

The effect of porosity is analyzed by comparing the criticality response of three GX microstructures having initial volume fractions of η = 0.60, 0.70 and 0.82 [Figure 60(b, e-f)]. Figure 77(a-b) show the variation of the critical time t_c as a function of the boundary velocity, which is varied between $v = 50$ and 250 ms^{-1}. The calculations are performed using loading configuration in Figure 10(c). Overall, the higher the initial volume fraction η, the more sensitive is the GX. The variation in response with η is small at high impact velocities, with a delay time of t_c ~4 μs for all values of η

considered. The similarity in response is due to the fact that at high impact velocities, grain fracture (and fragmentation) occurs almost immediately upon impact, leading to high temperature increases in the grains near the impact surface. However, the sensitivity is significantly different at low impact velocities, with a critical time of $t_c = 9.0 \text{ and } 23.0\ \mu\text{s}$, for $\eta = 0.60$ and 0.82 respectively, for impact velocity $v = 50\ \text{ms}^{-1}$.

The effect of grain size on criticality is investigated using microstructures A, B and C (defined in Section 5.8.7). Figure 78(a-b) show the variation of the critical time, t_c as a function of the boundary velocity, which is varied between $v = 50 \text{ and } 250\ \text{ms}^{-1}$. The two plots show the data in both linear and logarithmic scales, allowing the trends and key parameters to be identified easily. The calculations are performed using loading configuration in Figure 10(c). The time to criticality for all three microstructures A, B and C overlap each other, indicating that the grain size distribution (monomodal, bimodal) does not affect the ignition sensitivity. This is also indicated by the hotspot distribution in the microstructures [see Figure 72(a-c)] which shows similar temperature increases for all cases. In all cases, the dominant heating mechanism is sliding friction at grain boundaries and at surfaces generated by grain fracture. It is noted that at higher load intensities including shock loading, there may be additional mechanisms (such as dislocations, phase transformation, and collapse of voids or defects) which may cause the response to be more sensitive to grain size or grain size distribution. Such factors are not considered here.

5.7.9 Critical Input Energy at Ignition

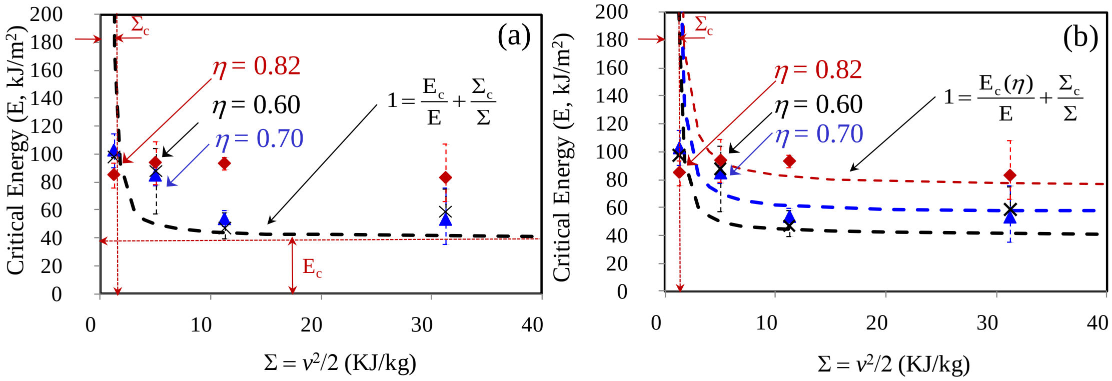

Figure 79: Critical input energy as a function of Σ for GXs with grain volume fractions between η = 0.60 – 0.82, the impact velocities are between v = 50–250 ms^{-1}.

One of the measures for assessing the impact sensitivity of an energetic material is the critical input energy E which is the energy absorbed by or imparted to the material per unit contact area up to the critical time of ignition t_c. Impact resulting in transfer of energy higher than E will lead to detonation [1, 46]. Thus the critical energy lends itself to being used as a parameter in empirical criteria for identifying conditions under which an explosive will ignite. In case of shock, the critical energy is found to be dependent on the shock velocity, shock pressure and shock duration [1]. However, for impact loading not leading to shock, energy localization is significantly affected by microstructural heterogeneity and grain level failure mechanisms. It is, therefore, important to recognize the difference and quantify the effects properly.

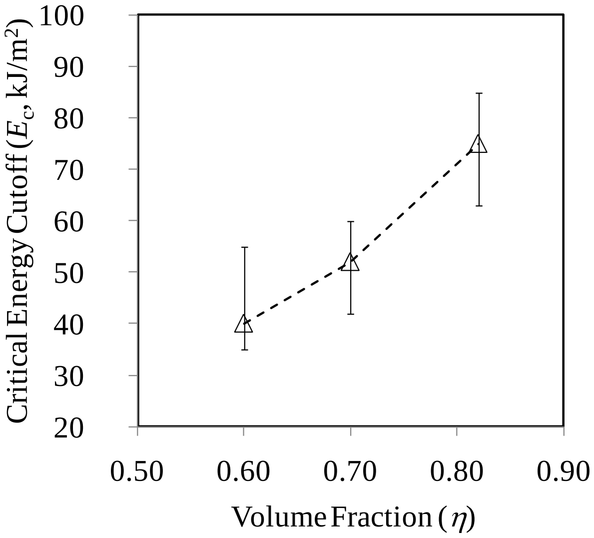

Figure 80: Critical input energy cutoff (E_c) as a function of η for GXs with grain volume fractions between η = 0.60 – 0.82, the impact velocities are between v = 50 – 250 ms^{-1}.

To analyze the effect of initial porosity of GX in this regard, Figure 79(a) shows the variation of the critical input energy as a function of $\Sigma = (v/2)^2$ for three calculations with GXs having initial volume fractions of $\eta = 0.60, 0.70$ and 0.82 [microstructures in Figure 60(b, e-f)]. The impact velocity is varied between $v = 50$ and $250\ \text{ms}^{-1}$. For $\eta = 0.60$ and 0.70, the critical energy absorbed is approximately the same. Overall, E decreases as the impact velocity increases for $\eta = 0.60$ and 0.70, but does not show significant variation with impact velocity for η = 0.82. For the higher porosities $(\eta = 0.60$ and $0.70)$, the grains need to be sufficiently compacted before fracture (and, therefore, the frictional dissipation which leads to higher temperatures) initiates. Consequently, at lower impact velocities, higher amounts of energy need to imparted to the specimen to achieve criticality. At higher impact velocities $(v \geq 250\,\mathrm{ms}^{-1})$, fracture occurs earlier, hence critical hotspots are generated at a lower energy threshold. On the other hand, for η = 0.82, the energy absorbed by the GX is similar at all impact velocities considered. This is likely due to the fact that, at higher volume fractions, intergranular friction and grain failure occur early. Consequently, most input energy is expended on causing failure. As a result, no significant impact velocity dependence of the critical input energy is seen.

James [1] earlier proposed an energy cutoff E_c within this context for explosives subject to shock loading. The particular form he used to characterize experimental data with this cutoff in mind is

$$1 = \frac{E_\mathrm{c}}{E} + \frac{\Sigma_\mathrm{c}}{\Sigma}, \tag{5.6}$$

where E_c is the cutoff input energy below which no ignition occurs and Σ_c is a cutoff velocity (or kinetic energy) measure below which an infinite amount of input energy is required. Equation (5.6) is henceforth referred to as the HJ relation. The reasoning behind the cutoffs in the HJ relation is that experimental data tend to asymptote towards E_c and Σ_c at very high and very how impact velocities, respectively [1]. Figure 79(a) also shows Equation (5.6) (black line) as a fit to the CFEM results for all the cases analyzed. The curve appears to be able to describe the data in the high and low velocity regimes for low volume fraction (η = 0.60), but considerably under-predicts the response (predicts ignition threshold values lower than the data points) for η = 0.70-0.82. Obviously, the data suggests a strong influence of microstructure on behavior and there is no master curve that can represent the response of materials with different microstructures.

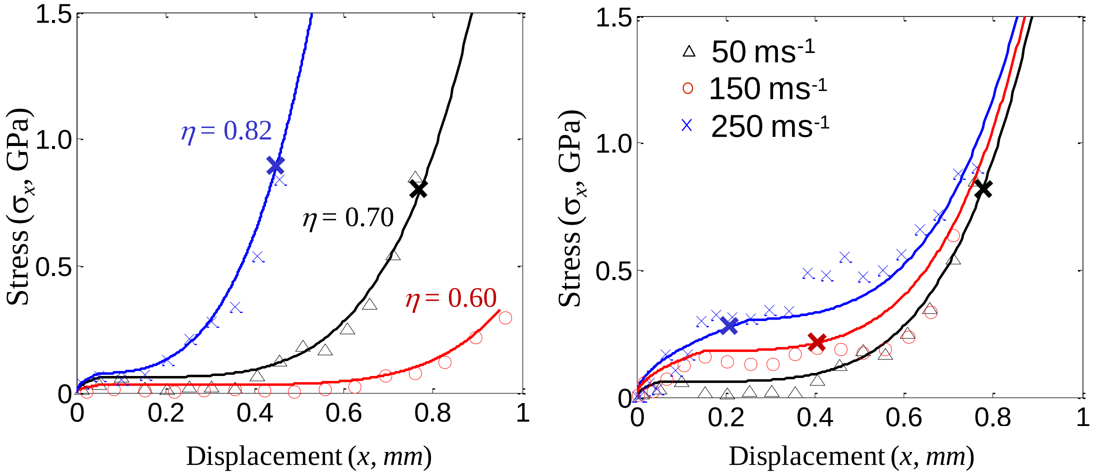

(a) (b)

Figure 81: Histories of stress for GXs (a) with grain volume fractions between η = 0.60 – 082 (v = 50 ms^{-1}, $\dot{\varepsilon} = 33.3\times10^3$ s^{-1}); and (b) under loading at impact velocities between v = 50 – 250 ms^{-1} (η = 0.70); the crosses show the points where criticality is reached.

To account the effect of the initial porosity, a microstructure-sensitive interpretation of Eq. (5.6) is used. Specifically, E_c is taken as a function of the initial porosity, leading to a modified HJ relation of the form,

$$1 = \frac{E_c(\eta)}{E} + \frac{\Sigma_c}{\Sigma}. \tag{5.7}$$

Equation (5.7) is fitted to the CFEM data for each initial porosity η level, as shown in Figure 79(b). E_c is obtained as a function of η from the fit. For the range of volume fractions and impact velocities considered, Eq. (5.7) provides a good fit to the

CFEM results. This shows that the modified HJ relation can be used to incorporate the effect of porosity (microstructure) in the description of the *E*-*v* relation.

The variation of E_c with η, is shown in Figure 80 for the three GX microstructures having initial volume fractions of η = 0.60, 0.70 and 0.82 [Figure 60(b, e-f)]. Overall, E_c increases approximately linearly with η, reflecting the fact that higher amounts of energy are absorbed by materials with higher packing densities prior to criticality in general. This can be explained by the trend in the time to criticality (t_c) curves for different microstructures at high impact velocities [see Figure 77(a-b)]. Since t_c does not change significantly with porosity (at high impact velocity), the energy absorbed E_c increases with volume fraction.

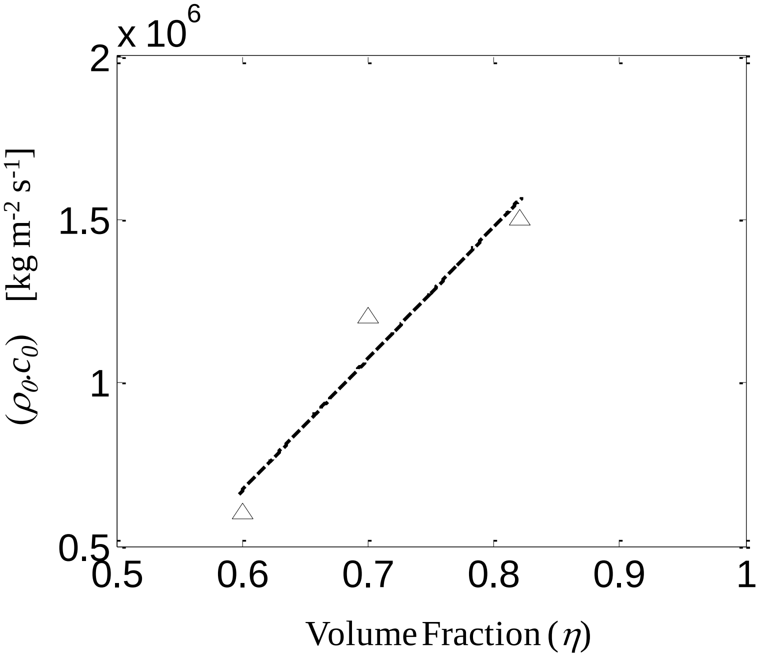

Figure 82: Variation of $\rho_0 c_0$ for GXs with grain volume fraction.

5.7.10 Time to Criticality and Critical Input Energy

Along with the critical input energy, the time to criticality is another parameter associated with the behavior of energetic materials. These two parameters are not independent of each other, rather, they are related. Together, they provide two perceptives toward the same phenomenon. Now the time required to reach thermal runaway t_c is considered.

For shock loading, the Rankine-Hugoniot is used to relate shock pressure to impact velocity. The shock pressure is assumed to be constant over the duration of interest. The issue is more complicated for non-shock loading. For small samples [loading configuration in Figure 10(c)], the stress in the loading direction varies with time and depends on microstructure and loading rate. This requires the history of stress to be quantified.

Hayes and Mitchell [23] suggested that material response during the compaction process is similar to that in a process involving phase changes, with the following characteristics:

1) an initial low–pressure region, where the response is elastic, followed by
2) a mixed-phase region where crushing of granules occur, and finally
3) a high-pressure region where the material is fully compacted.

Figure 81(a) shows the stress (σ_{ext}) as a function of displacement (x) of the loading surface, for GX microstructures with η = 0.60, 070 and 0.82. The impact velocity is $v = 100\ \text{ms}^{-1}$ and the grain size distribution is bimodal with δ = 120-360 μm. After an initial delay up to which the stress is approximately constant, it starts to increase. In the latter stages of loading, the increase is exponential with displacement.

The relations for a GX with $\eta = 0.70$ at different impact velocities between $v = 50 \text{ and } 250\ \text{ms}^{-1}$ are shown in Figure 81(b). At low impact velocities $(v = 50 - 100\ \text{ms}^{-1}),$ the response is relatively less sensitive to loading rate or impact velocity, indicating that there is very little crushing of the granules upon impact. At higher impact velocities $(v \geq 150\ \text{ms}^{-1}),$ however, high stress levels are seen, even at low displacement levels $(x < 0.4\ \text{mm})$, leading to early fracture of grains and intense frictional dissipation. The stress in the low displacement regime increases with impact velocity. As seen previously in Figure 81(a), at higher levels of overall displacement, the stress increases exponentially with displacement. To analyze the loading history for small samples with wave reflections, both regimes of the stress-displacement behavior need to be considered, since criticality can occur at either loading regime, depending on the impact velocity [see Figure 81(a-b)].

For different grain volume fractions, the stress-displacement relationship can be described by

$$\sigma_x = \rho_0 c_0 v + k\left(\frac{x}{l_0}\right)^{\gamma}, \tag{5.8}$$

where x is the displacement of the loading surface, ρ_0 is the effective density, c_0 is the effective initial longitudinal stress wave speed in the porous material, k is a constant, l_0 is the initial length of the specimen and γ is a function of the initial grain volume fraction.

The values of the constants are listed in Table 7. For this set of calculations, it is found that $\gamma = 1/\eta^4$. Equation (5.8) represents the superimposition of two distinct responses of the material during loading. Specifically,

(1) the first term on the right-hand side is obtained from the Rankine-Hugoniot equation or the linear elastic response equation of a medium, it represents the stress generated due to the elastic response of the initially porous medium as a function of the impact velocity; and

(2) the second term represents the increase of stress due to compaction, including the effects of wave reverberations in the samples.

Figure 81(a-b) also show fits of Equation (5.8) to the CFEM results. The curves appear to be able to describe the data well in the high and low velocity regimes for all volume fractions considered. Note that Eq. (5.8) accounts for the effects of both the impact velocity and the initial porosity. The effect of porosity is manifested through the first term (through $\rho_0 c_0$) and the second term (through parameter $\gamma = 1/\eta^4$). The variation of $\rho_0 c_0$ with η is shown in Figure 82. Over the range of conditions analyzed, the relationship between $\rho_0 c_0$ and η is approximately linear.

The loading history [Eq. (5.8)] can be used to relate the critical input energy to the time to criticality to obtain a general relation of the form

$$f(v,t) = c(\eta), \tag{5.9}$$

where $f(v,t)$ is a function of the impact velocity and time to reach criticality. To provide an analytical evaluation of *E,* note that the input energy is

$$E = \int_{t=0}^{t} \sigma_x \mathrm{d}x(t), \tag{5.10}$$

where, *t* is time, σ_x is the stress applied on the material and *x* is the displacement of the load surface.

Equation (5.8) can be used to derive the specific form of the *v*-*t* relation described in Eq. (5.9) from the modified James relation [Eq. (5.7)]. Specifically, integrating Eq. (5.8) yields a criticality condition in terms of time [as opposed to Eq. (5.7) which is in terms of energy]. The form is

$$\left(1-\frac{2\Sigma_{\mathrm{c}}}{v^2}\right)\left[1+k(\eta)v^{1/\eta^4-1}t^{1/\eta^4}\right]v^2 t = F(E_{\mathrm{c}},\eta), \tag{5.11}$$

where $k(\eta)$ is a function of initial porosity, $F(\cdot)$ is a function of the cutoff energy E_{c} and initial porosity (see Appendix A). The derivation of Eq. (5.11) is given in Appendix A. This equation incorporates the effects of microstructure, E_{c} and impact velocity. Note that the microstructure parameter η enters into Eq. (5.11) via (1) the energy flux across the impact face [Eq. (5.10)] and (2) the dependence of E_{c} on η. For the ranges of porosity and impact velocities considered in this chapter, $\Sigma_{\mathrm{c}} \ll v^2$, hence the approximation $(1-2\Sigma_{\mathrm{c}}/v^2) \approx 1$ can be used in Eq. (5.11).

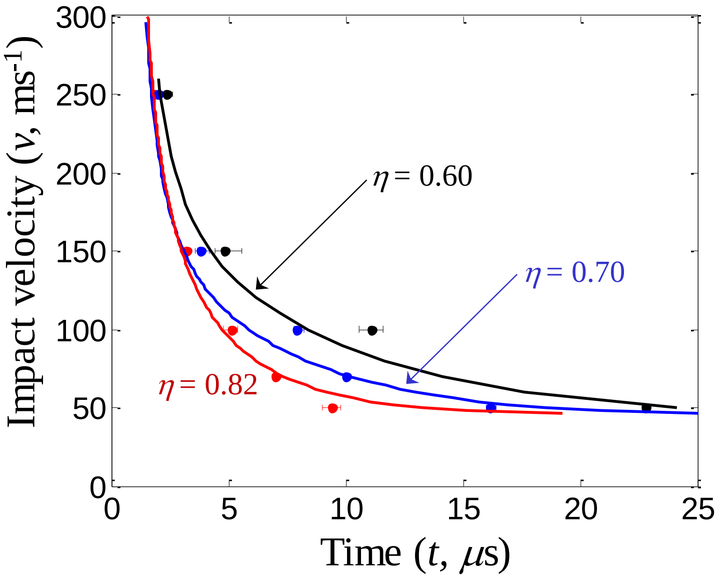

Figure 83: Relations between time to criticality and impact velocity, CFEM data and predictions of Eq. (5.11) for GX with η = 0.60 – 0.82 are shown.

Equation (5.11) provides a description of the relationship between the impact velocity and time required to reach criticality for a small sample with wave reflections. It incorporates the effects of both loading and wave reflections. Figure 83 shows the time to criticality as a function of impact velocity (the *v*-*t* relation) as predicted by Eq. (5.11) and the corresponding CFEM data (symbols) for GX with volume fractions between $\eta = 0.60 - 0.82.$ The prediction provides a reasonable description of the numerical data.

Table 7: Parameters used in Eqs. (5.6) - (5.11).

Parameter	Value	Units
k	500	GPa
l_o	3.0	mm
Σ_c	1.0	m^{2}s^{-2}

The specific form of Eq. (5.11) shown in Appendix A [Eq. (A.4)] highlights an important aspect of the material response accounted for in the modified HJ relation. At very high velocities, the first term becomes negligible. Hence the response is dominated by the second term which strongly depends on initial porosity. On the other hand, at low impact velocities, the second term becomes negligible and the response is dominated by the first term. The response in this regime is solely dependent on the impact velocity in a manner that is similar to what is seen for shock loading. The effect of microstructure is through the effective impedance $\rho_0 c_0$.

It is important to note that the term, $k(\eta)v^{1/\eta^4-1}t^{1/\eta^4}$ in Eq. (5.11) accounts for the effect of multiple wave reflections. For loading without wave reflections including loading associated with the long sample configuration in Figure 11(a) that primarily involves densification of GXs (relatively low impact velocities) and true shock loading, the second term in Eq. (5.8) can be neglected so that Eq. (5.11) reduces to the form $v^2 t = c(\eta)$. This relation is equivalent to the $P^2\tau = constant$ relation proposed by Walker and Wasley [46] for shock loading, as the particle velocity and the pressure are linearly related under such conditions.

5.8 Conclusions

This chapter has focused on two new developments.

The first is a systematic method for the characterization of hotspot fields resulting from non-shock impact loading of granular explosives (GXs) and polymer-bonded explosives (PBXs). This new method uses the radial distribution function (RDF) and yields quantifications of the distributions of the size and shape of hotspots and distances between hotspot as function of microstructures and loading.

The second development is a new criterion for establishing the ignition conditions of heterogeneous energetic materials under general conditions. This criterion, similar to a “yield” or failure criterion in mechanics of materials, links the hotspot size-temperature states in a loading event to the threshold size-temperature conditions of hotspots which are regarded as materials properties. Since hotspot quantification can be explicitly obtained through simulations (CFEM in the case of this analysis) or experiments regardless of loading and because threshold hotspot size-temperature pairs are material attributes, this criterion applies to both shock and non-shock conditions.

Both the hotspot quantification method and the new ignition criterion have been used to analyze the behavior of granular HMX and polymer-bonded HMX with different microstructures. For different loading configurations and materials, the study has yielded the critical impact velocity for ignition and critical time required for ignition as a function of material and impact velocity. The microstructural samples are from both real materials and systematic computations. The analysis also concerns different loading conditions (rates, wave reflections). The results show that fracture of energetic grains and subsequent friction along crack faces constitutes the most important heating mechanism in general.

For the PBXs at moderate and high impact velocities, grain fracture and friction are primarily responsible for heating. For the GXs, initial porosity plays the most important role in heating in terms of heating rate but not hot-spot size and spacing. In contrast, grain size of GX appears to have negligible influence on ignition. The effect of porosity is most pronounced at low impact velocities and negligible at high impact velocities when localized fracture and friction near impact face dominate.

Wave reflections from confined boundaries (associated with small samples and larger impactors) multiply stress and temperature increases, making even low velocity impact dangerous if loading is maintained over sufficiently long durations. While for large samples (no wave reflections), GX is more susceptible to ignition at all impact velocities. For small, confined samples, GX is more susceptible at high impact velocities, while PBX is more susceptible at low impact velocities, when deformed to the same level of total strain. For the range of impact velocities considered, PBX is 2-4 times safer (in terms of critical impact velocity) than HMX at high impact velocities.

The applicability of the critical input energy (E) relation proposed by James [1] for non-shock loading is examined, leading to a modified relation which is sensitive to microstructure and loading. The modified relation accounts for the variation of E_c with porosity. The relation in the v-t space accounts for the effects of both the input stress wave (compaction of material) and the reflection of the stress wave. Under the effect of the input wave only without reflections, the relation reduces to the $P^2\tau = constant$ relation of Walker and Wasley [46].

It is important to reiterate that, although the ignition criterion proposed in this chapter in theory applies to both non-shock and shock loading, the analyses so far have exclusively focused on non-shock conditions. The application to shock loading should be discussed in the future with appropriately configured computational calculations and experimental measurements of hotspot fields.

As a final observation, it must be mentioned that the stochastic nature of microstructural heterogeneities such as varying grain size and random constituent morphologies necessitate a statistical approach in the quantification of hotspot formation and the application of the ignition criterion developed here. Consequently, the issue of hotspot criticality needs to be further analyzed from a probabilistic viewpoint. This is the subject of Chapter 6.

CHAPTER 6: STOCHASTIC IGNITION MODEL

6.1 Introduction

This chapter focuses on developing a framework for computationally predicting and quantifying the stochasticity of the ignition process in PBXs under non-shock impact loading. Attention is specially focused on understanding the initiation of reaction in terms of hotspot dynamics at the grain scale and the stochasticity in macroscopic behavior. The latter feature, that is inherent in heterogeneous explosives, results from the interaction of deformation waves with material microstructure.

Terao [135] proposed a general approach for describing a variety of irreversible phenomena in a stochastic framework. The basic tenant is that fluctuations inherent in irreversible processes are not random events but are governed by the probability of the irreversible process passing the minimum entropy state. He showed that the average ignition time is related to activation energies (Hayes [23], Brill [136], and Henson [52]) and deduced a unified picture of experimental measurements through a stochastic analysis. Using this approach, Gilbert and Gonthier [137] analyzed the deformation-induced ignition response of granular HMX, by combining the temperature fields obtained from inert mesoscale calculations with a temperature threshold of 600 K to determine hotspots which have thermal runaway. One concern regarding this analysis is that it considers only the temperature and not the combined effect of the size and temperature of hotspots which is necessary for thermal runaway as shown in Tarver et al. [29]. Another inherent problem with this approach is that it does not capture the stochastic response arising out of variations in constituent properties, load condition, microstructural morphology and constituent distribution.

In this study, the focus is on the influence of microstructure geometry on the critical time to ignition and the critical impact velocity below which no ignition occurs. This is accomplished by accounting for three key issues. The first issue involves the analysis of thermal and mechanical responses of heterogeneous energetic materials at the micro-level using the framework developed in Chapter 2. The second issue has been detailed in Chapter 5 and concerns hotspot generation and an ignition criterion for the thermal runaway of critical hotspots. The third issue, the primary subject of this chapter, is the effect of random fluctuations in the microstructure geometry on the ignition response of PBX.

This issue is handled by subjecting sets of statistically similar microstructure samples to identical overall loading and characterizing the statistical distribution of the ignition responses of the samples. The quantification of this distribution as a function of microstructural attributes including grain volume fraction, grain size, specific grain-binder interface area, and the stochastic variations of these attributes is used to identify the microstructural attributes which play dominant roles in determining the ignition behavior of these materials.

This chapter is based on the work published in Ref. [138] in collaboration with Seokpum Kim and Dr. Yasuyuki Horie.

6.2 Stochastic Behavior Analyzed

In this analysis, the focus is on the stochasticity arising out of variations in microstructure geometry. The approach to assess the sensitivity of explosives combines the deterministic analysis using the micromechanical cohesive finite element method (CFEM) developed in Chapter 2 [79] and a stochastic treatment of the numerical results from a large number of microstructure instantiations. This is essentially the computational equivalent of carrying out a large number of experiments under the same conditions.

In the following analyses each sample represents a single microstructure instantiation. The method by which microstructures are generated is discussed in Section 6.2.1. A 'statistically similar set' consists of a number of microstructures having the same overall packing density η, average grain size d and grain size distribution. In addition to these attributes, the analysis also considers sets of microstructures having specified variations in the specific surface area of the grains (ΔS_v) and the grain size distribution. Specifically, the sensitivity of a particular PBX composition is evaluated by performing numerical 'experiments' on multiple instantiations of statistically similar microstructures.

The goal of this approach is to ascertain the dominant trends which relate microstructure to ignition sensitivity. Specifically, the variations at the microstructure level are related to the variations in the probability of ignition. The details of the materials analyzed are outlined in Section 6.2.1.

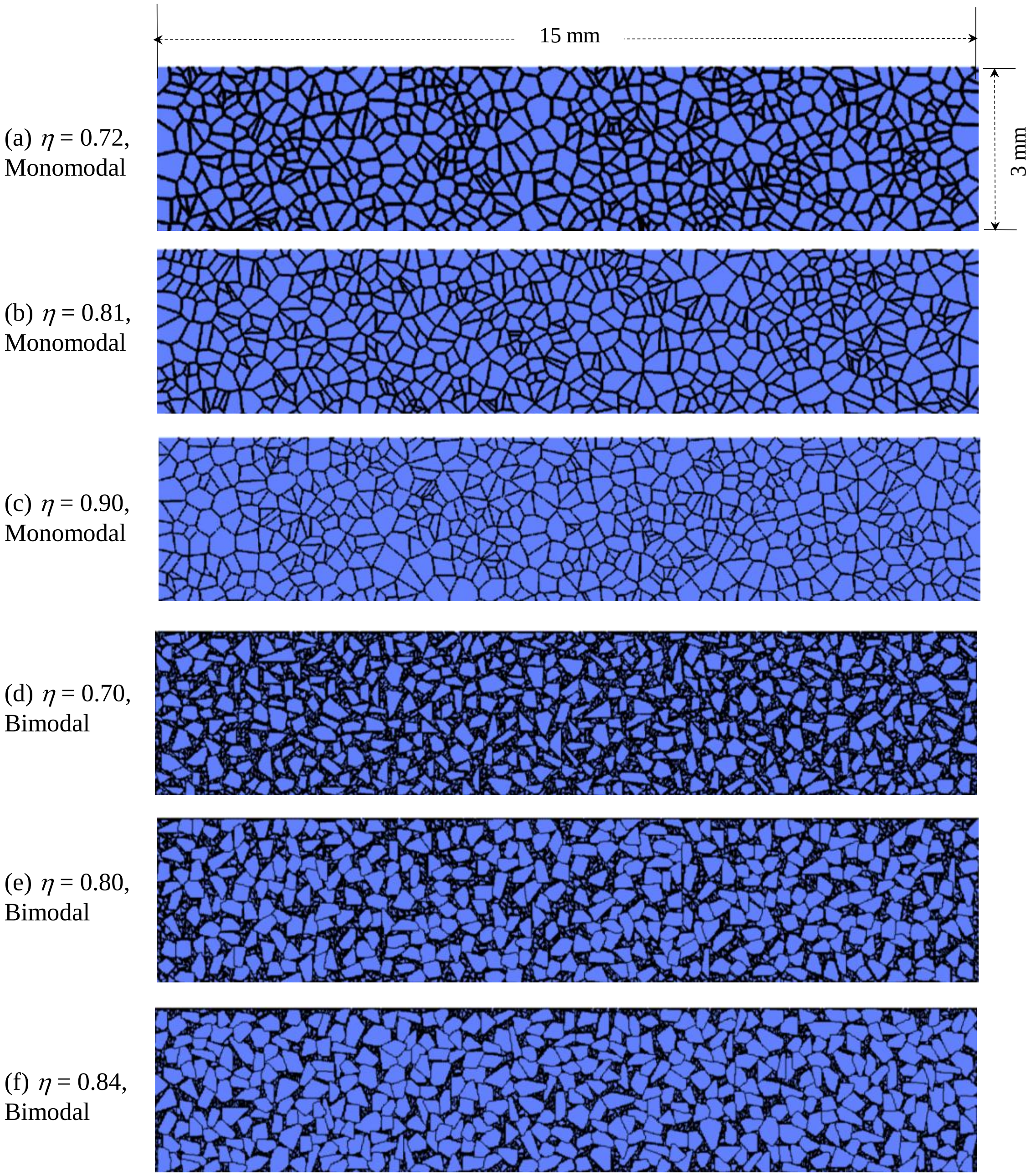

Figure 84: Microstructures with different grain volume fraction (η = 0.70 – 0.90) and grain size distributions (monomodal, bimodal).

6.3 Microstructures Analyzed

Calculations are performed on computationally-generated microstructures. However, the approach is equally applicable to scanned real microstructures as shown in Chapters 2-4. The benefits of using computationally-generated microstructures here are (1) large (>1,000) numbers of sample instantiations can be obtained and (2) sets of samples with attributes that conform to prescribed statistical distribution functions, averages and random fluctuations can be obtained in a controlled manner. These considerations are especially important for the current analyses, as will become clearer later.

Table 8: Microstructures analyzed in Chapter 6.

Microstructure	Grain volume fraction (η)	Average grain Size (μm)	Standard deviation (μm)	Average specific surface area, S_v (mm^{-1})
PBX – Monomodal	0.72	235.1	87.4	15.65
	0.81	250.1	90.0	16.38
	0.90	264.3	92.1	17.37
PBX – Bimodal	0.70	64.3 – 251.2	19.7 – 45.3	25.26
	0.80	61.0 – 301.7	21.4 – 31.6	21.06
	0.84	59.6 – 307.5	20.5 – 44.9	18.00

The microstructures generated have multifaceted grains with monomodal and bimodal distributions of sizes. The microstructures having monomodal size distributions are generated using the Voronoi tessellation function. This is a geometric method that allows the definition of a statistical sample space in a relatively straightforward way. The packing density is varied by properly altering the average thickness of the binder phase between neighboring grains. The mean grain size is 250 μm, with a standard deviation of 90 μm. Note that in the generation of microstructures using Voronoi tessellation, the energetic granules are effectively ‘grown’ in place, subject to spatial constraint, whereas in actual PBXs, the grains are grown in solution and pressed or cast to the desired density and composition. In [79], a limited study was carried out on the shape and size of grannules generated using Voronoi tessellation. It is found that the effect of the method on shape is on the same order as that on grain size distribution. Microstructures generated using particles from digitally scanned real material microstructures have been used by Barua et al. [79-80, 106, 112] and may be used in the future.

To generate microstructures with bimodal size distributions, a grain library is used. This library consists of grains extracted from monomodal microstructures which are generated using the Voronoi tessellation method. To achieve higher packing densities, the larger grains (d > 250 μm) are initially placed at random locations up to a specified volume fraction (e.g., $\eta = 0.40$). Subsequently, smaller grains (d < 100 μm) are placed between the larger grains, until the desired volume fraction ($\eta = 0.70 – 0.84$) is reached. The time required to generate a micrograph increases with the desired packing density. To reduce the time required in generating micrographs with high packing densities ($\eta >$ 0.80), a random shuffling algorithm is employed. Specifically, if a grain cannot be placed in the domain, the locations of the existing grains are randomly altered until an empty region can be found for that particular grain. Naturally, such a method cannot be used indefinitely, since beyond a certain packing density, grains of a particular size can no longer be accommodated. This method allows relatively high packing densities (up to

0.84) to be achieved. For the bimodal distributions, the two mean grain sizes are ~61 μm and ~287 μm. The average standard deviations for the smaller and larger sizes are 20.53 μm and 40.6 μm, respectively.

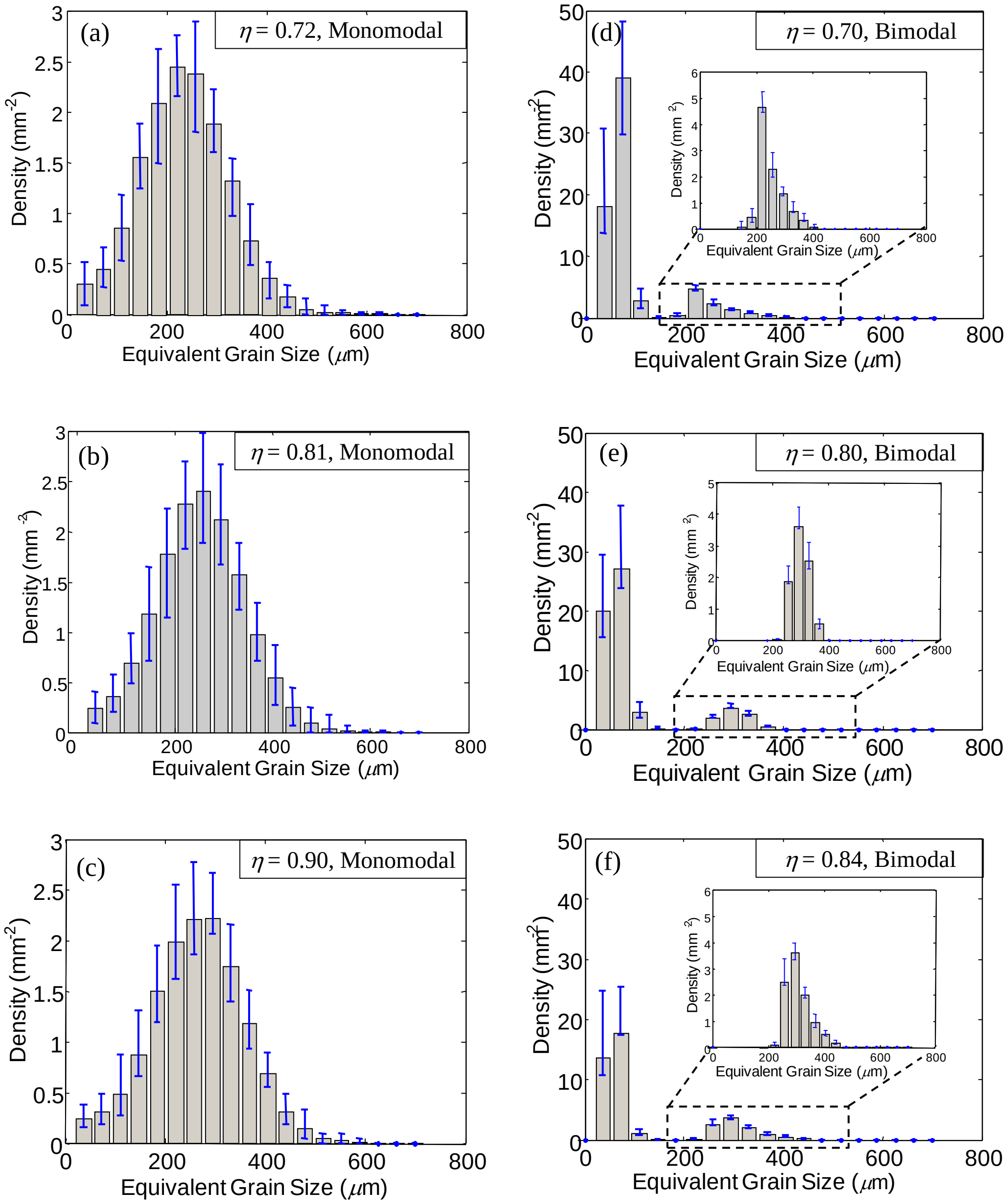

Figure 85: Grain size distributions for the microstructures shown in Figure 84.

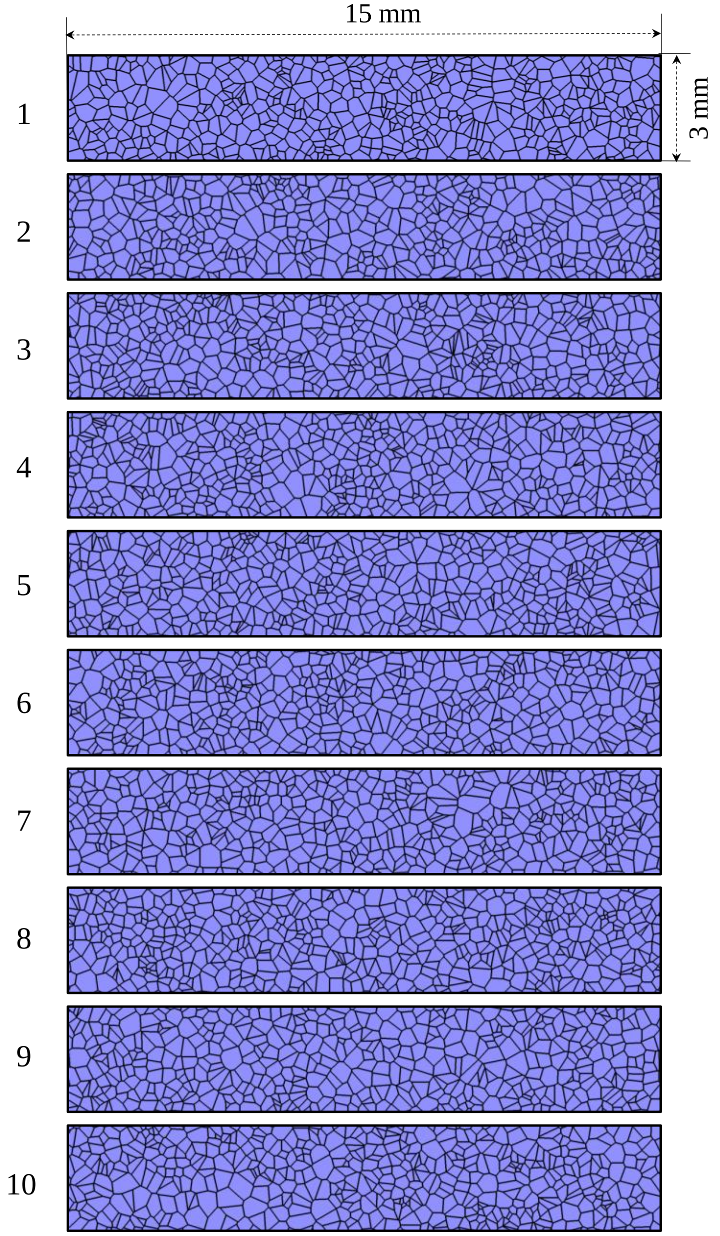

Figure 86: Multiple instantiations of microstructures having a grain volume fraction of η = 0.81 and the monomodal size distribution.

A total of six different microstructural configurations are considered. The volume fraction is in the range of η = 0.70 – 0.90, involving both the monomodal and bimodal grain size distributions. One representative micrograph is shown for each of the six configurations in Figure 84. The microstructures analyzed, along with their attributes are listed in Table 8. The grain size distributions for the microstructures in Figure 84 are shown in Figure 85. For each microstructural setting listed in Table 8, up to thirty statistically identical samples (random instantiations) are generated. To illustrate the random variations in microstructure geometry within one particular set, Figure 86 shows 10 microstructures having the same packing density of η = 0.81 and monomodal grain size distribution. Further details of the statistical approach of analysis are provided in Section 6.2.2.

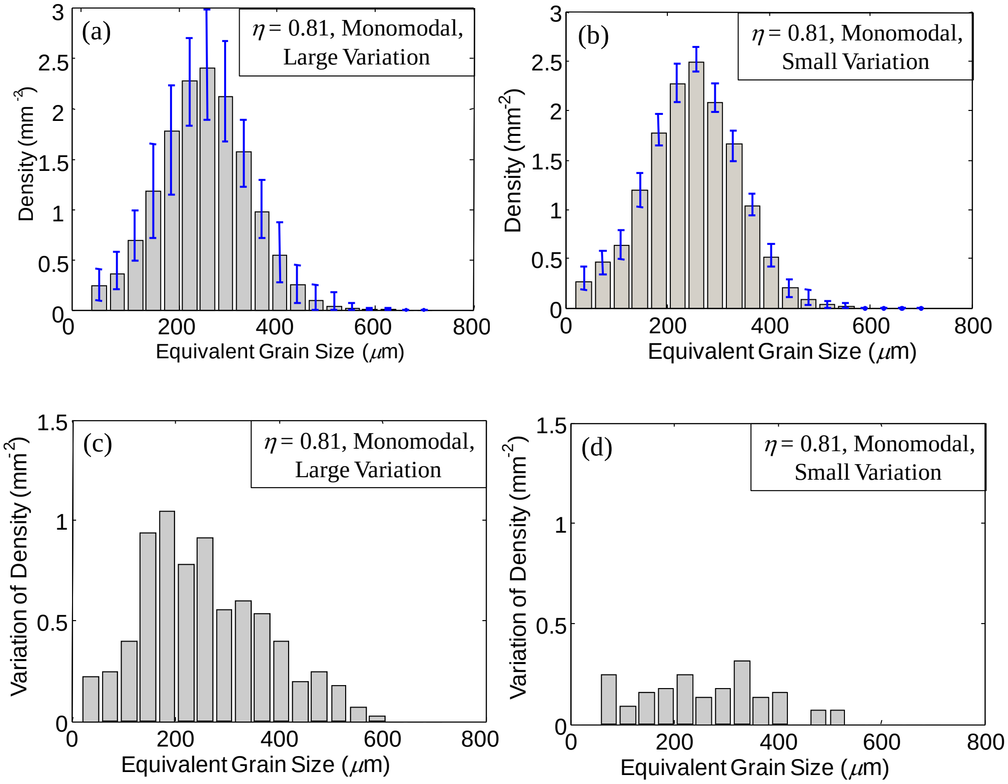

Figure 87: Grain size distributions for microstructures having the same grain volume fraction of η = 0.81 with (a) large grain size distribution variations and (b) small grain size distribution variations about the mean grain size distribution. Quantification of the variations are in (c) and (d), respectively.

The variations of grain size distribution within a particular set of microstructures with otherwise similar attributes (volume fraction, average grain size) can also affect the variability in the ignition response. For this purpose, two additional sets of microstructures are generated with large and small variations in grain size distribution. Figure 87(a-d) quantify the distributions of mean grain size and the distributions of the variations in the grain size relative to the mean grain sizes for these two sets of microstructures. The volume fraction of the grains is η = 0.81 and the size distribution is monomodal.

6.4 Quantification of Stochasticity

The stochastic nature of microstructural heterogeneities such as varying grain size and random constituent morphologies necessitates a statistical approach in the quantification of hotspot formation. This in turn requires an account of stochasticity in the application of the ignition criterion and hotspot threshold method described in Section 5.3. The analysis of hotspot criticality reflects such a probabilistic viewpoint.

To account for the stochastic variations in microstructures, sets of 10-50 microstructures with statistically similar attributes are constructed and used. The stochasticity analysis begins with running a fully dynamic thermomechanical impact response simulation and measuring the time to criticality for each sample in the microstructure sets. The different times to criticality in each set are taken together to quantify the stochastic variation in the behavior of the material with a particular attribute combination. The microstructural attributes considered are HMX volume fraction (η) which is often referred to as the packing density, grain size distribution (mean grain size

δ and standard deviation σ), area of the interface between the HMX phase and the polymer binder per unit volume (S_v, often referred to as the specific interface area), and the statistical variations of these quantities among samples in each microstructure set. These quantities measure the stochastic variations in the microstructures and, along with the load intensity represented by the impact velocity (v), constitute the input to the statistical model. On the other hand, the times to criticality measure the stochastic variations in material behavior and represent the output in the statistical model. The output also includes the threshold impact velocity below which no ignition is observed (v_c) for a particular statistical microstructure configuration (Figure 84).

Once an ensemble (or a set of microstructures) is defined, the distribution of the time to criticality can be uniquely determined for any given load intensity. For each set of microstructures having a given combination of statistically similar attributes, the time to criticality (t_c) is evaluated as a cumulative probability distribution. Naturally, the time to criticality is different for different instantiations of microstructure. The times to criticality ($\boldsymbol{t_c}$) obtained from all calculations in a set are

$$\boldsymbol{t_c} = \left(t_{c,1}, ..., t_{c,\xi}\right), \quad \xi = \text{number of instantiations.} \tag{6.1}$$

The data in Eq. (6.1) allows the cumulative probability distribution of t_c to be computed. The results are fitted to the Weibull distribution function [139]. By relating the variation of this distribution to the microstructural attributes (input parameters), the relationships between the ignition sensitivity and microstructure conditions of PBXs can be identified. The distribution function can also be used to determine other statistical measures of ignition response, such as the expected mean time to criticality t_{exp}, median time to criticality t_{50} and the critical impact velocity below which no ignition occurs (v_c). These measures can be related to empirical ignition thresholds for explosives, in the form of the Walker-Wasley relation [46] and the modified James relation discussed in Ref. [120].

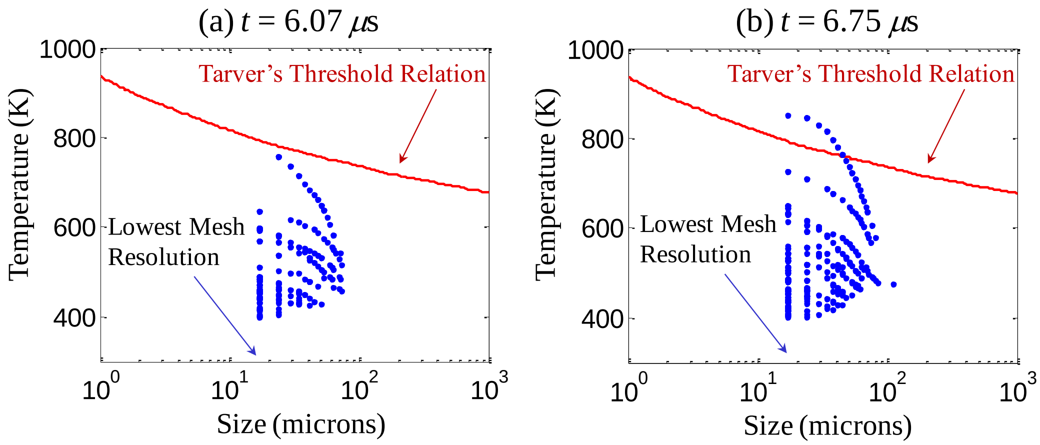

Figure 88: Size and temperature of hotspots relative to Tarver et al.'s ignition threshold at different times. The microstructure is that in Figure 84(f) with $\eta = 0.84$ and the impact velocity is $v = 90\ \mathrm{ms}^{-1}$.

6.5 Results and Discussion

The calculations first focus on the effects of (i) impact velocity, (ii) grain volume fraction $(\eta = 0.70 - 0.90)$, and (iii) grain size distribution (monomodal and bimodal). For all calculations presented, the initial temperature is $T_i = 300\ \mathrm{K}$. Two loading configurations are used, both involve a 15 mm × 3 mm rectangular microstructural region as shown in Figure 11(a) and Figure 11(b). The boundary velocity is varied between 100 and 250 ms^{-1}. To illustrate the processes at hand and the stochastic treatment of the results, a representative calculation is first discussed.

The analysis is performed in two steps. First, the calculations are carried out using loading configuration in Figure 11(a) to allow the temperature field to evolve with time under the effects of transient stress wave propagation. Following the calculations, the threshold method described in Section 5.3 is used to scan the microstructure for hotspots. Figure 88 illustrates the evolution of hotspots with time for a microstructure with a packing density of $\eta = 0.84$ in the time interval $t = 6.07 - 6.75$ μs. The impact velocity is $v = 90$ ms^{-1}. Each dot represents the detection of one hotspot with a particular combination of size and temperature. Failure mechanisms (transgranular fracture and sliding frictional heating along crack faces, intergranular interaction and heating due to binder deformation and crack face friction) cause energy dissipation and local temperature rise. Localized temperature increases lead to the hotspots. The use of multiple threshold temperatures in the hotspot detection algorithm allows hotspots of interests in the entire temperature-size space to be identified and analyzed. Figure 88(a-b) show that, as the threshold temperature is increased, the size and density of hotspots decrease. This finding suggests that there are fewer hotspots with higher temperatures. At the highest temperature, only 1-2 hotspots exist. These hotspots are the first to reach the threshold condition for thermal criticality. Obviously, the ignition of the material is determined by a small number of hotspots in the domain analyzed. Although some hotspots in Figure 88 appear to be close to the mesh resolution of 15 μm, it is important to point that the overall temperature fields and the temperature variations within hotspots are properly resolved with sufficient spatial resolution, as stated earlier. This situation should be viewed objectively with the proper information in mind. Hotspots have varying temperatures, as shown, e.g., in Figure 57 and Figure 61 in Chapter 5 (also in ref. [120]). Specifically, the temperature is highest at the center of a hotspot, causing a sharp spike to form at the center. As the cutoff temperature ΔT_{thres} is increased to identify hotspots with high temperatures, a hotspot is intersected only at the center and would appear smaller as only its central portion is included in the analysis. This accounting of the hottest central region of a hotspot should not be mistaken as the whole hotspot not having been represented by enough finite element data points spatially.

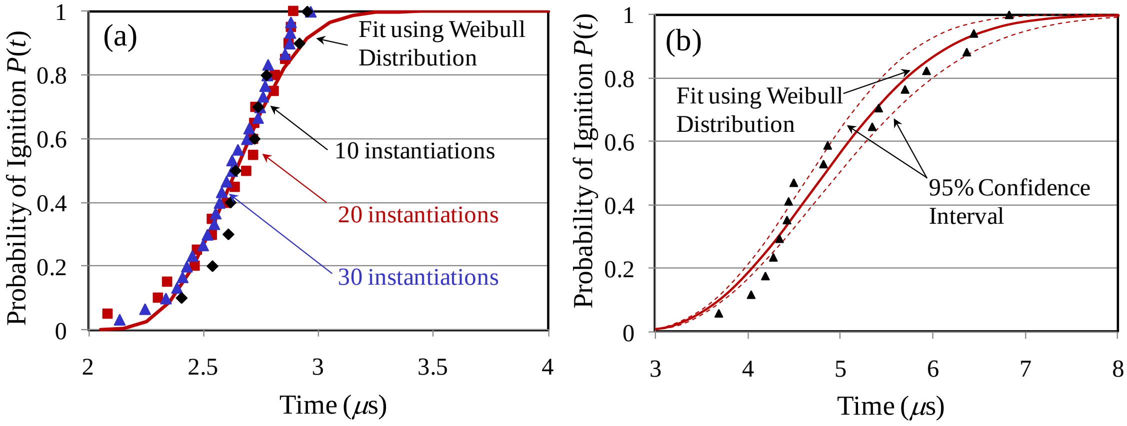

Figure 89: (a) Probability distributions of times to criticality obtained from calculations using 10, 20 and 30 different microstructure instantiations like that in Figure 85 with statistically similar microstructural attributes (η = 0.81, monomodal, S_v = 16 mm^{-1}) The impact velocity is v = 200 ms^{-1}. (b) Illustration of the Weibull distribution (red solid line) with the data points from calculations (black triangles). The 95% confidence interval bounds are shown using red dotted lines (η = 0.70, bimodal, v =100 ms^{-1}).

Figure 88(a) also shows Tarver et al.'s threshold [Eq. (5.1)] for thermal criticality. At t = 6.07 μs, no hotspot has reached any size-temperature combination required for criticality. At 6.75 μs, a few hotspots have reached or crossed the threshold curve. Once the criterion outlined in Section 5.3 is satisfied, the material is assumed to have reached the critical state for thermal runaway. The time (measured from the beginning of loading) at which this is taken as the time to criticality (t_c) and is obtained for different combinations of impact velocity, grain volume fraction and size distribution.

The variations in the time to criticality t_c among different samples subject to the same loading result from the variations in microstructure geometry. It is possible to generate ensembles with desired numbers of samples that share certain microstructural attributes that are similar to prescribed levels of accuracy. The microstructure attributes of initial interest in this regard are grain volume fraction and grain size distribution. The number of microstructure instantiations or the 'sample set size' required for a particular analysis depends on the complexity of the problem, the parameter ranges involved and the desired level of accuracy of the statistical analysis. The complexity of the calculations is evident from the fact that the simulation of the impact response of one sample has a wall clock time of approximately one week while running on 24 computing cores on a parallel computer cluster. The microstructure space analyzed here covers volume fractions in the range of η = 0.70 – 0.90, with both monomodal and bimodal grain size distributions for each volume fraction level. Specifically, six microstructural settings [three volume fraction levels (0.72, 0.81 and 0.90) for monomodal grains and three volume fraction levels (0.70, 0.80 and 0.84) for bimodal grains] are considered, as discussed in Section 6.2.1 and shown in Figure 85. The range of impact velocity of interest is v = 100 – 250 ms^{-1} and up to four different impact velocity levels (100, 150, 200, and 250) are considered for each microstructure set. The number of microstructure set and impact velocity combinations studied is 6×4=24.

Each of the six sets of microstructures must include multiple samples. Clearly, a higher number of instantiations in each set leads to a more accurate quantification of the probability distribution function of the ignition behavior. Wild and von Collani [140] used a sample size of 50 for their analysis of explosive sensitivity. To illustrate the effect of the sample set size on the results, an analysis is conducted with sample sets that include 10, 20 and 30 instantiations. The calculations are performed using microstructures with a packing density of η = 0.81 having a monomodal grain size distribution [representative microstructure shown in Figure 84(b)]. The impact velocity is v = 100 ms^{-1}. Figure 89(a) shows the probability distributions of the time to criticality for sample sizes of 10, 20 and 30. Clearly, the overall trend and the functional relation are captured well by all three sample sizes. Based on this result, the number of instantiations for each microstructural set is chosen to be 20 from here on. The resulting total number of calculations is approximately 500.

6.5.1 Confidence Level and Confidence Interval

In quantifying the safety of explosives, it is particularly important to establish confidence levels and confidence intervals for data reported. In the case of combustion in gases due to spark ignition, the 95% or 90% confidence interval is widely used in the presentation of probability estimates based on limited number of samples. For instance, Eckhoff et al. [141] represented the probability of ignition as a function of input energy and calculated the upper and lower limits of the probability distribution with a confidence level of 95%.

For the calculations presented in this chapter, it is assumed that the distribution of the values occurs on either side of the Weibull distribution of t_c in an unbiased manner. For such a situation, the confidence interval can be computed assuming the variation to be normally distributed around the Weibull distribution. Specifically, the confidence interval for a 95% confidence level is [142]

$$t_{bound,i} = t_{c,i}\left(\eta, v\right) \pm 1.96 \frac{\sigma}{\sqrt{\xi}}, \tag{6.2}$$

where $t_{bound,i}$ represents the upper and lower limits of the time to ignition for the i-th sample, σ is the standard deviation of the normal distribution of the variation, and ξ is the number of samples. To provide a quantitative perspective for this relation, Figure 89(b) shows the ignition times of a set of PBX microstructures with a packing density of η = 0.81 and a monomodal size distribution of grains. The impact velocity is 200 ms^{-1}. The probability distribution of t_c is fitted to a Weibull distribution as shown by the solid line in Figure 89(a). The confidence envelopes [shown in dotted lines in Figure 89(a)] represent the probabilistic bounds within which 95% of the results are expected to lie.

6.5.2 Probability Distribution of the Time to Criticality

Figure 90(a-f) show the probability distributions of the time to criticality t_c for microstructures with different volume fractions (η = 0.72 – 0.90) and grain size distributions (monomodal, bimodal). The impact velocity is in the range of v = 100 – 250 ms^{-1}. For each case, no critical hotspots are formed before a minimum cutoff time t_0. Both the minimum value and the overall distribution of the ignition time depend on microstructural attributes and loading condition.

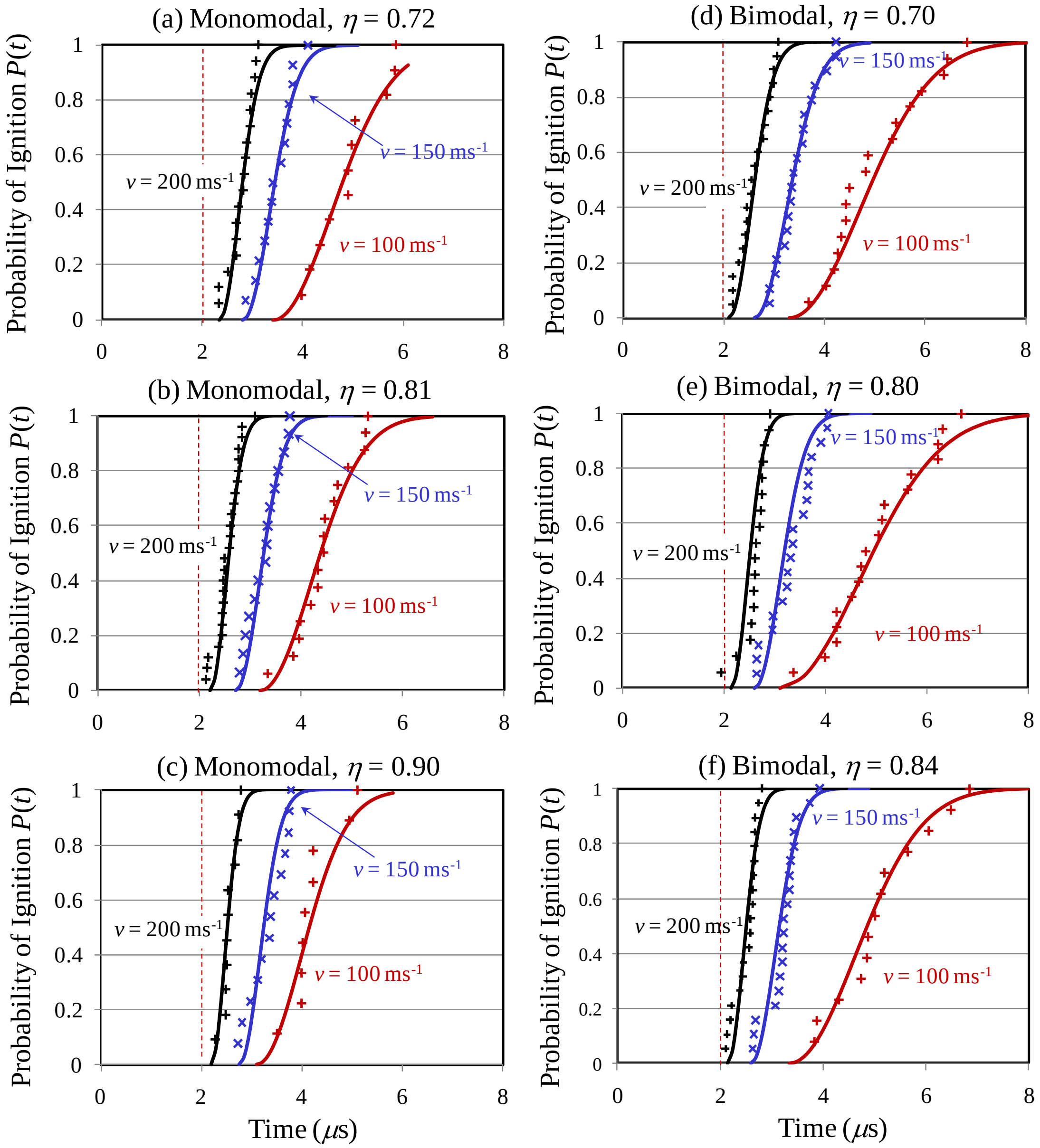

Figure 90: Cumulative probability distributions of the time to criticality for microstructures with different grain volume fractions (η = 0.72 - 0.90) and grain size distributions (monomodal, bimodal) for impact velocity v = 100 – 200 ms^{-1}.

The distribution of t_c is affected by impact velocity. In general, the time to criticality values span over a range, with lower impact velocities giving rise to wider ranges. This means that the distribution of time to criticality is more spread out at lower impact velocities, in other words, different samples show larger difference in behavior at lower impact velocities. This observation reflects the fact that at lower impact velocities (e.g., $v \leq 100$ ms^{-1}). The stresses and rates of deformation are lower, leading to longer times for failure to occur and hotspots to evolve; as a result, hotspots are more spatially spread out and more significantly influenced by random material heterogeneities. At high impact velocities (e.g., $v > 100$ ms^{-1}), on the other hand, severe deformation and grain failure occur near the impact surface early in the loading process, dissipation and heating are the most intense near the impact face and gradually decrease toward the front of the propagating stress wave. Consequently, dominant hotspots are more concentrated near the impact surface, resulting in shorter times to criticality for hotspots less variations among different samples in term of t_c.

Figure 90(a-c) show the distributions of the time to criticality for microstructures with monomodal grain size distributions. The packing density η is 0.72, 0.81 and 0.90, respectively. The corresponding results for microstructures with bimodal grain size distributions at η = 0.70, 0.80 and 0.84 are shown in Figure 90(d-f), respectively. As the packing density increases, the material becomes stiffer and generates higher levels of overall stress at the same impact velocity. Higher stresses lead to higher rates of dissipation and higher temperature increases. Consequently, the time to criticality is in general shorter at higher grain volume fractions. The distributions of t_c for the lower packing densities of η = 0.72 [Figure 90(a)] and η = 0.70 [Figure 90(d)] are over wider ranges compared with the distributions for the corresponding higher packing densities in Figure 90(b-c) and Figure 90(e-f).

Variations in the distribution of grain size also affect the sensitivity of PBX. In general, the time to criticality is more spread out for bimodal microstructures than for monomodal microstructures at the same packing density and the same load intensity [see, e.g., Figure 90(a-c) and Figure 90(d-f)]. The level of difference between the two types of microstructures depends on load intensity. At impact velocities above 150 ms^{-1}, the difference is small and the responses for both monomodal and bimodal distributions are similar. However, at lower impact velocities ($v \leq 100$ ms^{-1}), the distributions of t_c for bimodal microstructures are spread out over much wider ranges of time than the distributions for monomodal microstructures. The average particle sizes in monomodal distributions are larger than the average particle sizes in bimodal distributions, giving rise to higher levels of heterogeneity and more significant differences in behavior among different samples in the same set. In contrast, the smaller grains in microstructures with bimodal grain size distributions can rearrange and more effectively absorb the loading to keep stresses and temperature rises lower, leading to longer times to criticality and larger variations among samples in each set. Simply put, bimodal grain distributions lead to less sensitive PBXs under otherwise identical conditions.

6.5.3 Quantifying the Variation of Microstructural Attributes

Some microstructure attributes can be more easily and precisely controlled in materials design and synthesis. The overall packing density η and the average grain size are two such attributes. Other attributes are more difficult to control accurately, the distribution of grain size is one. The distributions of grain size of samples within a set of statistically similar microstructures which have, for example, the same packing density η and the same average grain size δ, may be quite different. As it turns out, the differences in grain size distribution among samples have a significant impact on the stochastic behavior of PBXs, as will be shown below. For this reason, it is necessary to define a parameter (or parameters) which can be used to quantify the variations among microstructures which are statistically "similar" according to some commonly used measures (such as packing density and average grain size) but may be different in ways that can make their behaviors vary significantly from each other.

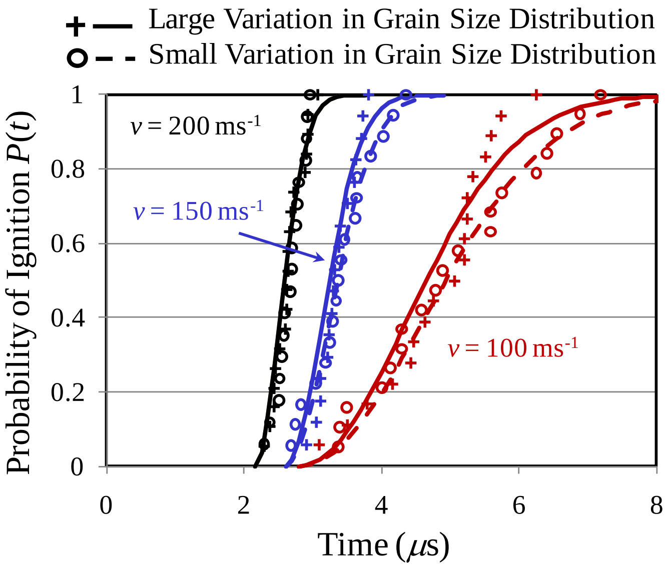

Figure 91: Cumulative probability distributions of the time to criticality for microstructures with different levels of variations in grain size distributions for $v = 100 - 200\ \mathrm{ms}^{-1}$ ($\eta = 0.81$).

To illustrate this point, the effect of the variations of grain size distribution among samples in a given microstructure set on the time to criticality is considered.

Figure 91 shows the distributions of the time to criticality for two sets of microstructures. One set has large (*L*) and the other has small (*S*) variations among the grain size distributions, as shown in Figure 87(a-b). Specifically, the two sets of microstructures have the same grain volume fraction of η = 0.81 and the same overall average size density histograms as represented by the grey columns. The variations of grain size distribution here referred the error bars in the histograms. These error bars show the range of the grain size density among the samples in a microstructure sample set. To understand the charts, note that each of the 20 microstructure samples (or instantiations) in a set has a histogram quantifying its grain size distribution. The heights of the grey columns represent the averages of the 20 histograms and the error bars denote the maximum and minimum densities among the 20 histograms. Figure 91 shows the results for three impact velocities between 100 – 200 ms^{-1}. At high impact velocities, the variations in the time to criticality are similar for both sets. However, at a lower velocity of $v = 100\ ms^{-1}$, the two sets show similar behavior at the low end of the curves (time to criticality up to $t \sim 5\ \mu s$) but diverge at the high end ($t > 5\ \mu s$) of the curves. Specifically, the set with large variations in grain size distributions (set *L*) has a steeper profile and less variation in response than the set with smaller variations in grain size distributions (set *S*). The outcome that set *L* has larger variations among the samples but shows smaller variations in response is inconsistent with the logically expected trend. *The result suggests that the samples in the two sets of microstructures are not sufficiently similar in a statistical sense. In other words, simply having the same packing density, average grain size and average grain size distribution is not sufficient to guarantee statistical similitude of microstructures when it comes to impact-induced ignition of PBXs.*

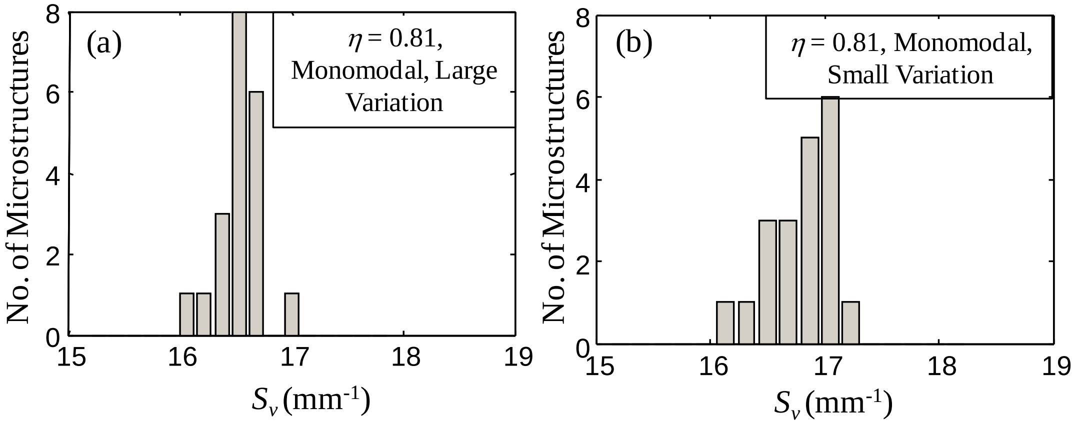

Figure 92: Interface area per unit volume (specific interface area) for microstructures with large and small variations in grain size distributions (η = 0.81, monomodal).

To understand the reason, the correlation between the variations in grain size distributions (shape of the histogram profiles) and the specific interfacial area (S_v) between the HMX grains and the polymer binder in the composite is considered. Figure 92(a-b) show the distributions of S_v for the 20 samples in each of the two sets of microstructures in Figure 87(a-d). Significant differences are seen between the two histograms, i.e., there is no common trend in the profiles of S_v. It is well known that the specific interfacial area is an important parameter determining the ignition behavior of PBXs [22, 24]. To properly delineate the statistical trends in behavior, more systematically constructed microstructure sample sets must be developed.

To this end, the effects of both the specific surface area S_v and its statistical variation ΔS_v on the ignition response is considered. Two sets of microstructures are presented in Figure 93, one with a large ΔS_v of 0.3290 mm^{-1} and the other with a small ΔS_v of 0.1985 mm^{-1}. For both sets of calculations, the microstructures have monomodal size distributions with the same packing density of η = 0.81 and the same average specific surface area, S_v of 16 mm^{-1}.

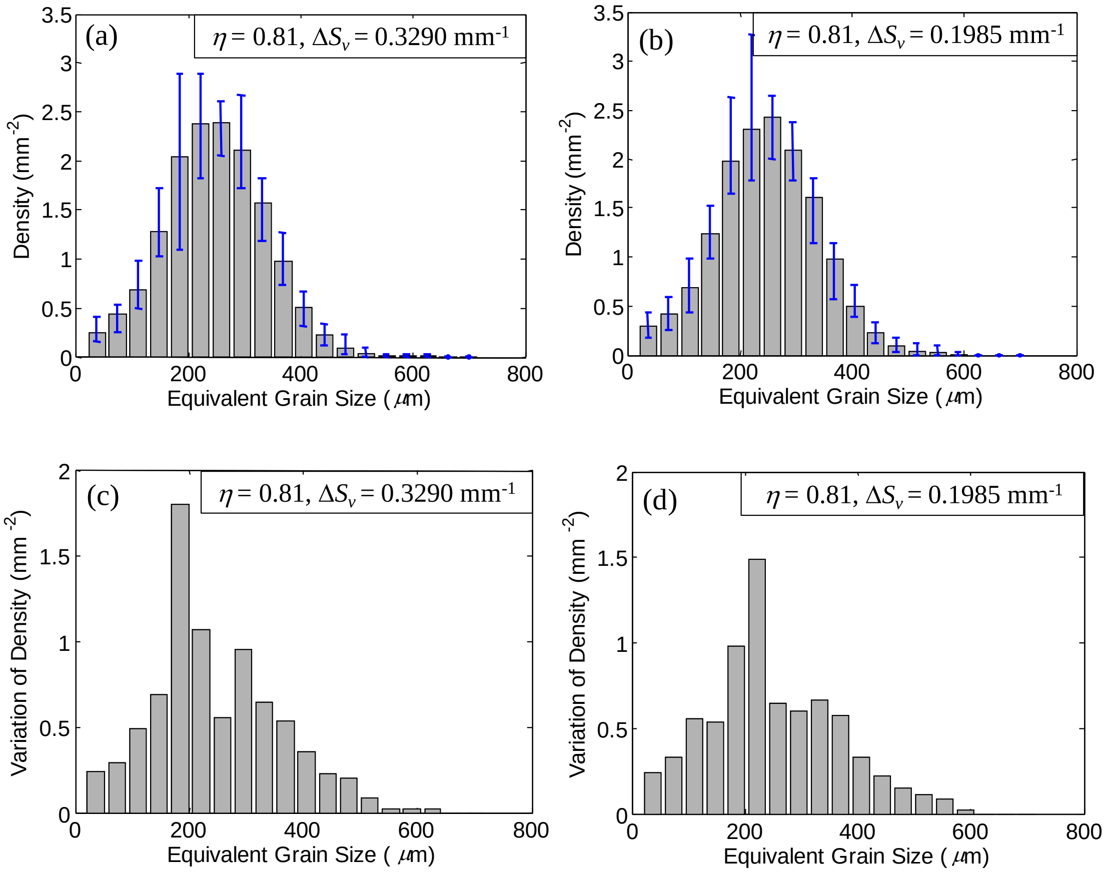

Figure 93: Grain size distributions for microstructures having the same grain volume fraction of η = 0.81 with different variation of the specific surface area of (a) ΔS_v = 0.3290 mm^{-1} and (b) ΔS_v = 0.1985 mm^{-1} about the mean S_v = 16 mm^{-1}. Quantification of the variations are in (c) and (d), respectively.

The distributions of the time to criticality for microstructures presented in Figure 93 are shown in Figure 94. The impact velocity is varied between 100 – 250 ms^{-1}. The results in Figure 94 show that higher values of ΔS_v correspond to higher spreads in the time to criticality. The difference in the spread of data increases as the impact velocity decreases. Specifically, at v = 100 ms^{-1}, for a ΔS_v of 0.3290 mm^{-1} t_c lies between 3.0 – 7. 0 μs, whereas for a ΔS_v of 0.1985 mm^{-1}, t_c lies between 4 – 6.5 μs. This shows that the variations in microstructures can be reasonably well quantified by ΔS_v in the context of impact-induced ignition of PBXs. In the following sections, ΔS_v is used to develop microstructure-performance scaling relationships.

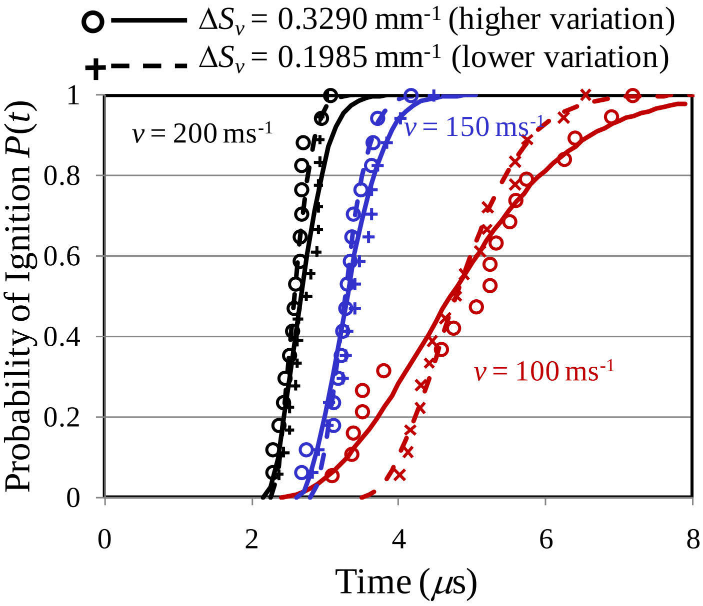

Figure 94: Cumulative probability distributions of the time to criticality for microstructures with different variations in interface area per unit volume (ΔS_v = 0.1985 – 0.3290 mm^{-1}) for v = 100 – 200 ms^{-1}.

6.5.4 Weibull Distribution Model for Ignition Sensitivity

Historically, the Weibull distribution [139] has been widely used in failure analysis and reliability prediction. The effect of the intensity of loading on the time to criticality can be compared to the effect of stress on the life of a mechanical component [140]. Thus, the Weibull distribution lends itself to be an excellent choice for modeling the sensitivity of explosives to impact loading. For instance, in [143] the Weibull model was applied to compare the sensitivities of RDX, HMX, PETN and other popular explosives with varying grain size distributions.

Physically, critical hotspots develop only after some time has elapsed from the onset of loading. To account for this effect, a modified form of the Weibull distribution function with a lower threshold time is used. The specific form used here is [144],

$$P(t) = 1 - e^{-\Phi(t)}, \quad \Phi(t) = \begin{cases} 0, & t < t_0; \\ \left(\dfrac{t - t_0}{\tau}\right)^m, & t \geq t_0. \end{cases} \tag{6.3}$$

In the above expressions, $P(t)$ is the cumulative probability, t is the time to criticality, t_0 is the cutoff or threshold time below which the probability of ignition is zero, τ is a scale parameter which affects the slope of the distribution curve and m is a shape parameter. The parameters m, τ and t_0 together determine the Weibull distribution function [Eq. (6.3)] for different material and load combinations. These parameters can be related to the microstructure (packing density, grain size, grain size distribution, interfacial area per unit volume and the statistical variations of these parameters) and impact velocity v. They can also be used to determine the threshold impact velocity v_c

below which no sample in a given material set reaches thermal criticality for ignition, as will be shown later. Determination of what microstructure attributes and loading intensity each of these parameters depends on and quantification of the dependence are the focus of the systematic analysis carried out in Sections 6.4.6 - 6.4.8. In particular, the objective is to establish explicit functional forms for the relations.

6.5.5 Physical Basis for the Weibull Distribution Model

The Weibull probability distribution function is a mathematical model independent of physical processes. The ignition of explosives is a physical process involving localized mechanical heating that is heavily affected by microstructural heterogeneity and the kinetics of chemical reactions. It is desirable to link physical mechanisms and associated variables affecting the ignition process to the model quantifying the probabilistic initiation behavior. Care needs to be taken so as to not oversimplify the problem.

To address this issue, Terao [135] and later Gilbert and Gonthier [137] used a probabilistic model to account for the stochasticity of ignition phenomena. In Terao's model, the stochasticity is accounted for by a function $\omega(t)$ which represents the probability of ignition per unit mass per unit time for a fixed amount of gas. Fundamentally for gases, ω is related to the probability of collision and subsequent reaction between molecules in a system. This probability depends on temperature T of the gas system. Terao's approach to modeling ignition in gases lends itself to the modeling of impact-induced ignition in solid high explosives. This is accomplished by accounting for the wave propagation process and temperature rise as functions of time and spatial distance from the impact surface.

Specifically for a loading event, the cumulative probability of ignition at time t is taken as $P(t)$. The inverse probability $\left[1-P(t)\right]$ is the probability of survival or the fraction of samples not having ignited at time t. Note that $P(0)=0$ and $P(\infty)=1$. Now, it can be shown that the ignition probability per unit volume per unit time is [135],

$$\omega(t)=-\frac{1}{V}\frac{d\left[\ln(1-P)\right]}{dt}, \tag{6.4}$$

where V is the volume of the specimen involved. For an impact-induced loading event in solid high explosive in one spatial dimension (plane loading waves), the volume of the specimen under stress increases linearly with time, that is, $V = A_c ct$, where A_c is the cross sectional area of the specimen and $c(\eta)$ is the effective wave velocity through the composite which depends on packing density η.

If a functional form of $\omega(t)V(t)$ can be determined, the explicit form of the probability distribution $P(t)$ can be obtained from the integration of Eq. (6.4). To identify the form of $\omega(t)V(t)$, another set of calculations is performed under conditions of uniform loading without stress wave propagation. Although for dynamic loading, it is hard not to generate stress waves in experiments, computationally a loading configuration can be devised to create the right conditions such that no stress wave front sweeps through the material. Such a configuration uses a linearly distributed initial velocity field with v = the imposed boundary velocity at x = 0 and v = 0 at x = 3 mm, as in loading configuration in Figure 11(b). This initial condition creates a state of nominally homogeneous uniaxial strain state over the 3 mm length of the specimen involving the initial velocity distribution. Throughout the calculation, the boundary velocity imposed at $x = 0$ is $v = 200$ ms^{-1}. The hotspot analysis focuses only on the 3 mm region, since only this region experiences the macroscopically homogenous state of stress without the influence of a propagating stress wave front. Under this condition, the volume V in Eq. (6.4) is the volume of the 3 mm region and is a constant which does not change with time.

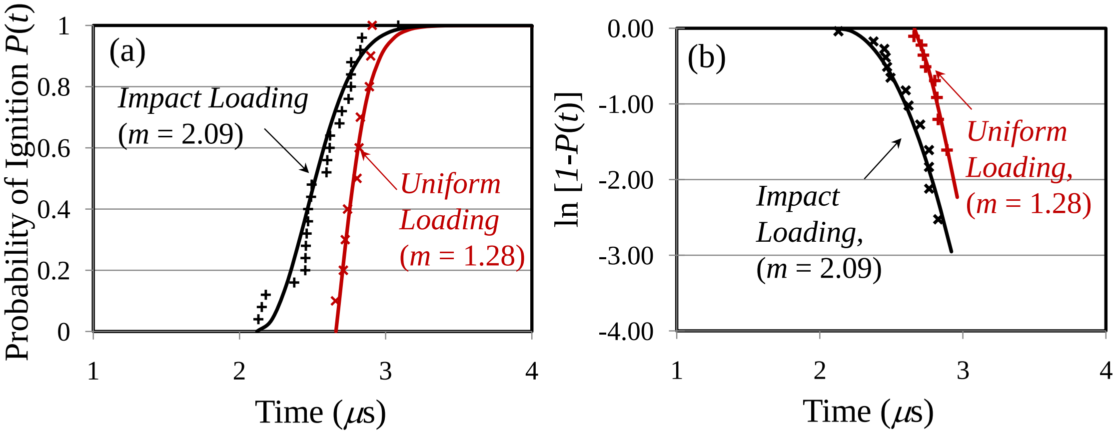

Figure 95: Comparison of the effects of uniform and transient impact loading on the shape parameter *m*; (a) in *P*-*t* space and (b) in (1-*P*)-*t* space (monomodal, $\eta = 0.81$, $v = 200$ ms^{-1}).

Figure 95(a) shows a comparison of the probability distributions of t_c for two calculations, one uses loading configuration in Figure 11(a) and the other uses loading configuration in Figure 11(b). Both cases involve an imposed boundary velocity of v = 200 ms^{-1} on monomodal microstructures having a volume fraction of η = 0.81. Figure 95(b) shows the variation of ln[1-*P*(t)] with the time to criticality t_c. The results are fitted to a power-law function of the form,

$$\int_0^t \omega(t)V(t)dt = -\ln\left[1-P(t)\right] = \left(\frac{t-t_0}{\tau}\right)^m. \tag{6.5}$$

Note that in Eq. (6.5), $P(t)=0$ and $\omega(t)=0$ when $t \le t_0$.

The fit for ln[1-*P*(t)] as a function of *t* can be used to determine the value of *m* [refer to Eq. (6.5)]. Using Eq. (6.5), one can determine the probability of ignition per unit time for volume *V* as

$$\omega(t)V(t) = \frac{m}{\tau^m}\left(t-t_0\right)^{m-1}. \tag{6.6}$$

Integrating Eq. (6.4) along with Eqs. (6.5) and (6.6), yields

$$\int_0^P d\left[\ln\left(1-P\right)\right] = -\frac{m}{\tau^m}\int_{t_0}^t \left(t-t_0\right)^{m-1} dt. \tag{6.7}$$

This yields the probability *P* as a function of *t* as

$$\ln\left(1-P\right) = -\left(\frac{t-t_0}{\tau}\right)^m. \tag{6.8}$$

Equation (6.8) can be recast into the modified Weibull distribution in Eq. (6.3). This derivation shows that the Weibull distribution as a quantification for the probability of ignition is not just a numerical fit, but rather a consequence of the physics of the ignition processes whose overall probability of ignition per unit time can be described by Eq. (6.6).

The parameter *m* determines the shape of the Weibull distribution curve and hence is often referred to as the shape parameter. Tsue et al. [145] analyzed the ignition time in the droplet experiment using the Weibull distribution and categorized the curves into three types which correspond to $m > 1$, $m < 1$, and $m = 1$, respectively, for droplets having a constant volume. The analysis revealed that $m > 1$ is caused by driving forces for ignition that intensify with time. If $m = 1$, the onset rate of ignition is independent of time. From the fitting in Figure 95(b), it can be seen that for the uniformly loaded case, *m* = 1.28 >1, reflecting that fact that the temperature and therefore the probability for ignition increases as the loading event progresses. For the case with wave propagation, *m* = 2.09, signifying a higher rate of increase of the probability for ignition resulting from the combined effects of increasing temperature (the increases of the peak and average temperatures behind the propagating wave front under non-shock loading was analyzed in Chapter 5 and also in Ref. [112]) and increasing volume of material involved. This value is close to the theoretical value of *m* = 2 for the special case with μ (and the overall average temperature) being constant behind the propagating wave front typically encountered during shock loading. Note that, however, for wave propagation considered here (non-shock loading), the spatial distribution of temperature is non-uniform behind the stress wave front, i.e., temperature increases are highest near the loading surface at the left end [see Figure 11(a)] and lowest near the stress wave front (toward the right). This non-uniformity of temperature causes the density of probability of ignition to be spatially non-uniform. Consequently, $\omega(t)$ must be interpreted as the average probability of ignition per unit time per unit volume for materials behind the current stress wave front.

Figure 96 shows the values of m obtained by fitting Eq. (6.3) to the computationally predicted ignition times for all combinations of microstructure (monomodal and bimodal, η = 0.70 – 0.90) and impact velocities (v = 100 – 250 ms^{-1}) considered. The values do not change significantly with microstructural attributes or impact velocity. The average value for all calculations is 2.081. This shows that under the conditions analyzed, m is primarily dependent on the loading configuration and is not significantly influenced by microstructure or loading intensity.

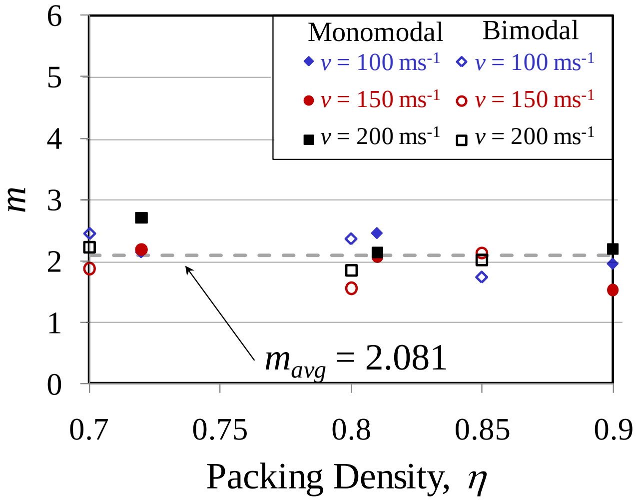

Figure 96: Weibull parameter *m* as a function of grain volume fraction over a range of impact velocity (v = 100 – 200 ms^{-1}).

6.5.6 Effect of Microstructure and Impact Velocity on Threshold Time t_0

The parameter t_0 quantifies the threshold time before which no ignition is observed. Figure 97(a-b) show the values of t_0 obtained from the Weibull analysis for all cases of microstructure (monomodal and bimodal; $\eta = 0.70 - 0.90$) and impact velocities ($v = 100 - 250 \text{ ms}^{-1}$) considered. For both monomodal and bimodal microstructures, as the boundary velocity increases, the threshold time t_0 decreases. This is expected since an increase in impact velocity leads to earlier fracture and frictional dissipation in the grains. This in turn, results in earlier formation of critical hotspots. The relationship between the threshold time and impact velocity can be quantified as

$$v^{n'} t_0 = C'(\eta), \tag{6.9}$$

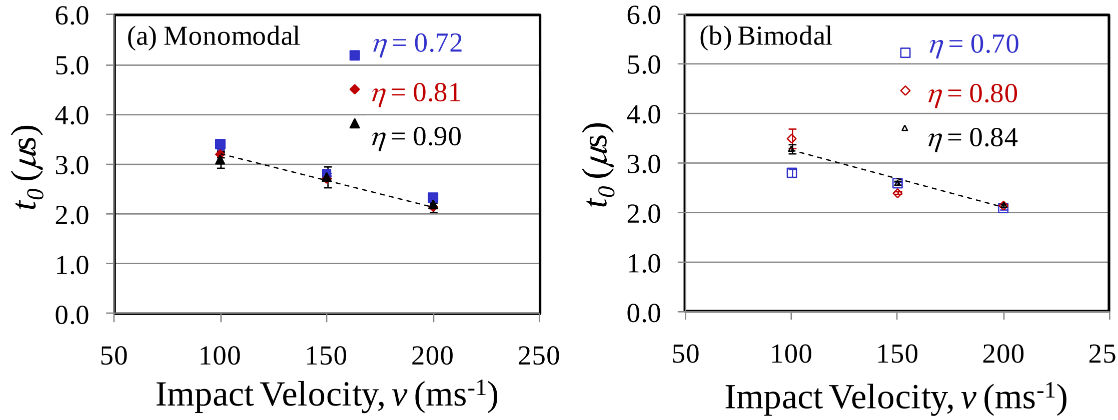

Figure 97: Threshold ignition time t_0 as a function of grain volume fraction over a range of impact velocity ($v = 100 - 200 \text{ ms}^{-1}$) for microstructures with (a) monomodal and (b) bimodal grain size distribution (the bounds show the 95% confidence intervals).

where n' and C' are functions of packing density η and are not sensitive to the monomodal or bimodal nature of the grain size distribution. At low impact velocities, the threshold time is lower for lower packing densities. Specifically, the threshold time decreases by ~16% as the packing density increases from 0.72 to 0.90. However, at higher impact velocities, this decrease is smaller. At 200 ms^{-1}, no significant effect of packing density on the threshold time is seen. Under the conditions analyzed, the grain size distribution does not significantly affect t_0. The values of n' and C' for the different microstructures analyzed are listed in Table 9.

Table 9: Parameters used in Eqs. (6.9), (6.14) and (6.15).

Microstructure	Grain volume fraction (η)	n	n'	C	C'	k'	$\rho_0 c_0$ (kg m^{-2}s^{-1})
PBX – Monomodal	0.72	0.42	0.23	21.20	7.34	17.0	3.29
	0.81	0.41	0.28	19.18	8.93	15.2	3.74
	0.90	0.40	0.26	17.87	8.36	12.5	4.73
PBX – Bimodal	0.70	0.37	0.22	15.03	5.99	10.0	3.36
	0.80	0.53	0.15	31.20	4.67	18.0	3.88
	0.84	0.46	0.31	23.96	9.83	9.5	4.44

6.5.7 Effect of Microstructure and Impact Velocity on Scale Parameter τ

The scaling parameter τ influences the overall slope (and spread) of the probability distribution of the time to criticality t_c. Figure 98(a-b) quantify the variation of τ as a function of impact velocity in the range of v = 100 to 200 ms^{-1}. The microstructures have grain volume fractions between η = 0.72 and 0.90 and different (monomodal and bimodal) size distributions. In general, τ varies with both microstructure and load intensity. For all microstructures, τ decreases (and $1/\tau$ increases) as the impact velocity increases. A higher τ corresponds to a wider range of distribution of t_c. At the same impact velocity, τ decreases as the grain volume fraction increases, indicating that the probability distribution of t_c narrows to a shorter time range. This is expected since higher grain volume fractions lead to higher stresses and earlier ignition, resulting in lower spreads in the probability distribution.

Grain size distribution also affects the variation of τ with v. For a particular impact velocity, τ is lower for monomodal distributions and higher for bimodal distributions. This difference is related to the fact that the range of time to ignition is higher for bimodal microstructures.

A value of $\tau = \infty$ $(1/\tau = 0)$ indicates that the probability of ignition is zero. The velocity at which this occurs (v_c) can be determined by extrapolating the curves in Figure 98(a-b) to the horizontal axis. To obtain this critical velocity v_c, an exponential relation between τ and v is used to fit the results. This relation is of the form

$$\frac{1}{\tau} = \frac{1}{\tau_{\text{ref}}}\left(\frac{v - v_c}{v_{\text{ref}}}\right)^{\alpha}, \qquad (6.10)$$

where τ_{ref} and v_{ref} are constants, v_c is the critical impact velocity below which no ignition is observed, and α is a fitting parameter that is a function of microstructure. The values of the constants τ_{ref} and v_{ref} are listed in Table 10.

Parameter α controls the variation of $1/\tau$ with impact velocity. $1/\tau$ decreases with α when the packing density and impact velocity are fixed. A scaling law is developed to quantify α as a function of the grain volume fraction η and the variation of the specific interface area ΔS_v. The resulting relation is

$$\alpha\left(\eta, \Delta S_v\right) = \alpha_0 \eta^{2.0} \left(1 + \frac{\Delta S_v}{\Delta S_0}\right)^{-3.6}, \tag{6.11}$$

Table 10: Parameters used in Eqs. (6.10) - (6.12).

Parameter	Units	Value
τ_{ref}	μs	1.0
v_{ref}	ms^{-1}	55.0
α_0	-	1.35
S_0	mm^{-1}	1.0
ΔS_0	mm^{-1}	20.0
v_0	ms^{-1}	21.5

where α_0 and ΔS_0 are constants, as listed in Table 10. This relation consists of a dimensionless term obtained by normalizing ΔS_v by reference value ΔS_0. Over the range of conditions analyzed, the specific surface area S_v does not affect α; therefore, it does not appear in Eq. (6.11). Overall, α increases with packing density η. It is particularly sensitive to the packing density, as indicated by the exponent of 2.0 above. This high sensitivity can be attributed to the high stresses carried by PBXs at higher packing densities.

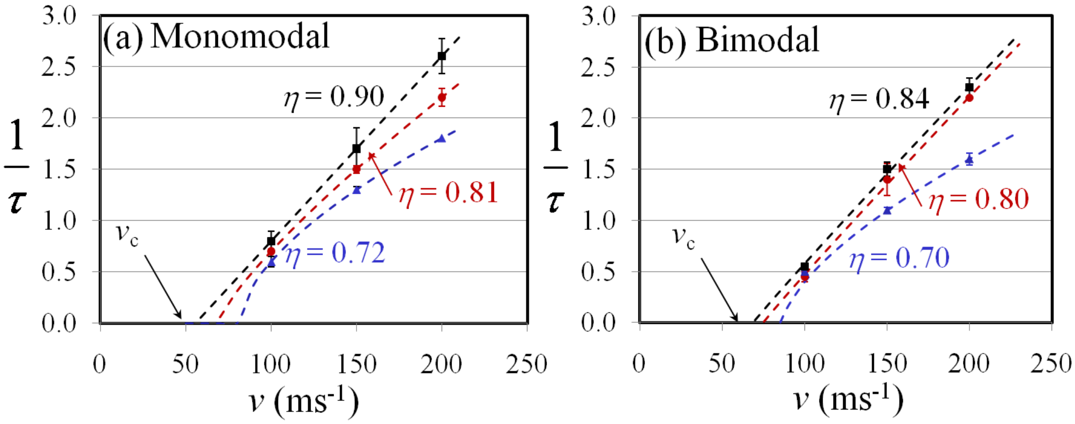

Figure 98: Scaling parameter τ as a function of impact velocity for microstructures with a range of grain volume fractions (η = 0.72 – 0.90), (a) monomodal and (b) bimodal grain size distributions. The bounds show 95% confidence intervals.

On the other hand, α decreases as the variation of specific surface area ΔS_v increases. This decrease can be explained by the physical effect of ΔS_v. As ΔS_v increases, the probability distribution of t_c becomes more spread out, which results in lower values of $1/\tau$. This, in turn, results in lower values of α.

6.5.8 Effect of Microstructure on Threshold Velocity v_c

The threshold velocity v_c is the impact velocity below which no ignition is observed. The existence of a threshold velocity was proposed by James [1, 133] based on the asymptotic nature of experimental data. The determination of v_c is important in design, manufacturing and transport of explosives as it relates to the safe handling limit. There have been numerous studies on low velocity impact testing of explosives [64-65, 146]. Most of the studies on explosive survivability focus on a limited number of "go"-"no-go" experiments performed on different batches of samples. For obvious reasons, such experiments are not amenable to studying the effects of microstructure or property variation on the stochastic response of energetic composites.

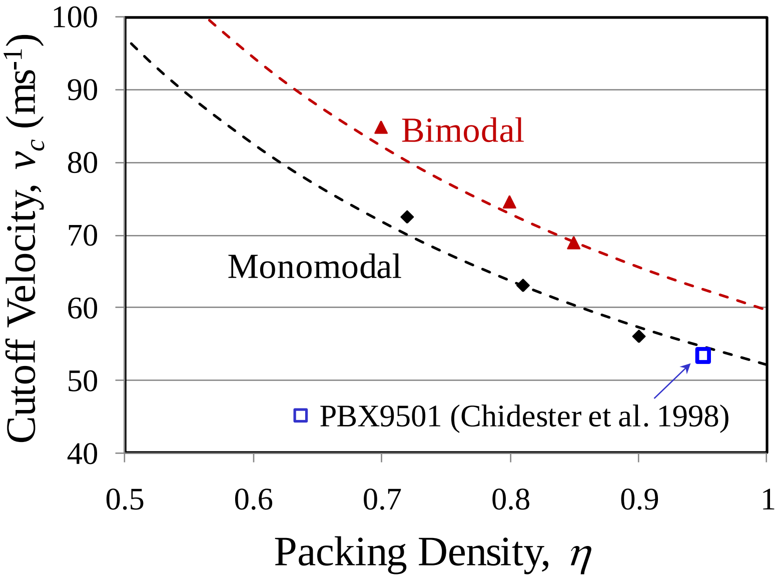

Figure 99: Comparison of experimental threshold velocity v_c for PBX9501 (Chidester et al. [146]) and numerically predicted values as a function of grain volume fraction (η = 0.70 - 0.90) and grain size distributions (monomodal, bimodal).

The Weibull model, on the other hand, can help establish a relationship between the threshold velocity and microstructure attributes. Analyzing the variation of $1/\tau$ with v makes it possible to obtain the threshold impact velocity as the impact velocity at which

$1/\tau$ goes to 0. This is done by fitting Eq. (6.10) to the results of calculations, yielding v_c as a function of microstructure.

Figure 99 shows the threshold velocity v_c as a function of the grain volume fraction for microstructures with both monomodal and bimodal grain size distributions. Clearly, the threshold velocity decreases as the grain volume fraction increases. This is expected since the same impact velocity induces higher overall stresses in microstructures with higher grain volume fractions. To better illustrate the trends, v_c can be expressed as a function of the grain volume fraction and the specific interface area in the form of

$$v_\mathrm{c}\left(\eta, S_v\right) = v_0 \eta^{-1.2}\left(1+\frac{S_v}{S_0}\right)^{0.3}, \tag{6.12}$$

where v_0 and S_0 are constants. Here, a dimensionless term is obtained by normalizing S_v using a reference value S_0. The values of the constants in Eq. (6.12) are listed in Table 10. Note that the variation in specific interface area (ΔS_v) does not affect the threshold impact velocity.

Equation (6.12) shows that a microstructure having a higher packing density is more prone to ignition and growth of reaction, provided that the specific interface area S_v is kept constant. If the two curves in Figure 99 for monomodal and bimodal microstructures are extended to a volume fraction of 1.0, the threshold velocities for η = 1.0 can be obtained. Note that, here, the η = 1.0 case is not a single crystal, but rather a polycrystalline aggregate of HMX grains. It is well known that a single crystal of HMX is hard to ignite [147]. However, a polycrystalline solid with weak grain boundaries can fracture along grain boundaries as well as in the interior of grains, leading to extensive local frictional dissipation. Hence, a polycrystalline HMX aggregate can be highly susceptible to impact-induced ignition.

The threshold velocities for the microstructures with the bimodal grain size distributions are higher than the corresponding values for microstructures with the monomodal distribution having the same overall grain volume fraction (see Figure 99). This reflects the fact that the specific interface area for the bimodal microstructures ($S_v \approx$ 25 mm^{-1}) is significantly higher than that for the monomodal microstructures ($S_v \approx$ 16 mm^{-1}). Equation (6.12) indicates that microstructures with smaller grain sizes are less susceptible to impact-induced ignition. However, a distribution with smaller grain sizes may affect other material attributes (such as strength and integrity) in different ways. Also, fine grains may give rise to smaller distances between hotspots, making detonation more homogeneous and influencing the propagation of the detonation wave. This issue is related more to the chemistry of the ignition process than to the thermo-mechanical response which is the focus of discussions here.

One way to validate the results from mesoscale calculations is to compare the predicted threshold velocity v_c with available experimental data. Using Eq. (6.12), it can determined that the threshold velocity for a PBX with 95% HMX is between 54 and 63 ms^{-1}, depending on the grain size distribution. Chidester and coworkers [146] measured the threshold impact velocities for a variety of high explosives. Specifically, the threshold velocity for PBX9501 with a density of 1.843 g-cm^{-3} was found to be approximately 53.04 ms^{-1}. Gruau et al. [65] reported that the minimum projectile velocity required for the ignition of PBX samples were 60-84 ms^{-1} in experiments. The range of threshold velocities obtained from this set of calculations correlates well with the available experimental data.

The approach outlined above for determining the threshold impact velocity is an approximation. The reason is that the threshold impact velocity obtained here is based on extrapolation of the data for higher impact velocities. A more accurate method for evaluating v_c is to run a series of calculations with successively lower impact velocities. This approach is similar to the Bruceton method [143]. However, there are two issues with this approach. The first is that it involves a large number of calculations since multiple cases need to be considered at velocities in the neighborhood of the threshold velocity. Secondly, a more serious issue encountered while using this approach is that at velocities near the threshold, enough time needs to be allowed for the material behind the stress wave to equilibrate. This necessitates a very large domain size and excessively long run times for the finite element calculations, even on parallel supercomputers.

6.5.9 Median Time to Criticality t_{50}

It is of interest to obtain some measure of the average or expected time to criticality as a function of microstructure and loading conditions. This type information is useful for comparing different types of explosives. It can also be used to validate the statistical model against well-established relations from experiments for the ignition of explosives, such as the Walker-Wasley relation [46] or the threshold relation proposed by James [1].

Two measures of average can be estimated from the Weibull distribution. The first is the expected time to criticality t_{exp}. This measure represents the weighted mean of the time to criticality $t_{exp} = t_0 + \tau \cdot \Gamma\left(1 + 1/m\right)$, where Γ is the gamma function. An alternative measure is the time at which 50% of the samples have developed critical hotspots or the time at which the probability of ignition is $P(t_{50}) = 0.5$. This time is denoted as t_{50} and it represents the median value of the Weibull distribution. The t_{50} is a commonly used measure for quantifying the sensitivity of explosives. It is analogous to h_{50} used in drop-weight testing, which is the drop height resulting in a probability of ignition of 0.5 [148]. In experiments dealing with spark ignition of gases, the criterion for defining the minimum ignition energy (MIE) is the spark energy level with a 50% probability of ignition [149]. In subsequent analyses, t_{50} is used as a measure of explosive sensitivity or susceptibility to ignition.

The Weibull distribution allows the probability distribution of the time to criticality t_c to be quantified as functions of microstructure and loading conditions. From the Weibull distribution, the median time to criticality t_{50} can be calculated as [150]

$$t_{50} = t_0 + \tau\left[\ln\left(2\right)\right]^{1/m}. \tag{6.13}$$

The variation of t_{50} as a function of critical impact velocity and microstructure parameters can be used to identify trends which determine ignition sensitivity in PBXs.

Equation (6.13) allows the Weibull form to be reduced to an ignition threshold relation similar to the James relation [1] in the v-t_{50} space (see Appendix B).

6.5.10 Impact Velocity and Median Time to Criticality t_{50}

The effect of grain volume fraction on the median time to criticality t_{50} is investigated using monomodal microstructures (Section 6.2.1). Figure 100(a-b) show the variation of t_{50} as a function of impact velocity in the range of $v = 100 \text{ and } 250 \text{ ms}^{-1}$. The calculations are performed using loading configuration in Figure 11(a). The curves are fitted to the functional form

$$\left(v - v_c\right)^n t_{50} = C\left(\eta\right) \tag{6.14}$$

to illustrate the overall trends, similar to what is done in Barua et. al. [120]. The values of n and C for the different microstructures analyzed are listed in Table 9. The calculation of t_{50} uses a set of 20 microstructure samples for each combination of packing density and loading condition. In general, as the impact velocity increases the time to criticality decreases. Higher grain volume fractions lead to more sensitive PBX. The variation in response with η is small at higher impact velocities and large at lower impact velocities. The diminishing effects of microstructure on response at high impact velocities reflects the fact that grain fracture occurs almost immediately upon onset of loading at high impact velocities, leading to high temperature increases in grains near the impact surface. The difference in t_{50} between the microstructures shown in Figure 100(a) at a high impact velocity of 200 ms^{-1} is 0.4 μs and 1.0 μs at 100 ms^{-1}.

Figure 100(b) compares the variations of t_{50} with impact velocity for monomodal and bimodal microstructures having the same grain volume fraction of $\eta \approx 0.80$. The calculations are performed for impact velocities between $v = 100$ and $250\ \mathrm{ms}^{-1}$. At high impact velocities ($v > 200\ \mathrm{ms}^{-1}$), t_{50} for both size distributions are similar with the monomodal distribution showing slightly higher t_{50} than the bimodal distribution. On the other hand, at lower impact velocities ($v < 200\ \mathrm{ms}^{-1}$), the monomodal microstructures have lower time to criticality and are, therefore, more susceptible to ignition than the bimodal microstructures. Specifically, at $v = 100\ \mathrm{ms}^{-1}$, the bimodal microstructures are ~20% safer than the monomodal microstructures.

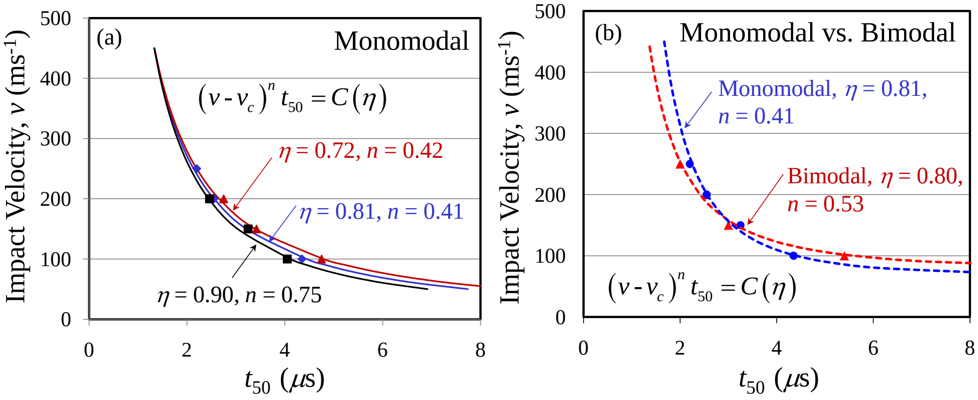

Figure 100: Relation between impact velocity and median time to criticality for (a) microstructures with a range of initial grain volume fractions having monomodal grain size distribution, (η = 0.72 – 0.90, v = 100 - 200 ms^{-1}); and (b) microstructures with monomodal and bimodal grain size distributions (η ~ 0.80, v = 100 - 200 ms^{-1}).

6.5.11 Axial Pressure and Median Time to Criticality t_{50}

The relation between axial stress (sometimes referred to as pressure, especially for shock loading) and time to criticality can provide important information regarding the key mechanisms governing ignition sensitivity. Several researchers have focused on the shock initiation threshold of PBX and GX [1, 23, 151-152]. The dependence of ignition sensitivity on input stress is a complex issue which involves two aspects: (1) the formation of critical hotspots and (2) the propagation of reaction in hotspots and associated thermal runaway. By analyzing the stress vs. time to criticality relationship from a statistical perspective using mesoscale calculations, the first issue can be addressed in some detail.

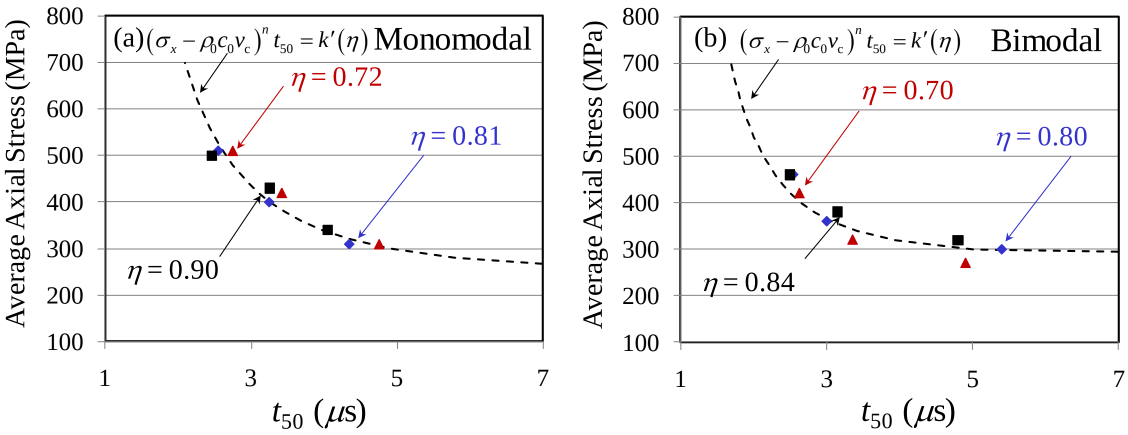

Figure 101: Relation between average axial stress and median time to criticality for (a) microstructures with a range of initial grain volume fractions having monomodal grain size distribution, (η = 0.72 – 0.90, v = 100 - 200 ms^{-1}); and (b) microstructures with a range of initial grain volume fractions having bimodal grain size distribution, (η = 0.70 – 0.84, v = 100 - 200 ms^{-1}).

The distribution of stress varies significantly with time and distance from the impact face [112]. One way to characterize stress is to analyze the average stress in the loading direction across the width of the specimen. To determine the relationship between the axial stress and the median time to criticality (σ_x–t_{50} relation), the average axial stress behind the propagating wave front is used.

The effect of grain volume fraction on the relationship between σ_x and t_{50} is first investigated using monomodal microstructures (defined in Section 6.2.1) having grain volume fractions between η = 0.70 and 0.90. Figure 101(a-b) show the variation of t_{50} with σ_x for microstructures having monomodal and bimodal grain size distributions for impact velocities between $v = 100 \text{ and } 200 \text{ ms}^{-1}$.The calculations are performed using loading configuration in Figure 11(a). The curves are fitted to a functional form which can be derived from Eq. (6.14) as

$$\left(\sigma_x - \rho_0 c_0 v_c\right)^n t_{50} = k'\left(\eta\right), \tag{6.15}$$

where ρ_0 is the effective density and c_0 is the effective initial longitudinal stress wave speed through the material. The values of ρ_0 and c_0 are provided in Table 9. Equation (6.15) is similar to the relation proposed by Walker and Wasley [46]. In general, Eq. (6.15) provides a good fit to the results from calculations. The relation between σ_x and t_{50} collapses to a single curve for all the monomodal and bimodal microstructures analyzed, suggesting that this relation is not sensitive to the microstructural mechanisms underlying the responses of PBXs under the conditions studied. Indeed, the primary heating mechanism is fracture and friction which is heavily influenced by shear stresses as well as hydrostatic pressure. To distinguish the differences in responses, it is important to consider the deviatoric part of the stress tensor. Indeed, recent results (not shown here) suggest that the equivalent stress can be used as a measure to evaluate the effect of microstructure on the time to criticality. Specifically, high input shear stresses (equivalent stress > ~0.5 GPa) almost invariably lead to the formation of critical hotspots irrespective of the packing density. On the other hand, at lower levels of the equivalent stress, microstructures having higher packing densities have a lower time to criticality and are, therefore, more susceptible to ignition. This issue shall be the subject of a future publication.

6.6 Conclusions

In this chapter, a statistical method for quantifying the ignition sensitivity of energetic materials is developed. The analysis focuses on the influence of random microstructure geometry variations on the critical time to ignition and the critical impact velocity below which no ignition occurs. These important quantities have been predicted based on basic material properties and microstructure attributes. Results show that the probability distribution of the time to criticality (t_c) largely follows the Weibull distribution. This probability distribution is quantified as a function of microstructural attributes including grain volume fraction, grain size and specific binder-grain interface area along with the stochastic variations of these attributes. The relations reveal that the specific binder-grain interface area and its stochastic variation have the most influence on the critical time to ignition and the critical impact velocity below which no ignition is observed. The predicted threshold velocity v_c for ignition is consistent with available experimental data for a PBX with 95% HMX content. The v_c for a bimodal distribution of grain sizes is lower compared with that for a monomodal distribution having the same overall packing density. Lower grain volume fractions lead to wider spreads in the distribution of the time to criticality. Microstructures having bimodal grain size distributions exhibits lower ignition sensitivity than microstructures having monomodal grain size distributions under the conditions analyzed.

This study has focused exclusively on the influence of microstructure geometry variations on the critical time to ignition at given load intensity and the critical impact velocity below which no ignition occurs. It must be pointed out that the ignition response is also affected by the stochasticity in constituent properties at the microstructure level and load conditions. Those effects have not been studied. Quantification of those effects is necessary for a complete picture of the stochastic nature of ignition sensitivity of solid high explosives to emerge.

CHAPTER 7: SUMMARY AND CONCLUSIONS

7.1 Summary

Understanding the behavior of energetic composites requires both theoretical and numerical representations of the meso scale and macro scale effects, as well as experimental observation/validation of the same. There exists a significant amount of information regarding the experimental characterization of such materials. Consequently, current, explosive formulation development is based on an Edisonian (i.e., experiment- and test-based) approach. To build predictive models that will enable the efficient development of new energetics for the next generation of munitions a better understanding of the impact sensitivity of energetic composites is required.

In the first part of this research (Chapter 2), a CFEM-based framework is developed, which accounts for microstructure, and the thermal-mechanical processes including large deformation, thermomechanical coupling, failure in the forms of microcracks in both bulk constituents and along grain/matrix interfaces, and frictional heating. In this approach, cohesive elements are embedded throughout the microstructure, along all elements boundaries allowing arbitrary fracture paths and patterns inside each phase and along the interfaces between the phases to be resolved. Using this approach, both digitized micrographs of actual materials and idealized microstructures can be analyzed. A systematic set of calculations are carried out focusing on the effects of composition, phase arrangement, phase size distribution and phase morphology on the evolution of temperature field, damage and failure. Calculations show that higher volume fractions of HMX granules correspond to more severe heating and a lower threshold for fracture initiation. In general, bimodal distributions of granule sizes are more beneficial to the mechanical integrity of the composites than monomodal distributions. Grains with planar facets increase the likelihood of failure through grain-matrix debonding relative to grains with rounded shapes.

The CFEM framework is used to systematically study energy localization in two phase HMX/Estane PBXs in Chapters 3. Here, the focus is to establish relationships between microstructural features such as grain size, distribution and contiguity and stress-strain response, failure and heating. The responses of the PBXs are explored over a range of initial temperatures, strain rates, and degrees of confinement. To study energy localization, a method for identifying hot spots is developed, allowing the size and temperature distributions of hot spots to be analyzed. This allows the spatial distribution of hotspots to be analyzed as functions of loading and microstructural attributes. Results show that at higher loading rates, harder binder response causes hot spots to be localized near the impact face. At lower loading rates, hot spots tend to be more spread out and associated with regions of intense shear deformation of the binder. The average temperature of the hot spots increases with strain rate. Also, the hotspot density increases with packing density η, with the rate of formation being proportional to η. On the other hand, the total number of hot spots appears insensitive to strain rate over the range of conditions analyzed. The analysis shows that stress triaxiality has a significant influence on the density and spatial distribution of hot spots. The hot spots are more densely populated, are more uniformly distributed spatially and have higher temperatures when the specimen is confined. The results are used to obtain an empirical relation to quantify the effects of microstructural attributes (volume fraction, grain size and shape) and loading conditions (degree of confinement) on the evolution of hot spots. This relation provides useful statistical information regarding hot spots and can be used as input, for instance, in continuum level reactive burn models.

The thermomechanical responses of the PBXs are distinct when the stress state is homogeneous as opposed to a transient stress state. In Chapter 4, the effect of transient stress wave is studied on the microstructure of HMX/Estane PBXs. The microstructural samples analyzed have an aspect ratio of 5:1 (15 mm × 3 mm), allowing the transient wave propagation process resulting from normal impact to be resolved. The analysis shows that the overall wave speed through the microstructures depends on both the grain volume fraction and interface bonding strength between the constituents and that the distance traversed by the stress wave before frictional dissipation initiates is independent of the grain volume fraction but increases with impact velocity. Energy dissipated per unit volume due to fracture is highest near the impact surface and deceases to zero at the stress wave front. On the other hand, the peak temperature rises are ~ 2 – 3 mm away from the impact surface. Scaling laws are developed for the maximum dissipation rate and the highest temperature rise as functions of impact velocity, grain volume fraction and grain-binder interfacial bonding strength.

In Chapter 5, a novel criterion for the ignition of granular explosives (GXs) and polymer-bonded explosives (PBXs) under shock and non-shock loading is developed. The formulation is based on integration of a quantification of the distributions of the sizes and locations of hotspots in loading events using a cohesive finite element method (CFEM) developed recently and the characterization by Tarver *et al.* [29] of the critical size-temperature threshold of hotspots required for chemical ignition of solid explosives.

The criterion, along with the CFEM capability to quantify the thermal-mechanical behavior of GXs and PBXs, allows the critical impact velocity for ignition, time to ignition, and critical input energy at ignition to be determined as functions of material composition, microstructure and loading conditions. The applicability of the relation between the critical input energy (E) and impact velocity of James [1] for shock loading is examined, leading to a modified interpretation which is sensitive to microstructure and loading condition. As an application, numerical studies are undertaken to evaluate the ignition threshold of granular HMX and HMX/Estane PBX under loading with impact velocities up to 350 ms^{-1} and strain rates up to 10^5 s^{-1}. Results show that, for the GX, the time to criticality (t_c) is strongly influenced by initial porosity, but is insensitive to grain size. Analyses also lead to a quantification of the differences between the responses of the GXs and PBXs in terms of critical impact velocity for ignition, time to ignition, and critical input energy at ignition. Since the framework permits explicit tracking of the influences of microstructure, loading and mechanical constraints, the calculations also show the effects of stress wave reflection and confinement condition on the ignition behaviors of GXs and PBXs.

In Chapter 6, a novel approach for computationally predicting and quantifying the stochasticity of the ignition process in polymer-bonded explosives under impact loading is developed [138]. The method, the computational equivalent of carrying out multiple experiments under the same conditions, involves subjecting sets of statistically similar microstructure samples to identical overall loading and characterizing the statistical distribution of the ignition response of the samples. It is shown that the probability distribution of the time to criticality (t_c) follows the Weibull distribution. Subsequently, the probability distribution is quantified as a function of microstructural attributes including grain volume fraction, grain size and specific binder-grain interface area along with the stochastic variations of these attributes. The relations reveal that the specific binder-grain interface area and its stochastic variation have the most influence on the critical time to ignition and the critical impact velocity below which no ignition is observed. The predicted threshold velocity v_c for ignition is consistent with available experimental data for a PBX with 95% HMX content. Finally, it is shown that the probability distribution in the Weibull form can be reduced to an ignition threshold relation similar to the James relation [1] in the *v*-*t* space.

7.2 Suggestions for Future Work

There are a number of avenues to extend this research in the field of ignition sensitivity of heterogeneous energetic materials. One area is the understanding of hotspot dynamics. Future studies need to address the aspect of growth and interactions among neighboring hotspots. In Chapter 5, hotspot characteristics are obtained using the size-temperature threshold. The thermal criticality analysis on the hotspot distribution is carried out by using available data on the critical size-temperature relationship of hotspots. However, the effect of hotspot density or shape on the ignition sensitivity is not known. Future studies can further explore this use by incorporating chemical kinetics calculations within the thermomechanical framework.

Under moderate shocks, where the pressure is in the order of hundreds of megapascals the timescale of impact-induced-deformation is of the order of microseconds, whereas the time taken to for a hotspot to evolve from thermal criticality to thermal explosion is of the order of several milliseconds or even seconds, depending upon the size and temperature of the hotspot. Clearly, a fully coupled thermal-mechanical-chemical approach is challenging, since it would require sufficient time resolution to capture both the mechanical deformation (~ microseconds) and the chemical reaction (~ milliseconds - seconds). One way to overcome this issue is to use a two step approach: (1) use the current CFEM framework to analyze the temperature rise as a result of thermomechanical dissipation processes and then (2) analyze the hotspot dynamics using a coupled chemical kinetics and heat conduction analysis (without accounting for further mechanical deformation). The assumption is that, once the initial shock wave has passed, further macroscale deformation does not occur in the sample and the evolution of hotspots is primarily controlled by chemical reactions and thermal conduction. This is a complex issue and care must be taken not to oversimplify the physics of the problem. Another aspect to be accounted for future analyses is the phase change and mass transport occurring as a result of the chemical reaction process.

Another aspect to consider is the experimental validation of the numerical predictions. Currently, a limited variety of data is available such as the stress-strain responses, times to ignition, critical impact velocities, etc for certain types of explosives. However, these are measurements obtained at the macro-level and do not directly provide information regarding the failure mechanisms occurring at the microstructure level. Thus it is difficult to directly correlate numerical predictions at the mesoscale with experimental results. Recent work being carried out at University of Illinois at Urbana-Champaign on high-speed thermal imaging microscopy may provide a validation technique for comparing the numerically obtained distributions of hotspots. Another type of validation could be the qualitative or quantitative comparison of experimentally obtained fractured surfaces of damaged crystals with numerically obtained fracture patterns.

Energetic crystals are anisotropic and crystal plasticity formulation of the constitutive models needs to be considered since it can be a significant source of heterogeneity at the microstructure level [153-154]. This should be fairly straight forward since considerable information is available in the literature about the elastic constants and constituent properties of energetic crystals [155-157]. The incorporation of crystal plasticity using a 3D framework would help in providing a more accurate representation of the energy localization occurring at the grain level. Moreover, such framework(s) could be used to analyze the effect of microstructural aspects such as grain morphology and clustering of particles.

The ultimate goal of research in the field of ignition sensitivity is to design explosives with desired characteristics. Such explosives would have tailored safety and performance attributes [31, 158-160]. The analysis carried out as part of this research provides trends and relationships between microstructure, loading conditions and certain performance parameters [such as Eq. (3.5), (4.2), (5.11), (6.3) and (6.12)]. Such relations help to capture the behavior at the microscale and scale it up to the macroscale. However, this is still a work in progress. For the purpose of design, it is important to develop a design space, keeping in mind the relative importance of the different microstructure parameters such as, but not limited to – composition, phases, material properties, particle size distributions, morphologies, interfaces, defects, etc. The stochastic analysis carried out in Chapter 6 provides a framework to quantify the effect of variation in microstructure parameters. Research is currently underway, which shall combine the stochastic effect of microstructure geometry with the effect of variations in material properties and random defects such as imperfect interfaces, which are inherently present in all microstructure samples. This is essential if a comprehensive link is to be made between microstructure and ignition sensitivity.

APPENDIX A

A.1 Derivation of Criticality Condition [Eq. (5.11)]

Equation (5.10) can also be rewritten as

$$E = \int_{x=0}^{x} \sigma_{ext} \mathrm{d}x. \tag{A.1}$$

The stress-displacement relation in Eq. (5.8) can be substituted into Eq. (A.1) to obtain the critical input energy *E* as

$$E = \int_{x=0}^{x} \left(\rho_0 c_0 v + K \left(\frac{x}{l_0} \right)^{\gamma} \right) \mathrm{d}x. \tag{A.2}$$

Substituting $x = vt$ (for a constant boundary velocity, *v*) into the above expression and integrating yield

$$E = \rho_0 c_0 v^2 t + \frac{K}{(\gamma+1) l_0^{\gamma}} (vt)^{(\gamma+1)}. \tag{A.3}$$

If the HJ relation in the form of Eq. (5.7) is used, the critical condition can be expressed as

$$1 = \frac{2\Sigma_{\mathrm{c}}}{v^2} + \frac{E_{\mathrm{c}}}{\rho_0 c_0 v^2 t + \frac{K}{(\gamma+1) l_0^{\gamma}} (vt)^{(\gamma+1)}}. \tag{A.4}$$

This relation can be recast into the more convenient form of

$$\left(1-\frac{2\Sigma_{\mathrm{c}}}{v^2}\right)\left[1+k(\eta)v^{1/\eta^4-1}t^{1/\eta^4}\right]v^2t=F(\eta), \tag{A.5}$$

where,

$$\begin{cases} k(\eta)=\dfrac{K}{\left(\dfrac{1}{\eta^4}+1\right)\rho_0 c_0 l_0^{\frac{1}{\eta^4}}}, \\ \\ \text{and}\quad F(\eta)=\rho_0 c_0 E_{\mathrm{c}}(\eta)\,. \end{cases} \tag{A.6}$$

Note that in Eqs. (A.2)-(A.6), $\rho_0 c_0$ is a function of η, as shown in Figure 82.

APPENDIX B

B.1 Derivation of Criticality Condition from Weibull Distribution

As mentioned Section 6.4.9 , the median time to criticality t_{50} can be obtained from the Weibull distribution [Eq. (6.3)]. The relation between τ and v [Eq. (6.10)] can be substituted into Eq. (6.13) to obtain a relation between v and t_{50} as

$$t_{50} = t_0 + \tau_{\mathrm{ref}} \left(\frac{v_{\mathrm{ref}}}{v - v_{\mathrm{c}}} \right)^{\alpha} \left[\ln(2) \right]^{1/m} . \tag{B.1}$$

This relation can be recast into the more convenient form of

$$\left(v - v_{\mathrm{c}} \right)^{\alpha} \left(t_{50} - t_0 \right) = F\left(\eta, S_v, \Delta S_v \right), \tag{B.2}$$

where

$$F\left(\eta, S_v, \Delta S_v \right) = \tau_{\mathrm{ref}}\left(\eta, S_v, \Delta S_v \right) v_{\mathrm{ref}}{}^{\alpha} \left[\ln(2) \right]^{1/m} . \tag{B.3}$$

REFERENCES

[1] H. R. James, "An extension to the critical energy criterion used to predict shock initiation thresholds," *Propellants Explos. Pyrotech.*, vol. 21, pp. 8-13, Feb 1996.

[2] S. J. P. Palmer, J. E. Field, and J. M. Huntley, "Deformation, strengths and strains to failure of polymer bonded explosives," *Proceedings of the Royal Society of London Series a-Mathematical Physical and Engineering Sciences*, vol. 440, pp. 399-419, Feb 1993.

[3] J. Corley, W. Riedel, S. Hiermaier, P. Weidemaier, and M. Thoma, "A combined experimental/computational approach for assessing the high strain rate response of high explosive simulants and other viscoelastic particulate composite materials," in *Shock Compression of Condensed Matter-2001, Pts 1 and 2, Proceedings*. vol. 620, M. D. Furnish, *et al.*, Eds., ed Melville: Amer Inst Physics, 2002, pp. 705-708.

[4] W. Fickett and W. C. Davis, *Detonation: theory and experiment*: Dover Publications, 2011.

[5] B. Asay, *Non-Shock Initiation of Explosives*. Berlin, Heidelberg :: Springer-Verlag Berlin Heidelberg, 2010.

[6] J. C. Foster Jr, D. S. Stewart, and K. Thomas, "Multi-Scale Statistical Design of HIgh Energy Density Materials," in *AIP Conference Proceedings*, 2007, p. 369.

[7] P. W. Chen, F. L. Huang, and Y. S. Ding, "Microstructure, deformation and failure of polymer bonded explosives," *Journal of Materials Science,* vol. 42, pp. 5272-5280, Jul 2007.

[8] G. T. Gray, W. R. Blumenthal, D. J. Idar, and C. M. Cady, "Influence of temperature on the high-strain-rate mechanical behavior of PBX 9501," in *Shock Compression of Condensed Matter - 1997*. vol. 429, S. C. Schmidt, *et al.*, Eds., ed Melville: Amer Inst Physics, 1998, pp. 583-586.

[9] R. K. Govier, G. T. Gray, and W. R. Blumenthal, "Comparison of the influence of temperature on the high-strain-rate mechanical responses of PBX 9501 and EDC37," 2008, pp. 535-538.

[10] D. A. Wiegand and B. Reddingius, "Mechanical properties of confined explosives," *J. Energ. Mater.*, vol. 23, pp. 75-98, Apr-Jun 2005.

[11] C. R. Siviour, P. R. Laity, W. G. Proud, J. E. Field, D. Porter, P. D. Church, P. Gould, and W. Huntingdon-Thresher, "High strain rate properties of a polymer-bonded sugar: their dependence on applied and internal constraints," *Proceedings of the Royal Society a-Mathematical Physical and Engineering Sciences*, vol. 464, pp. 1229-1255, May 2008.

[12] R. Menikoff, "Elastic-plastic response of HMX," *Research Highlights 2005*, 2005.

[13] P. W. Chen, H. M. Xie, F. L. Huang, T. Huang, and Y. S. Ding, "Deformation and failure of polymer bonded explosives under diametric compression test," *Polymer Testing*, vol. 25, pp. 333-341, May 2006.

[14] S. J. P. Palmer and J. E. Field, "The deformation and fracture of Beta-HMX," *Proceedings of the Royal Society of London Series a-Mathematical Physical and Engineering Sciences*, vol. 383, pp. 399-&, 1982.

[15] C. B. Skidmore, D. S. Phillips, S. F. Son, and B. W. Asay, "Characterization of HMX particles in PBX 9501," 1998, pp. 579-582.

[16] G. Liu and H. Yu, "Stereological characterization of particle contiguity," *Journal of Microscopy-Oxford*, vol. 181, pp. 82-87, Jan 1996.

[17] H. L. Berghout, S. F. Son, C. B. Skidmore, D. J. Idar, and B. W. Asay, "Combustion of damaged PBX 9501 explosive," *Thermochimica Acta*, vol. 384, pp. 261-277, Feb 2002.

[18] P. J. Rae, H. T. Goldrein, S. J. P. Palmer, J. E. Field, and A. L. Lewis, "Quasi-static studies of the deformation and failure of beta-HMX based polymer bonded explosives," *Proceedings of the Royal Society of London Series a-Mathematical Physical and Engineering Sciences*, vol. 458, pp. 743-762, Mar 2002.

[19] C. Liu, "Fracture of the PBX 9501 high explosive," Los Alamos National Laboratory, Los Alamos, NM 87545.

[20] D. M. Williamson, S. J. P. Palmer, and W. G. Proud, "Fracture Studies of PBX Simulant Materials," American Institute of Physics2005.

[21] C. M. Cady, W. R. Blumenthal, G. T. Gray, and D. J. Idar, "Mechanical properties of plastic-bonded explosive binder materials as a function of strain-rate and temperature," *Polymer Engineering and Science*, vol. 46, pp. 812-819, Jun 2006.

[22] R. J. Spear and V. Nanut, "Reversal of particle size/shock sensitivity relationship at small particle size for pressed heterogeneous explosives under sustained shock loading," *Journal of Energetic Materials*, vol. 7, pp. 77-114, 1989.

[23] D. B. Hayes and D. E. Mitchell, *Constitutive equation for the shock response of porous hexanitrostilbene (HNS) explosive*, 1978.

[24] B. A. Khasainov, B. S. Ermolaev, H. N. Presles, and P. Vidal, "On the effect of grain size on shock sensitivity of heterogeneous high explosives," *Shock Waves,* vol. 7, pp. 89-105, Apr 1997.

[25] A. D. Resnyansky and G. T. Gray, "Numerical simulations of the influence of loading pulse shape on SHPB measurements," in *Shock Compression of Condensed Matter-2001, Pts 1 and 2, Proceedings*. vol. 620, M. D. Furnish, *et al.*, Eds., ed Melville: Amer Inst Physics, 2002, pp. 315-318.

[26] E. M. Mas, B. E. Clements, and D. C. George, "Direct Numerical Simulations of PBX 9501," *AIP Conference Proceedings,* vol. 706, pp. 389-392, 2004.

[27] M. R. Baer, "Modeling heterogeneous energetic materials at the mesoscale," *Thermochimica Acta,* vol. 384, pp. 351-367, Feb 2002.

[28] D. J. Benson and P. Conley, "Eulerian finite-element simulations of experimentally acquired HMX microstructures," *Model. Simul. Mater. Sci. Eng.,* vol. 7, pp. 333-354, May 1999.

[29] C. M. Tarver, S. K. Chidester, and A. L. Nichols, "Critical conditions for impact- and shock-induced hot spots in solid explosives," *Journal of Physical Chemistry,* vol. 100, pp. 5794-5799, Apr 1996.

[30] R. A. Austin, D. L. McDowell, and D. J. Benson, "Numerical simulation of shock wave propagation in spatially-resolved particle systems," *Model. Simul. Mater. Sci. Eng.,* vol. 14, pp. 537-561, Jun 2006.

[31] H. J. Choi, R. Austin, J. K. Allen, D. L. McDowell, F. Mistree, and D. J. Benson, "An approach for robust design of reactive power metal mixtures based on non-deterministic micro-scale shock simulation," *J. Comput-Aided Mater. Des.*, vol. 12, pp. 57-85, Jan 2005.

[32] R. A. Austin and D. L. McDowell, "A dislocation-based constitutive model for viscoplastic deformation of fcc metals at very high strain rates," *Int. J. Plast.*, vol. 27, pp. 1-24, 2011.

[33] R. A. Austin, D. L. McDowell, and D. J. Benson, "Mesoscale simulation of shock wave propagation in discrete Ni/Al powder mixtures," *J. Appl. Phys.*, vol. 111, pp. 123511-123511-9, 2012.

[34] R. Menikoff, "Granular explosives and initiation sensitivity," *Detonation Theory & Application, T14,* vol. Special Feature, 2000.

[35] R. Menikoff, "Pore collapse and hot spots in HMX," presented at the APS Topical Conference, Portland Oregon, 2003.

[36] M. Ortiz and A. Pandolfi, "Finite-deformation irreversible cohesive elements for three-dimensional crack-propagation analysis," *International Journal for Numerical Methods in Engineering,* vol. 44, pp. 1267-1282, Mar 1999.

[37] S. K. Dwivedi and H. D. Espinosa, "Modeling dynamic crack propagation in fiber reinforced composites including frictional effects," 2003, pp. 481-509.

[38] B. Banerjee, C. M. Cady, and D. O. Adams, "Micromechanics simulations of glass-estane mock polymer bonded explosives," *Model. Simul. Mater. Sci. Eng.*, vol. 11, pp. 457-475, Jul 2003.

[39] Y.-Q. Wu and F.-L. Huang, "A micromechanical model for predicting combined damage of particles and interface debonding in PBX explosives," *Mechanics of Materials,* vol. 41, pp. 27-47, Jan 2009.

[40] R. Panchadhara and K. A. Gonthier, "Mesoscale analysis of volumetric and surface dissipation in granular explosive induced by uniaxial deformation waves," *Shock Waves,* vol. 21, pp. 43-61, Feb 2011.

[41] N. R. Barton, N. W. Winter, and J. E. Reaugh, "Defect evolution and pore collapse in crystalline energetic materials," *Model. Simul. Mater. Sci. Eng.,* vol. 17, Apr 2009.

[42] P. D. Peterson, J. T. Mang, M. A. Fletcher, B. W. Olinger, and E. L. Roemer, "Influence of pressing parameters on the microstructure, of PBX 9501," in *Shock Compression of Condensed Matter - 2003, Pts 1 and 2, Proceedings*. vol. 706, M. D. Furnish, *et al.*, Eds., ed Melville: Amer Inst Physics, 2004, pp. 796-799.

[43] P. A. Urtiew and C. M. Tarver, "Shock initiation of energetic materials at different initial temperatures (review)," *Combust. Explos.,* vol. 41, pp. 766-776, Nov-Dec 2005.

[44] D. J. Idar, J. W. Straight, M. A. Osborn, C. B. Skidmore, D. S. Phillips, and G. A. Buntain, "PBX 9501 high explosive violent reaction: Phase II baseline and aged experiments," 2000.

[45] Y. Hamate and Y. Horie, "Ignition and detonation of solid explosives: a micromechanical burn model," *Shock Waves,* vol. 16, pp. 125-147, Dec 2006.

[46] F. E. Walker and R. J. Wasley, "Critical Energy for Shock Initiation of Heterogeneous Explosives," *Explosivstoffe,* vol. 17, p. 9, 1969.

[47] M. R. Baer, C. A. Hall, R. L. Gustavsen, D. E. Hooks, and S. A. Sheffield, "Isentropic loading experiments of a plastic bonded explosive and constituents," *J. Appl. Phys.*, vol. 101, p. 12, Feb 2007.

[48] W. M. Trott, M. R. Baer, J. N. Castaneda, L. C. Chhabildas, and J. R. Asay, "Investigation of the mesoscopic scale response of low-density pressings of granular sugar under impact," *J. Appl. Phys.*, vol. 101, Jan 2007.

[49] R. Menikoff, "Compaction wave profiles in granular HMX," Los Alamos National Laboratory, Los Alamos, NM 87544.

[50] H. Kim, A. Lagutchev, and D. D. Dlott, "Surface and interface spectroscopy of high explosives and binders: HMX and Estane," *Propellants Explos. Pyrotech.*, vol. 31, pp. 116-123, Apr 2006.

[51] A. Tokmakoff, M. D. Fayer, and D. D. Dlott, "Chemical-Reaction Inititation and Hot-Spot Formation in Shocked Energetic Molecular Materials," *J. Phys. Chem.*, vol. 97, pp. 1901-1913, Mar 4 1993.

[52] B. F. Henson, B. W. Asay, L. B. Smilowitz, and P. M. Dickson, "Ignition chemistry in HMX from thermal explosion to detonation," in *Shock Compression of Condensed Matter-2001, Pts 1 and 2, Proceedings*. vol. 620, M. D. Furnish, *et al.*, Eds., ed, 2002, pp. 1069-1072.

[53] J. K. Dienes, Q. H. Zuo, and J. D. Kershner, "Impact initiation of explosives and propellants via statistical crack mechanics (vol 54, pg 1237, 2006)," *J. Mech. Phys. Solids*, vol. 54, pp. 2235-2240, Oct 2006.

[54] Y. Q. Wu and F. L. Huang, "A microscopic model for predicting hot-spot ignition of granular energetic crystals in response to drop-weight impacts," *Mechanics of Materials,* vol. 43, pp. 835-852, Dec 2011.

[55] R. V. Browning and R. J. Scammon, "Microstructural model of ignition for time varying loading conditions," in *Shock Compression of Condensed Matter-2001, Pts 1 and 2, Proceedings*. vol. 620, M. D. Furnish, *et al.*, Eds., ed Melville: Amer Inst Physics, 2002, pp. 987-990.

[56] R. Engelke and S. A. Sheffield, "Initiation and propagation of detonation in condensed-phase high explosives," *High-Pressure Shock Compression of Solids III,* vol. 3, p. 171, 1998.

[57] N. N. Thadhani, "Shock-induced chemical reactions and synthesis of materials," *Progress in Materials Science,* vol. 37, pp. 117-226, 1993.

[58] S. G. Cochran, "Statistical treatment of heterogeneous chemical reaction in shock-initiated explosives," California Univ., Livermore (USA). Lawrence Livermore Lab.1980.

[59] E. L. Lee and C. M. Tarver, "Phenomenological Model of Shock Initiation in Heterogeneous Explosives," *Physics of Fluids,* vol. 23, pp. 2362-2372, 1980.

[60] Y. Horie, Y. Hamate, D. Greening, and T. Dey, "Reactive burn modeling of solid explosives with a statistical treatment of hot spots in two spatial dimensions," in *AIP Conference Proceedings,* 2004, p. 989.

[61] A. L. Nichols III and C. M. Tarver, "A Statistical Hot Spot Reactive Flow Model for Shock Initiation and Detonation of Solid High Explosives," in *Twelfth*

International Symposium on Detonation, Office of Naval Research, San Diego, CA, 2002.

[62] L. Hill and B. Zimmermann, "On the Burn Topology of Hot-Spot Initiated Reactions," *Bulletin of the American Physical Society,* vol. 54, 2009.

[63] F. Baras, G. Nicolis, M. M. Mansour, and J. Turner, "Stochastic theory of adiabatic explosion," *Journal of statistical physics,* vol. 32, pp. 1-23, 1983.

[64] C. Gruau and D. Picart, "Numerical prediction of high explosive ignition under low velocity impact," *Foundations Civil and Environmental Eng,* vol. 12, pp. 33-48, 2008.

[65] C. Gruau, D. Picart, R. Belmas, E. Bouton, F. Delmaire-Sizes, J. Sabatier, and H. Trumel, "Ignition of a confined high explosive under low velocity impact," *Int. J. Impact Eng.,* vol. 36, pp. 537-550, Apr 2009.

[66] S. K. Chidester, C. M. Tarver, and C. G. Lee, "Impact ignition of new and aged solid explosives," in *AIP Conference Proceedings*, 1998, p. 707.

[67] M. R. Baer, D. K. Gartling, and P. E. DesJardin, "Probabilistic models for reactive behaviour in heterogeneous condensed phase media," *Combustion Theory and Modelling*, vol. 16, pp. 75-106, 2012.

[68] A. Needleman, "An analysis of tensile decohesion along an interface," *J. Mech. Phys. Solids*, vol. 38, pp. 289-324, 1990.

[69] V. Tvergaard and J. W. Hutchinson, "The relation between crack-growth resistance and fracture process parameters in elastic plastic solids," *J. Mech. Phys. Solids*, vol. 40, pp. 1377-1397, Aug 1992.

[70] V. Tvergaard and A. Needleman, "Effect of crack meandering on dynamic, ductile fracture," *J. Mech. Phys. Solids,* vol. 40, pp. 447-471, Feb 1992.

[71] A. Needleman and V. Tvergaard, "Mesh effects in the analysis of dynamic ductile crack-growth," *Engineering Fracture Mechanics,* vol. 47, pp. 75-91, Jan 1994.

[72] X. P. Xu and A. Needleman, "Numerical simulations of fast crack-growth in brittle solids," *J. Mech. Phys. Solids,* vol. 42, pp. 1397-&, Sep 1994.

[73] G. T. Camacho and M. Ortiz, "Computational modelling of impact damage in brittle materials," *Int. J. Solids Struct.,* vol. 33, pp. 2899-2938, Aug 1996.

[74] H. D. Espinosa, P. D. Zavattieri, and S. K. Dwivedi, "A finite deformation continuum discrete model for the description of fragmentation and damage in brittle materials," 1998, pp. 1909-1942.

[75] P. P. Camanho, C. G. Davila, and M. F. de Moura, "Numerical simulation of mixed-mode progressive delamination in composite materials," *Journal of Composite Materials,* vol. 37, pp. 1415-1438, 2003.

[76] K. Minnaar and M. Zhou, "Characterization of impact in composite laminates," *AIP Conference Proceedings,* vol. 620, p. 1208, 2002.

[77] J. Zhai and M. Zhou, "Finite element analysis of micromechanical failure modes in a heterogeneous ceramic material system," *Int. J. Fract.,* vol. 101, pp. 161-180, 2000.

[78] V. Tomar, J. Zhai, and M. Zhou, "Bounds for element size in a variable stiffness cohesive finite element model," *International Journal for Numerical Methods in Engineering,* vol. 61, pp. 1894-1920, 2004.

[79] A. Barua and M. Zhou, "A Lagrangian Framework for Analyzing Microstructural Level Response of Polymer-Bonded Explosives," *Model. Simul. Mater. Sci. Eng.*, vol. 19, p. 24, Jun 2011.

[80] A. Barua and M. Zhou, "Computational analysis of temperature rises in microstructures of HMX-Estane PBXs," *Comput. Mech.*, pp. 1-9, 2012.

[81] P. J. Rae, S. J. P. Palmer, H. T. Goldrein, J. E. Field, and A. L. Lewis, "Quasi-static studies of the deformation and failure of PBX 9501," *Proceedings of the Royal Society of London Series a-Mathematical Physical and Engineering Sciences*, vol. 458, pp. 2227-2242, Sep 2002.

[82] A. M. Gokhale, A. Tewari, and H. Garmestani, "Constraints on microstructural two-point correlation functions," *Scripta Materialia*, vol. 53, pp. 989-993, Oct 2005.

[83] D. Stoyan, W. S. Kendall, J. Mecke, and D. Kendall, *Stochastic geometry and its applications* vol. 8: Wiley Chichester, 1987.

[84] A. Gokhale, A. Tewari, and H. Garmestani, "Constraints on microstructural two-point correlation functions," *Scripta materialia*, vol. 53, pp. 989-993, 2005.

[85] H. Singh, A. M. Gokhale, S. I. Lieberman, and S. Tamirisakandala, "Image based computations of lineal path probability distributions for microstructure representation," *Materials Science and Engineering a-Structural Materials Properties Microstructure and Processing*, vol. 474, pp. 104-111, Feb 2008.

[86] A. Tewari, A. M. Gokhale, J. E. Spowart, and D. B. Miracle, "Quantitative characterization of spatial clustering in three-dimensional microstructures using two-point correlation functions," *Acta Mater.*, vol. 52, pp. 307-319, Jan 2004.

[87] C. M. Cady, W. R. Blumenthal, G. T. Gray, and D. J. Idar, "Determining the constitutive response of polymeric materials as a function of temperature and strain rate," 2003, pp. 27-32.

[88] E. M. Mas, Clements, B.E., "A viscoelastic model for PBX binders," *http://lib-www.lanl.gov/la-pubs/00818442.pdf,* 1996.

[89] M. Kaliske and H. Rothert, "Formulation and implementation of three-dimensional viscoelasticity at small and finite strains," *Comput. Mech.,* vol. 19, pp. 228-239, Feb 1997.

[90] H. H. Cady, A. C. Larson, and D. T. Cromer, "The crystal structure of alpha-HMX and a refinement of the structure of beta-HMX," *Acta Cryst.,* vol. 16, pp. 617-623, 1963.

[91] R. Menikoff, Sewell, T.D., "Constituent properties of HMX needed for meso-scale simulaitons," *Los Alamos National Lab.,* 2001.

[92] T. D. Sewell and R. Menikoff, "Complete equation of state for Beta-HMX and implications for initiation," Los Alamos National Laboratory2003.

[93] E. M. Mas, B. E. Clements, and D. C. George, "Direct numerical simulations of PBX 9501," Los Alamos National Laboratory, Los Alamos, NM 87545.

[94] C. B. Skidmore, D. S. Philips, B. W. Assay, D. J. Idar, P. M. Howe, and D. S. Bolme, "Microstructural effects in PBX-9501 damaged by shear impact.," *Shock Compression of Condensed Matter*, pp. 659-662, 1999.

[95] J. Zhai, V. Tomar, and M. Zhou, "Micromechanical simulation of dynamic fracture using the cohesive finite element method," *Journal of Engineering*

Materials and Technology-Transactions of the Asme, vol. 126, pp. 179-191, Apr 2004.

[96] H. Tan, C. Liu, Y. Huang, and P. H. Geubelle, "The cohesive law for the particle/matrix interfaces in high explosives," *J. Mech. Phys. Solids,* vol. 53, pp. 1892-1917, Aug 2005.

[97] F. P. Bowden and D. Tabor, *The friction and lubrication of solids* vol. 1: Oxford university press, 2001.

[98] M. Zhou, A. Needleman, and R. J. Clifton, "Finite-element simulations of shear localization in plate impact," *J. Mech. Phys. Solids,* vol. 42, pp. 423-458, Mar 1994.

[99] T. Belytschko, R. L. Chiapetta, and H. D. Bartel, "Efficient large scale non-linear transient analysis by finite elements," *International Journal for Numerical Methods in Engineering,* vol. 10, pp. 579-596, 1976.

[100] L. Green, A. Weston, and J. Van Velkinburg, "Mechanical and Frictional Behavior of Skid Test Hemispherical Billets," California Univ., Livermore. Lawrence Livermore Lab.1971.

[101] S. Chidester, L. Green, and C. Lee, "A frictional work predictive method for the initiation of solid high explosives from low-pressure impacts," Lawrence Livermore National Lab., CA (United States)1993.

[102] P. M. Dickson, G. R. Parker, L. B. Smilowitz, J. M. Zucker, and B. W. Asay, "Frictional heating and ignition of energetic materials," 2005.

[103] J. F. Peters, M. Muthuswamy, J. Wibowo, and A. Tordesillas, "Characterization of force chains in granular material," *Phys. Rev. E,* vol. 72, Oct 2005.

[104] C. R. Siviour and W. G. Proud, "Damage formation during high strain rate deformation of PBS9501," *AIP Conference Proceedings,* vol. 955, pp. 799-802, 2007.

[105] A. van der Heijden, R. H. B. Bouma, and A. C. van der Steen, "Physicochemical parameters of nitramines influencing shock sensitivity," *Propellants Explos. Pyrotech.,* vol. 29, pp. 304-313, Oct 2004.

[106] A. Barua, Y. Horie, and M. Zhou, "Energy localization in HMX-Estane polymer-bonded explosives during impact loading," *J. Appl. Phys.,* vol. 111, p. 11, 2012.

[107] N. K. Bourne and G. T. Gray, "Dynamic response of binders; teflon, estane (TM) and Kel-F-800 (TM)," *J. Appl. Phys.,* vol. 98, p. 9, Dec 2005.

[108] C. S. Smith and L. Guttman, "Measurement of internal boundaries in three-dimensional structures by random sectioning," *Trans. AIME,* vol. 97, p. 81, 1953.

[109] A. Barua and M. Zhou, "Heating in microstructures of HMX/Estane PBX during dynamic deformation," *Shock Compression of Condensed Matter,* vol. 1426, pp. 1475-1478, 2011.

[110] R. W. Armstrong and W. L. Elban, "Temperature rise at a dislocation pile-up breakthrough," *Materials Science and Engineering a-Structural Materials Properties Microstructure and Processing*, vol. 122, pp. L1-L3, Dec 1989.

[111] R. Menikoff, "Pore collapse and hot spots in HMX," in *Shock Compression of Condensed Matter - 2003, Pts 1 and 2, Proceedings*. vol. 706, M. D. Furnish, *et al.,* Eds., ed Melville: Amer Inst Physics, 2004, pp. 393-396.

[112] A. Barua, Y. Horie, and M. Zhou, "Microstructural level response of HMX–Estane polymer-bonded explosive under effects of transient stress waves," *Proceedings of the Royal Society A: Mathematical, Physical and Engineering Science*, vol. 468, pp. 3725-3744, 2012.

[113] N. N. Semenov, *Z. Physik,* vol. 20, 1928.

[114] D. A. Kamenetskii, *Zhur. Fiz. Khim.,* vol. 13, 1939.

[115] P. H. Thomas, "On the Thermal Conduction Equation for Self-Heating Materials with Surface Cooling.," *Trans. Faraday Soc.* , vol. 54, pp. 60-65, 1958.

[116] P. Gray and J. C. Lee, "The Combustion of Gaseous Hydraziene," *Transactions of the Faraday Society,* vol. 50, pp. 719-728, 1954.

[117] P. Gray and P. R. Lee, "Thermal Explosions and Effect of Reactant Consumtion on Critical Conditions," *Combustion and Flame,* vol. 9, pp. 201-&, 1965.

[118] T. Boddington, P. Gray, W. Kordylewski, and S. K. Scott, "Thermal Explosions with Extensive Reactant Consumption - A New Criterion for Criticality," *Proceedings of the Royal Society of London Series a-Mathematical Physical and Engineering Sciences,* vol. 390, pp. 13-30, 1983.

[119] T. Boddington, P. Gray, and G. C. Wake, "Criteria for Thermal Explosions with and without Reactant Consumption," *Proceedings of the Royal Society of London Series a-Mathematical Physical and Engineering Sciences,* vol. 357, pp. 403-422, 1977.

[120] A. Barua, S. Kim, Y. Horie, and M. Zhou, "Ignition Criterion for Heterogeneous Energetic Materials Based on Hotspot Size-Temperature Threshold," *J. Appl. Phys.,* vol. 113, pp. 064906-064906-22, 2013.

[121] H. E. Alper and P. Politzer, "Molecular dynamics simulations of the temperature-dependent behavior of aluminum, copper, and platinum," *International Journal of Quantum Chemistry,* vol. 76, pp. 670-676, Feb 2000.

[122] B. H. Zimm, "The Scattering of Light and the Radial Distribution Function of High Polymer Solutions," *Journal of Chemical Physics,* vol. 16, pp. 1093-1099, 1948.

[123] G. Mason, "Radial Distribution Functions from Small Packing of Spheres," *Nature,* vol. 217, pp. 733-&, 1968.

[124] G. X. Li, Y. F. Liang, Z. G. Zhu, and C. S. Liu, "Microstructural analysis of the radial distribution function for liquid and amorphous Al," *Journal of Physics-Condensed Matter,* vol. 15, pp. 2259-2267, Apr 2003.

[125] J. J. Dick, A. R. Martinez, and R. S. Hixson, "Plane impact response of PBX 9501 and its components below 2 GPa," Los Alamos National Lab., NM (United States)1998.

[126] A. G. Xu, G. C. Zhang, P. Zhang, X. F. Pan, and J. S. Zhu, "Dynamics and Thermodynamics of Porous HMX-like Material Under Shock," *Commun. Theor. Phys.,* vol. 52, pp. 901-908, Nov 2009.

[127] S. D. Herring, T. C. Germann, and N. Gronbech-Jensen, "Effects of void size, density, and arrangement on deflagration and detonation sensitivity of a reactive empirical bond order high explosive," *Phys. Rev. B,* vol. 82, Dec 2010.

[128] R. W. Armstrong, C. S. Coffey, V. F. Devost, and W. L. Elban, "Crystal Size Dependence for Impact Initiation of Cyclotrimethylenetrinitramine Explosive " *J. Appl. Phys.,* vol. 68, pp. 979-984, Aug 1990.

[129] H. Czerski and W. G. Proud, "Relationship between the morphology of granular cyclotrimethylene-trinitramine and its shock sensitivity," *J. Appl. Phys.,* vol. 102, p. 113515, 2007.

[130] P. M. Howe, R. B. Frey, B. Taylor, and V. Boyle, "Shock Initiation and the Critical Energy Concept " *Sixth Symposium (International) on Detonation,* pp. 11-19, 1976 1976.

[131] S. Lecume, C. Spyckerelle, and F. Sommer, "Structure of Pristine Crystal Defects Revealed by AFM and Microtomography," *AIP Conference Proceedings,* vol. 706, pp. 997-1000, 2004.

[132] A. Chakravarty, M. J. Gifford, M. W. Greenaway, W. G. Proud, and J. E. Field, "Factors affecting shock sensitivity of energetic materials," in *Shock Compression of Condensed Matter-2001, Pts 1 and 2, Proceedings*. vol. 620, M. D. Furnish, *et al.*, Eds., ed, 2002, pp. 1007-1010.

[133] H. R. James, "Shock initiation thresholds for insensitive high explosives," in *Shock Compression of Condensed Matter - 2007, Pts 1 and 2*. vol. 955, M. Elert, *et al.*, Eds., ed Melville: Amer Inst Physics, 2007, pp. 937-940.

[134] H. R. James, R. J. Haskins, and M. D. Cook, "Prompt shock initiation of cased explosives by projectile impact," *Propellants Explos. Pyrotech.,* vol. 21, pp. 251-257, Oct 1996.

[135] K. Terao, *Irreversible Phenomena Ignitions, Combustion and Detonation Waves*. Berlin, Heidelberg :: Springer-Verlag Berlin Heidelberg, 2007.

[136] T. B. Brill and K. J. James, "Kinetics and mechanisms of thermal decomposition of nitroaromatic explosives," *Chemical reviews,* vol. 93, pp. 2667-2692, 1993.

[137] J. Gilbert and K. A. Gonthier, "Meso-Scale Computation of Uniaxial Waves in Granular Explosive-Analysis of Deformation Induced Ignition," *50th AIAA Aerospace Sciences Meeting including the New Horizons Forum and Aerospace Exposition*, p. 12, 2012.

[138] A. Barua, S. Kim, Y. Horie, and M. Zhou, "Prediction of Probabilistic Ignition Behavior of PBXs from Microstructural Stochasticity," *J. Appl. Phys.*, vol. 113, pp. 184907-20, 2013.

[139] W. Weibull, "A statistical distribution function of wide applicability," *Journal of applied mechanics*, vol. 18, pp. 293-297, 1951.

[140] R. Wild and E. von Collani, "Modelling of Explosives Sensitivity Part 2: The Weibull-Model," *Economic Quality Control,* vol. 17, pp. 195-220, 2002.

[141] R. Eckhoff, M. Ngo, and W. Olsen, "On the minimum ignition energy (MIE) for propane/air," *J. Hazard. Mater.,* vol. 175, pp. 293-297, 2010.

[142] G. Snedegor and W. G. Cochran, "Statistical methods," *Statistical methods.*, 1967.

[143] R. Wild and E. von Collani, "Modelling of Explosives Sensitivity Part 1: The Bruceton Method," *Economic Quality Control,* vol. 17, pp. 113-122, 2002.

[144] Y. Li and M. Zhou, "Prediction of fracture toughness of Ceramic composites as function of microstructure: I. Numerical Simulations," *J. Mech. Phys. Solids*, 2012.

[145] M. Tsue, T. Kadota, D. Segawa, and H. Yamasaki, "Statistical analysis of onset of microexplosion for an emulsion droplet," in *Symposium (International) on Combustion*, 1996, pp. 1629-1635.

[146] S. K. Chidester, C. M. Tarver, and R. Garza, "Low amplitude impact testing and analysis of pristine and aged solid high explosives," in *Eleventh (International) Symposium on Detonation, ONR*, 1998, pp. 33300-5.

[147] J. J. Dick, "Measurement of the Shock Initiation Sensitivity of Low-Density HMX," *Combustion and Flame,* vol. 54, pp. 121-129, 1983.

[148] D. Preston, G. Brown, C. B. Skidmore, B. L. Reardon, and D. A. Parkinson, "Small-scale explosives sensitivity saftey testing: A departure from Bruceton," in *AIP Conference Proceedings*, 2012, p. 713.

[149] Y. Ko, R. Anderson, and V. S. Arpaci, "Spark ignition of propane-air mixtures near the minimum ignition energy: Part I. An experimental study," *Combustion and Flame*, vol. 83, pp. 75-87, 1991.

[150] H. Rinne, "Parameter estimation — Maximum likelihood approaches " in *The Weibull Distribution*, ed: Chapman and Hall/CRC, 2008, pp. 402-454.

[151] Y. Hamate, "A computational study of microstructure effects on shock ignition sensitivity of pressed RDX," in *AIP Conference Proceedings*, 2007, p. 923.

[152] L. J. Wen, Z. P. Duan, L. S. Zhang, Z. Y. Zhang, Z. C. Ou, and F. L. Huang, "Effects of HMX Particle Size on the Shock Initiation of PBXC03 Explosive," *Int. J. Nonlinear Sci. Numer. Simul.,* vol. 13, pp. 189-194, 2012.

[153] D. B. Hardin, J. J. Rimoli, and M. Zhou, "Thermomechanical Response of HMX Polycrystals to Simulated Impact Loading," *Bulletin of the American Physical Society*, vol. 58, 2013.

[154] J. Lloyd, J. Clayton, and D. McDowell, "Modeling Single-Crystal Microstructure Evolution due to Shock Loading," *Bulletin of the American Physical Society*, vol. 58, 2013.

[155] R. Menikoff and T. D. Sewell, "Constituent properties of HMX needed for mesoscale simulations," *Combustion Theory and Modelling*, vol. 6, pp. 103-125, 2002.

[156] T. D. Sewell, R. Menikoff, D. Bedrov, and G. D. Smith, "A molecular dynamics simulation study of elastic properties of HMX," *Journal of Chemical Physics*, vol. 119, pp. 7417-7426, Oct 2003.

[157] J. M. Zaug, "Elastic constants of β-hmx and tantalum, equations of state of supercritical fluids and fluid mixtures and thermal transport determinations," in *Proceedings of the 11th detonation symposium*, 1998.

[158] D. L. McDowell, J. Panchal, H.-J. Choi, C. Seepersad, J. Allen, and F. Mistree, *Integrated design of multiscale, multifunctional materials and products*: Butterworth-Heinemann, 2009.

[159] D. L. McDowell, H. J. Choi, J. Panchal, R. Austin, J. Allen, and F. Mistree, "Plasticity-related microstructure-property relations for materials design," *Key Engineering Materials*, vol. 340, pp. 21-30, 2007.

[160] D. L. McDowell, "Simulation-assisted materials design for the concurrent design of materials and products," *JOM*, vol. 59, pp. 21-25, 2007.